Investigation of Parameter Estimation Methodologies for Deadbeat-Direct Torque and Flux Control of IMs using Back-EMF Tracking for Motion Self-Sensing

by

Kang Wang

A dissertation submitted in partial fulfillment of

the requirement for the degree of

Doctor of Philosophy

Mechanical Engineering

at the

UNIVERSITY OF WISCONSIN – MADISON

August 2018

Data of final oral examination: 08/21/2018

The dissertation is approved by the following member of the Oral Committee:

Lorenz, Robert D., Professor, Mechanical Engineering

Jahns, Thomas M., Professor, Electrical Computer and Engineering

Zinn, Michael R., Associate Professor, Mechanical Engineering

Negrut, Dan, Professor, Mechanical Engineering

Bulent, Sarlioglu, Associate Professor, Electrical Computer and Engineering

Abstract

The objective of this research is to investigate a real-time parameter estimation system including two parameter estimation methodologies – injection-based method and model reference adaptive system (MRAS) method – to optimize the drive performance of induction machines (IM) deadbeat-direct torque and flux control (DB-DTFC) using encoder feedback and back-EMF tracking velocity feedback, including operation at low speeds.

The proposed investigations will also focus on developing on-line and off-line methodologies that take advantage of the torque and flux linkage decoupling of properly tuned DB-DTFC drives.

As part of this research, existing MRAS-based and signal injection-based methods used on field oriented controlled (FOC) drives using back-EMF/flux tracking vector controlled induction motor drive technologies will be used as the baseline to identify the achievable improvements.

This dissertation lays a foundation for integrating a real-time parameter estimation system with DB-DTFC into commercial IM drives. The outcome is an operating region-based control structure that combines two real-time parameter estimation techniques to achieve high speed and torque command tracking bandwidth with IM DB-DTFC drives that will have high dynamic stiffness over a wide operating range in self-sensing mode.

Acknowledgments

First, I would thank Professor Robert D. Lorenz for an opportunity to study at Wisconsin Electric Machines and Power Electronics Consortium (WEMPEC). His thoughts, support, and sprite motivated me to explore my graduate study and the research topics. In my research, his understanding and patience helped me to overcome difficulties. In my graduate life, his encouragement and guidance helped me to find out what kind of person I want to be. He taught me to have focus and dedication to the things I do, to have the courage to follow the heart, to pursuing a dream no matter how hard things are and to have unconditional caring and helping others. I feel really blessed that I went through this very important stage of my career with him. I deeply appreciate and am honored with the opportunities to work with him.

Second, I would like to thank Yaskawa Electric Corporation and Yaskawa America, Inc., for sponsoring this project. I would thank Noor Baloch, Dave Cisler, Shinya Morimoto and Steven Schifko, for their help. I appreciate the research opportunities and the time working with them.

Third, I would thank the committee members, Professor Thomas M. Jahns, Professor Michael R. Zinn, Prof. Dan Negurt and Prof. Bulent Sarlioglu for comments and suggestions on this thesis.

Fourth, I would thank WEMPEC family for helping me on this project and making a memorable experience.

I would like to thank Demont Helene, Jim Sember, Kyle Hanson, Ray Marion, Julie Spitzer, Naomi Welter and Kathy Young to make the graduate program successful.

I would thank many WEMPEC students who have direct or indirect contributions for this thesis: Muhammad Alvi, Le Chang, Zhe Chen, Hang Dai, Dan Erato, Huthaifa Flieh, Zheng Gao, Austin Gaspar, Aditya Ghule, Hasan Hakim, Ryoko Imamura, Ye Gu Kang, Shang-Chuan Lee, Mingda Liu, Wenbo Liu, Peter Meyer, Hung-Yen Ou-Yang, Marc Petit, Tim Polom, Gene Rush, Minhao Sheng, Yuying Shi, Tim Slininger, Yang Xu, Ruxiu Zhao, Hao Zheng and Guangqi Zhu. They provided me with many inspiring discussions and enjoyable moments.

I also thanks those students who have already graduated at the time of writing: Athavale Apoorva, Chris Bouxsein, Tyler Braun, Jiejian Dai, Cong Deng, Brent Gagas, Baoyun Ge, Di Han, Jae-Suk Lee, Hao Jiang, Silong Li, Ye Li, Yingjie Li, Jianyang Liu, Larry Juang, He Niu, Caleb Secrest, Boru Wang, Jiyao Wang, Kenan Wang, Yukai Wang, Teng Wu, Wei Xu, Yinghan Xu, Yida Yang, Chen-yen Yu, Yichao Zhang, Junjian Zhao, Ruonan Zhou and Bo Zhu,

I would thank my parents in China. They have supported me greatly.

Lastly, I would like to give special thanks to my wife, Xin S. Wang, and my daughter, Joy S. Wang, for supporting, accompanying and understanding.

Table of Contents

Nomenclature

Symbol	Description
$\underline{v}_{qds}$	stator voltage complex space vector
v_{ds}	d-axis stator voltage
v_{qs}	q-axis stator voltage
$\underline{i}_{qds}$	stator current complex space vector
i_{ds}	d-axis stator current
i_{qs}	q-axis stator current
$\underline{\lambda}_{qds}$	stator flux linkage complex space vector
λ_{ds}	d-axis stator flux linkage
λ_{qs}	q-axis stator flux linkage
$\underline{\Psi}_{qds}$	stator flux voltage complex space vector
ψ_{ds}	d-axis stator flux voltage
ψ_{qs}	q-axis stator flux voltage
T_e	electromagnetic torque
T_L	load torque
J_p	moment of inertia
P_{rated}	rated power
V_{rated}	rated voltage
I_{rated}	rated current
f_{rated}	rated frequency

T_{rated}	rated torque
ω_{rated}	rated angular velocity
s_{rated}	rated slip
P_B	base power
V_B	base voltage
I_B	base current
Z_B	base impedance
T_B	base torque
ω_B	base angular velocity
j	complex number $\sqrt{-1}$
ω	angular velocity [rad/s]
ω_e, θ_e	synchronous/excitation angular frequency [rad/s], position [rad]
ω_r, θ_r	rotor angular frequency [rad/s], position [rad]
R_s	stator resistance [Ω]
R_r	rotor resistance [Ω]
L_{ls}	stator leakage inductance [H]
L_{lr}	rotor leakage inductance [H]
L_m	magnetizing inductance [H]
L_s	stator inductance $L_s = L_m + L_{ls}$ [H]
L_r	rotor inductance $L_r = L_m + L_{lr}$ [H]
σ	leakage factor $\sigma = 1 - L_m^2/(L_sL_r)$
P	pole number
T_s	sample period
$\underline{a}$	space vector rotation operator $\underline{a} = \exp(j2\pi/3)$

s	Laplace operator
p	differential operator d/dt

Superscripts

$(\ )^{s}$	stationary reference frame
$(\ )^{r}$	rotor reference frame
$(\ )^{e}$	excitation reference frame
$(\ )$	arbitrary reference frame
$\hat{(\ )}$	estimated quantity
$(\ )^{*}$	reference quantity
$\dot{(\ )}$	time derivative operator d/dt ( )

Subscripts

$(\ )_{s}$	Stator
$(\ )_{r}$	Rotor
$(\ )_{dqx}$	complex vector

Block Diagrams

summation

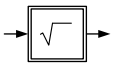

nonlinear operation/equation

multiplication

linear operator/gain

division

vector cross product

Abbreviations

WEMPEC	Wisconsin Electric Machine and Power Electronic Consortium
IM	induction machine
FOC	field oriented control
DFOC	direct-field oriented control
IFOC	indirect-field oriented control
DB-DTFC	deadbeat direct torque and flux control
VSI	voltage source inverter
IGBT	insulated-gate bipolar transistor
PWM	pulse-width modulation
SPWM	carrier-based sinusoidal pulse-width modulation
SVPWM	space vector pulse-width modulation
BPF	bandpass filter

Introduction

This section provides the research overview, research contributions and chapter summaries.

Research Project Background

A previous research included the fundamentals of DB-DTFC and its inherent decoupling of single step dynamic torque production from single step flux linkage changes. This decoupling means that flux signals can be injected along the DB-DTFC torque line without affecting torque ripple [1]–[3].

Prior UW-Madison research identified how model reference adaptive control (MRAC) techniques can be used to tune IM FOC drives by forcing the rotor flux linkage estimated from the current model to converge on that estimated by the voltage model. This basic principle can also be applied to stator flux linkage. Subsequent UW-Madison research documented that this approach enables DB-DTFC to achieve substantially superior parameter insensitivity compared to that of FOC, especially at high speeds.

Synchronous frame voltage injection methods for parameter estimation were also developed in previous UW-Madison research and are inherently appropriate for IM FOC drives. However, ripple torque is generally induced by voltage injection methods, and it is difficult to fully decouple this in FOC drives. By comparison, flux linkage injection along the DB-DTFC torque line should inherently produce zero torque ripple, and thus, torque ripple can be forced to be zero by proper estimation. This property is a key focus of the proposed work.

Research Contributions

Key contributions of this research are summarized as follows:

- Developed an operating region-based parameter estimation system integrates both MRAS-based and flux injection-based parameter estimation methods and estimates a full set of machine parameters over a wide operating range in the back-EMF based self-sensing mode.
- Developed a general solution for MRAS-based and flux injection-based parameter estimation in induction machine DB-DTFC drive with encoder feedback.
- Developed two approaches (high pass filter approach and injection signal decoupling approach) to reduce the erroneous and real speed ripple of the injection-based parameter estimation in self-sensing mode.

- Developed an electrical position estimation system to improve the signal quality of positive and negative sequence components/harmonics for flux injection-based parameter estimation.
- Development of back-EMF based self-sensing via observer in IM DB-DTFC, which includes back-EMF state filter, back-EMF tracking observer and cascaded motion observer.
- Developed the speed dependent back-EMF state filter bandwidth method to improve back-EMF self-sensing performance at low operating speeds.

Summary of Chapters

Chapter 1 reviews the state-of-the-art induction machine control strategies including current observers, flux observers, indirect field oriented control (IFOC), direct torque control (DTC), and deadbeat-direct torque and flux control (DB-DTFC). The different self-sensing methods and different parameter estimation methods in IM drives are also reviewed in this chapter. In the end, the opportunities are identified for this research.

Chapter 2 describes details of experimental hardware setup and DB-DTFC implementation. Machine parameters, hardware topology, and sensor gains are included in this chapter.

Chapter 3 presents the parameter sensitivity, including L_m, R_r, R_s, L_{ls}, and L_{lr}, for DB-DTFC with and without encoder feedback over a wide speed range. Compared the parameter sensitivity of DB-DTFC and IFOC drives by estimated torque and measured torque. It also includes system robustness of back-EMF tracking based self-sensing for DB-DTFC drives. In the end, the speed depended back-EMF state filter bandwidth is proposed for the improvement of the self-sensing performance.

Chapter 4 illustrates the methodology of both injection-based and MRAS-based parameter estimation of DB-DTFC and IFOC drives respectively. The appropriate injected carrier frequency selection method and the signal processing procedures are depicted in this chapter. In the latter part, it proposes the MRAS gains tuning methodology. It also presents the T-N test improvements with the real-time parameter estimation.

Chapter 5 presents the methodology of the injection-based and MRAS-based parameter estimation in the self-sensing mode. It starts with the further improvement of the injection based parameter estimation method. Then, it identifies the issues of the injection-based method in the self-sensing mode. The high pass filter method and the decoupling method are proposed for solving the problem. In the end, the MRAS-based method in the self-sensing mode is evaluated.

Chapter 6 presents the differences in performance between the two parameter estimation methods in both self-sensing mode and encoder feedback mode for DB-DTFC drives. The improvements of the two methods are identified. In addition, the absolute and relative DSP computational load for each method are evaluated.

Chapter 7 presents a real-time parameter estimation system by utilizing the advantages of the two parameter estimation methods: MRAS-based method and flux injection-based method. The system selects different methods at different operating regions with a certain executive sequence.

Chapter 8 presents two metrics to evaluate the system dynamics: the torque command tracking approach and the speed command tracking approach. The system torque command tracking and speed command tracking bandwidth are compared and analyzed with and without the proposed machine parameter system. The system dynamics improvements are also illustrated with the real-time parameter estimation system.

Chapter 9 presents the research conclusions and contributions to date and the planned future work.

Chapter 1

State-of-the-Art-Review

This chapter begins with the fundamentals of induction machine modeling, which provide a basis for further control algorithm discussion. Next, the discrete time current observer, flux observer, and motion observer technologies are depicted. Then, the algorithms for indirect field oriented control (IFOC), deadbeat-direct torque and flux control (DB-DTFC) will be reviewed and compared. The DB-DTFC algorithm for an IM drive system is illustrated both mathematically and graphically. Solutions for the voltage limited operation of DB-DTFC are presented. Then, the existing self-sensing technologies for an induction machine are reviewed. The research opportunities are presented at the end of this chapter.

1.1 Induction Machine Modeling

This section will present the basic mathematical model for an induction machine. In most industrial applications, three-phase symmetrical wound induction machines are commonly used. An electrical equivalent circuit for a three-phase induction machine has been shown in Fig. 1.1-1, where the rotor side quantities, including rotor leakage inductance and rotor resistance, have been transformed to the stator side [4]. This electric model has been

widely used for induction machine analysis. Based on this model, more sophisticated induction machine control technologies have been developed.

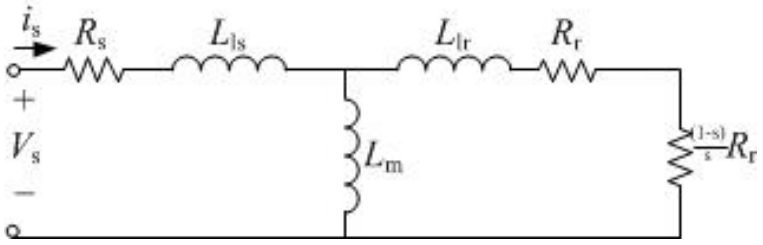

Fig. 1.1-1 Induction machine steady-state equivalent circuit

For a wound machine control system, the original three-phase reference frame can be transformed into two-phase notation or d-q reference frame. While the d-q transformations definitions are various, the transformation used in this thesis is given in (1.1-1), with the definition of rotation vector in (1.1-2). It is based on the assumption that the three phases are balanced [5].

$$\frac{2}{3}(f_a + af_b + a^2 f_c) = f_{qd} = f_q - jf_d \tag{1.1-1}$$

$$a = e^{\,j2\pi/3} \tag{1.1-2}$$

The transformation matrix of the three-phase reference frame to the stationary q-d reference frame is given in equation (1.1-3), which is equivalent to (1.1-1).

$$\begin{bmatrix} f_{qs}^{s} \\ f_{ds}^{s} \end{bmatrix} = \begin{bmatrix} \frac{2}{3} & -\frac{1}{3} & -\frac{1}{3} \\ 0 & -\frac{1}{\sqrt{3}} & \frac{1}{\sqrt{3}} \end{bmatrix} \begin{bmatrix} f_{as} \\ f_{bs} \\ f_{cs} \end{bmatrix} \tag{1.1-3}$$

The transformations from the stationary d-q axis to any arbitrary reference frame can be derived by (1.1-4). The angle θ represents the angle from the stationary reference frame to the arbitrary reference frame. For convenience, it is common to use a synchronous reference frame (1.1-5) and rotor reference frame (1.1-6). They are based on equation (1.1-4).

$$\begin{bmatrix} f_{qs}^{a} \\ f_{ds}^{a} \end{bmatrix} = \begin{bmatrix} \cos\theta & \sin\theta \\ -\sin\theta & \cos\theta \end{bmatrix} \begin{bmatrix} f_{qs}^{s} \\ f_{ds}^{s} \end{bmatrix} \tag{1.1-4}$$

$$\begin{bmatrix} f_{qs}^{e} \\ f_{ds}^{e} \end{bmatrix} = \begin{bmatrix} \cos\theta_e & \sin\theta_e \\ -\sin\theta_e & \cos\theta_e \end{bmatrix} \begin{bmatrix} f_{qs}^{s} \\ f_{ds}^{s} \end{bmatrix} \tag{1.1-5}$$

$$\begin{bmatrix} f_{qs}^{r} \\ f_{ds}^{r} \end{bmatrix} = \begin{bmatrix} \cos\theta_r & \sin\theta_r \\ -\sin\theta_r & \cos\theta_r \end{bmatrix} \begin{bmatrix} f_{qs}^{s} \\ f_{ds}^{s} \end{bmatrix} \tag{1.1-6}$$

Based on the transformations defined above, it is possible to transform all electrical and magnetic variables including voltages, currents, and fluxes to any arbitrary d-q reference frame [5]. Fig. 1.1-2 shows the complex vector model for the induction machine. The ω is the arbitrary reference frame speed. In the stationary reference frame, ω is zero, while in the rotor reference frame, ω is equal to the rotor speed, ω_r .

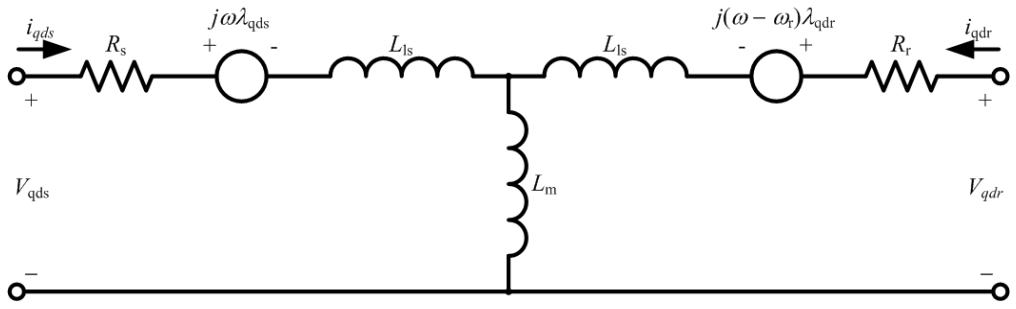

Fig. 1.1-2 Complex vector induction machine equivalent circuit [5]

The stator (λ_{qds}) and rotor (λ_{qdr}) fluxes shown in Fig. 1.1-2 are defined as functions of stator inductance (L_s), rotor inductance (L_r), and magnetizing (L_m) inductance and stator and rotor currents (i_{qds}, i_{qdr}), where R_s and R_r are stator and rotor resistance, as shown from (1.1-7)-(1.1-10). The electromagnetic torque is shown in (1.1-11). [5]

Definitions of flux linkages:

$$\lambda_{qds} = L_s\, i_{qds} + L_m\, i_{qdr} \tag{1.1-7}$$

$$\lambda_{qdr} = L_m\, i_{qds} + L_r\, i_{qdr} \tag{1.1-8}$$

Flux linkage differential equations:

$$\dot{\lambda}_{qds} = v_{qds} - R_s\, i_{qds} - j\omega\lambda_{qds} \tag{1.1-9}$$

$$\dot{\lambda}_{qdr} = -R_r\, i_{qdr} - j(\omega - \omega_r)\, \lambda_{qdr} \tag{1.1-10}$$

Torque equations:

$$T_e = \frac{3P}{4}\frac{L_m}{L_r}(i_{qs}\lambda_{dr} - i_{ds}\lambda_{qr}) = \frac{3P}{4}\frac{L_m}{\sigma L_s L_r}(\lambda_{qs}\lambda_{dr} - \lambda_{ds}\lambda_{qr}) \tag{1.1-11}$$

It should be noted that the electromagnetic torque of induction machine expression is not limited by (1.1-11). Instead, it can be represented by combinations of stator current, rotor current, stator flux linkage and rotor flux linkage, depending on different analysis purposes[5].

1.2 Flux and Current Observers

Based on the induction machine modeling, it is known that flux linkages play a key role in IM drives. In some electrical drives, flux linkages (λ_{qds} and λ_{qdr}) are often used as control

variables. It is because the electromagnetic torque is a function of the stator, rotor flux linkages and currents. However, it is impossible to measure the flux linkage of the induction machine directly. Thus, in order to obtain the flux linkage value for each sample instant, a discrete time flux linkage observer should be built [6], [7].

Several kinds of flux observer structures have been proposed [8]–[13]. There are three popular categories: the current model based flux observer, the voltage model based flux observer, and the current and voltage model combination style flux observer.

1.2.1 A Current Model-Based Flux Observer

Based on equations (1.1-9) and (1.1-10), the basic equation for the current model flux observer can be derived as follows:

$$\dot{\lambda}_{qdr} = \frac{R_r}{L_r} L_m \, i_{qds} - \left(\frac{R_r}{L_r} + j\omega - j\omega_r\right) \lambda_{qdr} \qquad (1.2\text{-}1)$$

By choosing the rotor reference frame, (1.2-1) can be simplified as (1.2-2).

$$\dot{\lambda}_{qdr} = \frac{R_r}{L_r} L_m \, i_{qds} - \frac{R_r}{L_r} \lambda_{qdr} \qquad (1.2\text{-}2)$$

The simplified equation for the rotor flux is shown in (1.2-2), which is the basic equation for an open-loop rotor flux observer. The corresponding state block diagram is given in Fig. 1.2-1.

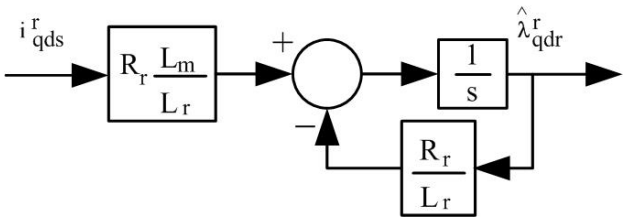

Fig. 1.2-1 Block diagram of rotor flux linkage calculated from the stator current and evaluated in the rotor reference frame [6]

Based on the estimated rotor flux linkage value, stator flux linkage can be estimated. The relationships between the stator flux linkage and the rotor flux linkages are shown in (1.2-3) and (1.2-4).

$$\lambda_{qds} = \frac{L_m}{L_r}\lambda_{qdr} + \sigma i_{qds} \tag{1.2-3}$$

$$\sigma = 1 - \frac{L_m^2}{L_s L_r} \tag{1.2-4}$$

The block diagram of the current model based flux observer in the continuous time domain is shown in Fig. 1.2-2. It was built in the stationary reference frame and the transformation to the rotor reference frame has been included in Fig. 1.2-2. The observer is in an open-loop control. This kind of observer is also highly sensitive to parameters (e.g. magnetizing inductances, stator resistance and rotor resistance) [6].

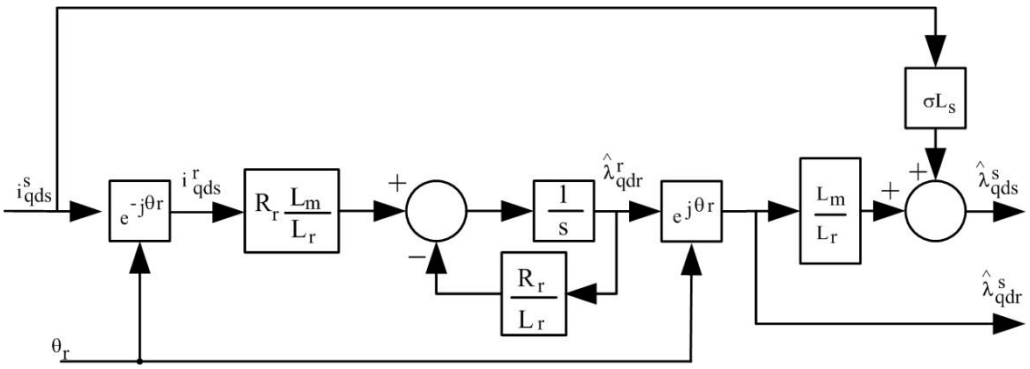

Fig. 1.2-2 Open-loop flux estimator using stationary frame current and rotor position [6]

1.2.2 A Voltage Model-Based Flux Observer

Another popular structure for a flux observer is based on stator voltage in the stationary reference frame. The stator flux linkage can be estimated by using the equation shown in (1.2-5).

$$\dot{\lambda}_{qds} = v^s_{qds} - R_s\, i^s_{qds} \tag{1.2-5}$$

Based on (1.2-5), the block diagram of a flux observer in a continuous time domain can be easily determined, which is shown in Fig. 1.2-3.

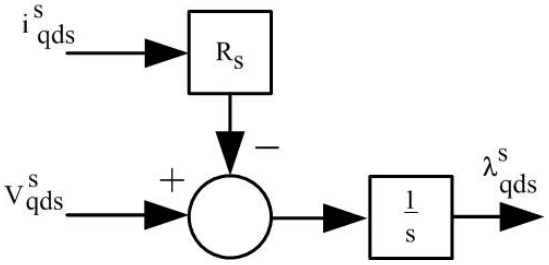

Fig. 1.2-3 Stationary frame stator flux linkage estimate, utilizing stator voltage and current [6]

Based on the figure shown above, the stator flux linkage estimates can be easily obtained. Then, the rotor flux linkage estimates can be found by the following relationship (1.2-6).

$$\lambda_{qdr} = \frac{L_r}{L_m}(\lambda_{qds} - \sigma i_{qds}) \qquad (1.2\text{-}6)$$

The state block diagram of this relationship is shown in Fig. 1.2-4

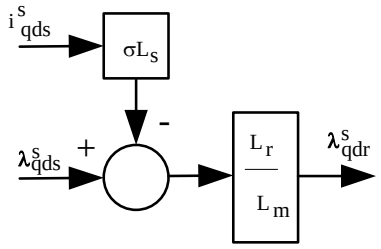

Fig. 1.2-4 Calculation of rotor flux linkage given stator flux linkage and stator current [6]

Fig. 1.2-3 and Fig. 1.2-4 can be combined into one single block diagram for both stator flux estimates and rotor flux estimates, which is shown in Fig. 1.2-5.

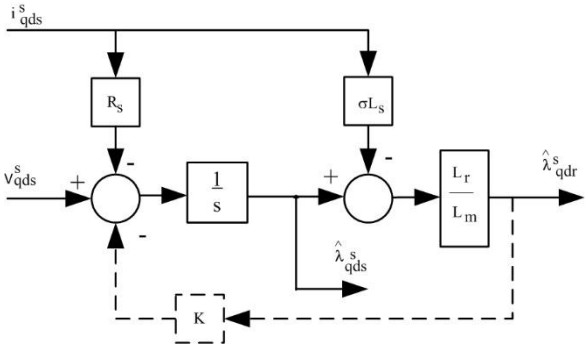

Fig. 1.2-5 Open loop stator and rotor flux linkage estimate, given stator voltage and stator current [6]

Generally, in industrial drives, no voltage sensor is used, and the commanded voltage is assumed to match the actual one. This is true during the motor medium and high-speed operations. However, during the low-speed operation, the commanded voltage will be different from the actual voltage, this due to the inverter non-linearities and dead-time effect.

Hence the voltage model flux observer estimates the flux based on the commanded voltage, the estimation accuracy of this kind of observer will be significantly degraded at low speeds operation [6].

1.2.3 Closed-Loop Flux Observer

A Gopinath style flux observer, shown in Fig. 1.2-6, is presented in this section. It is a combination of the current based flux observer and voltage based flux observer. This kind of flux observer takes advantage of both the current based flux observer and the voltage based flux observer. It can estimate the flux at both low speed and high speed[2].

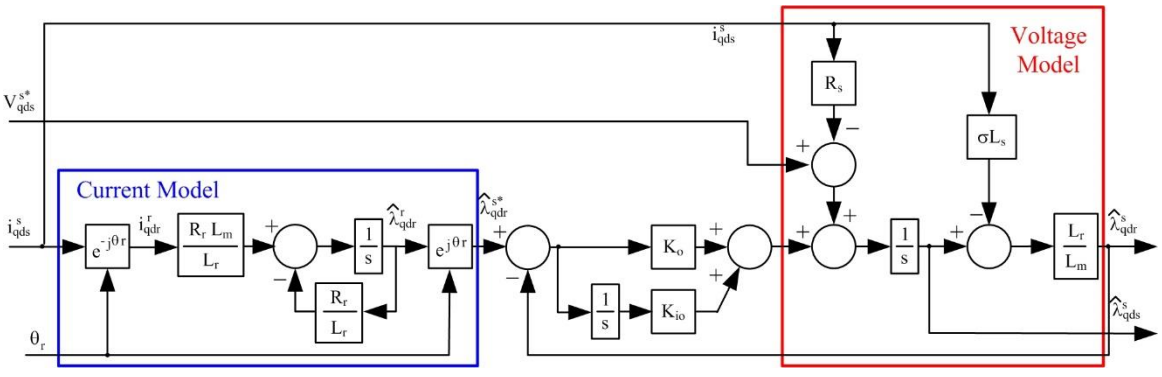

Fig. 1.2-6 Gopinath style flux observer in the continuous domain[2][6]

A PI-style controller has been placed in this Gopinath style flux observer in order to connect the current model and the voltage model. It is used to tune the bandwidth of the flux observer. The current model would dominate the flux estimates if frequency were below the bandwidth. Similarly, the voltage model would dominate the flux estimates if frequency were higher than the designed bandwidth. This was shown in previous work such as [6]–[8]. This kind of flux observer, it has been demonstrated, has high estimation accuracy with little phase delay. Estimation accuracy in the frequency domain is evaluated as in Fig. 1.2-7. Compared to high speed, the low-speed area is more sensitive to parameters, especially magnetizing inductance (L_m).

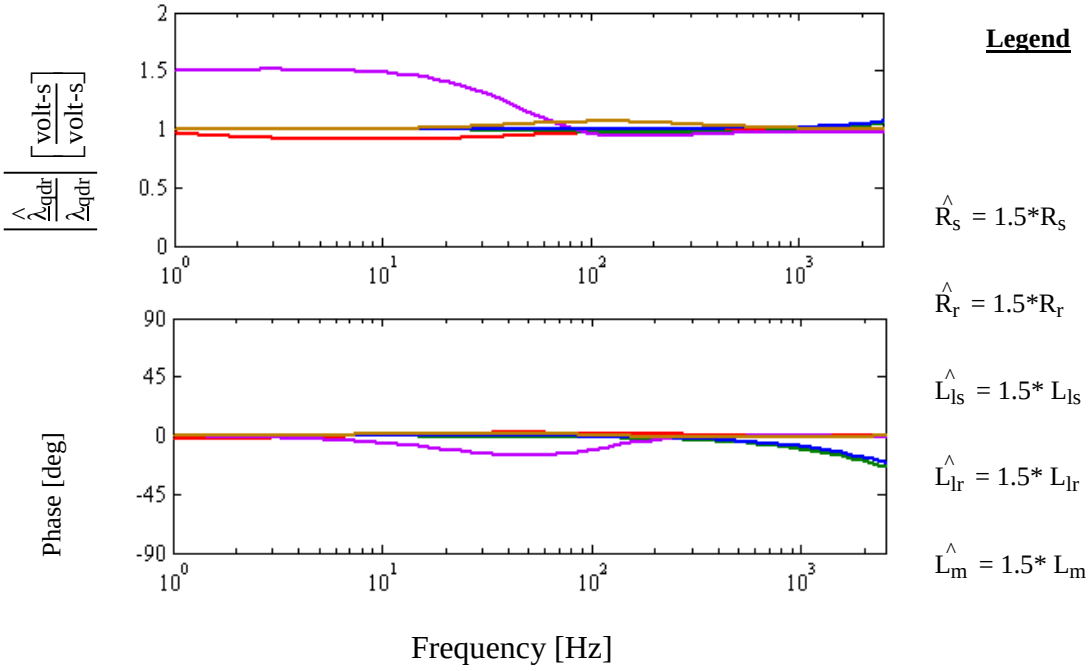

Fig. 1.2-7 Estimated accuracy of continuous time flux observer proposed in [2][6]

The discrete time block diagram of the Gopinath style flux observer can be developed in Fig. 1.2-8 [2], [12].

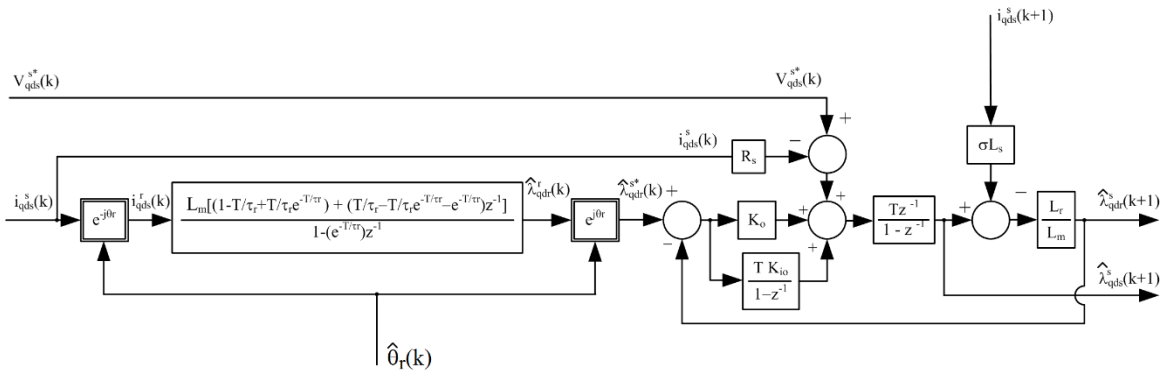

Fig. 1.2-8 Gopinath style flux observer in the discrete domain without flux observer [2]

To obtain an accurate flux estimate at the next sample instant, current estimates for the next sampling instant are necessary. Otherwise, the rotor flux estimates will be delayed by one sample instant. The relationship between rotor flux linkage and stator flux linkage in discrete time is shown as the following.

$$\lambda^{s}_{qdr}(k+1) = \frac{L_r}{L_m}\left(\lambda^{s}_{qds}(k+1) - \sigma L_s\, i^{s}_{qds}(k+1)\right) \tag{1.2-7}$$

The stator current differential equation is shown below [14].

$$\dot{i}_{qds} = \frac{1}{\sigma L_s}\left[v_{qds} - \left(R_s + \left(\frac{L_m}{L_r}\right)^2 R_r + j\sigma L_s\omega\right) i_{qds} + \frac{L_m}{L_r}\left(\frac{R_r}{L_r} - j\omega_r\right)\lambda_{qdr}\right] \tag{1.2-8}$$

Based on this equation, the stator current observer in d-axis and q-axis in continuous time can be depicted in Fig. 1.2-9.

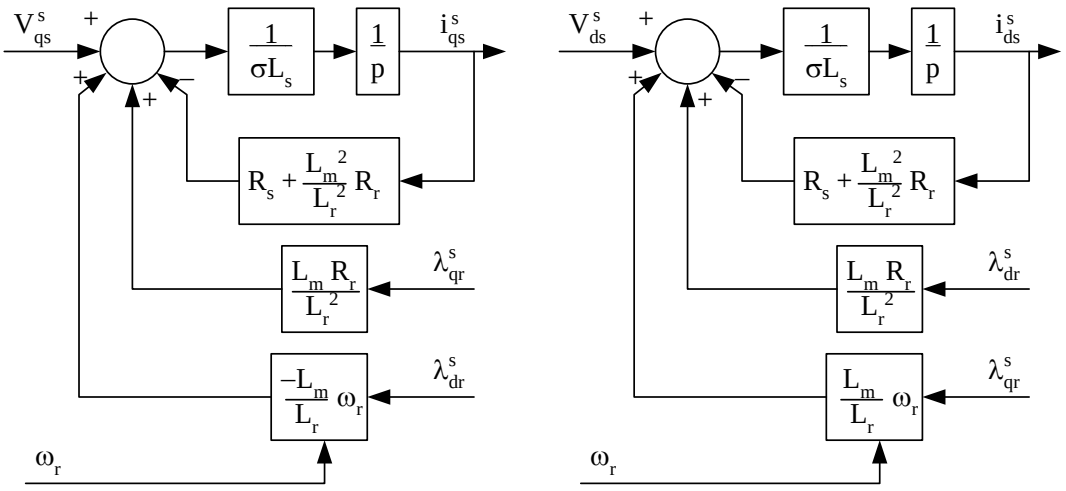

Fig. 1.2-9 Stator current non-linear state block diagram [3]

By adding the latch, the discrete time current observer represented in the complex vector can be provided in Fig. 1.2-10.

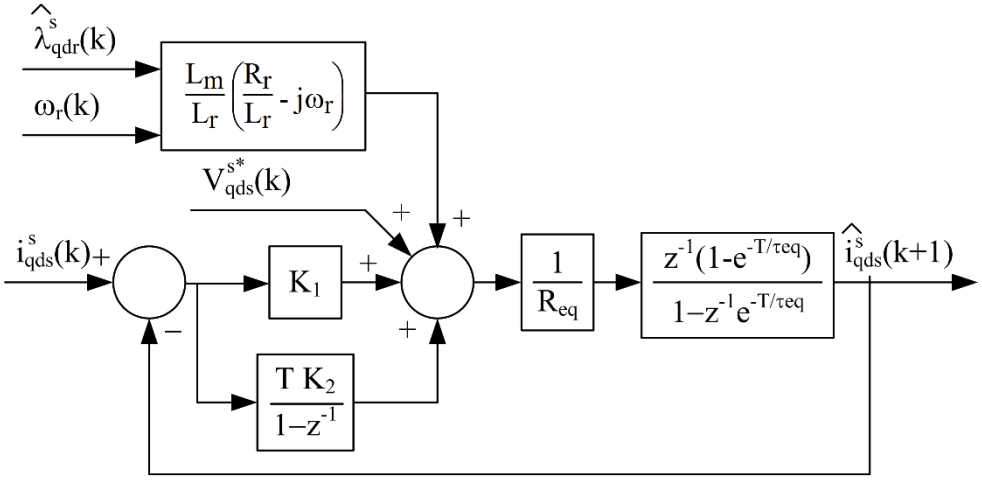

Fig. 1.2-10 Discrete time state block diagram of stator current observer [3]

The output of the current observer is stator current in the next sampling instant. If it was used in the Gopinath style flux observer, more accurate stator and rotor flux estimates would

be obtainable. The discrete time in the entire observer, which Gopinath style flux observer combines with the current observer, is shown in Fig. 1.2-11.

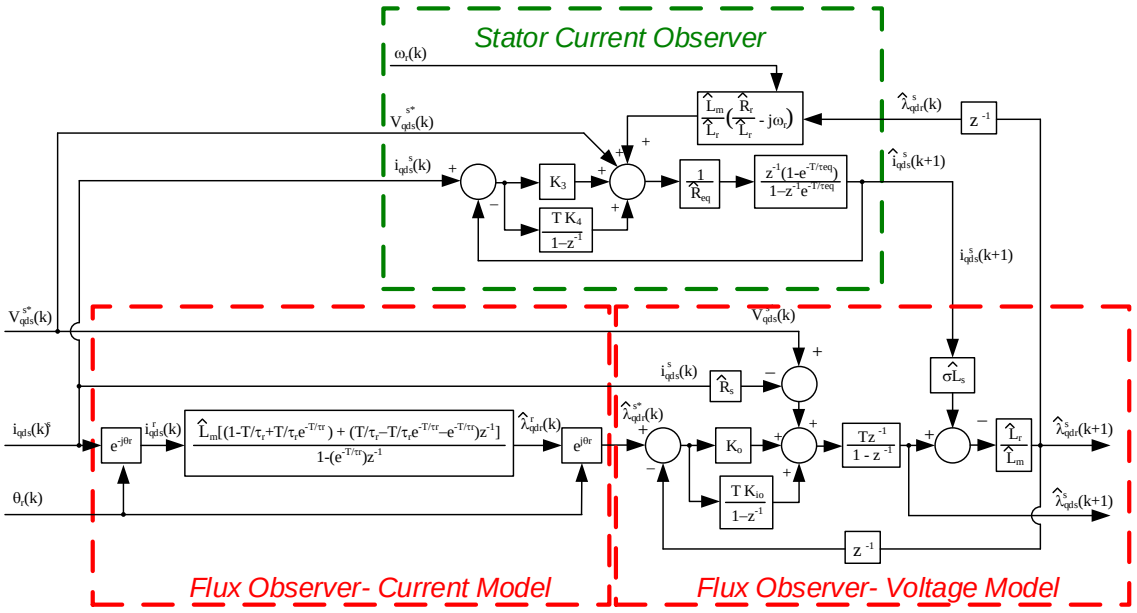

Fig. 1.2-11 The state block diagram of discrete time flux observer combining the current model, the voltage model, and the current observer [2]

The observer signal flow is shown in the following block diagram in Fig. 1.2-12.

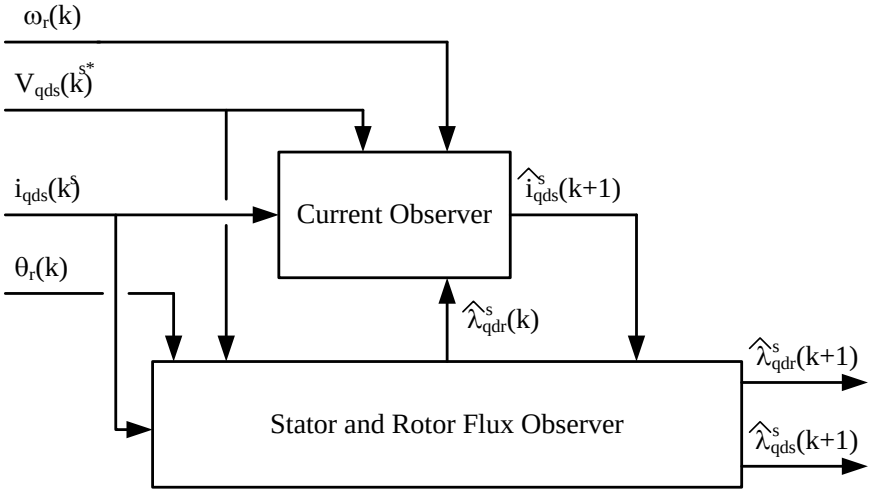

Fig. 1.2-12 Discrete time observer system signal flow [3]

1.3 Existing Control Methods for IM

1.3.1 Field Oriented Control

Field Oriented Control (FOC) has long been the norm for induction machine torque control due to its simplicity and high performance. The fundamental basis for FOC is to control the spatial orientation of electromagnetic fields within the machine. It is also referred to as vector control in some literature [4], [5]. This section aims to briefly outline FOC fundamentals and its practical implementations.

The equivalent circuit is shown in Fig. 1.1-2 is one induction machine circuit, created by changing the rotor side quantities into the stator side. An alternative equivalent circuit is given in Fig. 1.3-1. By selecting a particular turns ratio, leakage inductance on the rotor side can be contained in the magnetizing branch [4], [5].

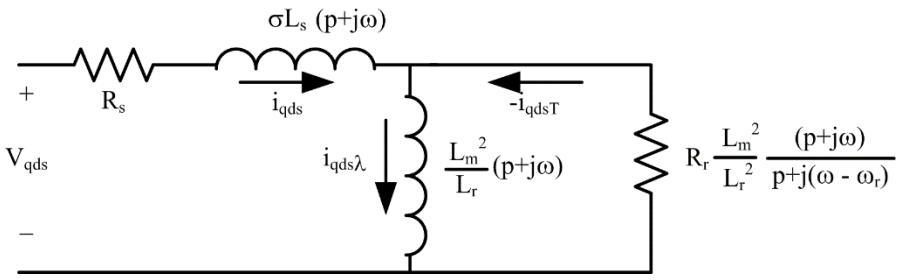

Fig. 1.3-1 Modified complex vector IM equivalent circuit without rotor inductance[4], [5]

From Fig 1.3-1, stator current has been split into two components: magnetizing flux production and torque production. The first component, magnetizing flux production, is purely

inductive, while its counterpart, torque production, is purely resistive. Conventionally, rotor flux linkage is aligned with the d-axis, and torque production current is aligned with the q-axis. Current regulators to control the d-axis and q-axis current are required for FOC. The references of d- and q-axis current can be computed based on desirable rotor flux and electromagnetic torque [4], [5].

The fundamental relationships to produce rotor flux and electromagnetic torque are provided as (1.3-1) and (1.3-2). Rotor flux, in steady-state, is exclusively determined by the d-axis current. For dynamic, the rotor time constant attempts to keep rotor flux linkage from instantaneous change. In addition, by perfect alignment, rotor flux linkage on the q-axis is zero so that the torque equation of (1.1-11) can be simplified as in (1.3-2).

$$\dot{\lambda}_{dr} = L_m \frac{R_r}{L_r} i_{ds} - \frac{R_r}{L_r} \lambda_{dr} \quad (1.3\text{-}1)$$

$$T_e = \frac{3P}{2} \frac{L_m}{L_r} \lambda_{dr} i_{qs} \quad (1.3\text{-}2)$$

1.3.2 Indirect Field Oriented Control with Current Vector Control

Physical implementations of FOC can be classified into two categories: Indirect Field Oriented Control (IFOC) and Direct Field Oriented Control (DFOC). IFOC uses a feedforward slip command to align the d-axis of the current vector with the rotor flux linkage. The rotor flux linkage is under open-loop control. On the other hand, DFOC uses either measured or

estimated rotor flux linkage to align the current vector with the rotor flux. A typical IFOC block diagram is shown in Fig. 1.3-2.

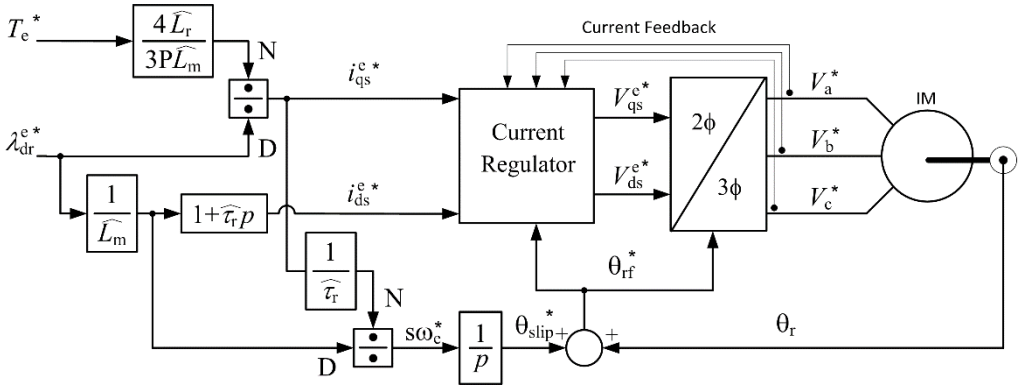

Fig. 1.3-2 Block diagram of IFOC on IM [4], [5]

A current vector regulator is used to regulate d-axis and q-axis current. Moreover, it is used to produce rotor flux on the d-axis and air-gap torque on the q-axis. The synchronous reference frame is commonly used in current regulators. For IFOC, slip frequency can be obtained based on (1.3-3). The synchronous speed can be calculated by summing calculated slip frequency and measured speed information. By assuming an ideal current regulator, air-gap torque and rotor flux can be built using (1.3-1) and (1.3-2).

$$\omega_{slip} = \frac{R_r L_m}{L_r} \frac{i_{qs}}{\lambda_{dr}} \tag{1.3-3}$$

IFOC is one of the most popular control methods for industrial drives because it is simple and only requires a current regulator and speed information. High-performance IFOC relies on accurate parameter values to achieve accurate axis alignment. It can be seen in Fig.

1.3-2 that the rotor flux linkage is under an open-loop control. This means that a slow rotor time constant would limit the change of rotor flux, which is based on (1.3-2). This results in slow torque dynamics during transient changes of the rotor flux [4], [5].

Current Vector Regulators

As discussed above, d- and q-axis current references (current commands) can be computed based on desirable rotor flux and electromagnetic torque, via either IFOC or DFOC. Current regulators are commonly built as PI regulators in the synchronous/electrical reference frame. The higher bandwidth of a current regulator, the faster the current response. In high-performance FOC, the back-EMF is normally decoupled. However, for any synchronous frame controller, a frame speed dependent cross-coupling exists and must be properly dealt with [7]. The state block diagram for current regulators on the d-axis and q-axis is provided in Fig. 1.3-3. Electrical characteristics of induction machines can be modeled as a symmetrical R-L load with cross-coupled frame speed dependent cross coupling [4], [5].

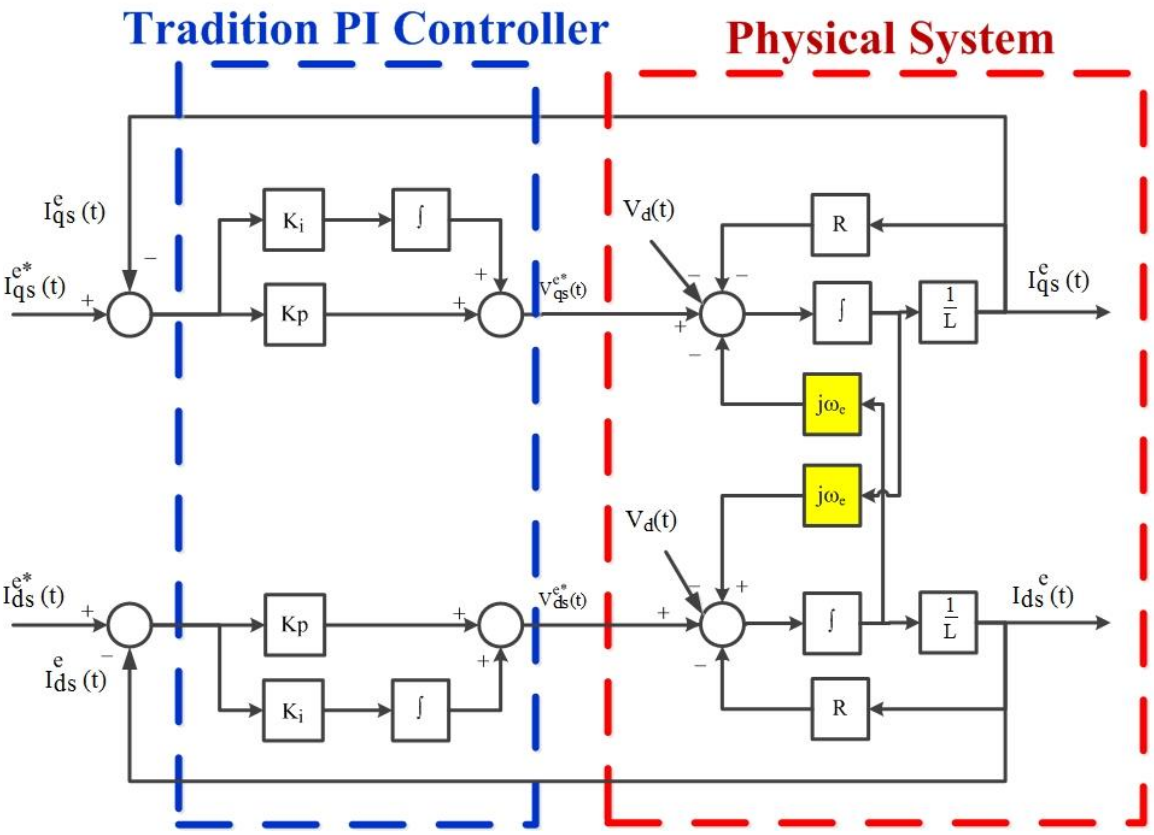

Fig. 1.3-3 Synchronous frame, PI current regulators on d- and q-axis with frame speed dependent cross-coupling, assuming back-EMF has already been decoupled [7][14]

In common current regulators, the controller zero, which can be obtained from (1.3-4), is used to cancel the control system pole. R and L are equivalent resistance and inductance from the stator side of induction machines [6].

$$\text{Zero}_{pi} = -\frac{R}{L} \tag{1.3-4}$$

The frame speed dependent cross-coupling between d- and q-axis was first recognized and properly dealt with in [16]. By considering the cross-coupled term, the real pole of the

system is no longer a simple resistance over inductance (i.e. R/L). Instead, the system pole has an asymmetric complex pole, which is frequency dependent as shown in (1.3-5).

$$s = -\frac{R}{L} - j\omega_e \tag{1.3-5}$$

Based on the equation (1.3-5), the desired real zero cannot cancel the system pole, especially at high-speed conditions. Therefore, the current regulator performance would degrade, since this frame is speed dependent and cross-coupled. Briz and Lorenz provided an alternative solution, the complex vector current regulator, to solve this problem. This solution is shown in [16][14]. It suggests using the q-axis and d-axis current regulators in the complex vector then designing the zero of the current regulator to have the theoretically correct asymmetric complex value. In this case, this zero/pole cancellation method will not be speed dependent. The state block diagram has been presented in Fig. 1.3-4.

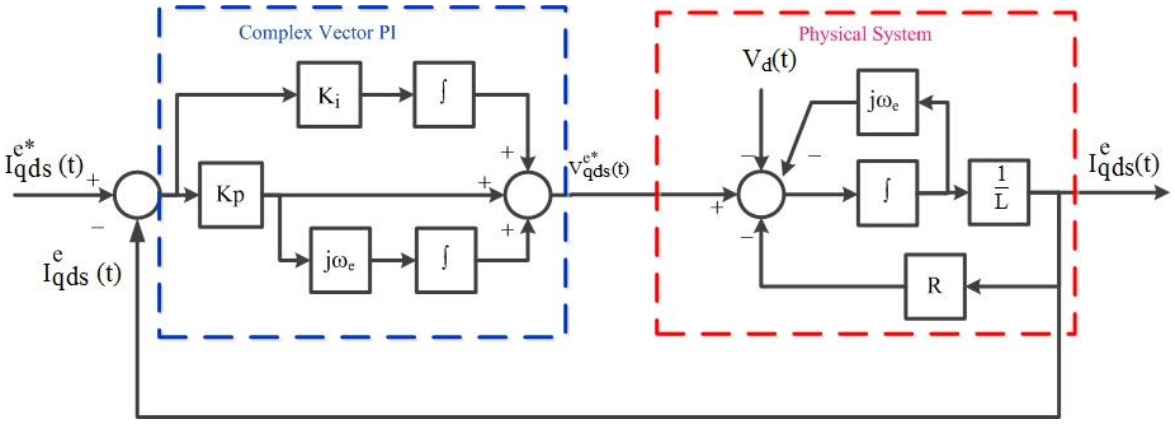

Fig. 1.3-4 Complex vector synchronous reference frame current regulators [7][14]

Based on the continuous time domain current regulator shown in Fig. 1.3-3, in order to implement the designed digital controllers in a DSP controller, a discrete time PI-based current regulator can be obtained, which is presented in Fig. 1.3-5.

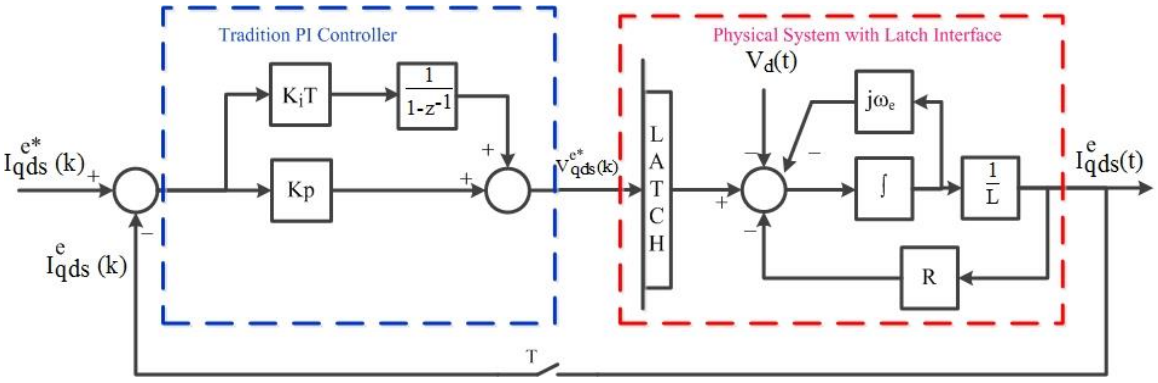

Fig. 1.3-5 Discrete time PI-based current regulator on synchronous reference frame [7][14]

Similarly, the block diagram for the discrete time complex vector current regulator has been proposed in Fig. 1.3-6[14][15]. The low switching frequency complex vector current regulator has been presented in [7].

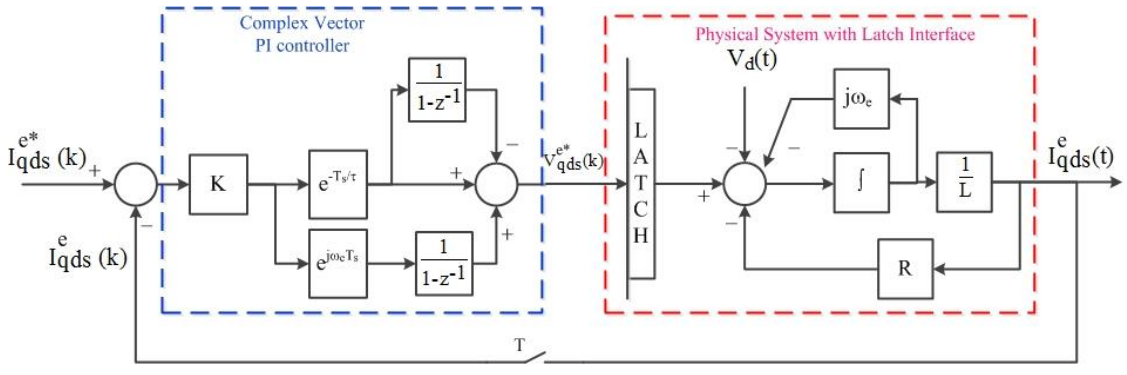

Fig. 1.3-6 Discrete time complex vector current regulator on synchronous reference frame [7][14]

It can be seen that complex gain values have been created in the complex vector controller. The complex vector also shows the cross-coupling relations between d-axis and q-axis.

Since the current regulator is indeed a PI regulator, the current regulator bandwidth is the main limitation for fast torque response [16], [17] and speed response [18] in IFOC drives for either with high switching frequency or low switching frequency.

1.3.3 Deadbeat-Direct Torque and Flux Control

Deadbeat Control

Deadbeat control is a well-established discrete time control method. The desired outputs could be achieved based on an inverse model in just one sampling instant, which is called “dead in one beat”[7][19][20]. Moreover, the definition of deadbeat only exists in a discrete time domain, and no counterpart exists in a continuous time domain [7][19].

If the system physical plant model in discrete time is $G_p(z)$, the closed-loop controller $G_C(z)$ is solved inversely based on $G_p(z)$. The relationship between plant model, $G_p(z)$, and deadbeat controller model, $G_C(z)$, can be derived from (1.3-8). In this case, the total system transfer function in discrete time will be Z^{-1} and “dead in one beat” can be realized. The general block diagram for the deadbeat controller can be presented as Fig. 1.3-7.

$$G_c(z) = \hat{G}_p(z)^{-1} \frac{G_{dr}(z)}{1 - G_{dr}(z)} \tag{1.3-6}$$

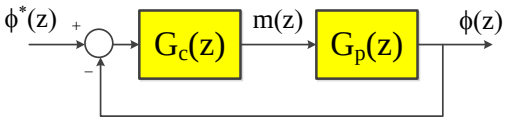

Fig. 1.3-7 General block diagram for deadbeat controller design[7][20]

Deadbeat-Direct Torque and Flux Control

Deadbeat-direct torque and flux control (DB-DTFC) is an improvement to the classic direct torque control, which makes both the air-gap torque and stator flux linkage fully responsive to its command in one sampling instant. It was proposed by B. Kenny at WEMPEC labs [21]. More efforts on DB-DTFC have been presented in [2], [3], [7], [22]–[25]

The system air-gap torque model can be inversely solved and subsequently expressed in terms of flux linkages and voltage second vectors. The control law seeks to apply the exact voltage second vector to achieve the desired air-gap torque and stator flux linkage by just one switching instant.

The induction machine torque can be expressed in terms of stator flux linkage and rotor flux linkage shown in (1.3-7). In addition, the flux differential equations (1.1-9) and (1.1-10) have been repeated for convenience.

$$T_e = \frac{3P}{4} \frac{L_m}{\sigma L_s L_r} (\lambda_{qs}\lambda_{dr} - \lambda_{ds}\lambda_{qr}) \tag{1.3-7}$$

$$\dot{\lambda}_{qs}^{s} = v_{qs}^{s} - \frac{R_s}{\sigma L_s} \lambda_{qs}^{s} + \frac{R_s L_m}{\sigma L_s L_r} \lambda_{qr}^{s} \tag{1.3-8}$$

$$\dot{\lambda}^{s}_{ds} = v^{s}_{ds} - \frac{R_s}{\sigma L_s}\lambda^{s}_{ds} + \frac{R_s L_m}{\sigma L_s L_r}\lambda^{s}_{dr} \quad (1.3\text{-}9)$$

$$\dot{\lambda}^{s}_{qr} = \frac{R_r L_m}{\sigma L_s L_r}\lambda^{s}_{qs} - \frac{R_r}{\sigma L_r}\lambda^{s}_{qr} + \omega_r \lambda^{s}_{dr} \quad (1.3\text{-}10)$$

$$\dot{\lambda}^{s}_{dr} = \frac{R_r L_m}{\sigma L_s L_r}\lambda^{s}_{ds} - \frac{R_r}{\sigma L_r}\lambda^{s}_{dr} - \omega_r \lambda^{s}_{qr} \quad (1.3\text{-}11)$$

The torque differential equation in continuous time can be expressed as (1.3-12).

$$\dot{T}_e = \frac{3P}{4}\frac{L_m}{\sigma L_s L_r}\left(\dot{\lambda}_{qs}\lambda_{dr} + \lambda_{qs}\dot{\lambda}_{dr} - \dot{\lambda}_{ds}\lambda_{qr} - \lambda_{ds}\dot{\lambda}_{qr}\right) \quad (1.3\text{-}12)$$

By using equations (1.3-8) to (1.3-11), substitute the flux linkage term into (1.3-12). Then, the result is shown in (1.3-13).

$$\dot{T}_e = \frac{3P}{4}\frac{L_m}{\sigma L_s L_r}\left[v_{qs}\lambda_{dr} - v_{ds}\lambda_{qr} - \frac{R_r L_s + R_s L_r}{\sigma L_r L_s}\left(\lambda_{qs}\lambda_{dr} - \lambda_{ds}\lambda_{qr}\right) - \omega_r\left(\lambda_{qs}\lambda_{qr} + \lambda_{ds}\lambda_{dr}\right)\right] \quad (1.3\text{-}13)$$

Based on the air-gap torque equation (1.3-7), the result in (1.3-13) can be simplified in the following relationship.

$$\dot{T}_e = \frac{3P}{4}\frac{L_m}{\sigma L_s L_r}\left[v_{qs}\lambda_{dr} - v_{ds}\lambda_{qr} - \omega_r\left(\lambda_{qs}\lambda_{qr} + \lambda_{ds}\lambda_{dr}\right)\right] - \left(\frac{R_r L_s + R_s L_r}{\sigma L_r L_s}\right)T_e \quad (1.3\text{-}14)$$

It has been shown in [19] that the continuous time derivative of air-gap torque can be approximated as the rate of change of torque over the switching period. The corresponding discrete time model can be derived as shown in (1.3-15).

$$\frac{T_e(k+1) - T_e(k)}{T_s} = \frac{3P}{4}\frac{L_m}{\sigma L_s L_r}\left[v_{qs}(k)\lambda_{dr}(k) - v_{ds}(k)\lambda_{qr}(k) - \omega_r(k)\left(\lambda_{qs}(k)\lambda_{qr}(k) + \lambda_{ds}(k)\lambda_{dr}(k)\right)\right] - \left(\frac{R_r L_s + R_s L_r}{\sigma L_r L_s}\right)T_e(k) \quad (1.3\text{-}15)$$

Solving (1.3-15) for stator voltage yields the following result.

$$v_{qs}(k)T_s = \frac{\lambda_{qr}(k)}{\lambda_{dr}(k)} v_{ds}(k)T_s + \frac{1}{\left(\frac{3P}{4}\frac{L_m}{\sigma L_s L_r}\right)\lambda_{dr}(k)} \left(\Delta T_e(k) + T_s\left(\frac{R_r L_s + R_s L_r}{\sigma L_r L_s}\right) T_e(k)\right) + \frac{T_s \omega_r(k)}{\lambda_{dr}(k)}\left(\lambda_{qs}(k)\lambda_{qr}(k) + \lambda_{ds}(k)\lambda_{dr}(k)\right) \quad (1.3\text{-}16)$$

The voltage second vectors, $v_{qs(k)}T_s$ and $v_{ds(k)}T_s$, are the system inputs for each sample instant. An infinite number of solutions can be found. (1.3-16) can be treated as a straight line with $v_{ds(k)}T_s$ and $v_{qs(k)}T_s$ as predictors and responses. Theoretically, the inverter output voltage will achieve the desirable air-gap torque within one sample instant, which means "dead-in-one-beat" is achieved. A unique stator voltage second solution can be computed when the desirable stator flux linkage for the next switching period is given as the additional constraint.

It has been shown by [7][21] that the DB-DTFC solution can be represented graphically by using the voltage-second plot. After stator flux linkage re-alignment for each switching period, the derived torque inverse model can be treated as a straight line on the voltage second plane. Where:

$$Y = v_{qs}(k)\, T_s \quad (1.3\text{-}17)$$

$$X = v_{ds}(k)\, T_s \quad (1.3\text{-}18)$$

$$M = \frac{\lambda_{qr}(k)}{\lambda_{dr}(k)} \quad (1.3\text{-}19)$$

$$B = \frac{4\sigma L_s L_r}{3PL_m\lambda_{dr}(k)}\left(\left(\frac{R_s}{\sigma L_s} + \frac{R_r}{\sigma L_r}\right) Te(k)T_s + \Delta Te(k)\right) + \omega_r T_s \frac{\lambda_{ds}(k)\,\lambda_{dr}(k) + \lambda_{qs}(k)\,\lambda_{qr}(k)}{\lambda_{dr}(k)} \quad (1.3\text{-}20)$$

The solution is presented in Fig. 1.3-8[7][21]. The shown stator flux vector has already been re-aligned with the d-axis. The rotor flux vector has rotated by a slip angle appropriately. Torque line model with parameters (1.3-17) to (1.3-20) has been overlaid. The grey vectors represent the possible voltage second solutions. The air-gap torque constraint is interpreted as the Volt.-sec vectors should point to the torque line model.

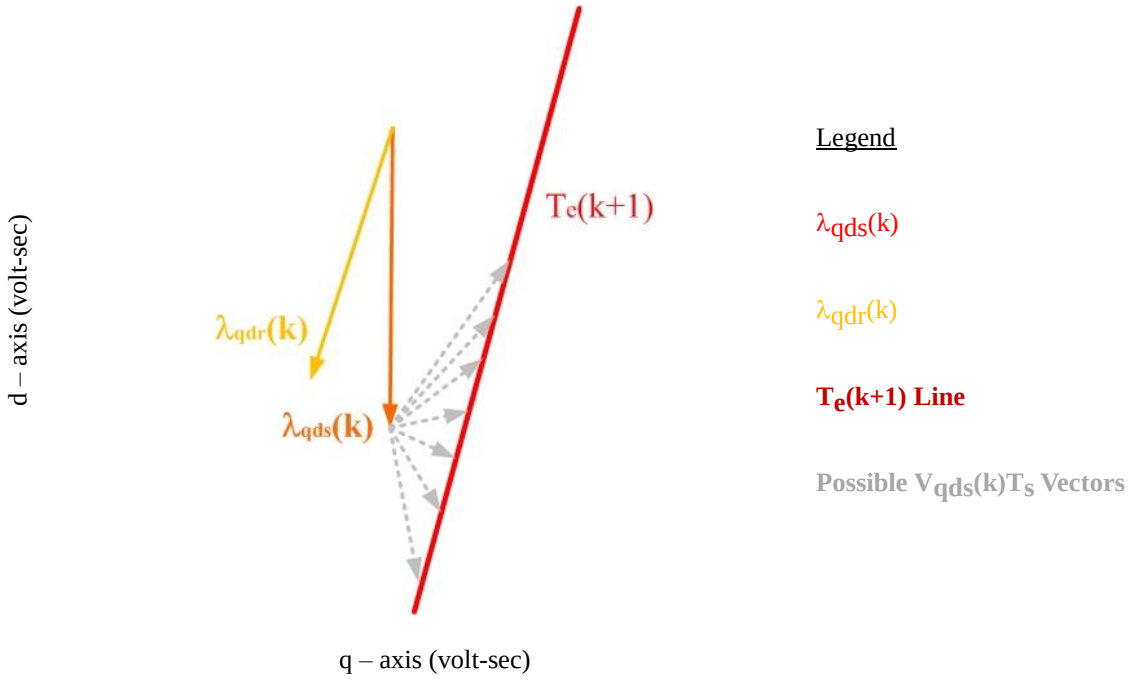

Fig. 1.3-8 Voltage vectors which will result in a given change in torque [7][21]

If feasible air-gap torque and stator flux magnitude are commanded, infinite solutions will be constrained to the flux command. Then, both the desirable air-gap torque and stator flux magnitude will be achieved simultaneously. Theoretically, two possible solutions are exhibited shown in blue dashed line in Fig. 1.3-9 [7][21].

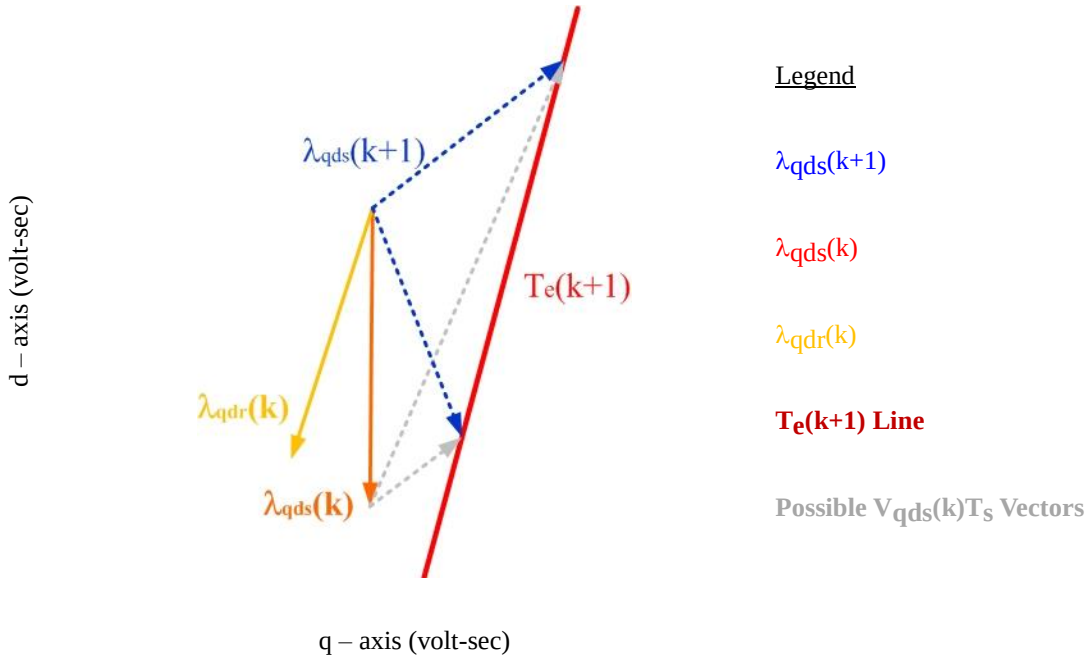

Fig. 1.3-9 Voltage vectors which will satisfy both the torque and stator flux magnitude command [7][21]

Normally, one solution is within the vol-sec hexagon and the other one is not. It is clear that the solution that can satisfy the voltage-second constraint will be chosen, which is shown in Fig. 1.3-10. Taking that into consideration, the voltage-second solution for each sample instant will be determined, if the machine is not operating at the voltage limit region (i.e. over-modulation range). However, when the desired vector solution lies out of the inverter hexagon, it means the DB regulator cannot achieve the desired torque in one sample instant. A common method to deal with these over-modulation conditions is scaling the vector back into the voltage hexagon. Since DB-DTFC operating at voltage limited condition is another wide research topic and has been partially covered in [26][24], it will not be further presented on in this thesis.

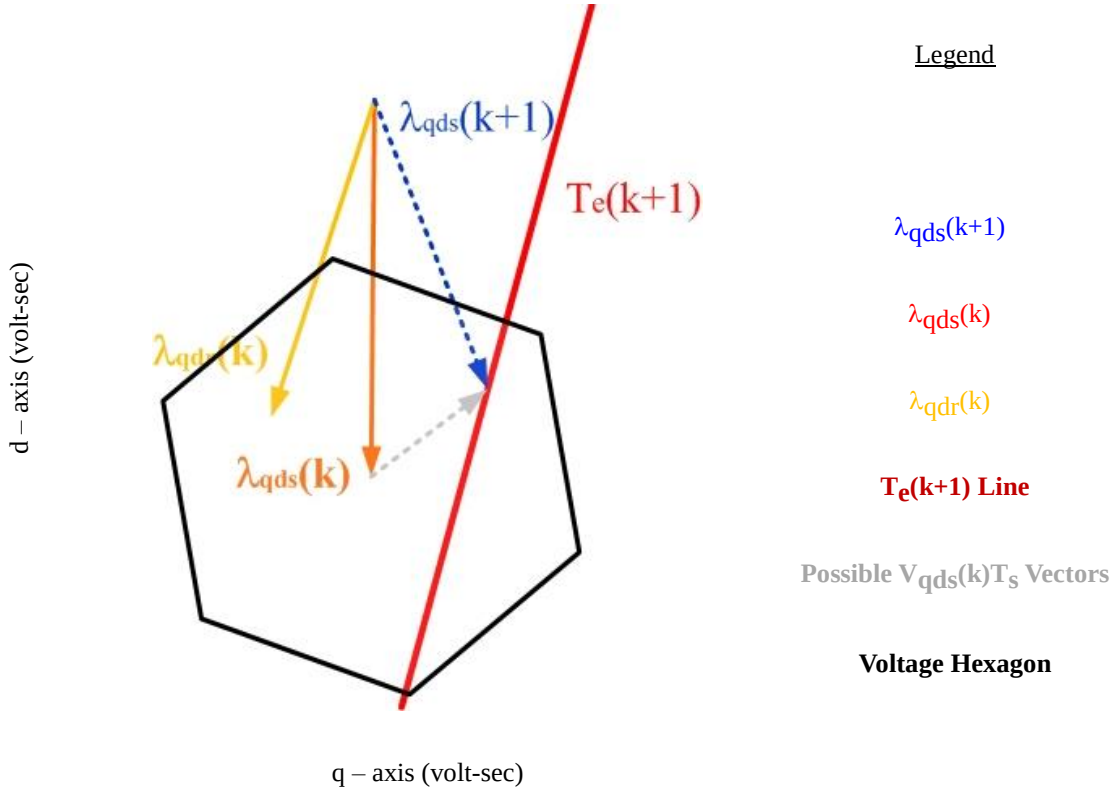

Fig. 1.3-10 Voltage second vector in inverter output hexagon. [7][21]

Kenny and Lorenz initially proposed DB-DTFC in 2001 [21]. Then, more efforts have been done to make further improvements for both induction machines and synchronous machines (especially permanent magnet synchronous machines) [2], [7], [12], [23], [25]–[27]. A properly formed discrete time flux observer and the current observer is proposed in [2][12] to ensure high estimation accuracy of flux estimates. Robust evaluation of DB-DTFC is covered in [28]. The stator flux magnitude as the access to manipulate loss is the primary

objective in[3][27][24]. The optimal trajectories operating at voltage limited region is illustrated widely in [26][29]for induction machines.

As discussed in many previous research papers, the system with flux observer and the DB-DTFC algorithm has very fast torque dynamics. It has been demonstrated that the DB-DTFC drive has a one-step torque response, which is much faster than IFOC drive. However, it uses the estimated torque for the high bandwidth torque command tracking comparison. It is necessary to examine the real torque command tracking bandwidth of DB-DTFC control system. Besides, there is no torque meter that can measure the air-gap torque dynamics at high bandwidth. Thus, instead of using estimated torque, another way which uses the measured state to demonstrate the DB-DTFC is necessary.

1.4 Existing Back-EMF Tracking Self-Sensing

Position information is critical for a high-performance electric drive, so usually, a position sensor (e.g. encoder, resolver) is installed to provide position information. In order to reduce additional cost and volume, noise problems and related reliability problems, the position self-sensing technologies have been studied for many years. Several papers have reviewed the existing self-sensing technology [30]–[32].

Within the last decade, significant improvements have been made in the area of self-sensing control of permanent magnet synchronous machines (PMSM), induction machines and brushless DC machines [6], [22], [33]–[36][10], [11], [13], [30], [31], [37] [38]–[42]. The primary methods for self-sensing control can be divided into two main categories: back-EMF based self-sensing technology [43](using back-EMF estimation with fundamental excitation) and high frequency injection (HFI) based self-sensing technology [22], [33], [36], [37](using excitation in addition to the fundamental). Each method has its own advantages and disadvantages. The HFI based methods (saliency-tracking methods) are suitable for zero-speed operations, but it may cause some torque ripple or may not be suitable for high speed. The back-EMF based method is normally used in medium and high speed operations, but it is not available for standstill operation since at the zero speed the machine's back-EMF is zero as well. The general structure for the back-EMF tracking is shown in Fig. 1.4-1. There are several ways, such as arctan method, model reference adaptive method, Kalman filter method or tracking observer method, for the signal processing to estimate the position and speed. The performance relies on the accuracy of the machine model, the design of the MRAC system, Kalman filter gain matrix, back-EMF observer and tracking observer.

Relevant research studies have been documented in the literature including terminal voltage integration [44], back-EMF state filter [45], [46], model reference adaptive control[47], [48], extended Kalman filter [49], etc. Although those techniques seem to follow

different paths, they are essentially very similar in principle, and therefore share similar properties.

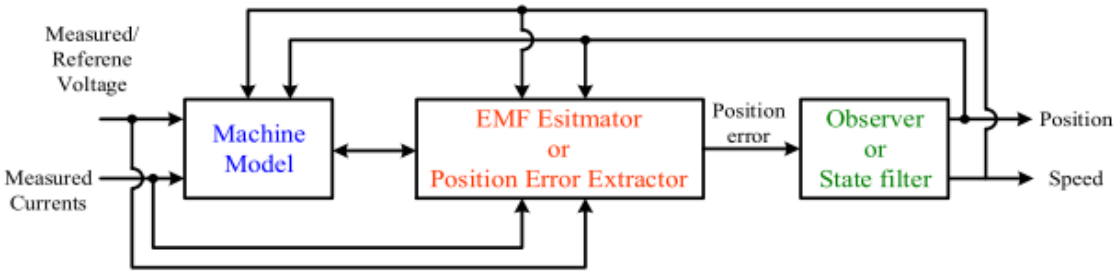

Fig. 1.4-1 General structure of back-EMF tracking for self-sensing [50]

1.4.1 Model Reference Adaptive System (MRAS) Method

Several "adaptive flux observers" have been proposed that estimate rotor flux and adapt the rotor velocity and certain machine parameters. These adaptive observers are essentially flux observers with MRAS acting in an outer loop. Many approaches are based on full order observers that also the estimate stator current and adapt the stator resistance at the same time. H. Kubota and G. Yang illustrated one form of an adaptive flux and velocity observer, based on the full order flux observer[51][52]. Jansen [6]proposed a velocity estimator in the form of a MRAS with an open-loop flux observer with a current model and voltage model as shown in Fig. 1.4-2. The voltage model is independent of rotor velocity and is used as the reference model. An adaptive controller produces a velocity estimate to force convergence of the flux estimates.

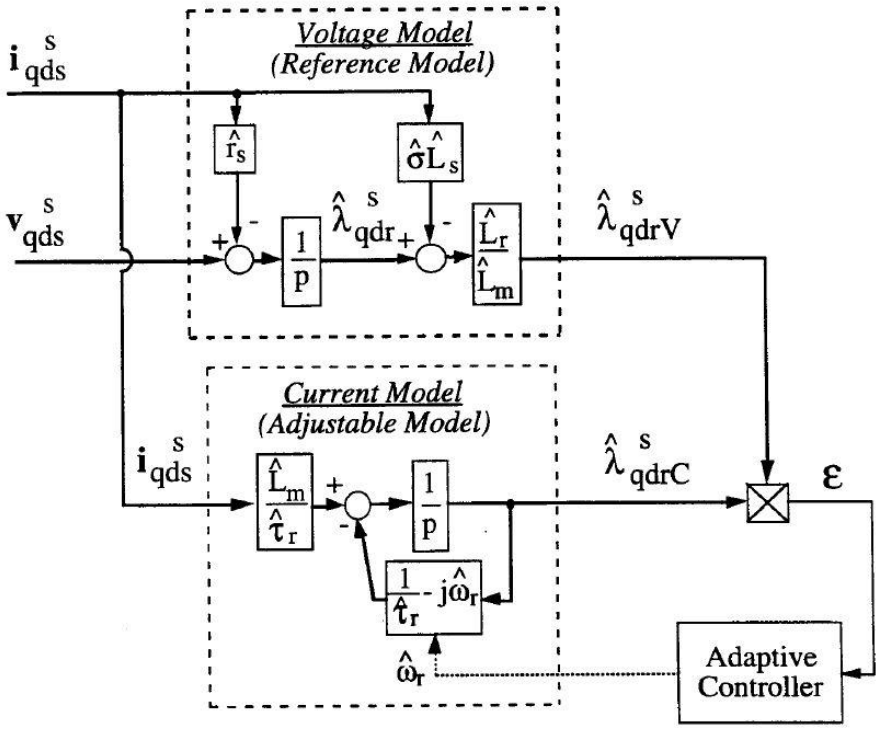

Fig. 1.4-2 Velocity estimation via MRAC based an open-loop flux observer [53]

The stator resistant and rotor time constants, which vary with the motor temperature, are identified by the following adaptive schemes. In order to satisfy the persistent excitation condition, the input variables have to contain more than two frequency components, and therefore, the superimposition of AC components on the field current command was proposed in order to estimate the motor speed and the rotor resistance simultaneously [51]. The compensation for parameter variation caused by temperature was provided. When amplitude

was 5% of the rated field current, the frequencies of the AC components superimposed on the field current were 1 and 3 Hz and were also provided.

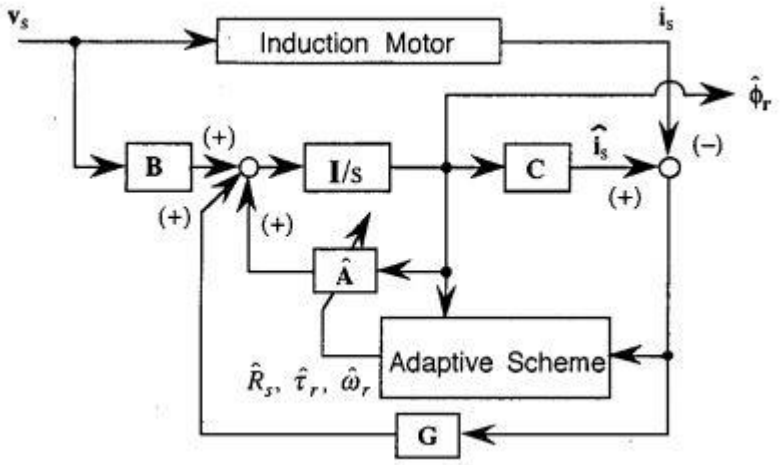

Fig. 1.4-3 Block diagram of adaptive flux observer[54]

1.4.2 Kalman Filter-based Method

Another back-EMF tracking technique for the induction machine is the Extended Kalman Filter (EKF) method. The EKF is indeed one kind of observer with varying gains. It is used for reducing the system noise to achieve better performance.

The Kalman filter is a linear system mathematical model. It normally is parallel to the system. The outputs are estimate unmeasured states, as shown in Fig. 1.4-4. The gain “K” in the Kalman filter is varying. It is based on an assumed system noise model, so it strongly depends on the system noise. Kalman filters use an optimal recursive algorithm based on the

least-square sense of the system noise to update the gain “K”. It is not sensitive to machine parameters. Thus, one drawback of the Kalman filters is that the bandwidth depends on the system noise. If the noise increases, K decreases which leads to more phase lag on the estimates.

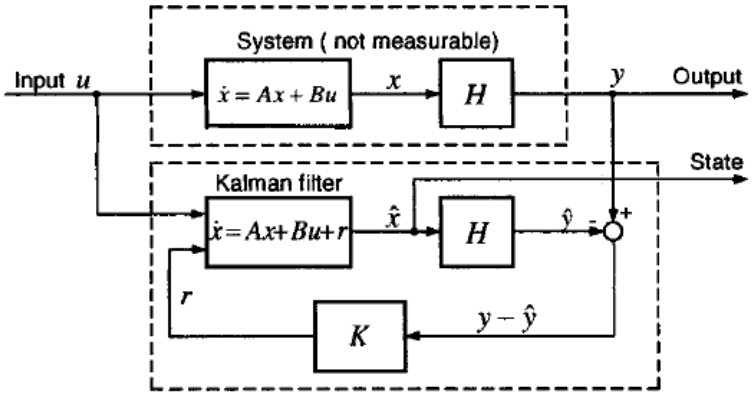

Fig. 1.4-4 Structure of the Kalman filter estimator [55]

The EKF method is derived from the Kalman filter to observer states of the non-linear system. The EKF is also known for its high convergence rate. In addition, estimation accuracy and convergence accuracy in steady state conditions require high frequency signals (the noise on the measured signals). These properties are the major advantages of the EKF for self-sensing control. In an induction machine dynamic model, if the dimension of the state vector is increased by adding an angular speed of the rotor, then the state model becomes nonlinear. The EKF method is used to estimate the parameters. In this case, the angular speed

is treated as a state and a parameter. The extended IM models based on EMF estimator are given by following equations, (1.4-1) and (1.4-2)[56]:

$$\dot{x_e}(t) = f_e[x_e(t), u_e(t), t] + w_{x1}(t) \quad (1.4\text{-}1)$$

$$A_e(x_e(t))\, x_e(t) + B_e\, u_d(t) + w_{x1}(t)$$

$$Z(t) = h_e(x_e(t)) + w_{x2}(t) \quad (1.4\text{-}2)$$

$$H_e\, x_e(t) + w_{x2}(t)$$

where x_e is estimated states, f_e is a nonlinear function of the states and inputs, A_e is system matrix, B_e is input matrix, H_e is measurement matrix, w_{x1} is process noise and w_{x2} is measurement noise. Based on this, the extended models of IM based on the stator flux and based on the rotor flux can be obtained. Thus, the EMF algorithm can be derived in the following equations, (1.4-3), (1.4-4) and (1.4-5)[56]:

$$N(k) = F_e(K)\, P(k)\, F_e(K)^T + F_u(k)\, D_u\, F_u(k)^T + Q \quad (1.4\text{-}3)$$

$$P(k+1) = N(k) - N(k)\, H_e^T * (De + He\, N(k)\, H_e^T)^{-1} H_e\, N(k) \quad (1.4\text{-}4)$$

$$\hat{x}_e(k+1) = \hat{f}_e(x_e(k), u_e(k)) + P(k+1)\, H_e^T D_\xi^{-1} * (Z(k) - H_e\, \hat{x}_e(k)) \quad (1.4\text{-}5)$$

where Q is the covariance matrix of the system noise (model error). D_ξ is the covariance matrix of the output noise (measurement noise. Du is the covariance matrix of the control input noise (input noise). P is the covariance matrix of state estimation error. N: covariance matrix of extrapolation error. Based on this dynamic model, the machine rotor

speed can be estimated by the algorithm provided by[56]. The system structure of the EKF algorithm is shown in Fig. 1.4-5.

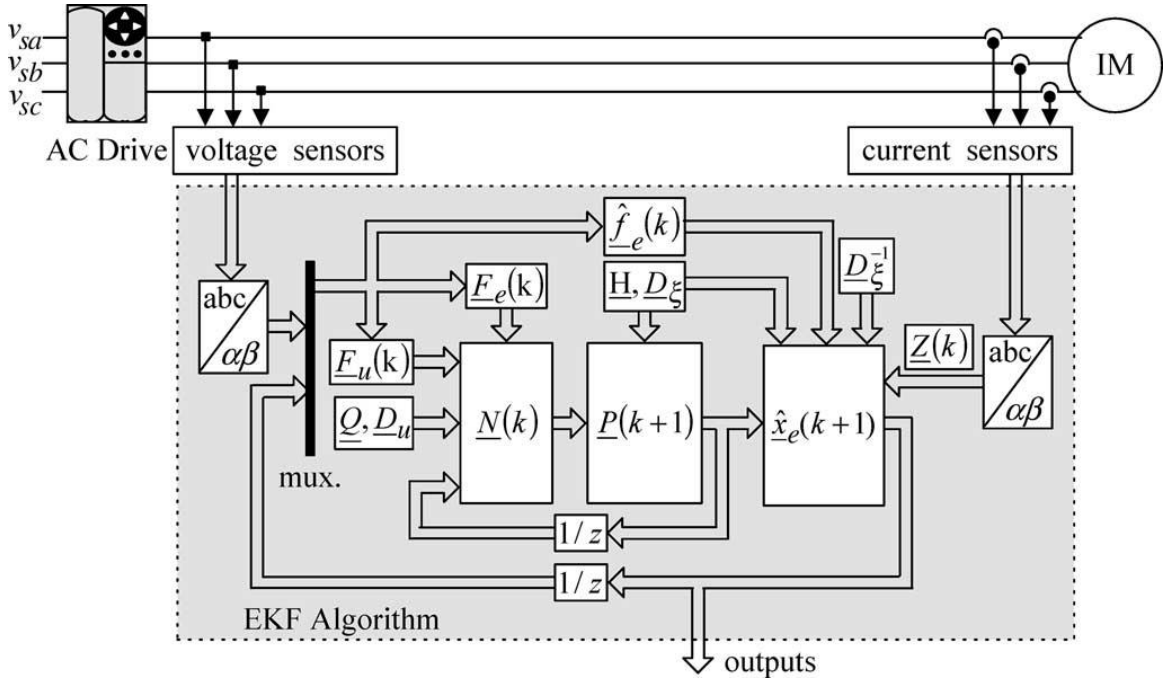

Fig. 1.4-5 Structure of the EKF algorithm [56]

The covariance matrix (e.g. *Q*, *P* and *N*) tuning is an important work in the EKF method. Another drawback is that the estimation accuracy depends on the matrices *Q*, *P* and *N*. Some other drawbacks include instability due to linearization and erroneous parameters, costly calculation of Jacobian matrices, biasedness of its estimates, and lack of analytical methods for suitable selection of model covariance [57]. The EKF method for back-EMF tracking can also be used in the IPM machine drive system, which has been done in [56].

1.4.3 Observer-Based Method

Another method for velocity estimation is based on observers[58], [59], [60] and [61]. The observer is a physical model based on measured states (e.g. phase current and voltage) as inputs. The observer operates parallel to the physical system and estimates the system states. In a closed-loop observer, an observer compares the measured state and the estimated state. This observer can be used to estimated other states in the system.

Jones [62] proposes a state observer for IPMSM. The observer reconstructs the machine's electrical and mechanical states. It is fed by measured current and voltage. It runs in rotor reference frame. The error between the measured current and estimated current is used as a feedback to correct the error in the estimated position. This method is very sensitive to the machine parameters.

Kim [15][63]proposes a reduced order observer to estimate the back-EMF in PMSM drive. In his study, by using a closed-loop back-EMF state filter shown in Fig. 1.4-6-a and a back-EMF tracking observer shown in Fig. 1.4-6-b, the rotor position and the machine speed are estimated for closed-loop motion control in IPM drive system. The close-loop back-EMF state filter shown in Fig. 1.4-6-a is indeed a current observer without the back-EMF path. That's why it can estimate the back-EMF. In back-EMF tracking observer shown in Fig. 1.4-6-b, the T_e^* is the command feed forward path to achieve zero-phase lag for command

tracking. In addition, the estimated velocity depends on machine parameters and estimated the flux linkage. With some compensation methods (back-EMF compensation), the test machine can be operated with a speed as low as 150rpm.

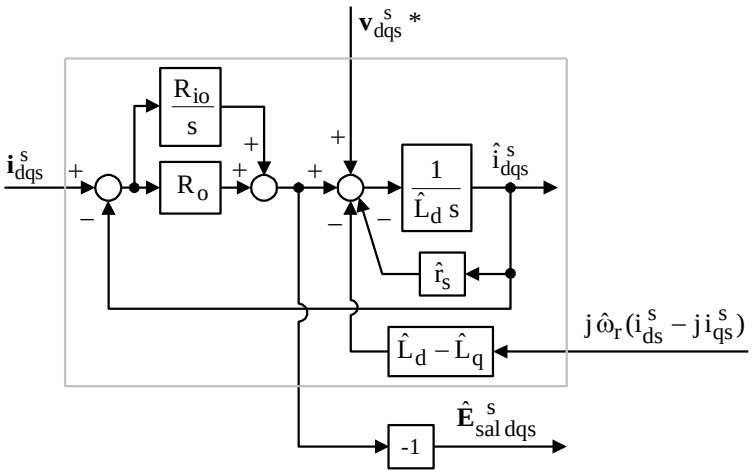

Fig. 1.4-6-a Stationary reference frame saliency back-EMF state filter or current observer [63]

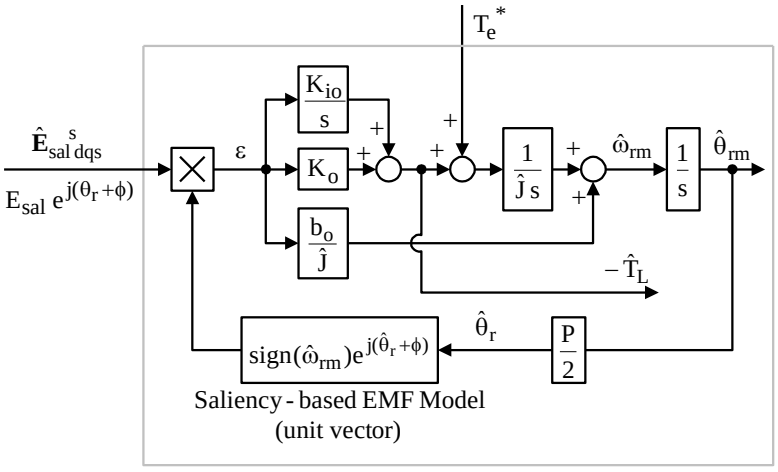

Fig. 1.4-6-b Enhanced Luenberger style saliency back-EMF tracking observer [63]

It is important to know that this approach does not overcome the low and zero speed limitations. In addition, there is an inherent tradeoff in the integrated system between the sensitivity to the mechanical system model and to the stator resistance estimation.

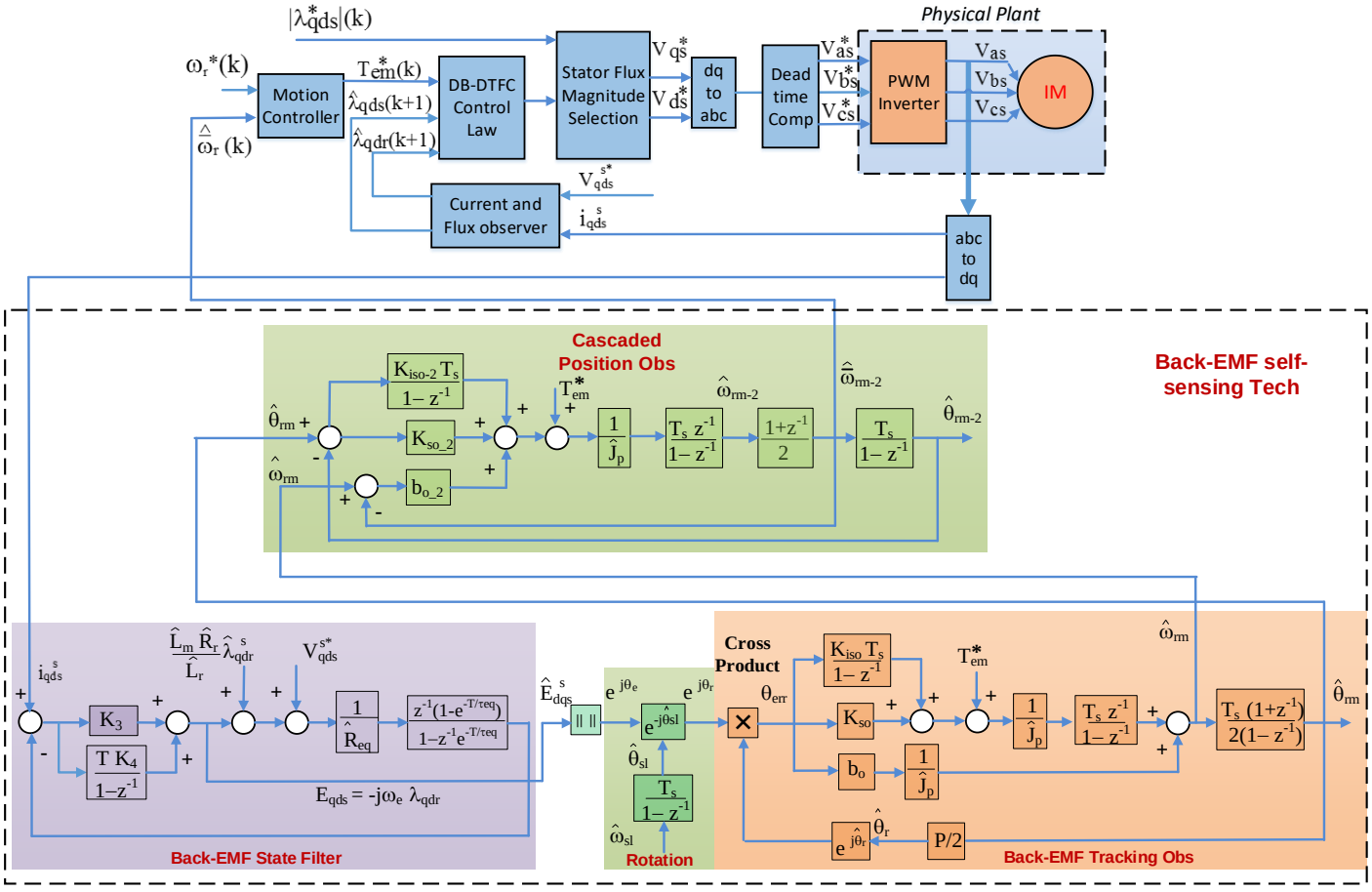

Fig. 1.4-7 Block diagram for IM DB-DTFC self-sensing with the back-EMF state filter, back-EMF tracking observer and cascaded motion observer [63]

In [64], a design basis for using a back-EMF state filter and tracking observer as "sensor replacements" in motor drives is presented. The observer performance was also discussed. In [46], the strategy of IPM self-sensing by cascading a back-EMF state filter and a

tracking observer is proposed. As opposed to the IPM machine, the electrical speed in the IMs is different from the rotor speed. For the IMs, if the excitation frequency is ω_e and the slip frequency is ω_{slip}, the rotor speed is $\omega_r = \omega_e - \omega_{slip}$. Thus, a slip frequency rotation block is needed between the back-EMF state filter and the back-EMF tracking observer, which is shown in the green block of Fig. 1.4-7. To implement the back-EMF state filter/current observer, it is necessary to split it into components in q- and d- axes. It is clear from the Fig. 1.4-7 that the back-EMF can be written as (1.4-6) in a complex vector format.

$$\hat{E}^{s}_{qds} = -j\hat{\omega}_e \hat{\lambda}^{s}_{qdr} \frac{\hat{L}_m}{\hat{L}_r} \qquad (1.4\text{-}6)$$

A cascaded enhanced Luenberger style motion observer is helpful to improve the back-EMF self-sensing performance, especially in the low speed operations. The discrete time block diagram is shown in Fig. 1.4-7. This cascaded motion observer functions as a zero-lag filter that can filter out the noise on $\hat{\theta}_{rm}$ signal without causing any phase lag [64]. The resulting lower noise signal, $\hat{\omega}_{rm\_2}$ can be used to improve the self-sensing performance at low speed without degrading the stiffness of the drive。

The cascaded motion observer is fed by an estimated position signal, $\hat{\theta}_{rm}$, and estimated average velocity signal, $\hat{\omega}_{rm}$, from the back-EMF tracking observer. The gains for the cascaded motion observer "b_{o_2}", "K_{o_2}" and "K_{io_2}" are determined by its bandwidth. Since the characteristic equation of the back-EMF tracking observer is the same as gains for

the cascaded motion observer, "b_{o_2}", "K_{o_2}" and "K_{io_2}" can be obtained in a similar method as a back-EMF tracking observer gains calculation.

Thus, the block diagram of an observer-based closed-loop back-EMF tracking self-sensing control in an IM DB-DTFC drive system can be drawn in Fig. 1.4-7. It includes a back-EMF state filter, back-EMF tracking observer, and a cascaded motion observer. The proposed method can also be implemented in an IFOC drive, but IFOC drives strongly depend on position information for coordinate transforms in the current regulator. IFOC torque dynamics degrade with errors in the estimated position, especially at low speeds in the self-sensing mode. Thus, DB-DTFC, which has one step torque and flux response with no current regulator, is more suitable and stable to integrate with self-sensing technology。

The DB-DTFC back-EMF based self-sensing has been implemented in an induction machine drives over a wide speed range. At low speeds, the back-EMF based self-sensing performance degrades due to the signal-to-noise ratio degrades. Many factors, such as the state filter bandwidth, machine parameters, estimated slip frequency and inverter nonlinearity (reference voltage), determine the back-EMF based self-sensing performance, especially at low speeds.

Although the parameter sensitivity of DB-DTFC drive has been investigated in previous research, the parameter sensitivity of the proposed synergy, DB-DTFC drive with

back-EMF based self-sensing, has not been explored. The robustness and estimation accuracy of the back-EMF based self-sensing technology and a suitable state filter bandwidth selection approach have not been explored yet.

1.5 Existing Parameter Estimation in IM Drives

The machine parameters would impact on induction machine drives performance significant. The parameter estimation techniques are more and more popular in the last forty years. The paper in last decades covered all induction machine parameters, including magnetizing inductance, rotor resistance, stator resistance, stator leakage inductance and rotor leakage inductance (L_m, R_r, R_s, L_{ls} and L_{lr}). Besides, both the indirect field oriented control (IFOC) and the standard direct torque control (DTC) drives are sensitive to the machine parameters, especial to rotor resistance and leakage inductance. The estimation accuracy of the rotor resistance and the leakage inductance not only impacts the encoder based induction machine drives but also impacts on the drive's performance in self-sensing mode significant. Many of the presented self-sensing techniques has demonstrated the machine parameter variations would impact the self-sensing performance at different operating points[65]–[68]. Overall the estimation approaches are generally categorized as offline estimation and real-time estimation [69] and [70].

1.5.1. Standstill Parameter Estimation

If the motor is locked, the standard locked rotor test could provide rotor resistance information and leakage inductance. When the rotor is locked, the slip value is one, as shown in Fig. 1.5-1, which makes the rotor circuit like a short circuit. Instead of flowing through the iron-loss resistance and magnetizing inductance, the major component of current will flow through the rotor resistance because of low resistance magnitude and iron-loss resistance R_m and magnetizing inductance X_m can be ignored. Both the leakage inductance and rotor resistance can be estimated through this test. Here, the leakage inductance in the stator and rotor are assumed to be identical.

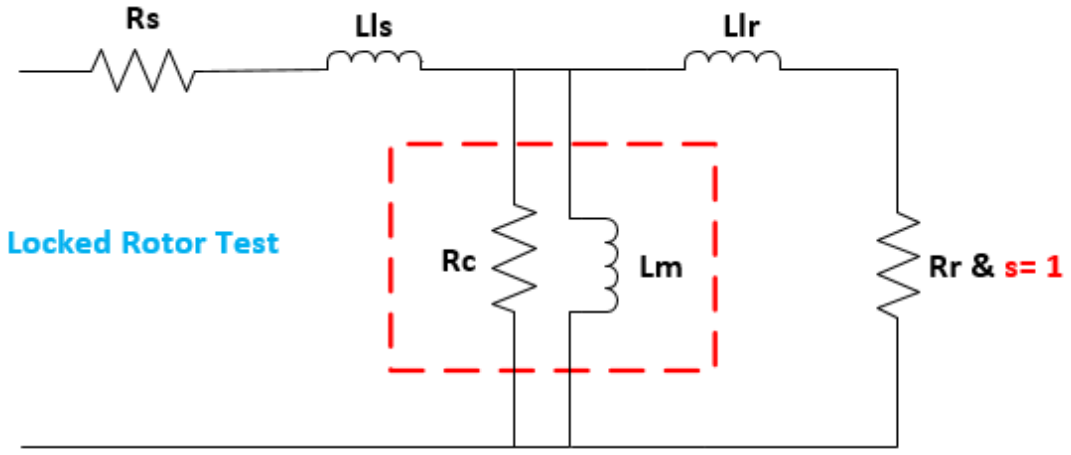

Fig. 1.5-1 Equivalent circuit for locked rotor test

Time Domain Response

A simple method for rotor resistant and rotor time constant estimation of the induction machine is proposed in [71]. "Γ" type equivalent circuit of the induction machine is used,

when the source is composed only two phases. A DC voltage is injected to the two of the three phases. In this case, all current only flows into the magnetizing inductance shown in Fig. 1.5-2 (a). After removing the DC signal, the magnetizing inductance will be discharged and all the current will go through the rotor side, showed in Fig. 1.5-2 (b). During the discharging, the stator side voltage can be obtained in the time domain. In Fig. 1.5-2 (c), the voltage waveform at the stator side is decaying as an exponential function of the rotor time constant. The rotor time constant can be measured by the initial slope.

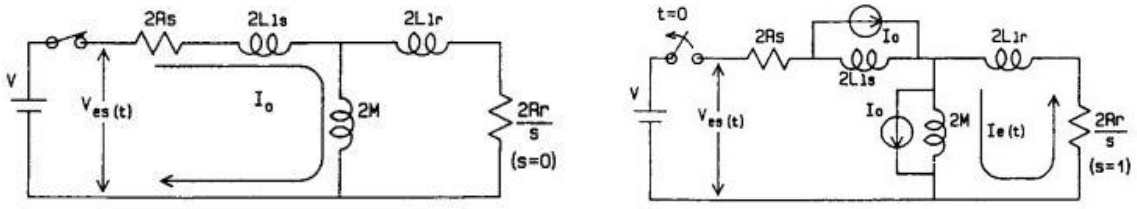

(a) injected DV voltage at the stator side (b) after removing the DC voltage

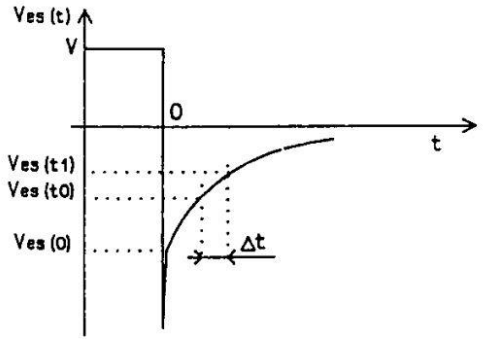

c) voltage waveform at the stator side after removing the DC voltage

Fig. 1.5-2 The procedure of the self-commissioning approach proposed in [71]

With the same principle, applying the DC component approach is also proposed in [72], [73]. Similarly, the [74] proposed a method by using a single-phase AC current instead of DC

voltage. All the proposed methods in [75]–[77] can be treated as a time domain approach to estimate the machine parameters. This method is simple and easy to implement. However, in the time domain approach, the signal measurement issue, which is affected by noise, data processing errors, will lead to the final estimation accuracy.

Recursive Least Square Approaches

The recursive least square (RLS) method [78]–[85], which is one kind of the adaptive filters, is also can be used for parameter estimation. The RLS method is derived from the dynamic model of the induction machine. It does not need any specialized voltage signal injected into the machine. It also does not require any encoder installation, which is suitable for the machine self-commissioning. It has a fast convergence rate with highly correlated input signals. Based on the induction machine mathematical model, the relationship between voltage and current can be derived as (1.5-1) [79]at standstill condition.

$$\frac{i_{qds}^{s}}{v_{qds}^{s}} = \frac{B_1 s + B_0}{s^2 + A_1 s + A_0} \tag{1.5-1}$$

where

$$A_1 = \frac{R_s L_r + R_r L_s}{\sigma L_s L_r} \qquad A_0 = \frac{R_s R_r}{\sigma L_s L_r}$$

$$B_1 = \frac{1}{\sigma L_s} \qquad B_0 = \frac{R_r}{\sigma L_s L_r}$$

The RLS estimation method can be modeled in both discrete time form and continues time form. After RLS regression model converging to the true value, the estimation of A_0, A_1, B_0 and B_1 can be obtained based on measured current and voltage.

The RLS method is one of the adaptive algorithm, which belongs to Kalman filters family[78]. It has a significant computation complexity. In the RLS algorithm, the calculation of signal derivatives is required. Thus, the measured noise such as current ripple can cause a significant error on the parameter estimation after the first and the second derivatives. Besides, the inverter nonlinearity, which causes the error between the command voltage and the real terminal voltage, can also lead to the serious problem without property compensation.

1.5.2. Real-time Parameter Estimation

For medium and high power induction machines, many research has been done for the real-time parameter estimation recently. In terms of real-time parameter estimation, there are different methods, which can be categorized as signal injection based solutions and non-signal injection based solutions. In the amount of non-signal injection method, the model reference adaptive system (MRAS) approach is popularly used. No matter using which approach, each approach has its own advantages and disadvantages, which are discussed as follows:

Signal Injection-Based Approaches

Signal injection-based approaches are commonly used for parameter estimation, and can be used in rotating [69], [86]–[88] and standstill conditions [68], [89]–[91]. The signal

injection based real-time parameter estimation approach injects a signal (voltage, flux or other variables) to make the system produce the harmonics at the carrier frequency rather than at the fundamental frequency [86], [87], [92]. After the data processing technique, the harmonics can be separated from the frequency spectrum. Based on the machine mathematical equation, the relationship between the produced harmonics and the machine parameters can be derived. By using these, the machine parameters can be obtained in real time. However, in the traditional signal injection approach, the main disadvantage is the secondary effects, including torque ripple caused by the injection signals.

One of the signal injection approach was proposed in [86], which used a rotating vector. A prescribed negative sequence current is injected, shown in Fig. 1.5-3. By detecting the negative sequence voltage, the rotor resistance can be estimated. The mathematical equations for the relationship between the negative harmonics and the rotor resistance are also included in this paper. However, the signal is injected under the traditional IFOC control algorithm, which will cause the torque ripple at the injection signal frequency due to the cross coupling between the q-axis and d-axis for the IFOC drive. Besides, two times separate injections (two different injection frequencies) rather than one-time injection are required for solving the mathematical expressions.

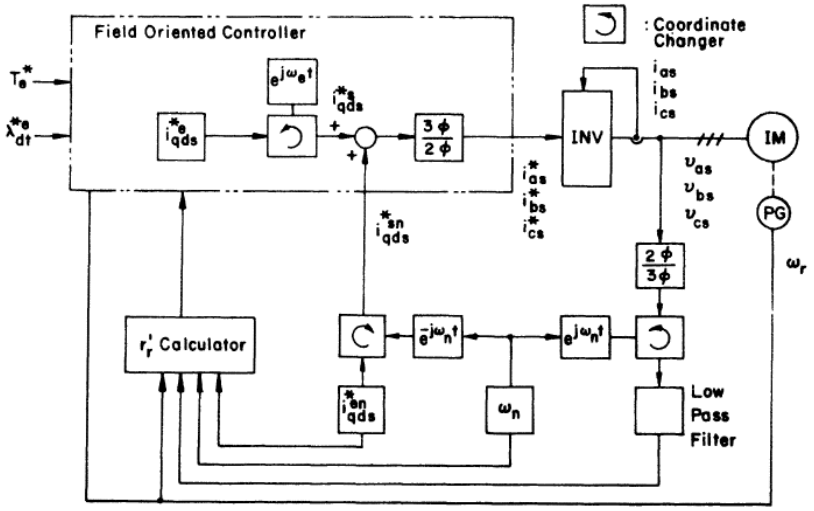

Fig. 1.5-3 Configuration block diagram for the method proposed in [86]

In [87], a pulsating signal is used for injection. The pulsating current signal is injected only on the d-axis. This method is based on the analysis of voltages and currents by using the Fast Fourier Transform Algorithm. In [48], [93], [88], [94], the similar d-axis injection method is presented. In [93], the parameters are derived from only those signal components that are most relevant to the parameters being calculated. Based on the spectral analysis, the proposed method works online in a similar way to the standard “no-load” and “locked-rotor” test.

However, the torque ripple is caused by cross-coupling of d-axis and q-axis in current regulator for IFOC drives. In the traditional PI current regulator, the cross-coupling is significant, which will lead to large torque ripple by the injected signal. For some other current regulator, like complex vector current regulator has been proposed in [4] and [5], has already decoupled the cross-coupling of the back-EMF term. However, only the fundamental

frequency term $j\omega_e$ is decoupled in the traditional complex vector current regulator, shown in Fig. 1.5-4. The injected signal, which is in the frequency ω_c rather than the ω_e, will still cause the cross-coupling between the d-axis and q-axis. These cross coupling will result in torque ripple especially at high speeds.

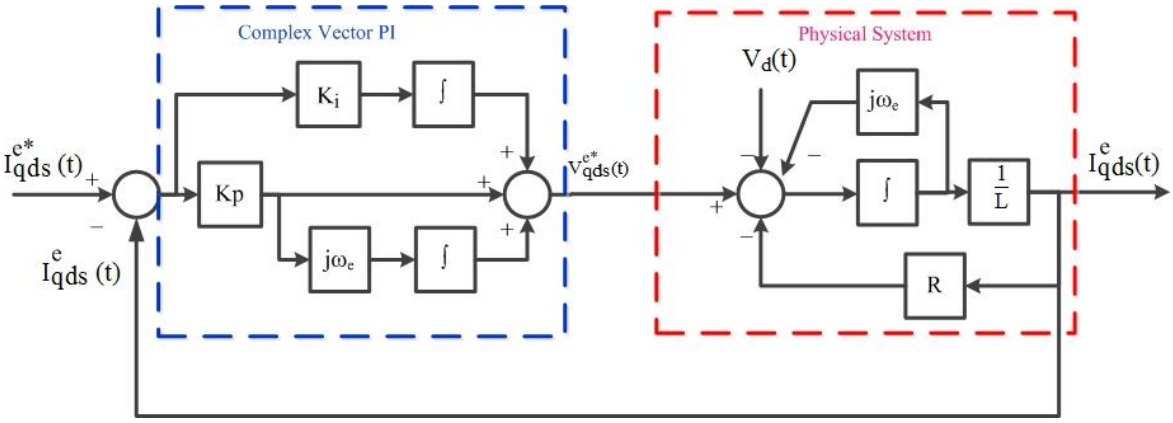

Fig. 1.5-4 Complex vector synchronous reference frame current regulators

Even with the cross-coupling decoupling technique, the torque ripple cannot be eliminated. Since the IFOC is sensitive to the machine parameters, the d-axis and q-axis cannot be fully decoupled with inaccurate parameters.

In [95], [96], the flux and torque injection approaches are implemented in DTC drives for stator estimation. However, in DTC drives, torque and stator flux regulation are controlled with hysteresis loops, which yields undesired torque ripple and varying switching frequencies.

A suitable real-time parameter identification approach without affecting torque dynamics and its integration with low switching frequency DB-DTFC drives should be

explored. In addition, the injection signal frequency and the rotor bar skin effect will affect the estimation accuracy.

In addition, at low speeds, the current and speed ripple will affect the estimation accuracy, since the signal-to-noise ratio will increase significantly at low speeds in self-sensing mode. Besides, the quality of the harmonics components also affects the estimation accuracy of injection-based parameter estimation. A proper approach to improving the quality of the harmonic components has not been investigated yet.

Model Reference Adaptive System Approaches

The model reference adaptive system (MRAS), as shown in Fig. 1.5-5, is one of the major approaches of parameter estimation methods without injecting signals [97]–[103]. The main idea of this method is that there are two ways to obtain one quantity. One is through measurement and the other is through calculation. The “reference” is usually based on measured values. The “model” is usually based on calculated values. The calculated model parameters will converge to the measured value (accurate value) by forcing the error signal to zero.

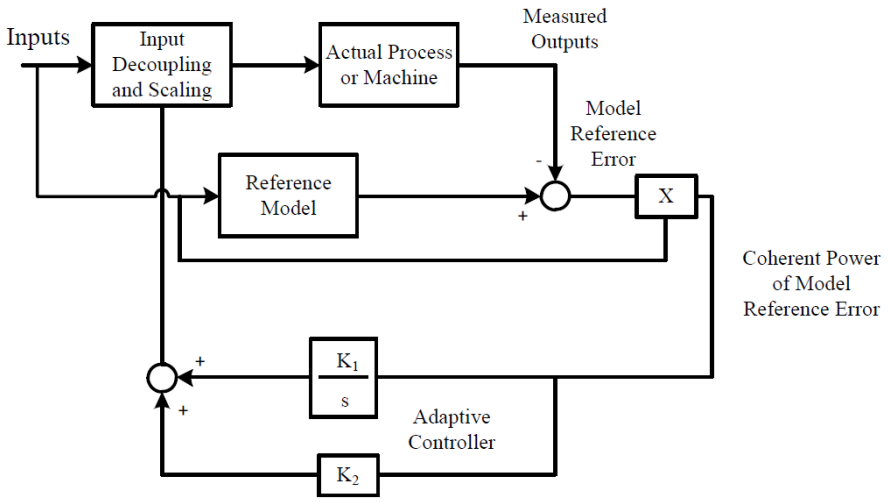

Fig. 1.5-5 State block diagram of the continuous time implementation of MRAS based adaptive command feedforward.

The MRAS-based parameter estimation method in induction machine drives has been discussed in [97]–[103]. By using different quantities for "model" output converging to "reference" model output, the different parameters can be estimated. In [98], L_m/τ_r is treated as an adaptive parameter for the MRAS system. Based on terminal voltages and currents, a nonlinear open loop rotor flux observer in the synchronous frame is built for estimated the rotor flux in both steady and transient state. With the rotor flux error converging to zero, the L_m/τ_r can be estimated.

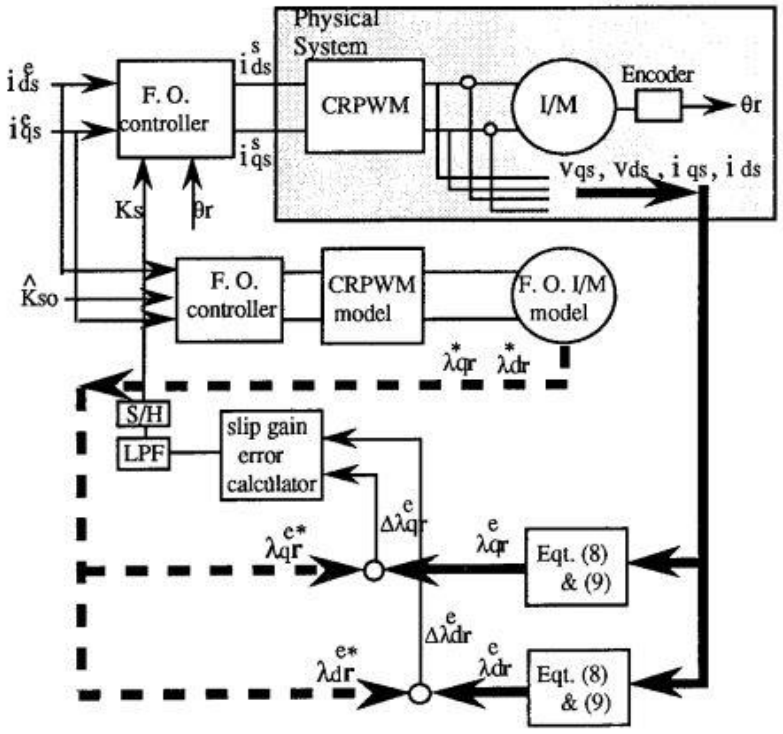

Fig. 1.5-6 MRAS based parameter estimation proposed in [98]

In [97], the rotor time constant is treated as the adaptive parameter. By utilizing the torque calculation through the (1.5-2) and (1.5-3), the torque error can be obtained. With updating the rotor time constant to the real value, the torque error is converging to zero. Only at medium and high speeds, the rotor time constant can be estimated precisely. Since at high speeds the voltage term dominates the flux estimation for the torque calculation, the $\hat{T}_s$ term in (1.5-2) provides an accurate estimation for the reference. However, at low speeds, the errors in the stator resistance and inverter nonlinearity will affect the $\hat{T}_s$ estimation accuracy. This would cause the final rotor resistance estimates to deviate from the real value. This approach is based on the flux observers. In [74] and [75], the similar flux observer based MRAS approach is proposed.

$$\hat{T}_s = \frac{3}{2}\frac{P}{2}\hat{\lambda}^s_{qds}\, i^s_{qds} \tag{1.5-2}$$

where, $\dot{\lambda}^s_{qds} = = V^s_{qds} - R_s i^s_{qds}$

$$T_{em} = \frac{3P}{4}\frac{L_m}{L_r}(i_{qs}\lambda_{dr} - i_{ds}\lambda_{qr}) \tag{1.5-3}$$

where, $\lambda_{qr} = L_m\, i_{qs} + L_r\, i_{qr}$

$\lambda_{dr} = L_m\, i_{ds} + L_r\, i_{dr}$

Instead of using flux, the reactive power can also be used as the converging quantity for MRAS system. The methods, which proposed in [101]–[105], can be categorized as the reactive power-based MRAS system. Reactive power reference model is formulated in (1.5-4), which can be calculated by the terminal voltage and current. It can be used as the "reference". By submitting the (1.5-5) and (1.5-6) into (1.5-4) and canceling the stator resistance, the reaction power yields (1.5-7), which can be used as the "model" part in MRAS system.

$$Q = V^e_{qs}\, i^e_{ds} - V^e_{ds}\, i^e_{qs}\, V^e_{qs}\, i^2_{qs} \tag{1.5-4}$$

$$V_{qs} = R_s i_{qs} + \omega_e \lambda_{ds} \tag{1.5-5}$$

$$V_{ds} = R_s i_{ds} - \omega_e \lambda_{qs} \tag{1.5-6}$$

$$Q^* = \omega_e\, L_s\, i^2_{ds} + \omega_e\, L_\sigma\, i^2_{qs} \tag{1.5-7}$$

where, $L_\sigma = L_s - L_m^2 / L_r$

Based on (1.5-7), the Fig. 1.5-7 can be implemented as the "model" part in the MRAS system, which contains the machine parameters.

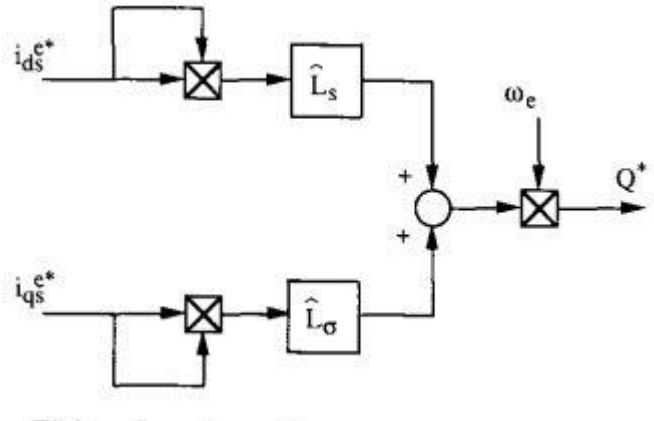

Fig. 1.5-7 Reactive power "model" for MRAS system in [103]

The L_s and L_σ estimates should be only machine saturation level dependent. This method overcomes the major drawback, which is stator resistance dependency, in the flux observer-based MRAS proposed in [98]–[100]. However, this model can only estimate the stator inductance and leakage inductance. The rotor resistance, which is a key parameter for the high performance motor drive, cannot be estimated through this approach.

Since DB-DTFC use the flux observer voltage model at medium and high speed ranges for the flux estimation, it is less parameter sensitive among these ranges. However, at low speeds, DB-DTFC performance may degrade due to the usage of the flux observe current model, which is sensitive to machine parameter mismatch. In terms of the model reference adaptive system (MRAS) based real-time parameter estimation method, the MRAS controller gains will affect the MRAS system converging time and stability. Thus, considering the rotor bar effect, the methodology for choosing appropriate injected signal frequencies for estimating different parameters has not been explored. In addition, the methodology for MRAS gains tuning for optimized converting time has not been explored either.

From the literature review, the real-time parameter estimation research has been primarily focused on IFOC drives. Also, the most improvements by real-time parameter estimation technologies are evaluated using encoders for the velocity feedback. Thus, the improvements for DB-DTFC drives with real-time parameter estimation technologies have not been explored yet. In addition, the effects of using real-time parameter estimation technologies with back-EMF-based self-sensing have not been quantitatively evaluated. Moreover, with back-EMF based self-sensing, the torque production sensitivity to machine parameters mismatch and speed estimation error in DB-DTFC drives has not been considered and compared to the existing FOC drives in the literature. It is also interesting to explore the highest velocity loops bandwidth that the IM DB-DTFC drives can achieve in the back-EMF self-sensing mode with different estimation methods.

1.6 Summary of Research Opportunities Identified

The following research opportunities have been identified in the state-of-the-art-review:

1.6.1 Robustness of Back-EMF based Self-sensing

- Investigate and evaluate the parameter sensitivity of the proposed synergy, DB-DTFC drive with back-EMF based self-sensing
- Investigate and evaluate the robustness and estimation accuracy of the back-EMF based self-sensing technology

- Develop a suitable methodology for improving the DB-DTFC drive with back-EMF based self-sensing performance at low speeds

1.6.2 High Bandwidth Speed Command Tracking of DB-DTFC

- Develop methodology of high bandwidth speed command tracking measurement of DB-DTFC drive
- Investigate and evaluate the speed command tracking performance difference between IFOC drive and DB-DTFC drive
- Investigate and evaluate the effects of machine parameters for the high bandwidth speed command tracking performance.

1.6.3 Real-time Parameter Estimation for Encoder-Based DB-DTFC

- Investigate and evaluate the rotor bar skin effect for the injection-based parameter estimation performance.
- Develop the methodology of injection-based parameter estimation approach in DB-DTFC drive
- Develop a methodology to select appropriate injected signal frequencies by considering the rotor bar effect for different parameter estimations
- Develop methodology of MRAS gains tuning for optimized converting time in MRAS-based parameter estimation

1.6.4 Real-time Parameter Estimation with Back-EMF Based Self-sensing

- Investigate the secondary effect of injection-based parameter estimation method in the DB-DTFC back-EMF based self-sensing mode
- Develop methodology of decoupling approach of the injection-based parameter estimation method without affecting torque and speed dynamics
- Develop a methodology for improving the quality of the injected harmonic components

1.6.5 Comparative Evaluation and Improvements with Two Real-time Parameter Estimation Methods

- Investigate and evaluate the improvements for DB-DTFC drives with two real-time parameter estimation technologies
- Investigate and quantitatively evaluate the effects and difference of using two real-time parameter estimation technologies with and without using back-EMF-based self-sensing
- Investigate and evaluate absolute and relative computational load and processing power requirements for each of the method
- Investigate and evaluate the torque production sensitivity to machine parameters mismatch and speed estimation error in DB-DTFC drives in self-sensing mode.
- Investigate and evaluate the highest velocity loops bandwidth that the IM DB-DTFC drives can achieve in the self-sensing mode with each method.

Chapter 2

Experimental Test Setup

In this chapter, the test setup, which is used to gather all experimental results in this thesis, is described. The hardware test setup for this research project was designed by YASKAWA Electric Corporation, Japan (YEC) & YASKAWA America Inc. (YAI). Both hardware setup and software development will be presented.

2.1 Hardware and Interconnects

2.1.1 Overall System

The following equipment is used for this lab:

1. Two back-to-back coupled induction machines;
2. Two magnetic encoders installed on the test side and load side;
3. Two standard A1000 machine drives;
4. AIX dual DSP controller;
5. Yaskawa R1000 energy saving unit;
6. Onosokki TS-2800 torque transducer;
7. Yokogawa WT-1800 power analyzer;

8. Four communication interface cards (one is for the AIX side, the other one is for A1000 drive side);

9. DELL XPS 8700 PC;

A block diagram of the test stand topology is shown in Fig. 2.1-1. The control boards embedded in Yaskawa A1000 drives are bypassed on both test side and load side since both load machine and test machine must be controlled for research purpose. That means A1000 drives are utilized as rectifiers and inverters.

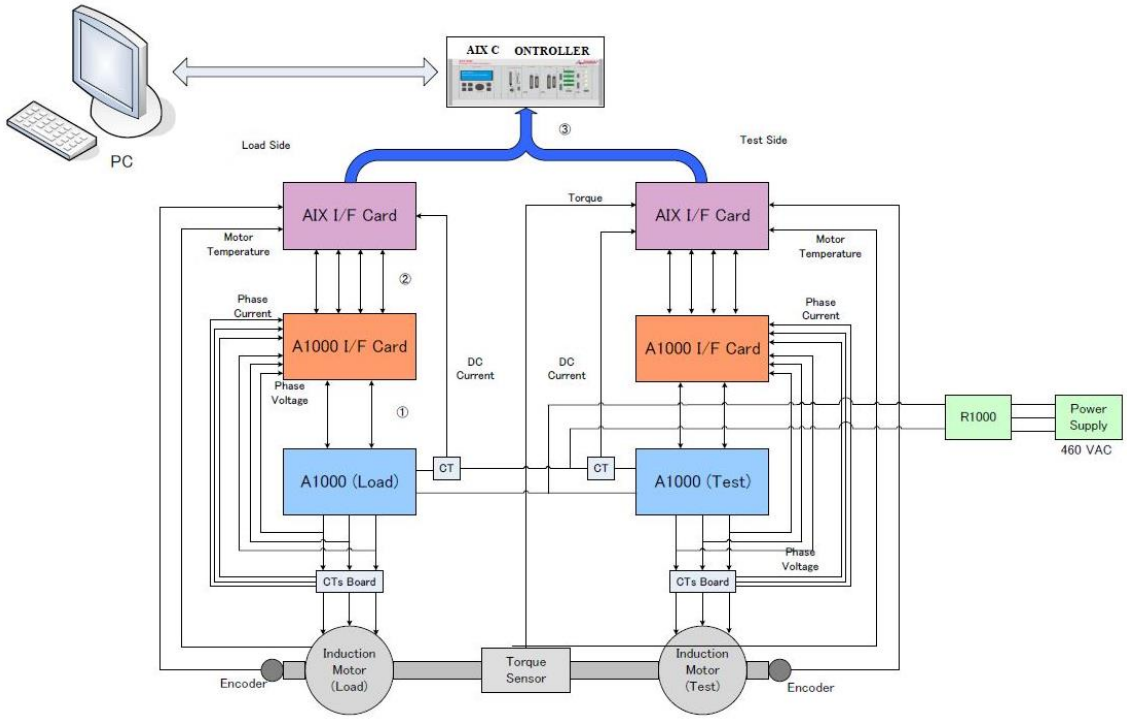

Fig. 2.1-1 The hardware setup block diagram

2.1.2 Induction Machine

The induction machines used in the test bench are two identical Marathon model 213THTL7726 CE induction machines. The rated speed is 1765[RPM] (i.e. 185[rad/s]). The stator is configurable for 230 or 460V RMS-LL operation. In this project, machines are configured for 460V operation with a frequency of 60 Hz. The parameters of the selected induction machine are shown in Table 2.1-1.

Table 2.1-1 The induction machine nominal parameters

Rated Voltage	V_r	=	460 V-rms-ll
Rated Speed	f_r	=	60 Hz
Rated Power	P_r	=	5.6 kW
Rated Torque	T_r	=	30 Nm
Rated Flux	λ_r	=	0.99Volt-sec
Rated Slip	s_r	=	2 %
Pole Number	P	=	4
Stator Resistance	$\hat{R}_s$	=	0.70 Ω
Rotor Resistance	$\hat{R}_r$	=	0.57 Ω
Magnetizing Inductance	$\hat{L}_m$	=	10.1 mH
Stator Leakage	$\hat{L}_{ls}$	=	4.7mH
Rotor Leakage	$\hat{L}_{lr}$	=	6.0mH

By using identical machines for both the test side and load side, it is possible to evaluate the performance over the entire operating space. The machines are coupled together

using a torque transducer, which leads to a resonant of test dynamometer at 79.5Hz. Experimental results about the resonant frequency will be illustrated in the next chapter. Photos of the test stand are included in appendix B.

2.1.3 Inverter and Sensors

Standard Yaskawa inverters

Standard Yaskawa three-phase voltage source inverters are installed. The inverter DC bus voltage is 650V. Gate drive signal is sent by an AIX controller through interface boards.

Current Sensors

KOHSHIN HC-PDG series Hall-Effect current sensors are installed to measure the three line currents of induction machines. The current sensor specifications are described in Table 2.1-2 below.

Table 2.1-2 KOHSHIN HC-PDG Current Sensor Specifications

Primary current measuring range	I_{PM} = 150 A
Sensor Gain	G_{Sensor} = 4.25
Linearity Error	ε_L = < 1 %
90% Response Time	t_{rise} = 3 μs

Similar sensors are used widely in electrical drives today and do not represent an excessive cost requirement for drive systems. Note that the primary operating range of the current sensors is significantly larger than the drive system requirement.

Position Sensor

Position sensing of the machine shaft is achieved by the use of an Avtron AV56 magnetic encoder mounted directly on the machine shaft. The specifications for the encoder can be found in the following Table 2.1-3.

Table 2.1-3: Avtron AV56 Encoder Specifications

Disc Resolution	N	4096 Lines
Maximum Mechanical Speed	ω_{max}	5,000 RPM
Electrical Freq Response	f_{max}	165 kHz
Maximum Supply Voltage	V_{max}	15 VDC

The encoder is an incremental type; therefore, the absolute position of the shaft is not sensed. Since the encoder is quadrature type, the encoder provides 16384 (4*4096) unique patterns per revolution to the DSP.

2.2 Software and Signal Flow

The overall control block diagram for DB-DTFC has been shown in Fig. 2.2-1. The current observer and flux observer are important and necessary to the DB-DTFC technology. Motion observer, motion controller, current observer, flux observer and the DB-DTFC algorithm will be discussed individually in the following sections.

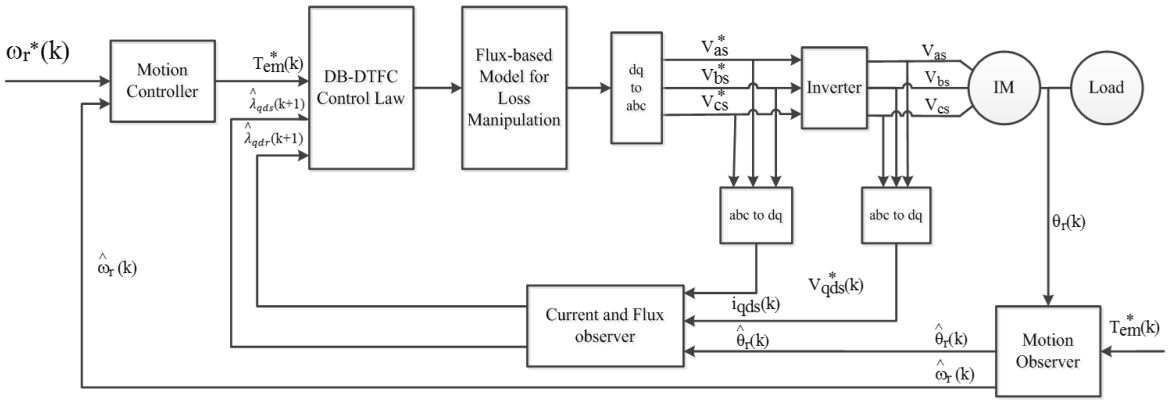

Fig. 2.2-1 Overall control diagram for DB-DTFC software implemented in AIX controller.

2.2.1 Sensor Calibration and System Protection

Before DB-DTFC control algorithm implementation, three-phase current sensor and DC bus voltage sensor should be calibrated when machines are operating under V/f control. The sensor scaling gains are shown in Table 2.2-1.

Table 2.2-1 Three-Phase Current Sensor and DB Bus Voltage Sensor Gains

	Gains Value		Offset Value
Phase_A	4.16	offset	0.09
Phase_B	4.20	offset	0.12
Phase_C	4.14	offset	0.04
DC Bus Gain	89.65		

These gains are properly scaled for use in later machine tests use. Both hardware protection and software protection are implemented to prevent damage to the dynamometer. The protections are listed as following.

- *Overcurrent protection* - If any of the machine line currents exceed the programmed limit (1.5pu), the PWM output would be disabled.
- *Over speed protection* - If the machine axis velocity is measured above a predetermined maximum value (1.2pu), the PWM output would be disabled.
- *DC link overvoltage* - If the DC link voltage is measured above a predetermined maximum value (700V)), the PWM output would be disabled.
- *Dead-time protection* – Set hardware dead-time in AIX controller XCI card to 1.6ms and set software dead-time in DSP code to 2.0ms.

2.2.2 Motion Observer

The output of the encoder for position detection contains quantization noise. The quantization noise is determined by encoder resolution and sampling frequency. If the sampling frequency for the position is 1kHz, the position and average velocity revolution can be calibrated as (2.2-1). The ripple on the calculated average velocity for the blue line shown in Fig 2.2-2 is actually the quantization errors due to position sensor interface. The system torque dynamics would be degraded if the sampling frequency is reduced. This is a tradeoff. The calculated average velocity from the encoder feedback is not suitable for advantageous machine control system (i.e. DB-DTFC).

$$\bar{\omega}_{res} = \frac{\frac{1}{4096*4}}{\frac{1}{1000}\sec\frac{1\min}{60\sec}} = 3.7\ [RPM] \approx 0.4\ rad/s \qquad (2.2\text{-}1)$$

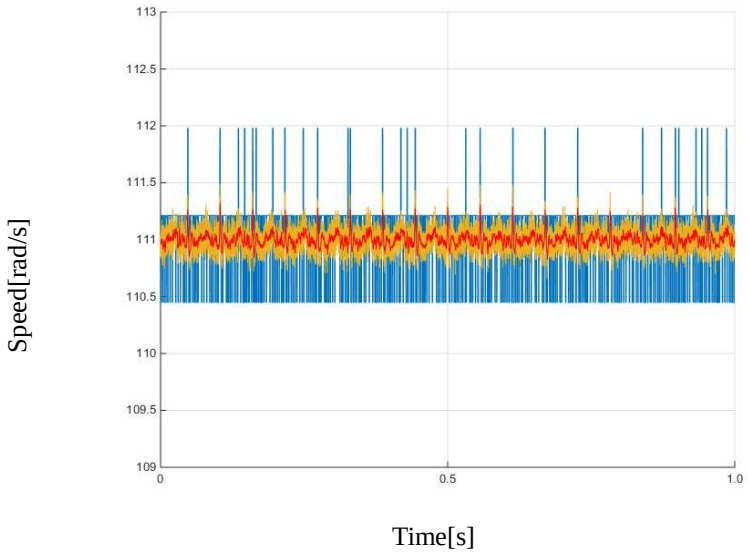

Fig. 2.2-2 Velocity feedback signals used for motion controller on the testbench at 1kHz

A much more smooth and accurate speed feedback can be provided by a Luenberger-style motion observer with nearly zero lagging property. The state block diagram of this motion observer is shown in Fig. 2.2-3.

The torque command from the motion controller is fed as the command feedforward in order to achieve nearly zero lagging property. The bandwidth of motion observer is determined by b_o, k_{so} and k_{iso}. The instantaneous velocity estimates, orange line and red line shown in Fig. 2.2-2, are much smoother than the calculated average speed. In sum, estimated instantaneous velocity from the motion observer has less noise than the calculated average velocity for the switching frequency in 1 kHz, and the estimated instantaneous velocity signal for the switching frequency in 1 kHz has less noise than the switching frequency in 10kHz.

Therefore, the estimated instantaneous velocity from this motion observer for switching frequency is used for velocity feedback in the motion controller.

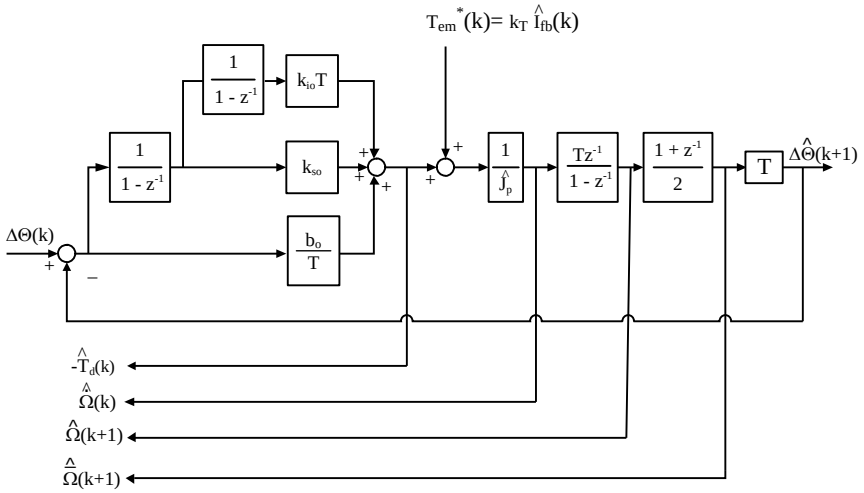

Fig. 2.2-3 Digital implementation of a Luenberger style, discrete time state observer

The bandwidth of motion observer can be tuned by different b_o, k_{so} and k_{iso} values. The observer gains to obtain desired bandwidths can be calculated by characteristic equations shown in (2.2-2), (2.2-3) and (2.2-4). The z_1, z_2 and z_3 are corresponding to three poles in three loops of motion observer.

$$b_o = J_p \frac{(1- z_1 z_2 z_3)}{T} \tag{2.2-2}$$

$$k_{so} = J_p \frac{(3-(z_1 z_2 + z_2 z_3 + z_1 z_3)) -2 b_a T}{T^2} \tag{2.2-3}$$

$$k_{iso} = J_p \frac{(3- z_1- z_2- z_3) - k_{sa}T^2 - b_a T}{T^3} \tag{2.2-4}$$

Where, $z = e^{2\pi fT}$

2.2.3 Motion Controller

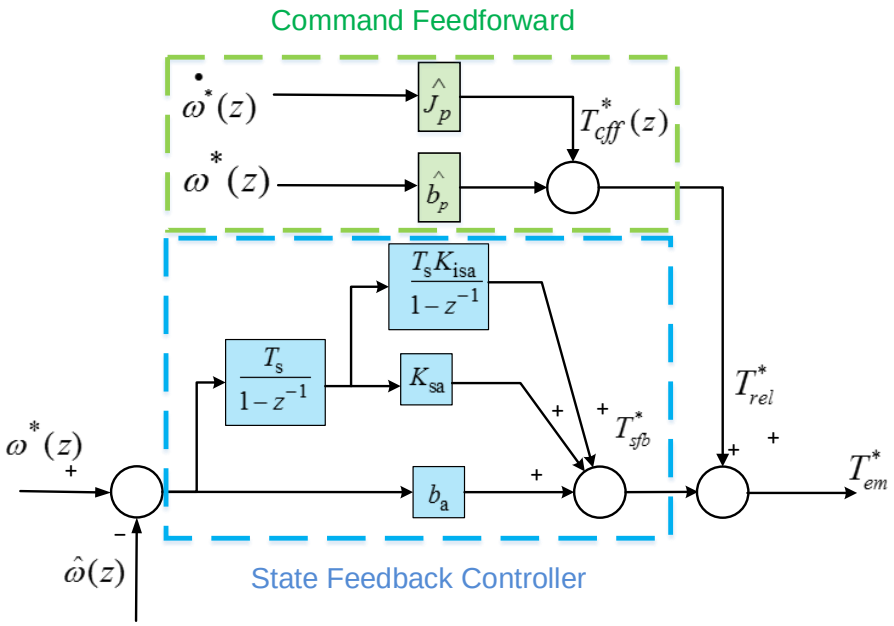

Fig. 2.2-4 Digital state feedback motion controller with velocity, position, and integral position loops

To regulate machine shaft velocity, a motion controller was developed to produce torque commands for the DB-DTFC torque modulator. In order to achieve good tracking performance, a state feedback motion controller shown in Fig. 2.2-4 is used.

The motion controller closes loops on velocity, position, and integrated position. In addition to the closed loops, an additional torque command reference term performs as the current reference (or rather, the command feedforward in the industry). State feedback motion controller is primarily responsible for disturbance rejection and the feedforward path is responsible for the torque reference. Based on physical plant, the characteristic equation for the system is shown in (2.2-5).

$$z^3 + \frac{\left(-3J_p+Tb_aT^2k_{sa}+T^3k_{isa}\right)}{J_p}z^2 + \frac{\left(3J_p-2Tb_a-T^2k_{sa}\right)}{J_p}z + \frac{\left(-J_p+Tb_a\right)}{J_p} \qquad (2.2\text{-}5)$$

2.2.4 Flux and Current Observers

The flux observer is essential and necessary to the DB-DTFC implementation since no flux sensors can be installed. In the following test, a Gopinath style flux observer is used, which is a combination of a current based flux observer and a voltage based flux observer. The significant advantage of this kind of flux observer is its high estimation accuracy at both low speeds and high speeds [6] [7].

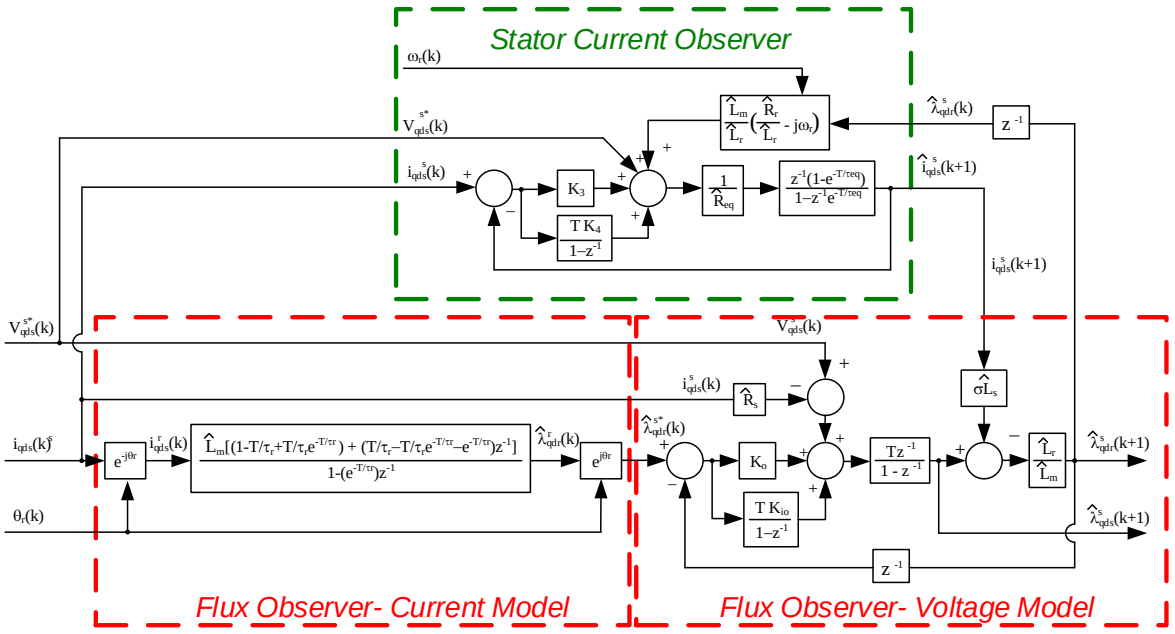

Fig. 2.2-5 Discrete time flux observer and current observer with high switching frequency approximations

While the flux observer proposed in [6] [7] has been built only in the continuous time domain, the counterpart in the discrete time domain has been proposed in [12][13]. The block diagram for the flux observer used at high switching frequencies has been shown in Section 1.2 and repeated in Fig. 2.2-5 for convenience.

In the current model, measured current can be used to estimate rotor flux relationship from machine fundamental equations, and shown in (2.2-6). The difference equation for discrete time implementation is shown in (2.2-7).

$$\dot{\lambda}^{r}_{qdr} = \frac{R_r}{L_r} L_m i^{r}_{qds} - \frac{R_r}{L_r} \lambda^{r}_{qdr} \tag{2.2-6}$$

$$\begin{aligned} \lambda^{r}_{qdr}(k) = & \left(1 - \frac{\tau_r}{T_s} + \frac{\tau_r}{T_s} e^{-T_s/\tau_r}\right) L_m i^{r}_{qds}(k) \\ & + \left(\frac{\tau_r}{T_s} - \left(\frac{\tau_r}{T_s} + 1\right) e^{-T_s/\tau_r}\right) L_m i^{r}_{qds}(k-1) + e^{-T_s/\tau_r} \lambda^{r}_{qdr}(k-1) \end{aligned} \tag{2.2-7}$$

The voltage model for flux observer is built based on the stator flux linkage differential equation on the stator reference frame. The difference equation for discrete time implementation is shown in (2.2-8) and (2.2-9).

$$\dot{\lambda}^{s}_{qds} = V^{s}_{qds} - R_s i^{s}_{qds} \tag{2.2-8}$$

$$\frac{\lambda^{s}_{qds}(k+1) - \lambda^{s}_{qds}(k)}{T_s} = V^{s}_{qds}(k) - R_s i^{s}_{qds}(k) \tag{2.2-9}$$

The bandwidth of a Gopinath-style flux observer is determined by two gains, K_1 and K_2. The characteristic equation of the closed loop flux observer is shown in (2.2-10). A similar technique as described in Section 2.2.2 to place the desired poles in the characteristic equation can be used for tuning.

$$z^2 + \frac{\left(-2\hat{L}_m+\hat{L}_rTK_1+\hat{L}_rT^2K_2\right)}{\hat{L}_m}z + \frac{\left(\hat{L}_m-\hat{L}_rTK_1\right)}{\hat{L}_m} \qquad (2.2\text{-}10)$$

Since the estimated flux in next sampling is needed for the DB-DTFC algorithm, a current observer is developed to provide estimated current value in next sampling instant. It is used for calculating estimate rotor flux. The block diagram for the current observer is shown in Fig. 2.2-6. The characteristic equation of the current observer, for tuning purposes, is shown in (2.2-11).

$$z^2 + \frac{\left(-R_{eq} - R_{eq}e^{-\frac{T}{\tau_{eq}}} + K_3 - K_3e^{-\frac{T}{\tau_{eq}}} + TK_4 - TK_4e^{-\frac{T}{\tau_{eq}}}\right)}{R_{eq}}z + \frac{\left(R_{eq}e^{-\frac{T}{\tau_{eq}}} - K_3 + K_3e^{-\frac{T}{\tau_{eq}}}\right)}{R_{eq}} \qquad (2.2\text{-}11)$$

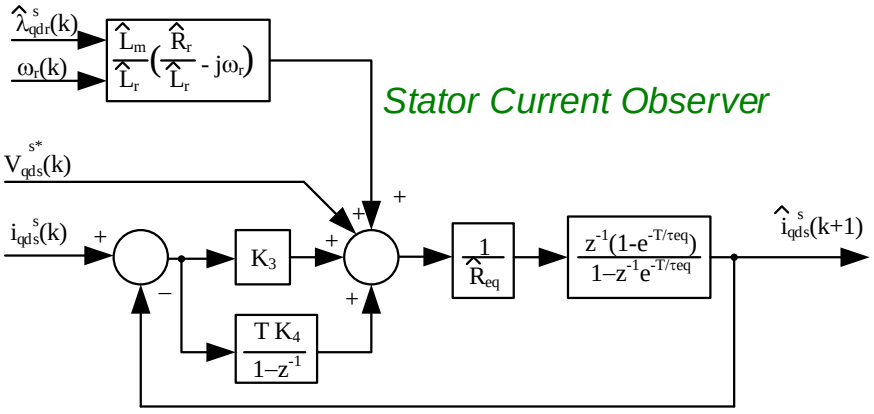

Fig. 2.2-6 Discrete time state block diagram of stator current observer[12]

2.2.5 Deadbeat Torque Modulator

The details of the deadbeat torque modulator were presented in Chapter One. The torque modulator takes in the necessary observed flux linkages and machine parameters and returns the stator voltage commands. This section will outline a practical method for solving

the DB-DTFC solution. In Chapter One, the DB-DTFC torque line solution was presented and is repeated below for reference.

$$Y = v_{qs}(k)T_s \tag{2.2-12}$$

$$X = v_{ds}(k)T_s \tag{2.2-13}$$

$$M = \frac{\lambda_{qr}(k)}{\lambda_{dr}(k)} \tag{2.2-14}$$

$$B = \frac{4\sigma L_s L_r}{3PL_m\lambda_{dr}(k)}\left(\Delta T_e(k) + \left(\frac{R_rL_s+R_sL_s}{\sigma L_sL_r}\right)T_e(k)\,T_s\right) + T_s\omega_r(k)\left(\frac{\lambda_{qs}(k)\lambda_{qr}(k) + \lambda_{ds}(k)\lambda_{dr}(k)}{\lambda_{dr}(k)}\right) \tag{2.2-15}$$

To simplify (2.2-15) two constants are defined in (2.2-16)(2.2-17).

$$C_1 = \frac{3P\ L_m}{4\ \sigma L_sL_r} \tag{2.2-16}$$

$$C_2 = \left(\frac{R_rL_s+R_sL_r}{\sigma L_rL_s}\right) \tag{2.2-17}$$

By substituting (2.2-16) and (2.2-17) into (2.2-15) the following result is reached:

$$v_{qs}(k)t_s = \frac{\lambda_{qr}(k)}{\lambda_{dr}(k)}\,v_{ds}(k)t_s + \frac{1}{\left(\frac{3P\ L_m}{4\ \sigma L_sL_r}\right)\lambda_{dr}(k)}\left(\Delta T_e(k) + t_s\left(\frac{R_rL_s+R_sL_s}{\sigma L_sL_r}\right)T_e(k)\right) + \frac{t_s\omega_r(k)}{\lambda_{dr}(k)}\left(\lambda_{qs}(k)\lambda_{qr}(k) + \lambda_{ds}(k)\lambda_{dr}(k)\right) \tag{2.2-18}$$

It is clear that the Volt.-sec vector that needs to be applied to the stator voltage can be solved for a given $\Delta T_e(k)$. The required variables for solving the stator voltage are the calculated observer quantities: $\underline{\lambda}_{qds}(k)$, $\underline{\lambda}_{qdr}(k)$, $\omega_r(k)$, and $T_e(k)$. If the stator resistance is

assumed to be negligible the entire stator voltage vector is used to drive the stator flux in a particular direction as shown in (2.2-19).

$$\Delta\underline{\lambda}_{qds}(k) = v_{qds}(k)T_s \tag{2.2-19}$$

It was shown graphically in [26] that the stator flux constraint could be represented as a circle where the flux vectors have a constant radius. This is depicted below as an equation.

$$\sqrt{\lambda_{qs}^{*\,2}+\lambda_{ds}^{*\,2}} = \left|\lambda_{qds}^{*}\right| \tag{2.2-20}$$

It has also been shown in [19] that voltage vectors must satisfy the following relationship.

$$\sqrt{\lambda_{qs}^{*\,2}+\lambda_{ds}^{*\,2}} = \left(\lambda_{qs}(k) + V_{qs}(k)T_s\right) + \left(\lambda_{ds}(k) + V_{ds}(k)T_s\right) \tag{2.2-21}$$

Squaring each side of (2.2-21) yields the following resultant.

$$\lambda_{qs}^{*\,2}+\lambda_{ds}^{*\,2} = \left(\lambda_{qs}(k) + V_{qs}(k)T_s\right)^2 + \left(\lambda_{ds}(k) + V_{ds}(k)T_s\right)^2 \tag{2.2-22}$$

By expanding (2.2-22) and substituting the torque line relationship, $V_{qs}\,T_s = m\,V_{ds}\,T_s + b$, as shown in (2.2-12) through (2.2-15) the following equations are reached.

$$\begin{aligned} 0 = {} & \left(m^2+1\right)\left(v_{ds}T_s\right)^2 + \left(2\lambda_{ds}m+2bm+2m\lambda_{qs}\right)\left(v_{ds}T_s\right) \\ & +\left(b^2 +2\,b\,\lambda_{qs}+\left(\lambda_{qs}^2+\lambda_{ds}^2\right) - \left(\lambda_{qs}^{*\,2}+\lambda_{ds}^{*\,2}\right)\right) \end{aligned} \tag{2.2-23}$$

A new term $\Delta\lambda_S(k)$ may be defined to simplify (2.2-23).

$$\Delta\lambda_s(k) = \left|\underline{\lambda}_{qds}(k+1)\right|^2 - \left|\underline{\lambda}_{qds}(k)\right|^2 \tag{2.2-24}$$

(2.2-24) can now be simplified to the following resultant

$$0 = (m^2+1)(v_{ds}T_s)^2 + (2\lambda_{ds}m+2bm+2m\lambda_{qs})(v_{ds}T_s) + (b^2+2b\lambda_{qs}+\Delta\lambda_s(k)) \quad (2.2\text{-}25)$$

The roots of (2.2-25) can be found by the quadratic equation as shown below.

$$v_{ds}T_s = \frac{-(2mb + 2m\lambda_{qs} + 2\lambda_{ds})^2 \pm \sqrt{(2mb + 2m\lambda_{qs} + 2\lambda_{ds})^2 - 4(m^2 + 1)(b^2 + 2b\lambda_{qs} - \Delta\lambda_s)}}{2(m^2 + 1)} \quad (2.2\text{-}26)$$

Since $\lambda_{dr}(k)$ is in the denominator of the m term (slope) the control law becomes unsolvable when $\lambda_{dr}(k) = 0$. To avoid this problem, the control law is calculated in the re-aligned reference frame as stated in Section 1.3.4. The stator flux linkage is aligned with the d-axis, which results in a finite value of $\lambda_{dr}(k)$. Therefore, $\lambda_{qs} = 0$ and the control law can be further simplified as shown in (2.2-27).

$$V_{ds} = \frac{-(2mb + 2\lambda_{ds})^2 \pm \sqrt{(2mb + 2\lambda_{ds})^2 - 4(m^2 + 1)(b^2 - \Delta\lambda_s)}}{2(m^2 + 1)} \quad (2.2\text{-}27)$$

The positive root provides the desired voltage vector. In the case that the desired stator flux circle does not intersect the torque line, no solution can be found. This represents an unfeasible commanded machine state. For the case, the commanded stator voltage is greater than the available inverter voltage the commanded voltage is scaled back to the maximum feasible voltage vector defined by the largest circle that fits in the inverter hexagon.

$$V_{ds}T = \frac{-(2mb + 2\lambda_{ds})^2 \pm \sqrt{(2mb + 2\lambda_{ds})^2 - 4(m^2 + 1)(b^2 - \Delta\lambda_s)}}{2(m^2 + 1)} \quad (2.2\text{-}28)$$

2.2.6 PWM Dead-time Compensation

Once the voltage command vectors are calculated the values are converted from two phase to three phase values. The three-phase PWM values are then converted to the modulation index by the following equation.

$$M_{index} = 0.5 + \frac{V^*}{V_{bus}} \quad (2.2\text{-}29)$$

In the inverter, the necessary blacking time is used for avoiding shootthrough of the DC link. In this case, a small time delay should be added to the gate signal of the turning-on device to guarantees that both switches in an inverter leg never conduct simultaneously. A new dead-time compensation technique based on a back calculation of the current phase angle is proposed and experimentally verified by [20]. A block diagram showing the implementation is presented in Fig. 2.2-7. Since the reconstructed current is free from PWM noise the instant of zero crossing is easily determined [20].

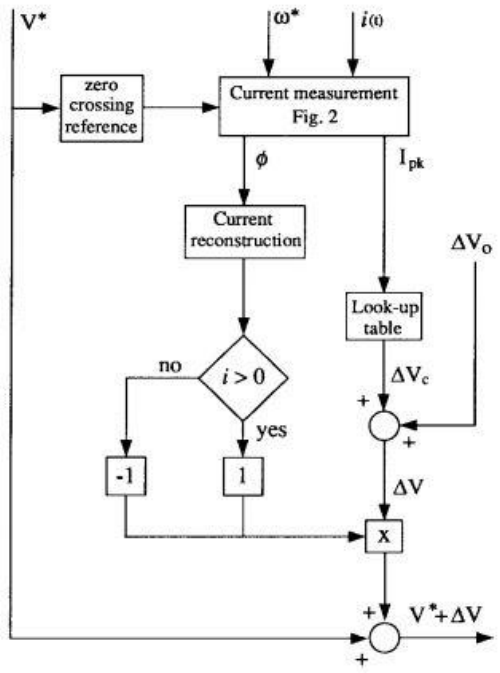

Fig. 2.2-7 Block diagram of the proposed dead-time compensation algorithm [20]

2.3 Summary

This chapter has outlined the test bench setup for the experimental evaluation. The control cube contains a power analyzer, an AIX controller, gate signal interface boards, Yaskawa A1000 drives and a Yaskawa R1000 energy saving unit. Two identical induction machines with a torque transducer in the middle are mounted on the test bench. Also, a sensor calibration, a motion observer, and a motion controller in this project are introduced. Then, a flux observer, current observer and DB-DTFC algorithm implementation have been reviewed. Dead-time compensation is introduced at the end of this chapter.

Chapter 3

Robustness of DB-DTFC Back-EMF Based Self-sensing

This chapter is going to introduce the parameter sensitivity of both DB-DTFC and IFOC drives, which are constructed based on machine parameters. Due to rotor flux orientation, it is well known that standard IFOC drives performance is affected by inaccuracy of the rotor time constant, i.e. $\tau_r = L_r/R_r$. With detuned rotor time constant, torque and rotor flux in IFOC are not decoupled, leading to a degraded torque control over the entire operating space.

3.1 Parameter Sensitivity Comparison with IFOC

Based on many published papers, DB-DTFC is insensitive to machine parameters over medium and high speed. It is fundamental because DB-DTFC drives utilize a properly developed flux observer in the stationary reference frame and a closed loop torque control scheme. Rotor flux orientation is not used in DB-DTFC. At medium and high speed, the voltage model is insensitive to all the parameters (i.e. negligible voltage drop on stator resistance assumed), which yields precise torque and flux control regardless of parameter uncertainty. However, the stator resistance dependency and inverter nonlinearity undermine

the voltage model at low speeds, and the current model has to be used for flux linkage estimation. Since the rotor flux field orientation in IFOC and the current model in flux observer follow the same physical principle, it can be expected that DB-DTFC at low speeds and IFOC possess similar parameter sensitivity to the rotor time constant.

Experimental evaluation regarding parameter sensitivity of IFOC and DB-DTFC drives is shown from Fig. 3.1-1 to Fig. 3.1-5. Torque responses are obtained from an additional flux observer with well-tuned parameters. The output of this particular flux observer is only used to evaluate real torque response, instead of feedback control in DB-DTFC.

With intentionally over-tuned/detuned magnetizing inductance, torque control accuracy of IFOC and DB-DTFC is compared in experimental results as shown in Fig. 3.1-1, for low (left) and high (right) speed operation, respectively.

The yellow lines are the torque command. The orange lines are estimated torque of DB-DTFC drive. Then, redo the test, while the test machine is operated in IFOC control algorithm. The blue lines are estimated torque of IFOC drive. For low speed operation (left), considerable torque estimation errors are observed due to the dominance of the current model. For high speed operation (right), torque estimates from the flux observer track the real torque regardless of parameter errors, since the voltage model, which is not sensitive to machine parameters, dominates the flux observer. Therefore, DB-DTFC performance degrades at low speed, which has similar performance to IFOC drives. The torque ripple of IFOC drive in low

speed is caused by machine asymmetry, which is verified in the following section. Since the DB-DTFC is a closed loop control for torque and flux loop, the torque ripple of DB-DTFC is significantly reduced compared to the torque ripple of IFOC drive.

Evaluations are conducted for rotor resistance at low speed and high speed in Fig. 3.1-2, for stator resistance at low speed and high speed in Fig. 3.1-3, for stator leakage inductance at low speed and high speed in Fig. 3.1-4, for rotor leakage inductance at low speed and high speed in Fig. 3.1-5 respectively.

From Fig. 3.1-1 to Fig. 3.1-5, the following conclusions can be drawn:

- Both DB-DTFC and IFOC are sensitive to L_m and R_r at low speed.
- IFOC are still sensitive to L_m and R_r at high speed, however, DB-DTFC is less sensitive to L_m and R_r at high speed.
- The most critical parameters are L_m and R_r. Both DB-DTFC and IFOC are insensitive to L_{lr} L_{ls} and R_s over the entire speed range.
- DB-DTFC has less torque ripple than IFOC.
- Since torque estimates are used as feedback and forced to track the reference in DB-DTFC, the obvious torque errors seem small at low speeds compared to IFOC drives.

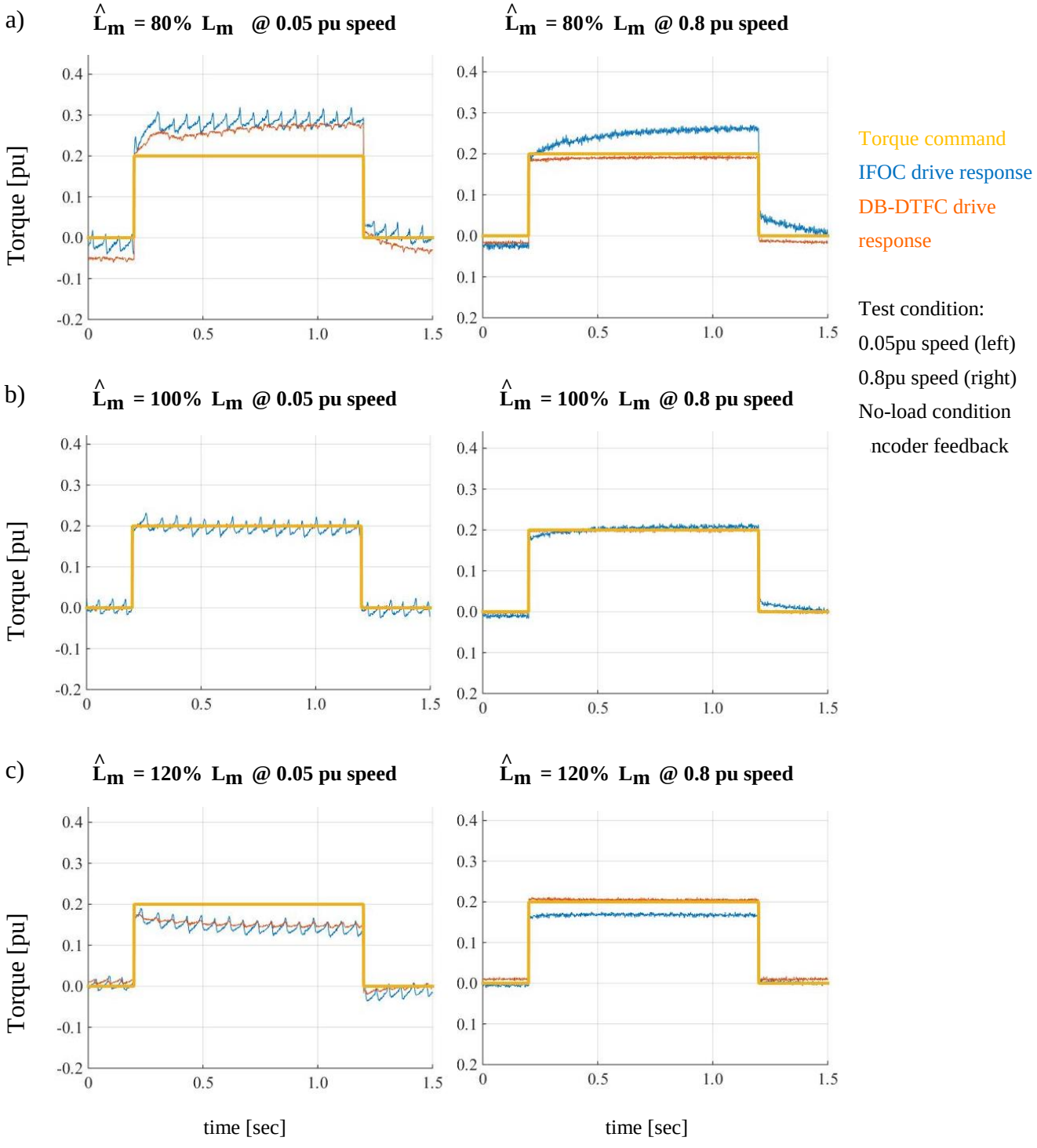
a)
$\hat{L}_m$ = 80% L_m @ 0.05 pu speed
$\hat{L}_m$ = 80% L_m @ 0.8 pu speed
b)
$\hat{L}_m$ = 100% L_m @ 0.05 pu speed
$\hat{L}_m$ = 100% L_m @ 0.8 pu speed
c)
$\hat{L}_m$ = 120% L_m @ 0.05 pu speed
$\hat{L}_m$ = 120% L_m @ 0.8 pu speed
Torque [pu]
time [sec]
Torque command
IFOC drive response
DB-DTFC drive response
Test condition:
0.05pu speed (left)
0.8pu speed (right)
No-load condition
ncoder feedback

Fig. 3.1-1 Experimental results of torque control at low speed and high speed with various magnetizing inductance L_m a) 80% L_m b) 100% L_m c) 120% L_m

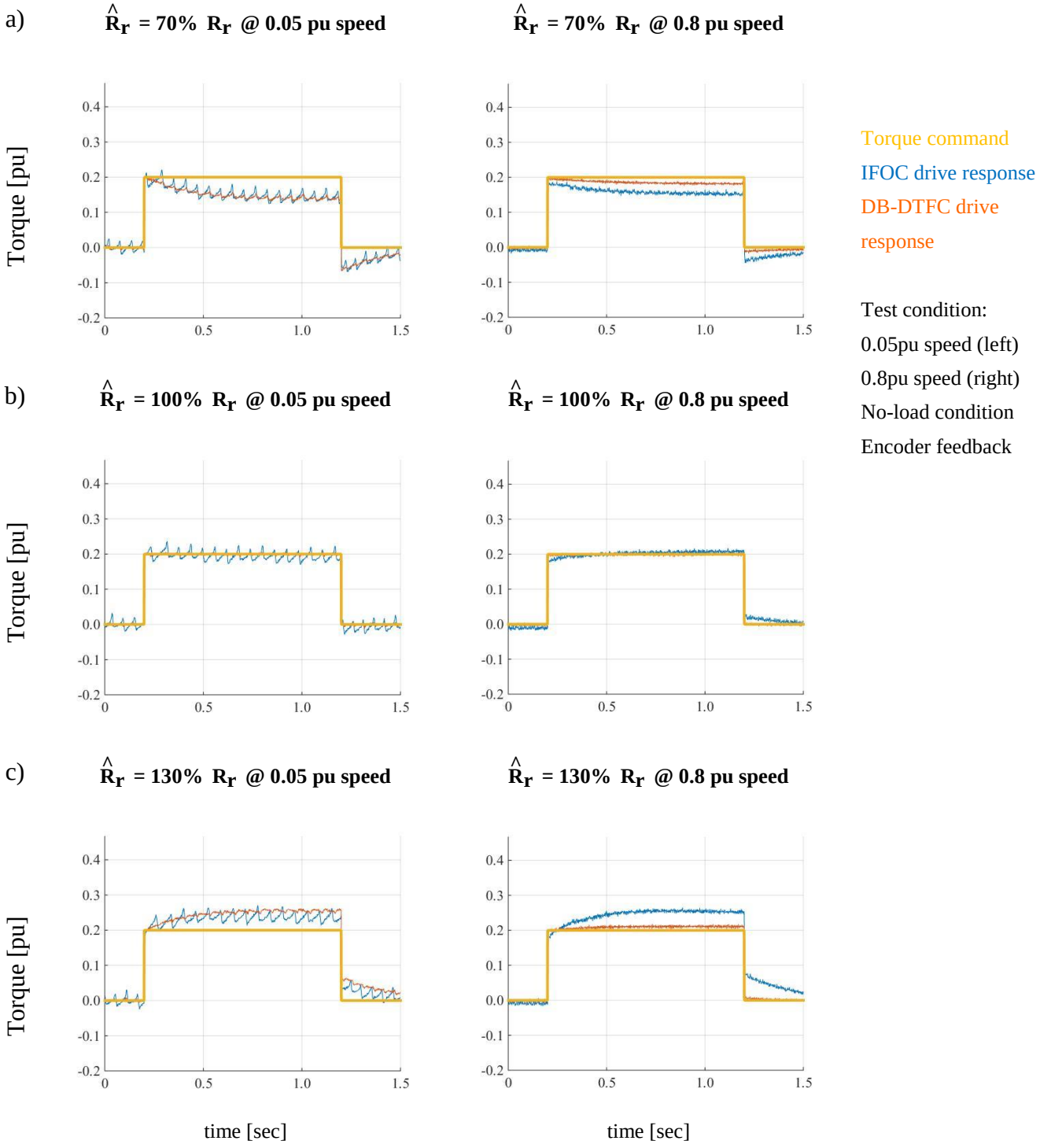

Fig. 3.1-2 Experimental results of torque control at low speed and high speed with various rotor resistance R_r a) 80% R_r b) 100% R_r c) 120% R_r

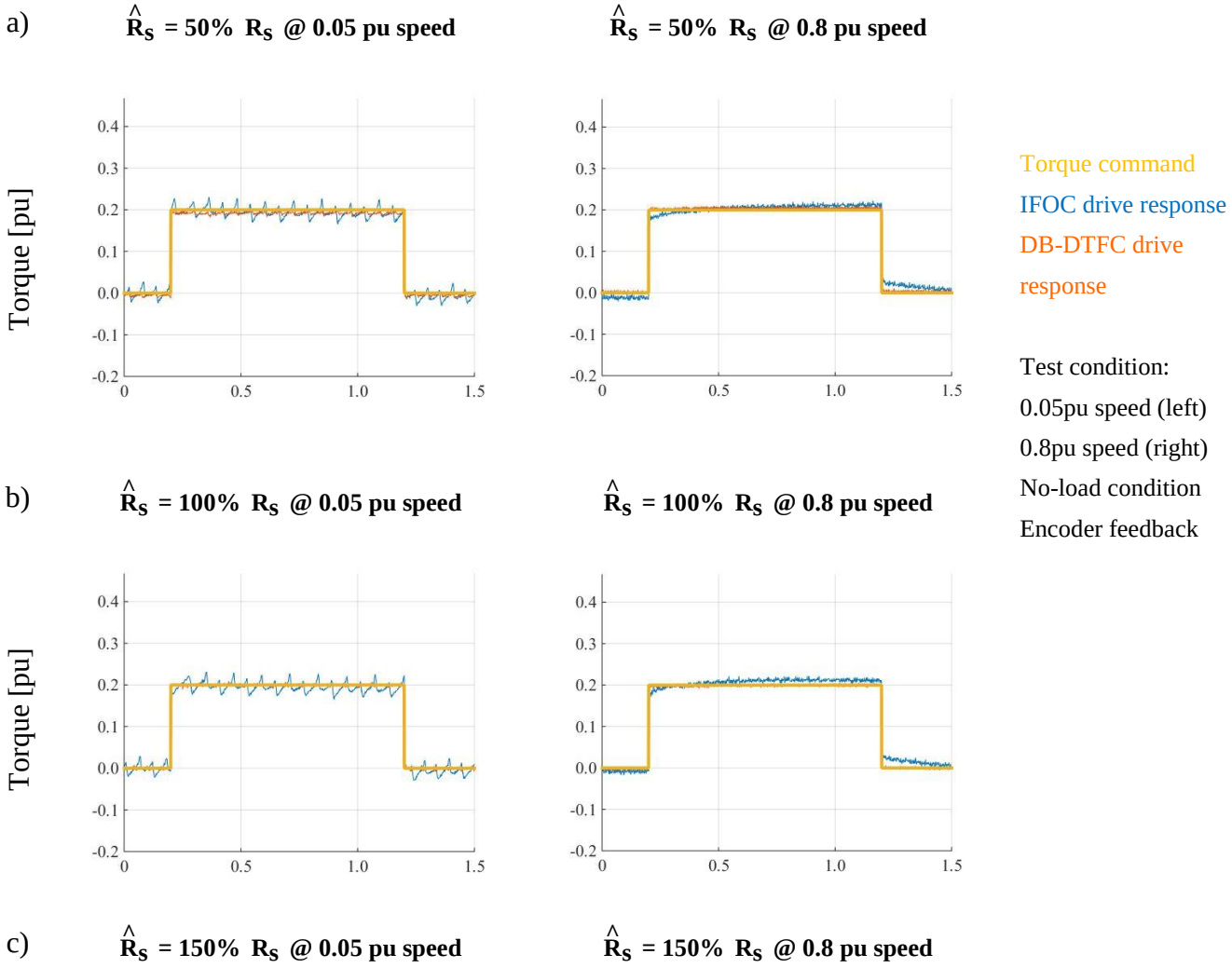

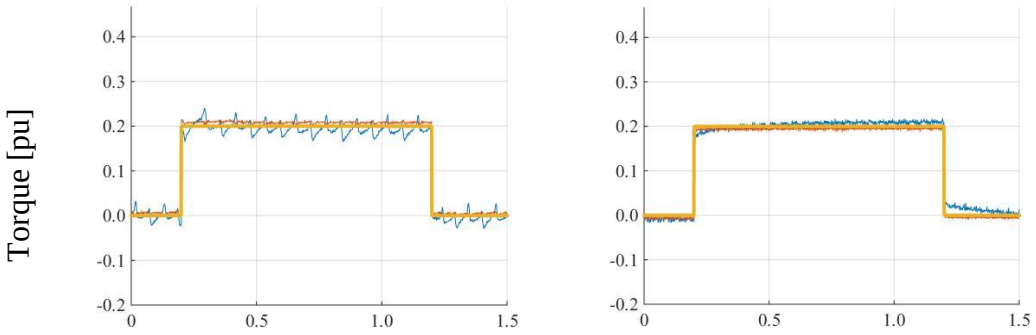

Fig. 3.1-3 Experimental results of torque control at low speed and high speed with various stator resistance R_s a) 80% R_s b) 100% R_s c) 120% R_s

a) $\hat{L}_{ls}$ = 50% L_{ls} @ 0.05 pu speed

$\hat{L}_{ls}$ = 50% L_{ls} @ 0.8 pu speed

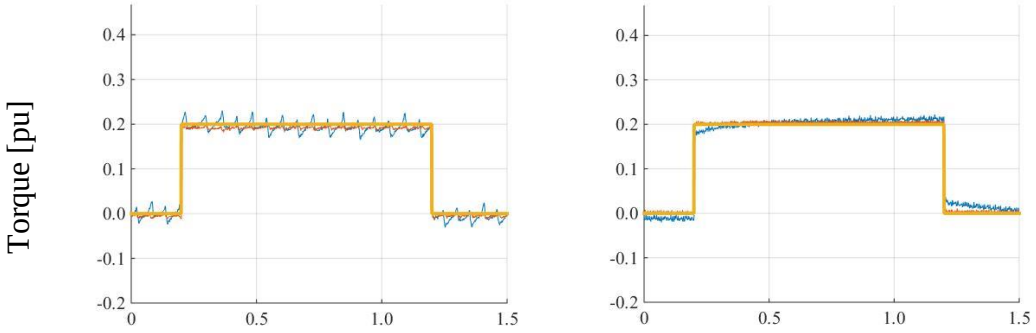

b) $\hat{L}_{ls}$ = 100% L_{ls} @ 0.05 pu speed

$\hat{L}_{ls}$ = 100% L_{ls} @ 0.8 pu speed

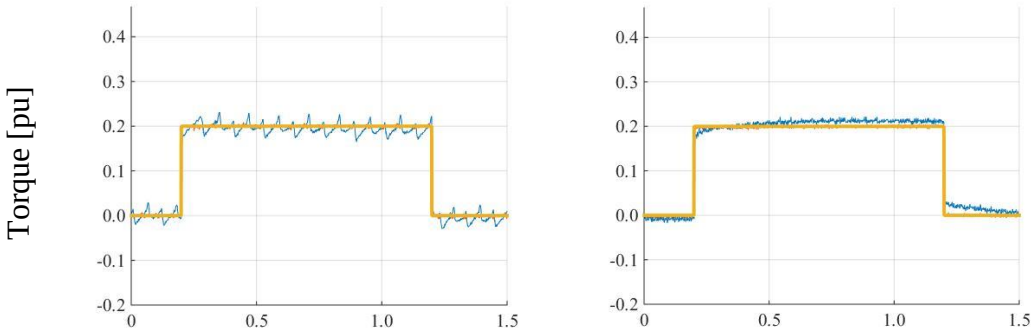

c) $\hat{L}_{ls}$ = 150% L_{ls} @ 0.05 pu speed

$\hat{L}_{ls}$ = 150% L_{ls} @ 0.8 pu speed

Torque command
IFOC drive response
DB-DTFC drive response

Test condition:
0.05pu speed (left)
0.8pu speed (right)
No-load condition
Encoder feedback

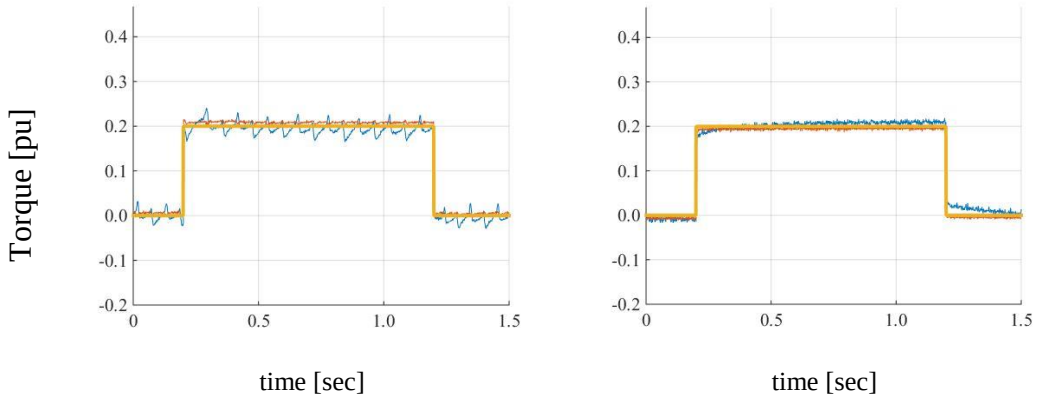

Fig. 3.1-4 Experimental results of torque control at low speed and high speed with various stator leakage inductance L_{ls} a) 80% L_{ls} b) 100% L_{ls} c) 120% L_{ls}

a) $\hat{L}_{lr}$ = 50% L_{lr} @ 0.05 pu speed $\hat{L}_{lr}$ = 50% L_{lr} @ 0.8 pu speed

b) $\hat{L}_{lr}$ = 100% L_{lr} @ 0.05 pu speed $\hat{L}_{lr}$ = 100% L_{lr} @ 0.8 pu speed

c) $\hat{L}_{lr}$ = 150% L_{lr} @ 0.05 pu speed $\hat{L}_{lr}$ = 150% L_{lr} @ 0.8 pu speed

Torque command
IFOC drive response
DB-DTFC drive response

Test condition:
0.05pu speed (left)
0.8pu speed (right)
No-load condition
Encoder feedback

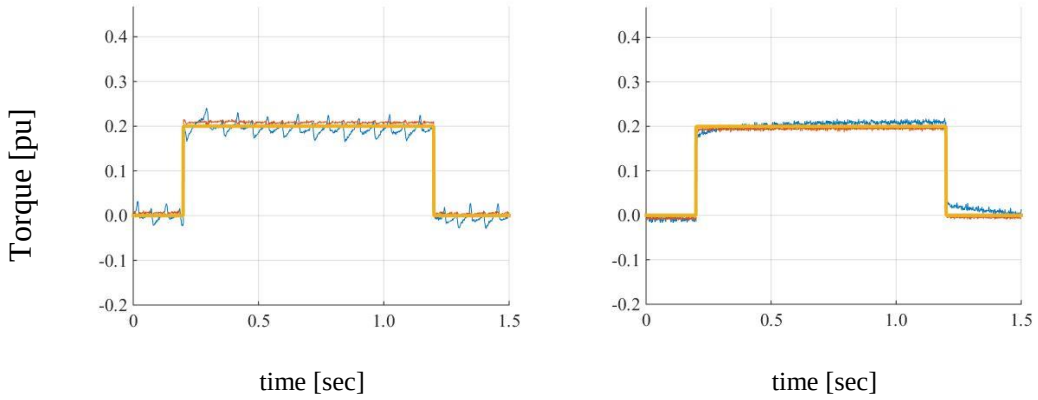

Fig. 3.1-5 Experimental results of torque control at low speed and high speed with various rotor leakage inductance L_{lr} a) 80% L_{lr} b) 100% L_{lr} c) 120% L_{lr}

3.2 Parameter Sensitivity with Measured Torque

For general applications, torque sensors are not available, and therefore it is difficult to obtain real torque. However, in Yaskawa testbench, there is a torque meter in the middle of the test and the load machine, so it is possible to obtain the measured DB-DTFC and IFOC torque responses from torque meter. Since the torque meter has very low measurement frequency, it is used only to compare the torque response of DB-DTFC and IFOC drive in steady state conditions. Fig. 3.2-1 and Fig. 3.2-2 present experimental evaluation with magnetizing inductance variation and rotor resistance, which double verify that IFOC is sensitive to L_m and R_r over entire speed range, despite that, DB-DTFC is only sensitive to L_m and R_r at low speed.

a) $\hat{L}_m = 80\%\ L_m$ @ 0.05 pu speed

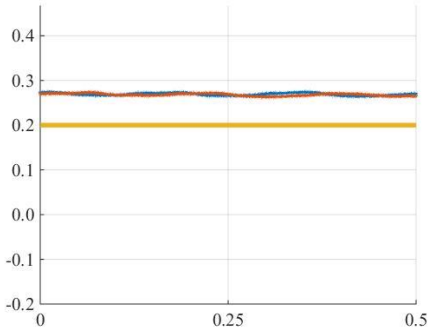

$\hat{L}_m = 80\%\ L_m$ @ 0.8 pu speed

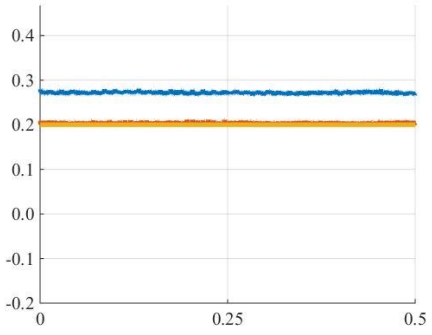

b) $\hat{L}_m = 100\%\ L_m$ @ 0.05 pu speed

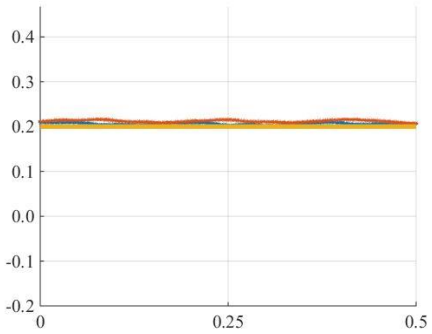

$\hat{L}_m = 100\%\ L_m$ @ 0.8 pu speed

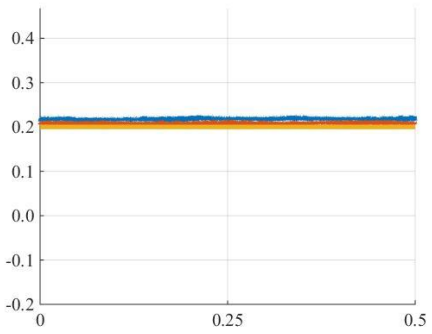

Torque command

Measured FOC drive response

Measured DB-DTFC drive response

Test condition:

0.05pu speed (left)

0.8pu speed (right)

No-load condition

Encoder feedback

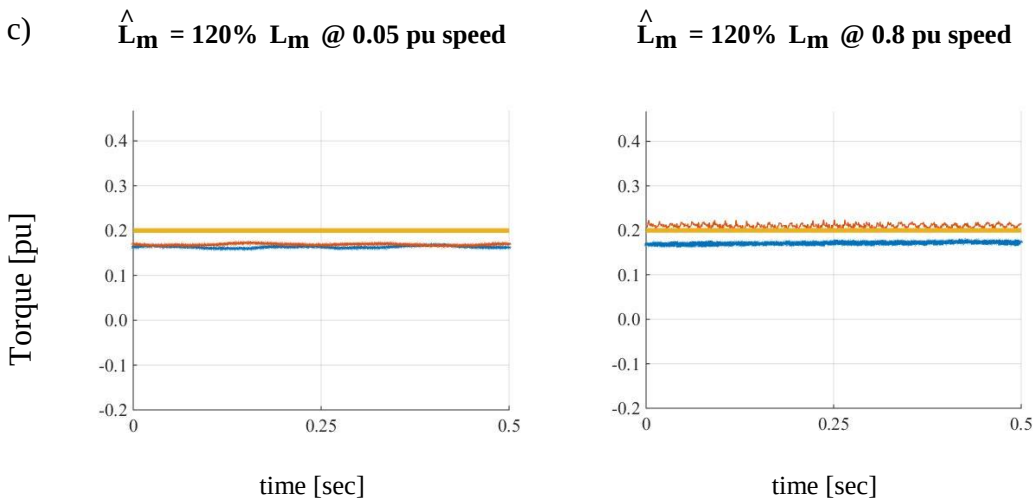

Fig. 3.2-1 Experimental results of torque control at low speed and high speed with various magnetizing inductance L_m a) 80% L_m b) 100% L_m c) 120% L_m

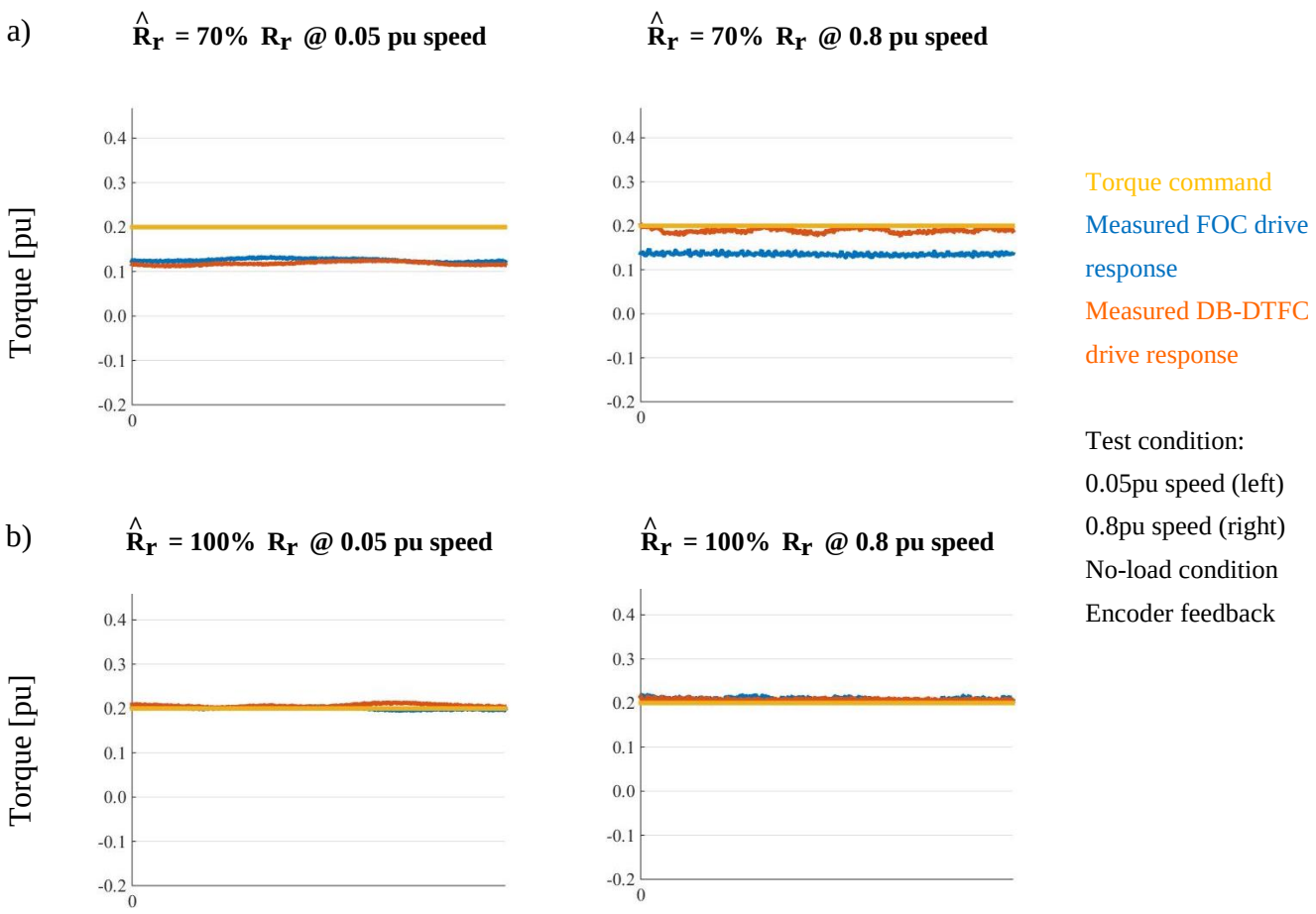

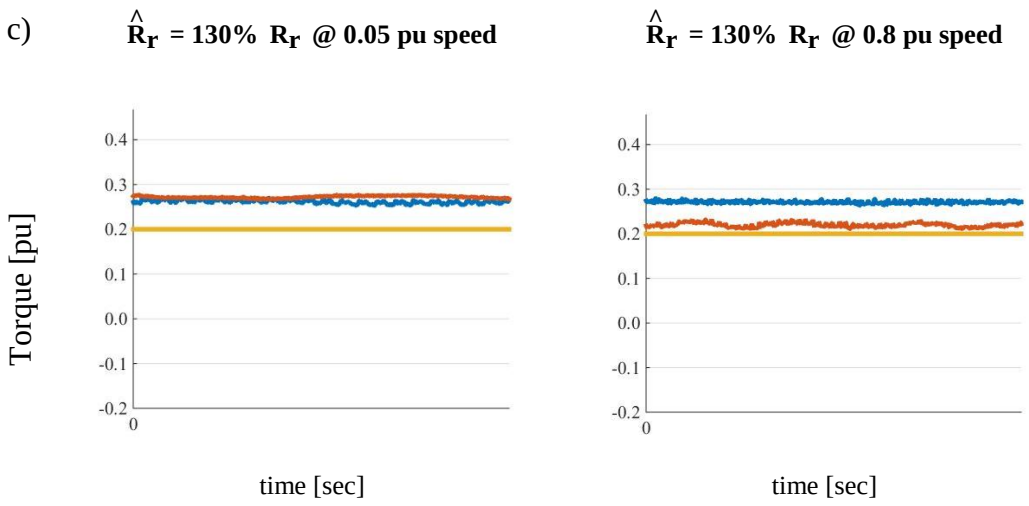

Fig. 3.2-2 Experimental results of torque control at low speed and high speed with various rotor resistance R_r a) 80% R_r b) 100% R_r c) 120% R_r

3.3 Parameter Sensitivity of DB-DTFC Back-EMF Self-Sensing

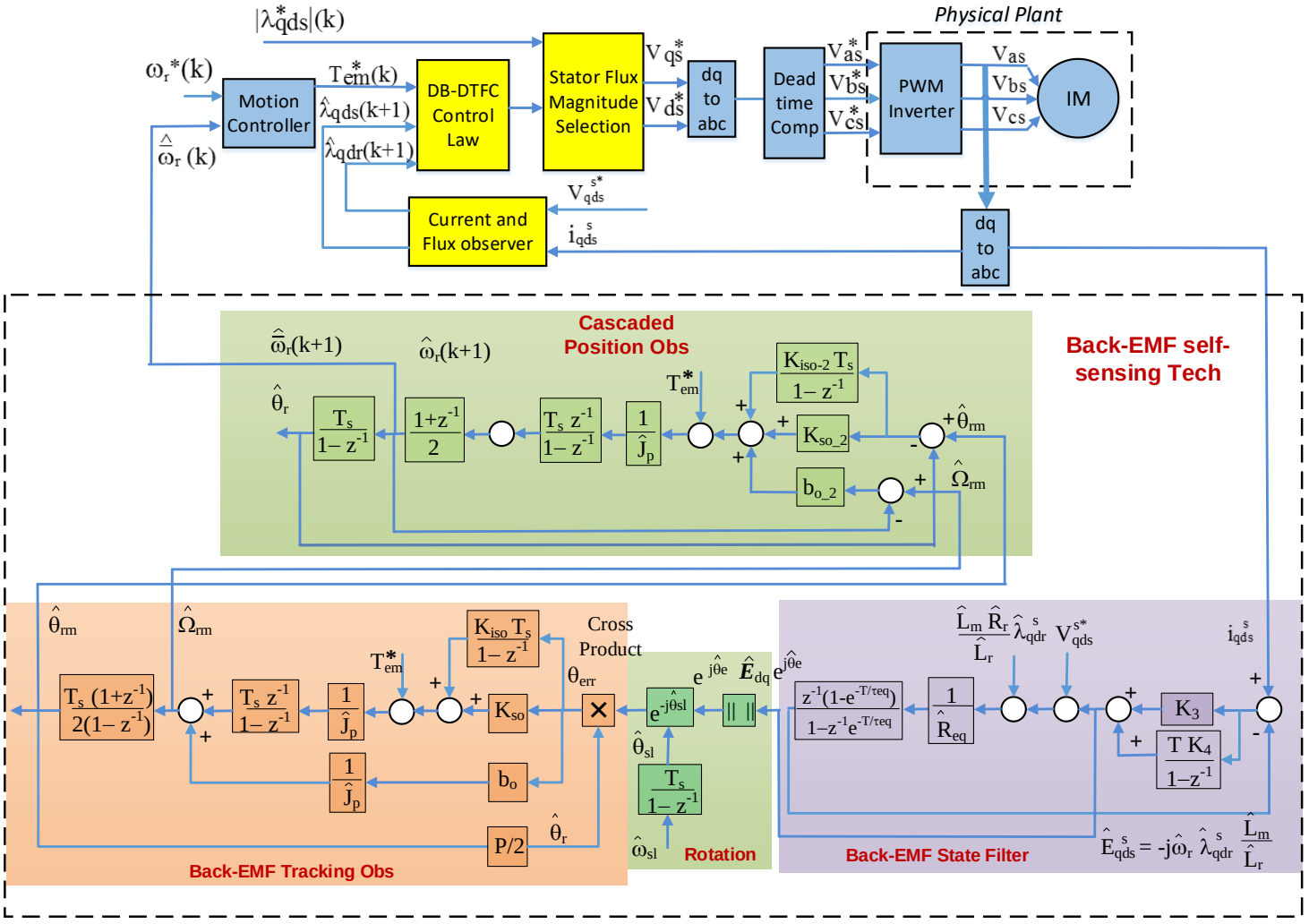

Fig. 3.3-1 Block diagram for observer-based back-EMF self-sensing in IM DB-DTFC drives

Fig. 3.3-1 shows a block diagram for observer-based back-EMF self-sensing in IM DB-DTFC drives. The DB-DTFC control law is based on physical inverse models of AC machines shown in yellow block. With feasible torque and flux commands in each sample instant, the discrete time current and flux observers calculate the stator and rotor flux estimates

in the next sample instant. By using these estimates, the DB-DTFC control law solves for Volt.-sec vectors based on the inverse torque model to achieve the torque and flux commands in just one sample instant. The back-EMF self-sensing technology at the bottom contains includes three parts: the back-EMF state filter, the back-EMF tracking observer and the cascaded position observer.

As opposed to the IPM machine, the electrical speed in the IMs is different from the rotor speed. For the IMs, if the excitation frequency is ω_e and the slip frequency is ω_{slip}, the rotor speed is $\omega_r = \omega_e - \omega_{slip}$. Thus, a slip frequency rotation block is needed between the back-EMF state filter and the back-EMF tracking observer, which is shown in the green block of Fig. 3.3-1.

Fig. 3.3-2 shows the comparison between estimated average velocities from a back-EMF tracking observer (dark color), an encoder-based motion observer (medium color) and cascaded motion observer (light color), when using cascaded motion observer estimated velocity signals as feedback. Since the estimates from back-EMF tracking observer start deteriorating significantly under 0.2 pu, Fig. 3.3-2 does not include back-EMF tracking observer estimates at 0.1 pu and 0.05 pu velocity. In Fig. 3.3-2, the estimates from the back-EMF tracking observer (dark color) at 0.2 pu, 0.3 pu and 0.4 pu speed have more noise than the estimates from the cascaded motion observer and the encoder-based motion observer, which are shown in light color and medium color, respectively. Even at 0.1 pu and 0.05 pu

speed, the estimated average velocity from the cascaded motion observer (light color) and encoder based motion observer (medium color) are overlaid together, which matches the sine wave speed test results.

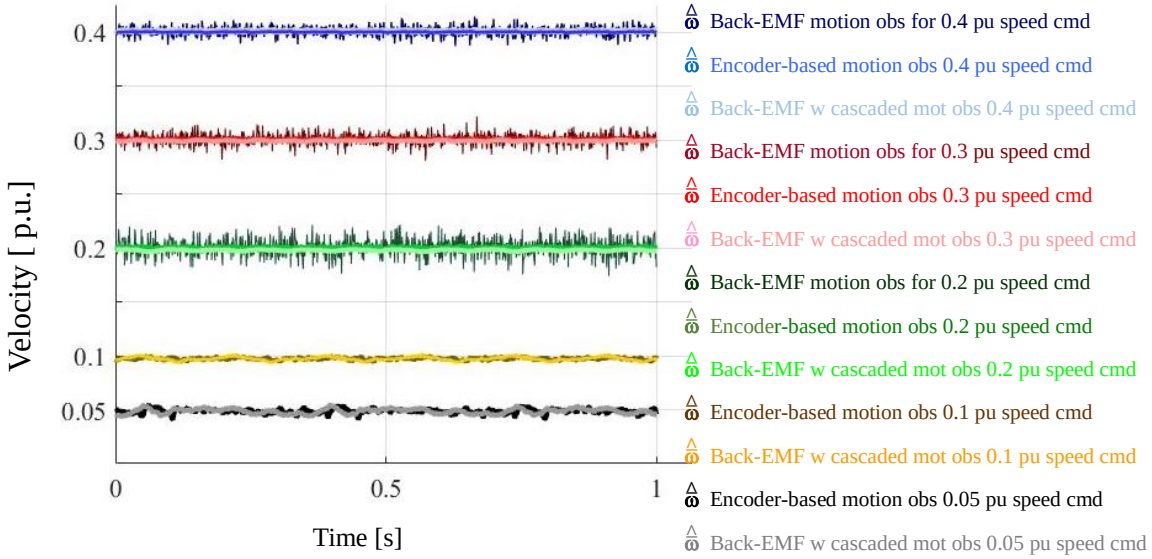

DB-DTFC with back-MEF self-sensing

Motion controller	f_s = 1 kHz EVs: 20 Hz 2 Hz 0.4 Hz
Back-EMF state filter	f_s = 10 kHz EVs: 200 Hz 40 Hz
Back-EMF based motion observer	f_s = 1 kHz EVs: 20 Hz 2 Hz 0.4 Hz

Fig. 3.3-2 Back-EMF-based cascaded motion observer, back-EMF tracking observer and encoder-based motion observer signal comparison at different constant velocities

Though parameter sensitivity of DB-DTFC control algorithm has been discussed in the previous section, the parameter sensitivity of the whole the proposed synergy of back-EMF tracking based DB-DTFC self-sensing has now yet been discovered. From Fig. 3.3-1, the back-EMF self-sensing block also contains machine parameter. By detuning, well-tuning and over-tuning the machine parameters, the velocity estimation accuracy can be compared at different speeds, as shown in Fig. 3.3-3.

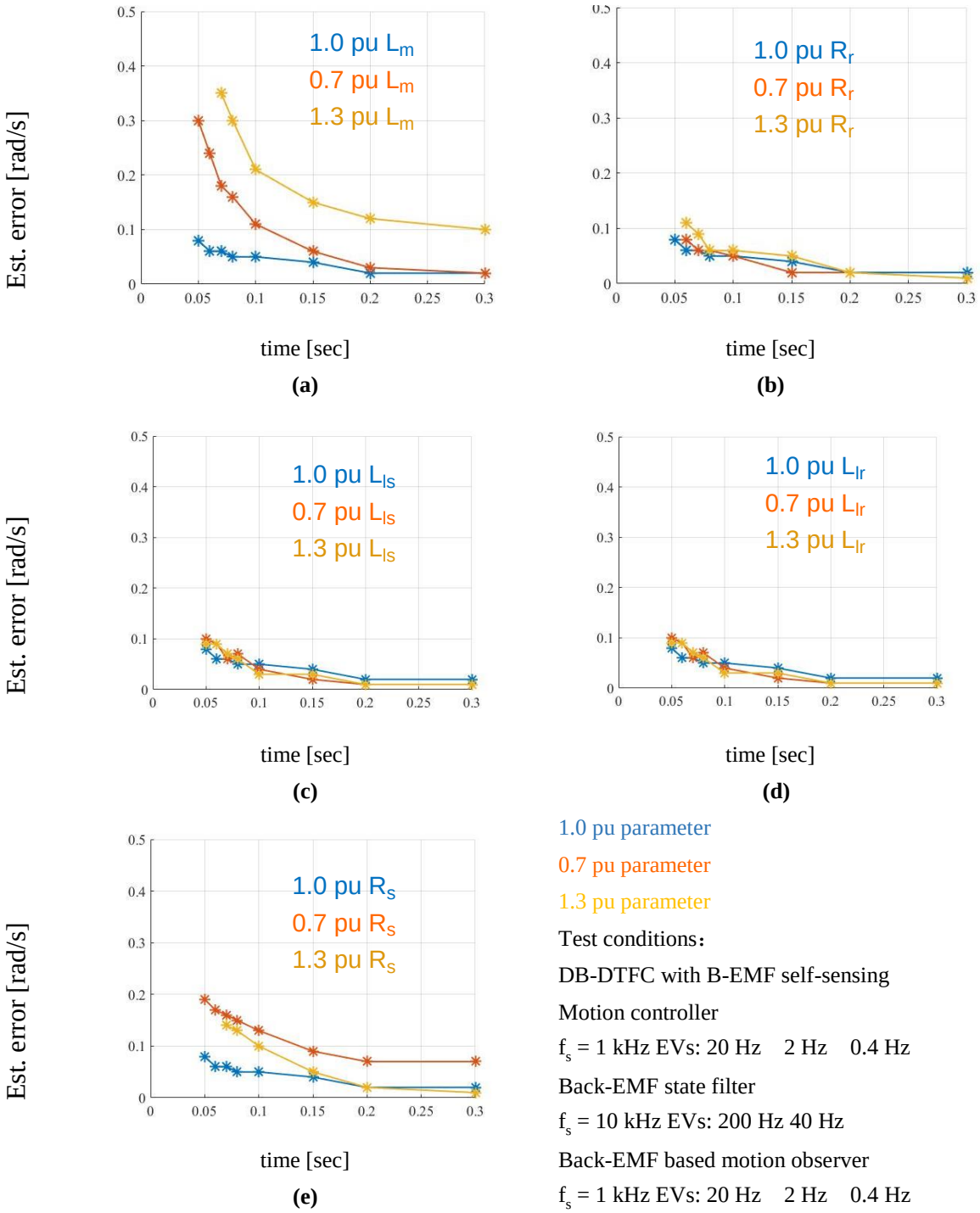

Fig. 3.3-3 The velocity estimation accuracy of the proposed back-EMF self-sensing

From the Fig. 3.3-3 (a), it can be seen that the proposed back-EMF self-sensing synergy is sensitive to magnetizing inductance at low speeds (< 0.2 pu) range. The synergy is insensitive to rotor resistance, stator leakage inductance and rotor leakage inductance, which are shown in Fig. 3.3-3 (b), (c) and (d).

However, at extra low speeds (< 0.06 pu) range, stator resistance affect the velocity estimation accuracy. The equation of the flux observer voltage model can be derived as (3.3-1).

$$\dot{\lambda}^{s}_{qds} = = V^{s}_{qds} - R_s i^{s}_{qds} \qquad (3.3\text{-}1)$$

At extra low speeds, both the voltage term (V^{s}_{qds}) and the term ($R_s\, i^{s}_{qds}$) will affect the estimation accuracy. It means the flux observer voltage mode is sensitive to stator resistance at extra low speeds. The error on the stator resistance would lead to the flux observer estimation accuracy degradation, which causes the additional velocity estimation error.

The Table 3.3-1 concludes the parameter sensitivity of IFOC, DB-DTFC and the proposed back-EMF self-sensing method respectively. For IFOC and DB-DTFC, the produced torque is used for the parameter sensitivity comparison at different speeds. For the back-EMF self-sensing technique, the velocity estimation accuracy is used for the comparison at different speeds. In the self-sensing mode, the DB-DTFC flux observer bandwidth is tuned as low as 1~3 Hz. In this range, the flux observer is sensitive to Rs, since the voltage model still dominates the whole flux observer. It is necessary to separate the extra low-speed (< 0.06 pu, 3.6 Hz) from the low speed range.

As discussed above, both the IFOC and DB-DTFC are sensitive to machine parameters, especially Lm and Rr. At extra low speed, DB-DTFC is sensitive to Rs as well. However, at medium and high speed, the DB-DTFC is insensitive to any machine parameter. For the back-EMF self-sensing technology, it is only sensitive to Lm at low speeds.

Table 3.3-1 Parameter sensitivity of IFOC, DB-DTFC and back-EMF self-sensing technology

	Torque sensitivity					**Velocity sensitivity**	
Para.	Extra Low	Low speed		Medium/High speed		Low speed	High speed
	DB-DTFC	IFOC	DB-DTFC	IFOC	DB-DTFC	Back-EMF SS	
L_m	**High**	**High**	**High**	**High**	Low	**High**	Low
L_{ls}	Low	Low	Low	Low	Low	Low	Low
L_{lr}	Low	Low	Low	Low	Low	Low	Low
R_s	**High**	Low	Low	Low	Low	Low	Low
R_r	**High**	**High**	**High**	**High**	Low	Low	Low

3.4 Speed Dependent Back-EMF State Filter Bandwidth

The back-EMF based self-sensing has a good performance at medium and high speeds, which has been discussed in many papers. In an induction machine drive, how to improve the back-EMF self-sensing performance at low speeds is a problem. In the traditional way, the bandwidth of the motion controller in the Fig. 3.3-1 is reduced as the motor speed decreases. It is a simple way to keep the system stable at low speed, however, the lower motion

controller bandwidth will lead to lower system dynamic stiffness. In the proposed back-EMF self-sensing methodology in this thesis, a back-EMF state filter cascades a tracking observer, which is shown in Fig. 3.4-1. The back-EMF state filter bandwidth and tracking observer bandwidth are the two degree-of-freedom of the proposed self-sensing system. The back-EMF state filter bandwidth is default set to 200 Hz. At low speed operations, back-EMF state filter bandwidth does not longer need that a high value. Thus, as the motor speed decreases, the bandwidth of the back-EMF state filter bandwidth can be decreased. The most advantage of this approach is to make the system more stable at low speeds without sacrificing the whole system dynamic stiffness.

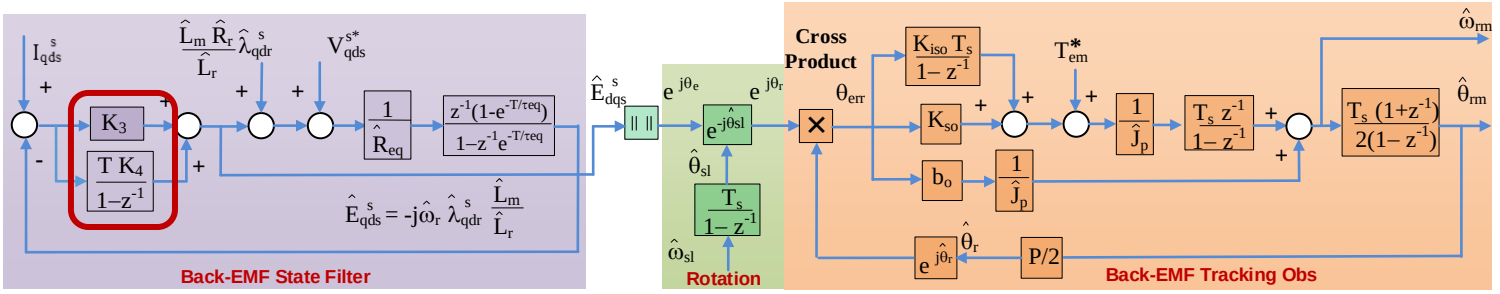

Fig. 3.4-1 Back-EMF state filter cascading a tracking observer for self-sensing

In Fig. 3.4-2, by using the fixed back-EMF state filter bandwidth and speed dependent back-EMF state filter bandwidth, the speed ripple of the estimated velocity can be compared, especially at low speeds

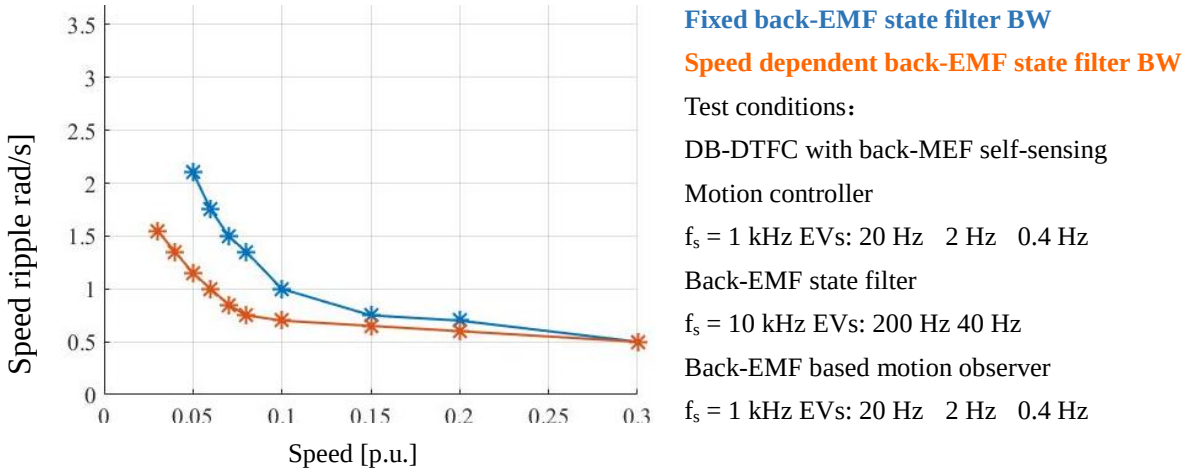

Fig. 3.4-2 Speed ripple comparison with and without the speed dependent back-EMF state filter bandwidth approach

In Fig. 3.4-2, the speed ripple with fixed back-EMF state filter bandwidth is in blue line and the speed ripple with speed dependent state filter bandwidth is in orange line. From the plot, with variable back-MEF state filter bandwidth, the lowest operating speed can be pushed lower and the speed ripple is reduced since the state filter bandwidth decreases.

3.5 Summary

This chapter presents the parameter sensitivity of a DB-DTFC drive for induction machines. Key conclusions are summarized as follows:

- Theoretically, the observer-based back-EMF tracking method is available at zero speed for IM self-sensing.
- DB-DTFC only depends on estimated speed, so the actual position estimation error does not lead to system instability in the motion control loop.

- The estimated slip frequency, which is sensitive to machine parameters, is needed by the back-EMF tracking observer to estimate rotor speed.
- IFOC are sensitive to L_m and R_r over the entire speed range, however, DB-DTFC is only sensitive to L_m and R_r at low speeds.
- The most critical parameters are L_m and R_r. Both DB-DTFC and IFOC are insensitive to L_{lr}, L_{ls} and R_s over most of the speed range.
- DB-DTFC systematically has less torque ripple than IFOC.
- At medium and high speed conditions, DB-DTFC has significantly less parameter sensitivity than IFOC.
- At low speeds, both IFOC and DB-DTFC drives are sensitive to magnetizing inductance and rotor resistance due to their use of the current model for flux estimation.
- In the self-sensing mode, the flux observer bandwidth is reduced to benefit from the filtering function of the flux observer voltage model.
- The flux observer bandwidth cannot be decreased to low values since the volt-second errors from the inverter become significant and yield flux estimation errors.
- The proposed back-EMF self-sensing technology is sensitive to L_m in the low speed (<0.2 pu) range.

- In the extra low speed (<0.06 pu) range, R_S affects the flux observer estimation accuracy due to the voltage model performance degradation.
- In the traditional method, as the motor speed decreases, the bandwidth of the tracking observer decreases to keep the system stable, which leads to lower system dynamic stiffness.
- The back-EMF state filter bandwidth is another degree-of-freedom for the self-sensing system.
- At low speed, the back-EMF state filter does not need of high bandwidth.
- As the motor speed decreases, the bandwidth of the back-EMF state filter bandwidth can be decreased, without sacrificing the system dynamic stiffness
- A speed dependent back-EMF state filter bandwidth method can improve the self-sensing performance at low speeds.

Chapter 4

Real-time Parameter Estimation for Encoder-Based DB-DTFC

Unlike the MRAS-based approach, a signal injection-based alternative extracts parameter information from the intentionally induced harmonics. Because it utilizes harmonics instead of fundamental components, the method can be generally applied over the entire operating ranges including at very low speeds and in light loading conditions. A significant concern for injection schemes is the potential for induced torque ripple, which is first discussed in this section. A carrier signal model for parameter estimation and experimental results are shown in the next section.

4.1 Signal Injection for IFOC Drives

Researchers have been using a variety of injection signals to extract parameter and rotor information. The rotating vector injection in some previous research would produce additional torque ripple at the carrier frequency due to the interaction of fundamental MMF at the harmonic frequencies. Another method is the pulsating vector injection scheme. This method is to inject a voltage signal in the synchronous reference frame, which is shown in Fig. 4.1-1. For IFOC drives, d-axis is usually used for pulsating voltage injection to avoid torque ripple.

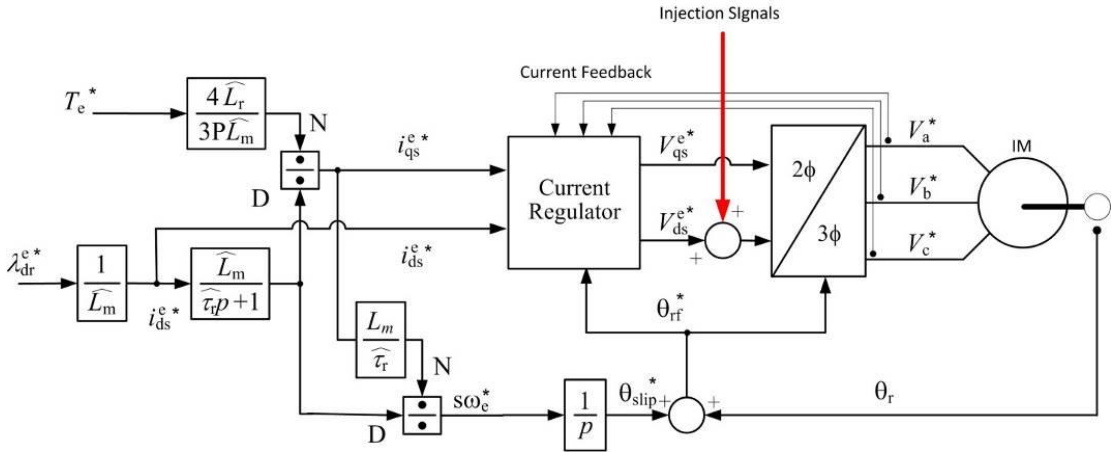

Fig. 4.1-1 A high frequency signal injection scheme with pulsating vector injection

Some papers claim that injects the voltage vector on the d-axis would not produce any torque. Despite this claim, some torque ripple occur. The ripple is worse for high speed operation. Assuming the d-axis voltage injection signals are $V_c \sin(\omega t)$, the system can be simplified as Fig. 4.1-2, where the induction motor is modeled as R-L load with back EMF coupling. This block diagram has also been widely used for current regulator design.

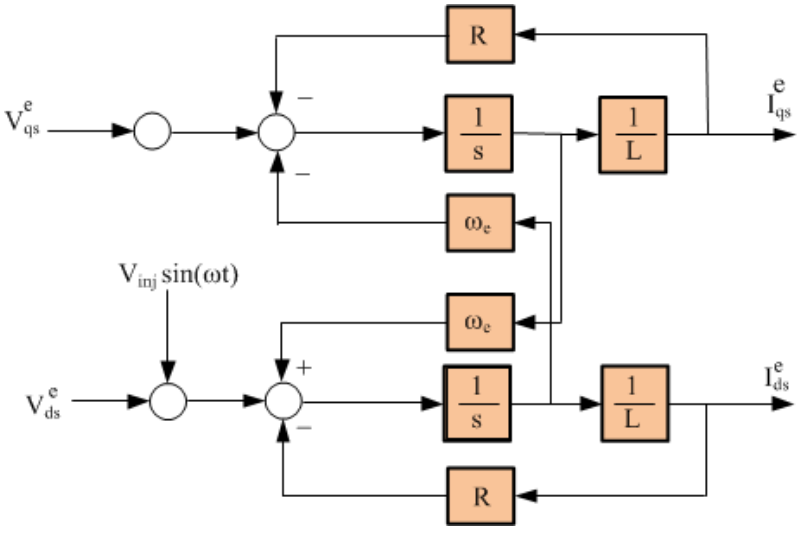

Fig. 4.1-2 d-axis injection in IFOC drives

Due to the cross-coupling between the q- and d-axes, pulsating voltage injection on the d-axis is cross-coupled to the q-axis, which is proportional to speed.

4.2 Signal Injection for DB-DTFC Drives

In DB-DTFC drives, q- and d- axes are not used, therefore most of the reported injection-based parameter identification methods cannot be directly applied. A more direct way to inject a signal without affecting torque output is proposed as a pulsating flux injection on the torque line.

It has been recognized in DB-DTFC that the torque model line on the Volt-sec. plane gives the exact same torque for all the Volt-sec. vectors that are connected to the torque line. This property of the torque line can be used to advantage since any pulsating carrier signal along this line is independent of the torque and torque dynamics. Fig. 4.2-1 depicts this type of "pulsating, carrier frequency injection on the torque line".

By periodically varying stator flux command, the Volt-sec. solutions for each switching interval are periodically oscillating along the torque line, resulting in the high frequency component on the current response while generating virtually no torque ripple. The graphical solutions are shown in the top of Fig. 4.2-1.

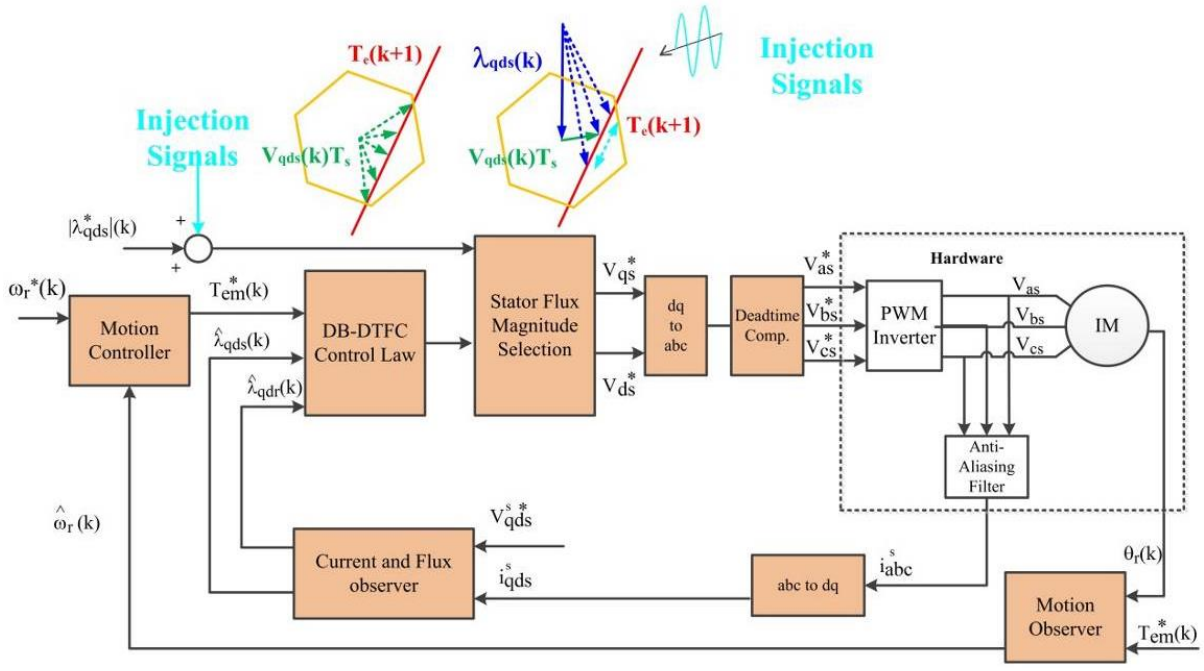

Fig. 4.2-1 Signal injection schemes in the DB-DTFC drives along the torque line [106]

Experimental evaluation of injection-induced torque ripple at low speed and high speed is shown in Fig. 4.2-2 for both IFOC and DB-DTFC drives. The stator flux perturbation magnitude is set at 0.03pu for DB-DTFC drives, and the d-axis voltage injection magnitudes for IFOC drives are adjusted to achieve the same magnitude of current harmonics in order to form a fair comparison. It is seen in Fig. 4.2-2 (b) that injecting signals along the torque line induces virtually zero torque ripple in DB-DTFC drives, while IFOC drives with d-axis voltage vector injection induces significant torque ripple in Fig. 4.2-2 (a). Note that the current harmonic amplitudes are nearly identical as shown in Fig. 4.2-2 (c) and Fig. 4.2-2 (d). For IFOC drives, the torque ripple at low speed (blue line) is less than the torque ripple at high

speed (orange line), which is because the d-axis and q-axis are cross-coupled lighter at low speed than it is at high speed.

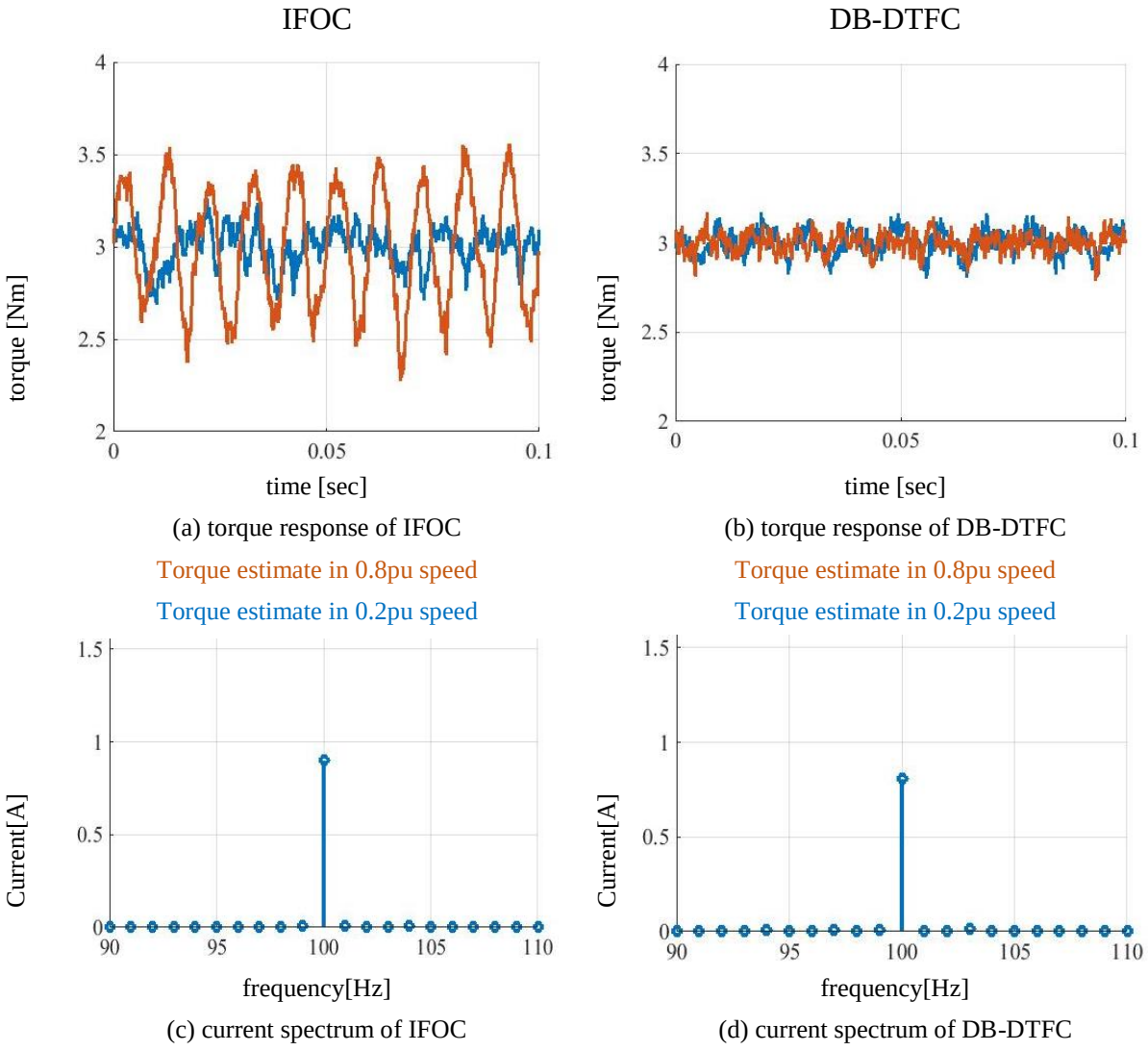

(a) torque response of IFOC

(b) torque response of DB-DTFC

(c) current spectrum of IFOC

(d) current spectrum of DB-DTFC

Fig. 4.2-2 Experimental results of torque ripple with flux injection for IFOC and DB-DTFC drive operating at 0.8 pu and 0.2 pu speed, 0.8 pu flux, and 100Hz sinusoidal carrier signal injection.

4.3 Injection-based Parameter Estimation

4.3.1 Carrier Frequency Component Model

The signal injection in DB-DTFC drives acts like a pulsating vector, containing a positive and a negative sequence component rotating at the same frequency. With the fundamental frequency denoted as ω_e and the injection frequency as ω_c, a positive sequence component at the frequency of $\omega_p = \omega_e + \omega_c$ and a negative sequence component at $\omega_n = \omega_e - \omega_c$ can be obtained parameter estimation.

The following derivation process is to achieve a carrier signal model for an induction machine, which starts with the fundamental flux linkage definition, i.e. repeated in (4.3-3) and (4.3-4) and the differential equations, i.e. repeated in (4.3-1) and (4.3-2). It is noted that this set of equations applies for any arbitrary reference frame.

$$V_{qds} = R_s i_{qds} + j\omega\lambda_{qds} + \dot{\lambda}_{qds} \tag{4.3-1}$$

$$V_{qdr} = R_r i_{qdr} + j(\omega - \omega_r)\lambda_{qdr} + \dot{\lambda}_{qdr} \tag{4.3-2}$$

$$\lambda_{qds} = L_s\ i_{qds} + L_m\ i_{qdr} \tag{4.3-3}$$

$$\lambda_{qdr} = L_m\ i_{qds} + L_r\ i_{qdr} \tag{4.3-4}$$

From (4.3-1) to (4.3-4), the voltage equations with stator and rotor current terms can be obtained as (4.3-5) and (4.3-6). The flux linkage terms are substituted by the current terms from (4.3-3) and (4.3-4).

$$V_{qds} = (R_s + pL_s + j\omega L_s) i_{qds} + (\mathbf{p}L_m + j\omega L_m) i_{qdr} \quad (4.3\text{-}5)$$

$$V_{qdr} = (\mathbf{p}L_m + j(\omega - \omega_r) L_m) i_{qds} + (R_r + \mathbf{p}L_r + j(\omega - \omega_r) L_r) i_{qdr} \quad (4.3\text{-}6)$$

For squirrel-caged rotor induction machine, the rotor voltage can be assumed as zero, i.e. $V_{qdr} = 0$. The following steady-state equations can be derived from (4.3-5) and (4.3-6).

$$V_{qds} = (R_s + j\omega L_s) i_{qds} + j\omega L_m i_{qdr} \quad (4.3\text{-}7)$$

$$0 = j(\omega - \omega_r) L_m i_{qds} + (R_r + j(\omega - \omega_r) L_r) i_{qdr} \quad (4.3\text{-}8)$$

It is noted that (4.3-7) and (4.3-8) apply for both fundamental and carrier frequency components. Since the carrier frequency components are interested in this section, the term ω can be replaced by ω_p for positive sequence components, and ω_n for negative sequence components. The derived equation (4.3-7) and (4.3-8) can be written to (4.3-9) and (4.3-10). The general voltage and current variables are replaced by negative sequence components for example. It is also valid for positive sequence counterparts.

$$V_{qds\_n} = (R_s + j\omega_n L_s) i_{qds\_n} + j\, \omega_n L_m i_{qdr\_n} \quad (4.3\text{-}9)$$

$$0 = j(\omega_n - \omega_r) L_m i_{qds\_n} + [\, R_r + j(\omega_n - \omega_r) L_r \,] i_{qdr\_n} \quad (4.3\text{-}10)$$

As (4.3-9) and (4.3-10) are expressed in complex vector forms, both current vector and voltage vector can be projected to the d-axis current (i_{qs_n}=0). The derived equation (4.3-7) and (4.3-8) can be reduced to (4.3-11) and (4.3-14). Note

$$V_{qs\_n} = \omega_n L_s i_{ds\_n} + \omega_n L_m i_{dr\_n} \quad (4.3\text{-}11)$$

$$V_{ds\_n} = R_s i_{ds\_n} - \omega_n L_m i_{qr\_n} \quad (4.3\text{-}12)$$

$$0 = (\omega_n - \omega_r) L_m i_{ds\_n} + R_r i_{qr\_n} + (\omega_n - \omega_r) L_r i_{dr\_n} \tag{4.3-13}$$

$$0 = -(\omega_n - \omega_r) L_r i_{qr} + R_r i_{dr\_n} \tag{4.3-14}$$

It is noted that (4.3-14) can be manipulated as (4.3-15), and further substituted in (4.3-12) to express q-axis rotor current by the d-axis stator current as (4.3-16).

$$i_{dr\_n} = (\omega_n - \omega_r) \frac{L_r}{R_r} i_{qr\_n} \tag{4.3-15}$$

$$i_{qr\_n} = \frac{-(\omega_n - \omega_r) L_m R_r}{R_r^2 + (\omega_n - \omega_r)^2 L_r^2} i_{ds\_n} \tag{4.3-16}$$

With the generally held assumption of (4.3-17), (4.3-15) and (4.3-16) can be further deduced as (4.3-18) and (4.3-19), respectively.

$$R_r << \left| (\omega_n - \omega_r) L_r \right| \tag{4.3-17}$$

$$i_{qr\_n} = \frac{-L_m R_r}{(\omega_n - \omega_r) L_r^2} i_{ds\_n} \tag{4.3-18}$$

$$i_{dr\_n} = -\frac{L_m}{L_r} i_{ds\_n} \tag{4.3-19}$$

By substitution of carrier component current relationship (4.3-18) and (4.3-19) into the voltage equations (4.3-11) to (4.3-14), some valuable results can be obtained as (4.3-20) and (4.3-21). The harmonic components of voltage and current can be extracted from the stator voltage and current, and the corresponding impedance can be calculated online.

$$V_{qs\_n} = \omega_n \left(L_s - \frac{L_m^2}{L_r} \right) i_{ds\_n} \approx \omega_n \sigma L_s i_{ds\_n} \tag{4.3-20}$$

$$V_{ds\_n} = R_s i_{ds\_n} + \frac{\omega_n}{(\omega_n - \omega_r)} \frac{L_m^2}{L_r^2} R_r i_{ds\_n} \tag{4.3-21}$$

The derived model in (4.3-20) and (4.3-21) applies not only for the negative sequence component, $\omega_n = \omega_e - \omega_c$, but also for the positive sequence component, which is $\omega_p = \omega_e + \omega_c$ following the same derivation process. Once the carrier components of voltage and current are obtained, the parameters can be obtained from the impedance calculation. With the known carrier injection frequency, leakage inductance L_{lk} can be calculated from (4.3-20). The stator resistance R_s and effective rotor resistance, $R_r' = (L_m/L_r)^2 R_r$ can be calculated based on (4.3-21) by using both the positive sequence and negative sequence.

In addition to the parameter information obtained from the induced carrier frequency components, the fundamental components can be utilized to achieve a complete set of parameters. For the sake of simplicity, the traditional T-type equivalent circuit Fig. 4.4-1 (a) is modified as Γ type equivalent circuit Fig. 4.4-1 (b), in which the magnetizing inductance path and the equivalent rotor resistance path are orthogonal to each other. The impedance seen from the input voltage can be described as (4.3-22), from which the magnetizing inductance and rotor resistance can be estimated.

$$V_{qds\_f} = \left(R_s + j\omega_e \sigma L_s + j\omega_e \frac{L_m^2}{L_r} \| \frac{R'_r}{s} \right) i_{qds\_f} \tag{4.3-22}$$

4.3.2 Signal Processing Procedures

The carrier frequency components, including both the positive and negative sequence components, can be obtained after signal processing. The signal processing is generally described as Fig. 4.3-1. There are five steps in the signal processing procedure to obtain positive, negative and fundamental sequence components. In this plot, the current signals are taken as an example for the signal processing procedures. The similar method can be extended to process the voltage signals as well.

Before the signal processing, in stage one, the current spectrum can be obtained in the Fig. 4.3-1-0 by using fast Fourier transform (FFT). The fundamental component is in the frequency ω_e and the positive and negative components are in $(\omega_c + \omega_e)$ and $(\omega_c - \omega_e)$ respectively.

In the first stage, the sampled current and voltage in the stationary reference frame are transformed to the synchronous reference frame. The fundamental component is in the frequency zero and the positive and negative components are in $(+\omega_e)$ and $(-\omega_e)$, which is shown in Fig. 4.3-1-1.

Second, by using a high pass filter, the fundamental components can be removed. The positive and the negative sequence components remain in frequency $(+\omega_e)$ and $(-\omega_e)$, which is shown in Fig. 4.3-1-2.

Third, by rotating an angle of θ_c in the negative direction (or positive direction) from the synchronous reference frame, the positive (or negative) sequence components are shown as DC values, which is in zero frequency, which is shown in Fig. 4.3-1-3.

Forth, high pass filter can be used to filter out the positive (or negative) sequence components. Then, only the negative (or positive) sequence components at a frequency of $2f_C$, which is shown in Fig. 4.3-1-4.

Fifth, by rotating back an angle of $2\theta_c$, the negative (or positive) components are extracted as the DC values, which is shown in Fig. 4.3-1-5.

Sixth, by applying a low pass filter, the noise on the negative (or positive) components are removed to improve the signal quality for the parameter calculation.

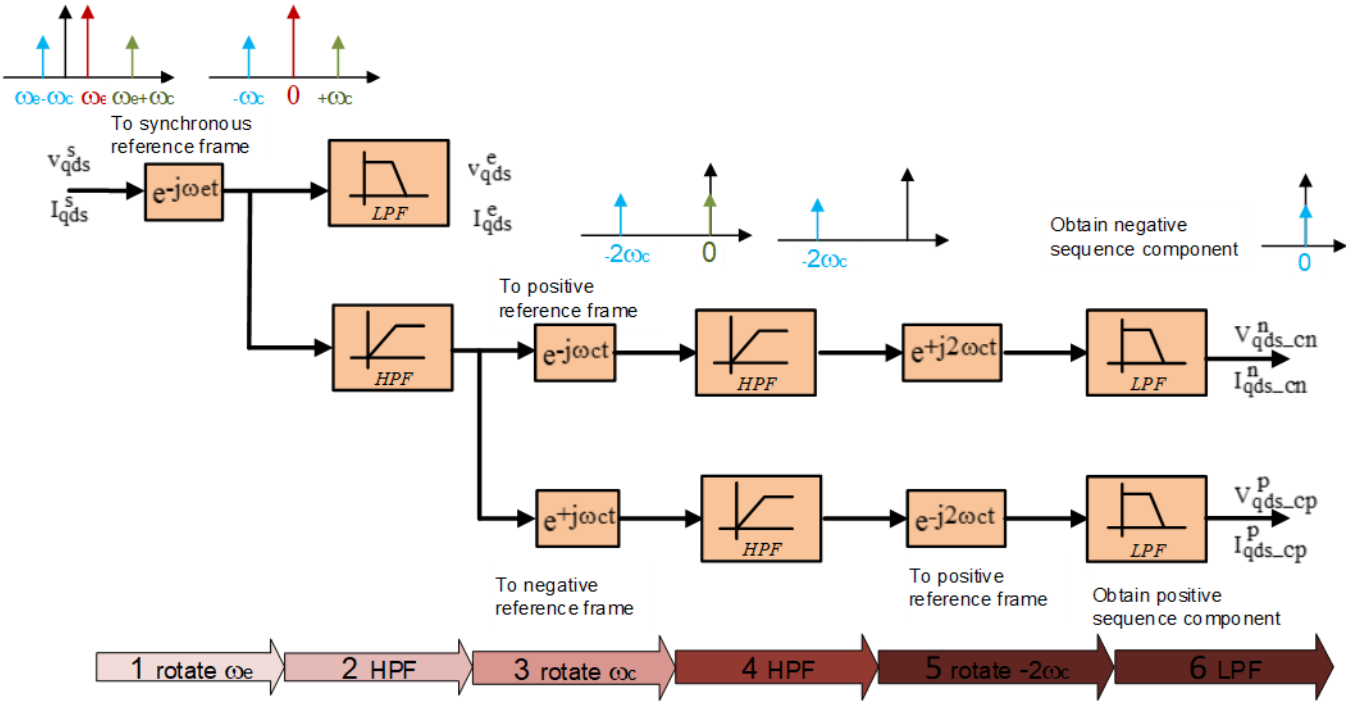

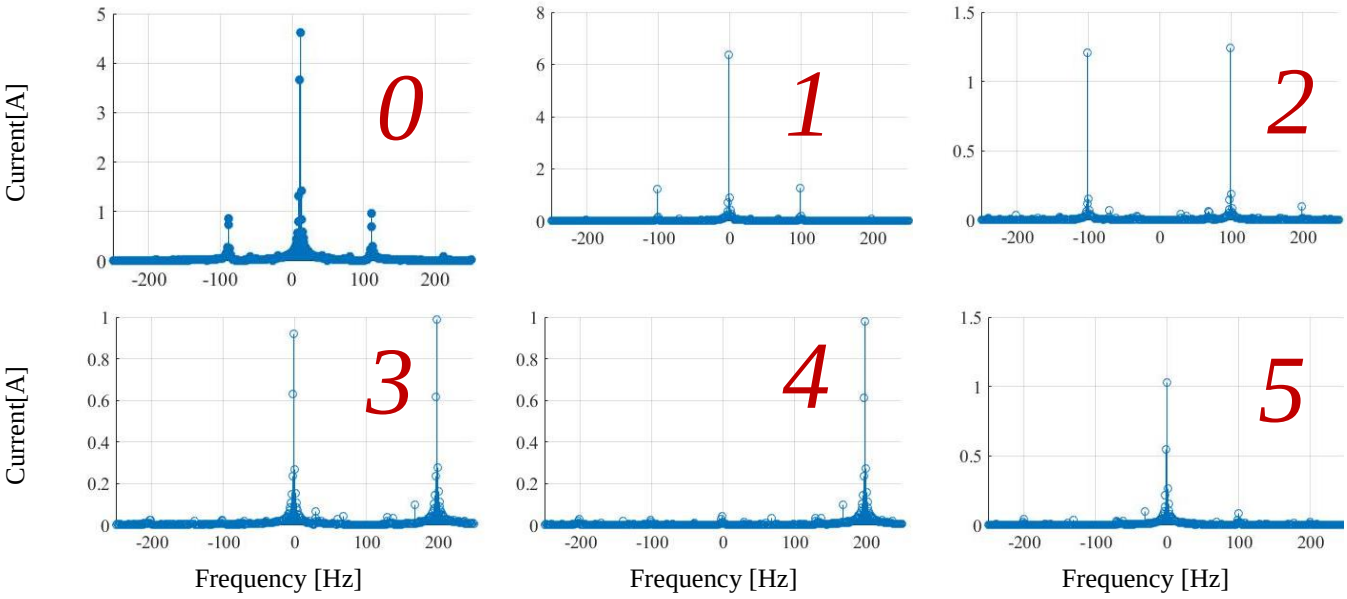

Fig. 4.3-1 Real-time signal processing scheme to extract the positive and the negative components

After the signal processing, the following variables can be obtained. Machine physical parameters can be estimated based on those variables.

1) Fundamental components: V_{qds}, i_{qds}, ω_e, ω_r
2) Positive sequence components: $V^{p}_{qs\_cp}$, $V^{p}_{ds\_cp}$, $i^{p}_{ds\_cp}$ (no q-axis component because aligned to d-axis current), $\omega_p = \omega_e + \omega_c$
3) Negative sequence components: $V^{n}_{qs\_cn}$, $V^{n}_{ds\_cn}$, $i^{n}_{ds\_cn}$ (no q-axis component because aligned to d-axis current), $\omega_n = \omega_e - \omega_c$

First of all, leakage inductance can be estimated using either the positive sequence or negative sequence components by following (4.3-20). The equations are shown as (4.3-23) and (4.3-24), respectively. The final estimate of leakage inductance can be calculated by the mean value of the two.

$$\hat{\sigma L}_{s\_p} = \frac{V^{p}_{qs\_cp}}{\omega_p i^{p}_{ds\_cp}} \quad \text{calculated by positive sequence component} \qquad (4.3\text{-}23)$$

$$\hat{\sigma L}_{s\_n} = \frac{V^{n}_{qs\_cn}}{\omega_n i^{n}_{ds\_cn}} \quad \text{calculated by negative sequence component} \qquad (4.3\text{-}24)$$

Assuming the leakage inductance values are identical in the stator and the rotor, then the stator and rotor leakage inductance can be estimated as (4.3-25).

$$\hat{L}_{ls} = \hat{L}_{lr} = 0.25*(\hat{\sigma L}_{s\_p} + \hat{\sigma L}_{s\_n}) \qquad (4.3\text{-}25)$$

The second step is to estimate resistance, by using both the positive and the negative components in (4.3-21). The resulting equations are (4.3-26) and (4.3-27) respectively, where $R_r' = (L_m/L_r)^2 R_r$. The estimate of stator resistance (i.e. $\hat{R}_S$) and effective rotor resistance (i.e. $\hat{R}_r'$) can be calculated from the two equations.

$$V^{p}_{ds\_cp} = \left(R_s + \frac{\omega_p}{(\omega_p - \omega_r)} R_r' \right) i^{p}_{ds\_cp} \quad \text{by positive sequence component} \qquad (4.3\text{-}26)$$

$$V^{n}_{ds\_cn} = \left(R_s + \frac{\omega_n}{(\omega_n - \omega_r)} R_r' \right) i^{n}_{ds\_cn} \quad \text{by negative sequence component} \qquad (4.3\text{-}27)$$

The magnetizing inductance estimate can be obtained only from the fundamental component. Referring to the Γ type equivalent circuit in Fig. 4.3-2(b), the variable of $\frac{L_m^2}{L_r}$ can be estimated by the magnetizing current and the voltage across the magnetizing branch as (4.3-28). The voltage and current can be calculated from the equivalent circuit as (4.3-29) and (4.3-30).

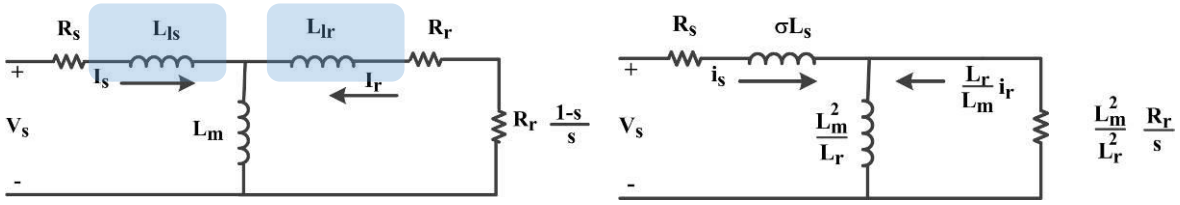

(a) traditional T type equivalent circuit (b) modified Γ type equivalent circuit

Fig. 4.3-2 Equivalent circuit model for induction machines

$$\frac{\hat{L}_m^2}{\hat{L}_r} = \frac{V_{qdm}}{i_{qdm}} \frac{1}{\omega_e} \tag{4.3-28}$$

$$V_{qdm} = V_{qds} - \hat{R}_s\, i_{qds} - j\omega_e \hat{\sigma} \hat{L}_s \tag{4.3-29}$$

$$i_{qdm} = i_{qds} - \frac{V_{qdm}}{\hat{R}_r'/slip} \tag{4.3-30}$$

With the knowledge of $\frac{\hat{L}_m^2}{\hat{L}_r}$, the magnetizing inductance and the rotor resistance can be estimated from(4.3-31) to (4.3-34).

$$\frac{L_m^2}{L_r} = \frac{(L_r - L_{lr})^2}{L_r} \approx \frac{(L_r^2 - 2\, L_r L_{lr})}{L_r} = L_r - 2\, L_{lr} \tag{4.3-31}$$

$$\hat{L}_r = \frac{\hat{L}_m^2}{\hat{L}_r} + 2\hat{L}_{lr} \tag{4.3-32}$$

$$\hat{L}_m = \frac{\hat{L}_m^2}{\hat{L}_r} + \hat{L}_{lr} \tag{4.3-33}$$

$$\hat{R}_r = \frac{\hat{L}_r^2}{\hat{L}_m^2} \hat{R}_r' \tag{4.3-34}$$

4.3.3 Rotor Bar Skin Effect of Injection Based Parameter Estimation

Theoretically Analysis

The injection based parameter estimation method is based on the positive, negative and fundamental components to calculate machine parameters. However, parameters are frequency-dependent due to skin effects/proximity effects, since the depth of the rotor bar cannot be ignored. The Table 4.3-1 shows the skin depth results of general aluminum at different injection frequency.

Table 4.3-1 Skin effect depth at different frequencies

Frequency (Hz)	Skin Effect Depth (cm)	Materials
20	1.99	Aluminum
30	1.50	Aluminum
40	1.30	Aluminum
80	0.92	Aluminum
100	0.82	Aluminum
200	0.58	Aluminum

The rotor bar depth of test machine is 2.1 cm, which is closed to 1.99cm. It means with the frequency larger than 20 Hz, rotor bar depth is larger than skin effect depth. If the injected frequency is larger than 20 Hz, the final estimates of the injection-based parameter estimation will be larger than the real values due to the rotor bar skin effect. Thus, skin effect should be considered in flux injection-based parameter estimation.

Experimental Verification

The rotor bar skin effect is also can be verified by the experimental method by using the impedance analyzer WK 6500B in this thesis. The machine effective resistance can be measured with and without the rotor bar by the impedance analyzer respectively.

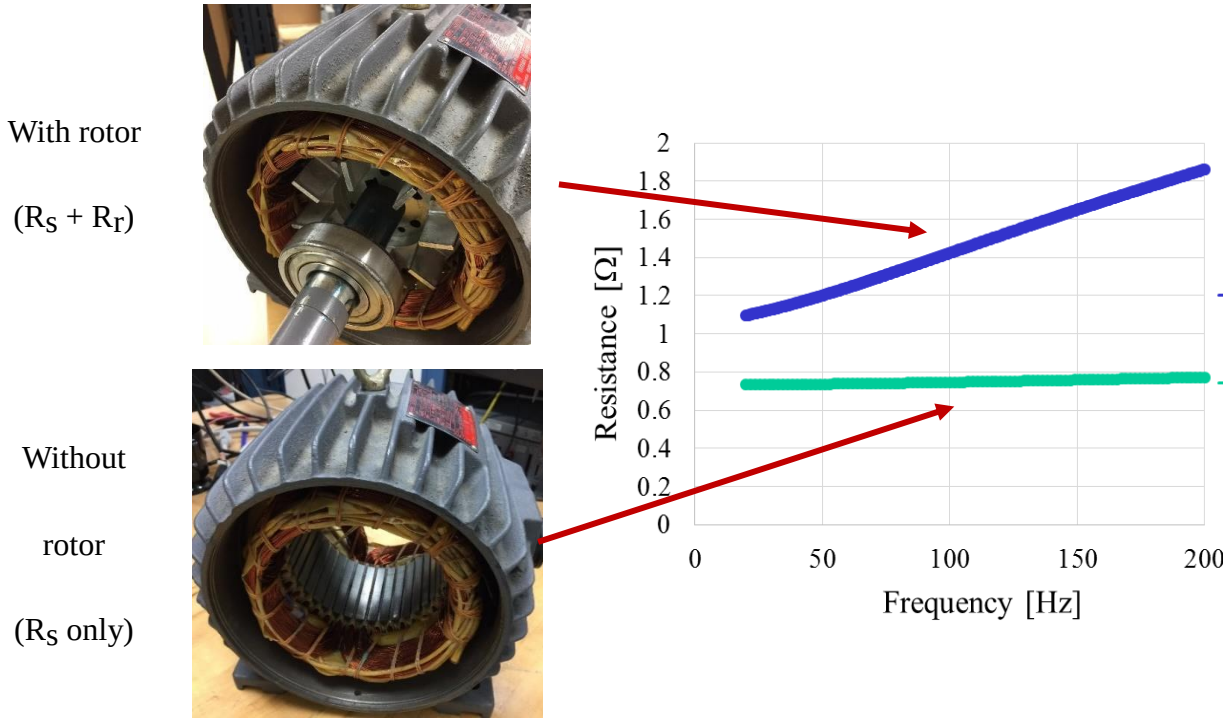

Fig. 4.3-3 Equivalent circuit model for induction machines

In Fig. 4.3-3, the experimental results show the effective resistance comparison between the machine with and without rotor at the different carrier frequency. With the rotor bar, the effective resistance increases as increases (shown in the blue line), which shows the carrier frequency dependent property. However, without the rotor bar, the effective resistance is almost equal to real stator resistance, which doesn't change too much as carrier frequency

increases (shown in green line). It can be seen in Fig. 4.3-3 that the rotor resistance depends on carrier frequency significant, which is consistent with the analysis above.

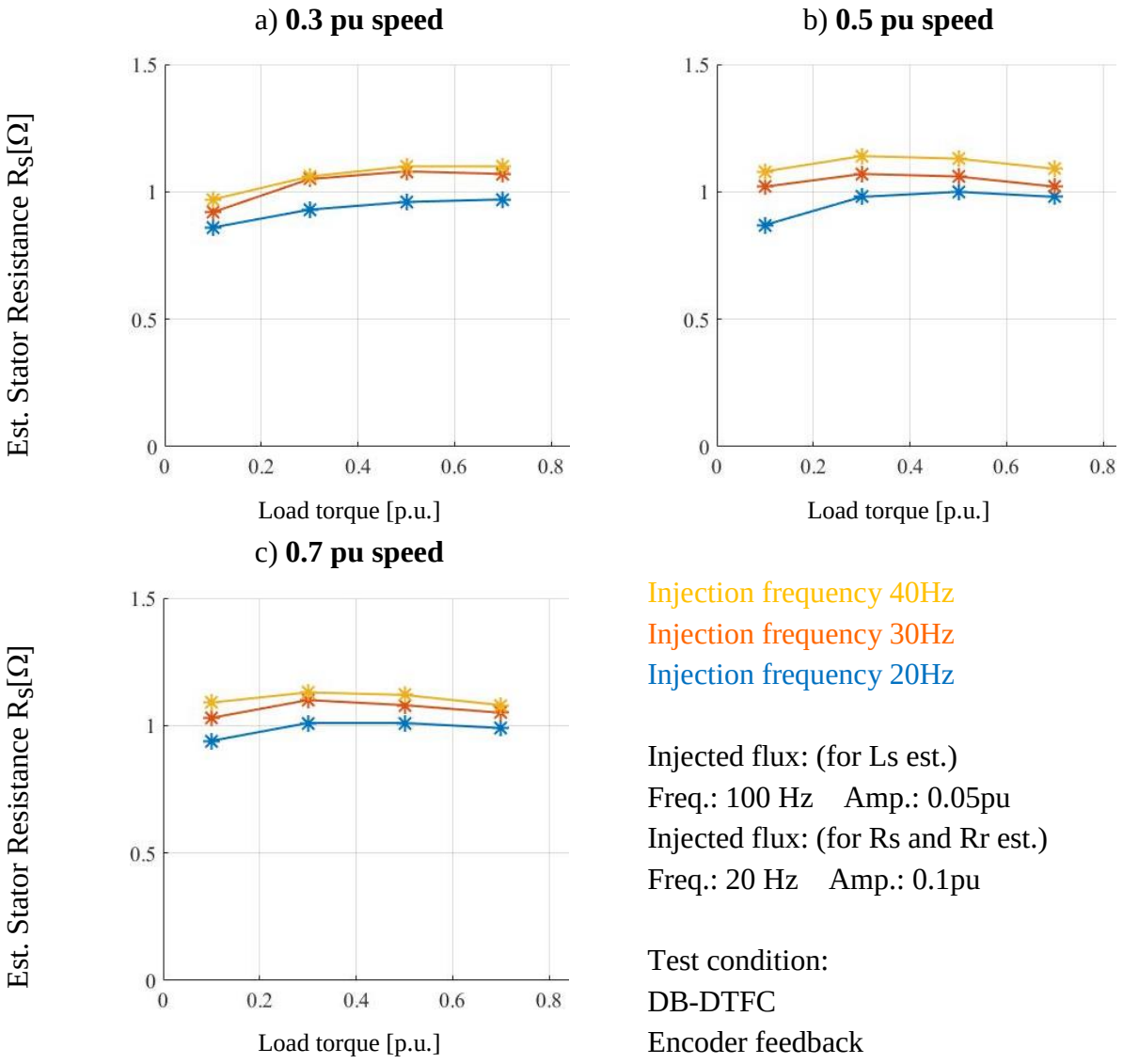

Fig. 4.3-4 Stator resistance estimation with different injected carrier frequencies

In Fig. 4.3-4, the stator resistance can be estimated by injecting flux with different carrier frequencies, 20 Hz, 30 Hz and 40 Hz separately. Based on the (4.3-26) and (4.3-27), the stator resistance can be obtained. Estimated R_s are frequency-dependent at different

speeds. For higher carrier frequencies, the estimated R_s values are higher. Since the machine temperature in each test maintains at 37.8 °C, the estimated R_s are not affected too much by different loads.

The similar experimental results can be obtained for the rotor resistance estimation, which is shown in Fig. 4.3-5. This is another experimental verification for the rotor skin effect of the proposed injection-based parameter estimation.

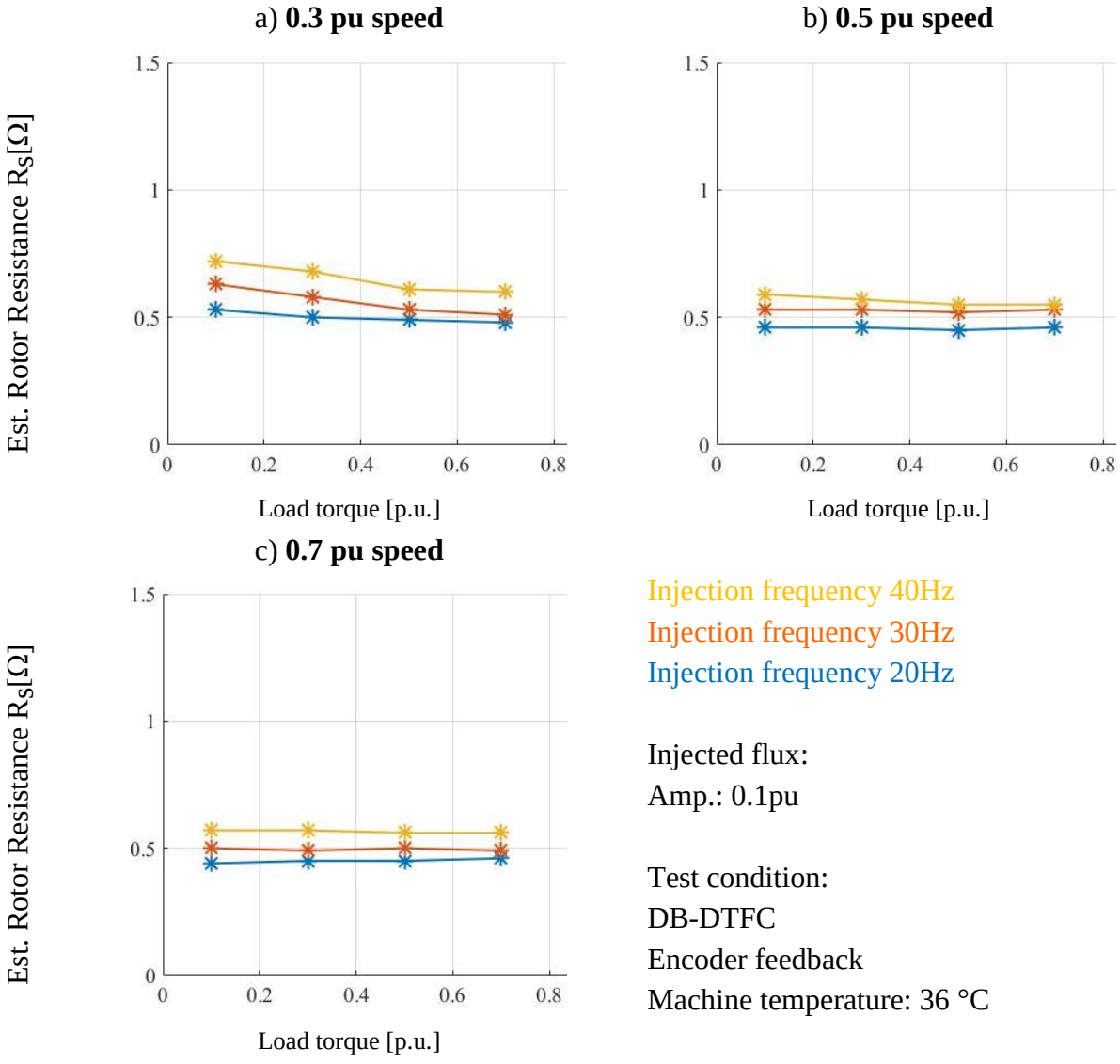

Fig. 4.3-5 Rotor resistance estimation with different injected carrier frequencies

Curve Fitting Approach for Accuracy Parameter Estimation

From Fig. 4.3-3, it is apparent that the rotor resistance is frequency dependent due to the rotor bar skin effect. Take the rotor resistance estimation for an example, the estimate with 40 Hz carry frequency is higher than the estimate with a 30 Hz carry frequency, shown in the blue dot in Fig. 4.3-6. After obtaining the rotor resistance at different frequencies (30 Hz and 40 Hz), a quadratic curve fitting method can be used for rotor resistance estimation at 20 Hz frequency. The Fig. 4.3-6 shows the rotor resistance before and after curve fitting. Since the skin effect only happens with the carrier frequency higher than 20 Hz, the real rotor resistance can be obtained from the orange line in Fig. 4.3-6, which is the resistance around 20 Hz.

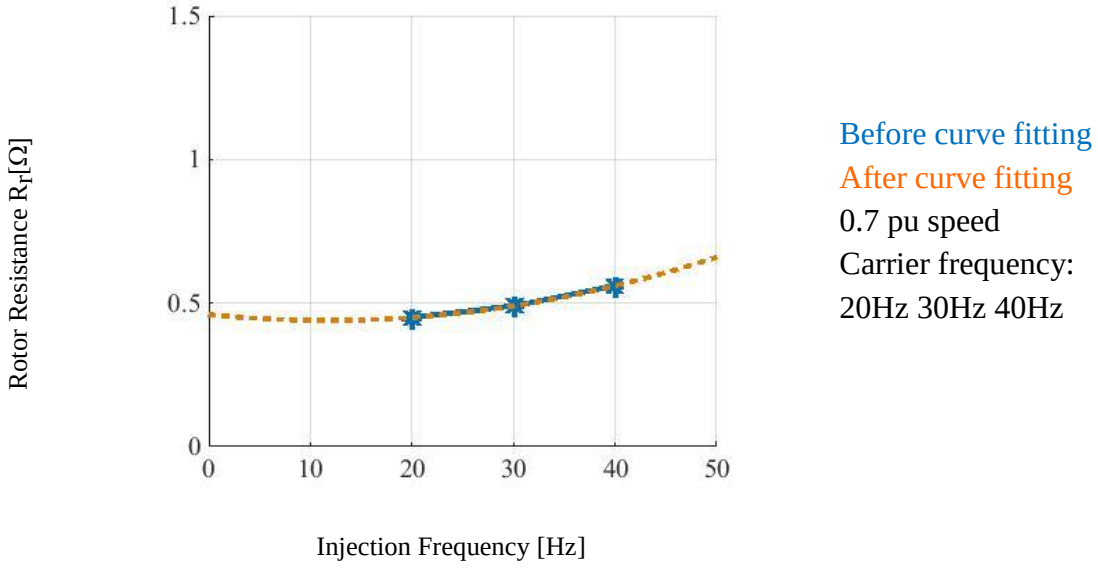

Fig. 4.3-6 Rotor resistance data and curve fitting method

4.4 Appropriate Injected Frequency Selection

In previous sections, the flux injection-based parameter estimation for DB-DTFC drives is proposed without inducing any torque ripple. However, the rotor bar skin effect will affect the estimation accuracy, if the inappropriate injected frequency is selected.

In general, the injected carrier signal frequency selection has the following three considerations:

1. High-frequency injection is suitable for the L_{ls} estimation. A synchronous frame injected signal frequency that is high (>60Hz) makes the leakage inductance reactance (blue block in Fig. 4.4-1 (a)) dominate the impedance. It's a challenge to estimate the resistance term, but the L_{ls} can be easily estimated in this case.
2. The synchronous frame injected signal frequency should be high enough to be separated from the "zero" fundamental frequency. Considering the rotor bar skin effect, the injected frequency should be low enough to avoid causing the skin effect. However, the injected frequency cannot be too low, since it would be different to extract the positive and negative components, if the injected frequency is closed to the fundamental frequency.
3. The injected frequency can be calculated based on the (4.4-1). Since the f_{cal} make leakage inductance reactance closing to R_S, the more accurate resistance reactance. If the f_{cal} is large enough to cause the skin effect, the f_{cal} should be adjusted a little bit

to f_{cal_adjust} and be injected again. Thus, two estimated value R_{cal} and R_{cal_adjust} can be obtained. Then, using the curve fitting method to calculate the final estimated value for both rotor resistance estimation and stator resistance estimation.

$$2\pi f_{cal} * L_{ls} \approx R_r \tag{4.4-1}$$

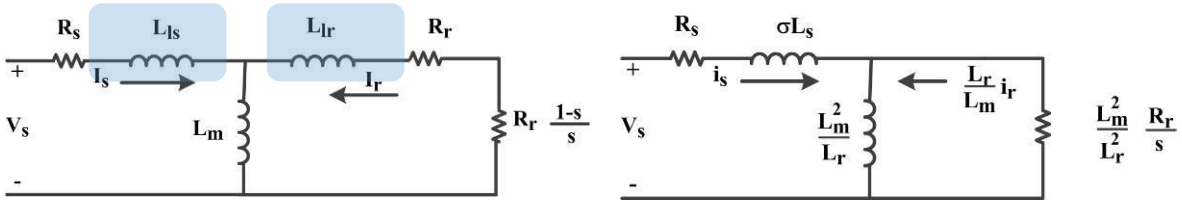

(a) traditional T type equivalent circuit (b) modified Γ type equivalent circuit

Fig. 4.4-1 Equivalent circuit model for induction machines

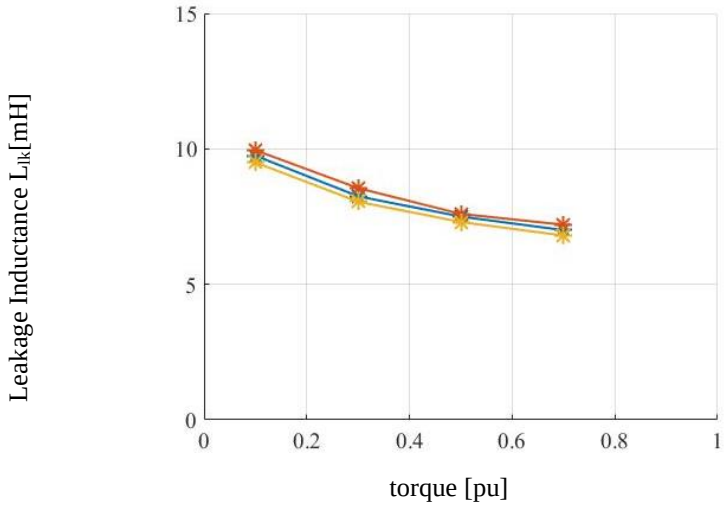

Injected flux signal:
Freq: 100 Hz
Amp: 0.05pu

Fig. 4.4-2 Leakage Inductance estimation with 100 Hz carrier frequency injection

The injection-based parameter estimation approaches are implemented on the test stand. The experimental results are shown in Fig. 4.4-2 and Fig. 4.4-3. For Leakage Inductance estimation, the carrier frequency at 100 Hz is chosen and for resistance estimation,

the carrier frequency at 20 Hz is selected. Saturation effect on both magnetizing and leakage inductance is significant in Fig. 4.4-2 and Fig. 4.4-3 (c). The resistance is not considerably affected by loading levels in Fig. 4.4-3 (a) and (b). Since the machine temperature in each test maintains at 36 °C, the estimated R_s and R_r are not affected too much by different loads.

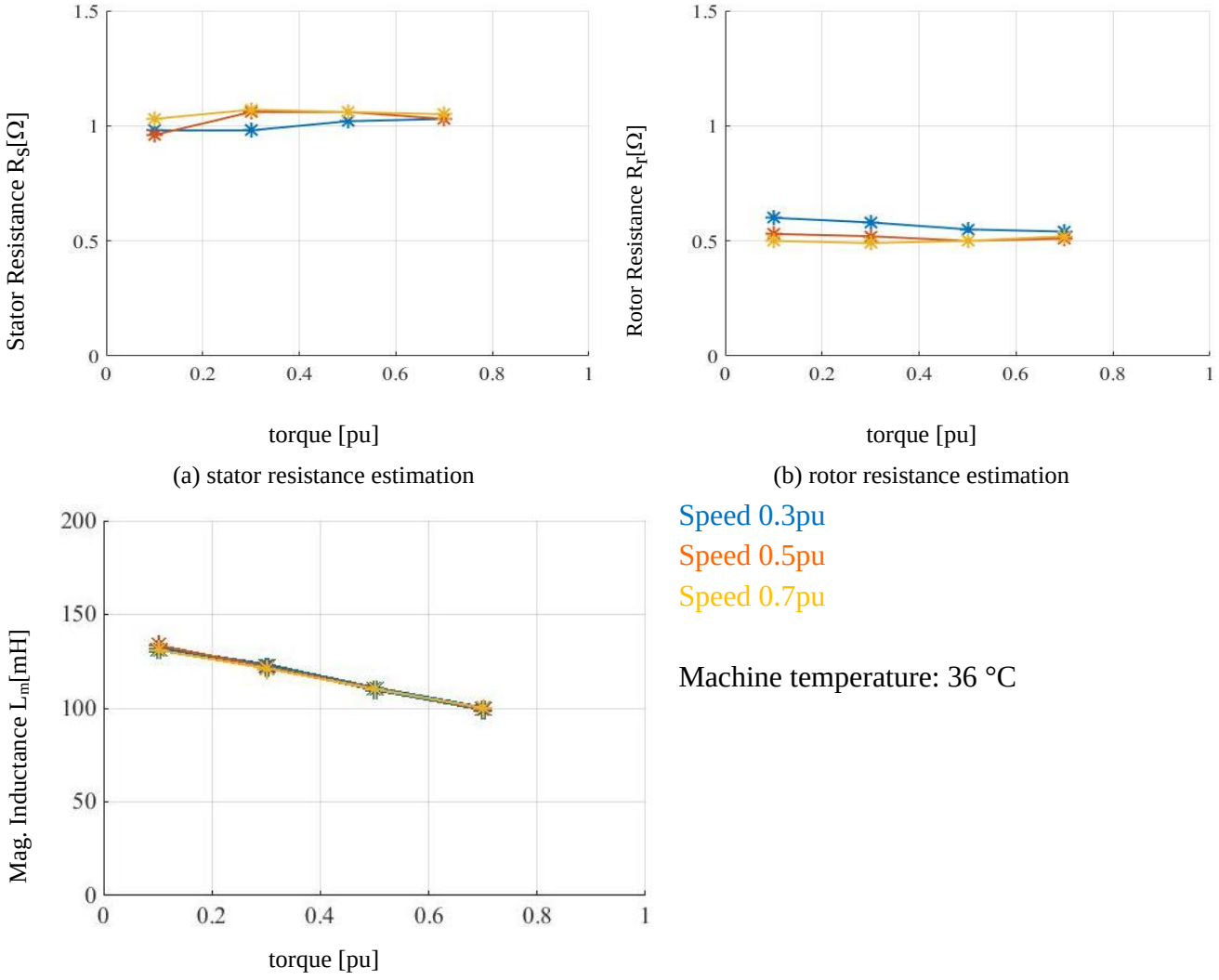

(a) stator resistance estimation

(b) rotor resistance estimation

(c) mag. inductance estimation

Fig. 4.4-3 Experimental results of parameter estimation using the signal injection based approach in DB-DTFC with injected signals at 0.1 pu flux, 20 Hz

4.5 Model Reference Adaptive System

As discussed in previous sections, DB-DTFC drives are not sensitive to parameters at high speed whereas at low speed the performance degrades due to the use of the rotor parameter dependent current model. Accurate parameters are therefore required to avoid such performance degradation. The magnetizing inductance is mostly affected by saturation, and the rotor resistance varies with operating temperature and frequency. Thus, the real-time parameter estimation can enhance DB-DTFC drives.

Since a flux observer combining the current and the voltage models have already been embedded in DB-DTFC, these models are available to be used in a model reference adaptive system (MRAS). The fundamental principle of MRAS-based parameter identification is that the flux linkage can be estimated independently by the current and the voltage models. The estimates from the voltage model are insensitive to the rotor resistance and the magnetizing inductance, and thus, they can be used as the reference. The estimates from the current model depend on the two parameters, which are adaptively estimated by forcing the current model to track the voltage model.

The dynamics of parameter adaptation are determined by the “MIT-rule” shown as (4.5-1), in which ϕ is a general form of estimated parameter and e stands for the model reference error. According to the MIT rule, convergence dynamics are proportional to the sensitivity of parameter error.

$$\frac{d}{dt}\phi(t) = -\text{const}\ \frac{de(t)^2}{d\phi} = -\text{const}\ e(t)\frac{de(t)}{d\phi} \tag{4.5-1}$$

For the magnetizing inductance estimation, the difference between flux linkage magnitude estimates from the current and the voltage models is used as the model reference error. For relatively high speed operation, the voltage model flux estimates are nearly equal to the real flux linkage since it is simply an integration of terminal voltage and not affected by machine parameters. Using rotor flux linkage orientation, the flux linkage estimate from the current model at steady state is shown in (4.5-2), and its sensitivity to the estimated magnetizing inductance can be derived as (4.5-3). Following the MIT rule, the adaptation dynamics of the magnetizing inductance is determined as (4.5-4).

$$\left|\hat{\lambda}_{qdr}\right| = \hat{L}_m i_{ds}^e \tag{4.5-2}$$

$$\frac{d\left|\hat{\lambda}_{qdr}\right|}{d\hat{L}_m} = i_{ds}^e \tag{4.5-3}$$

$$\frac{d}{dt}\hat{L}_m = \text{const}\left(\left|\lambda_{qdr}\right| - \left|\hat{\lambda}_{qdr}\right|\right) i_{ds}^e \tag{4.5-4}$$

The rotor time constant adaptation can be derived by following the same approach. It is well known that the slip frequency of an induction machine is associated with rotor time constant, as is the air-gap torque. Hence, the torque estimates from the voltage and current model are used to form the model reference error, and the q-axis current is correlated to obtain the coherent power. The parameter convergence characteristic equation is provided as (4.5-5).

$$\frac{d}{dt}\hat{\tau}_r = \text{const}\left(T_e - \hat{T}_e\right) i_{qs}^e \tag{4.5-5}$$

As shown schematically in previous papers, an adaptation of the magnetizing inductance and the rotor time constant is integrated into the existing flux observer structure. The current model is adaptively enhanced based on the voltage model flux estimates. It is also noted that an additional damping term is included to smooth the convergence dynamics. The tuning of the MRAS controller is a balance of convergence speed and the signal-to-noise ratio.

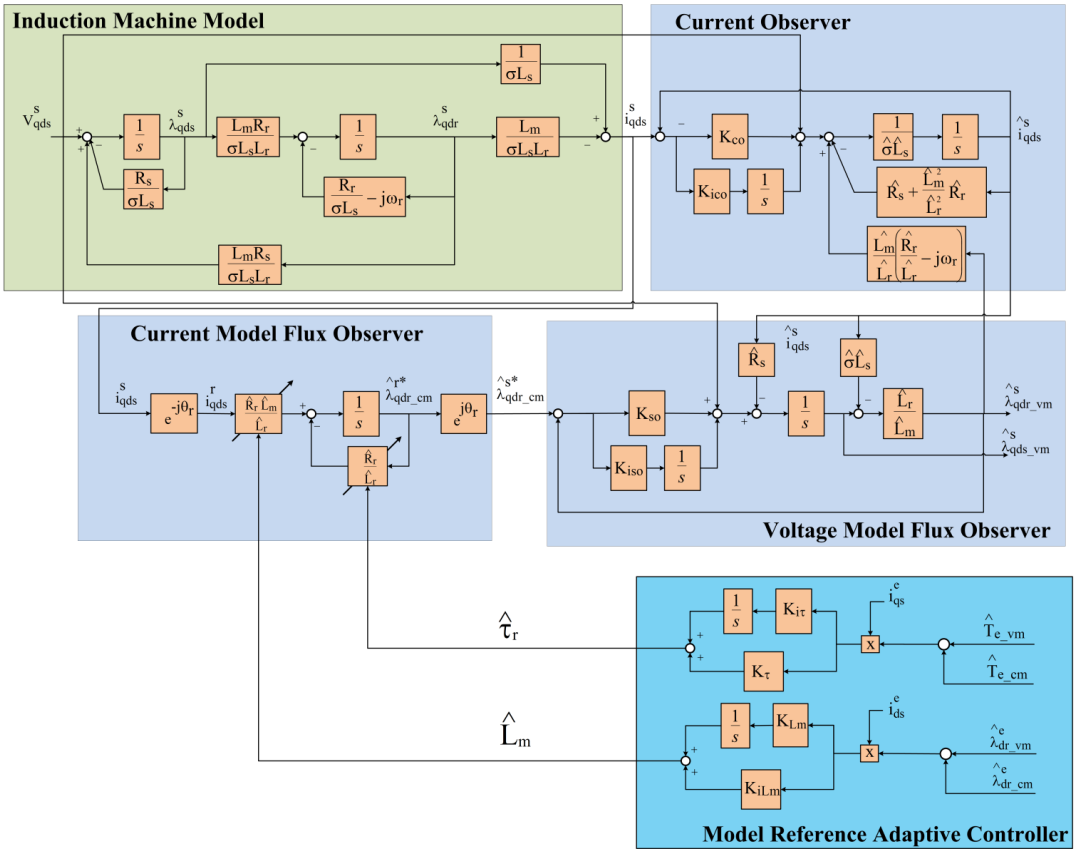

Fig. 4.5-1 An overall block diagram of flux observer based MRAS scheme [106]

Fig. 4.5-2 illustrates typical convergence cases in experiments for the magnetizing inductance and rotor time constant estimation. The orange traces in Fig. 4.5-2 (a) and (c) are

the estimates from the voltage model, which are utilized as the reference. After invoking MRAS, the flux and torque estimates from the current model are adaptively converged to the reference. Correspondingly, the magnetizing inductance and the rotor time constant are converged so that both the current and voltage model provide identical estimates.

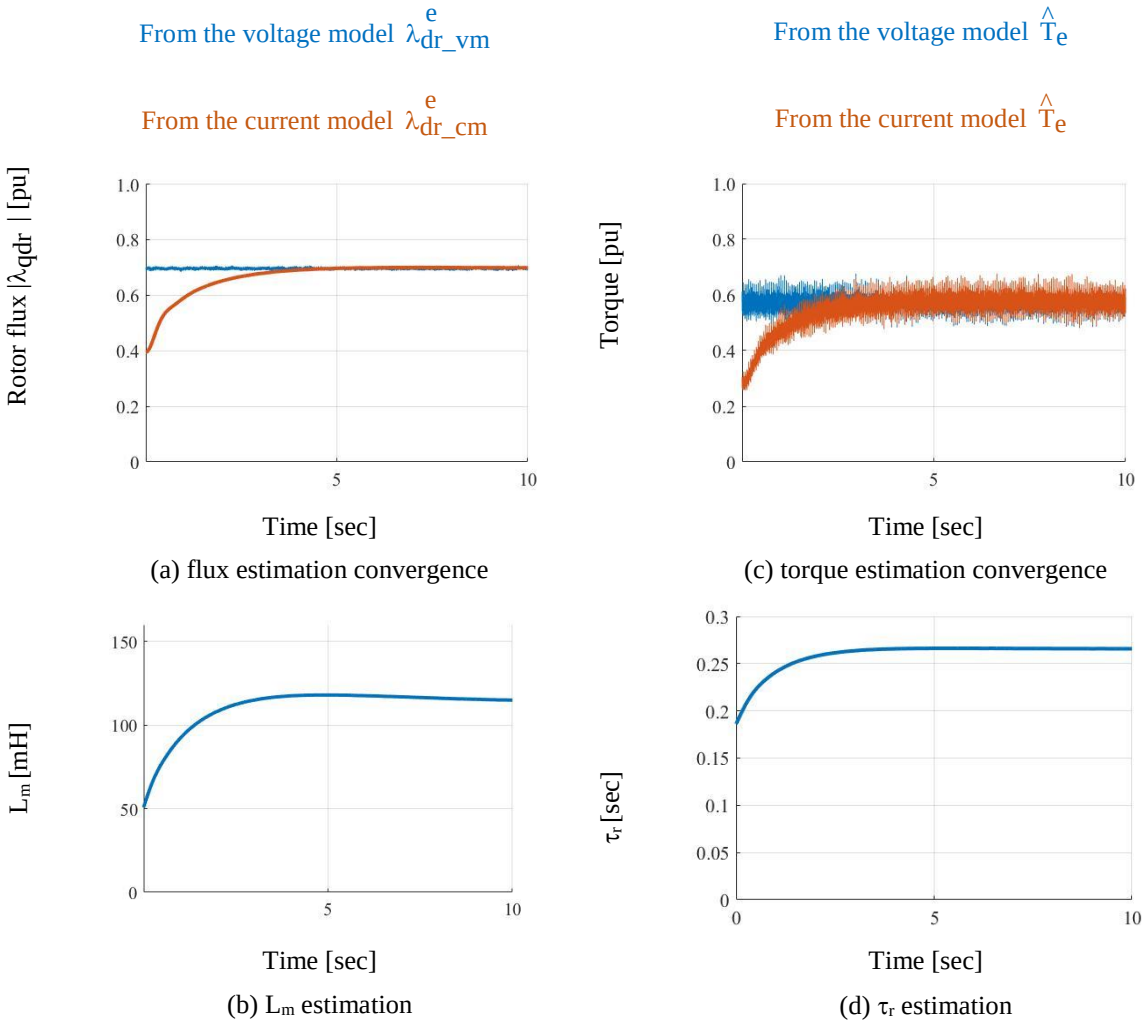

(a) flux estimation convergence

(c) torque estimation convergence

(b) L_m estimation

(d) τ_r estimation

Fig. 4.5-2 Experimental results parameter convergence at 0.7 pu speed, 0.6 pu torque, 0.9 pu flux.

With MRAS invoked and estimation dynamics converged, parameter estimation results at different operating points are shown in Fig. 4.5-3. The rotor resistance in Fig. 4.5-3 is

calculated based on the estimated rotor time constant and the magnetizing inductance. The plot also clearly presents the MRAS estimated saturation effects on the magnetizing inductance with increasing torque and/or flux. The rotor resistance is not directly dependent on torque or flux variation.

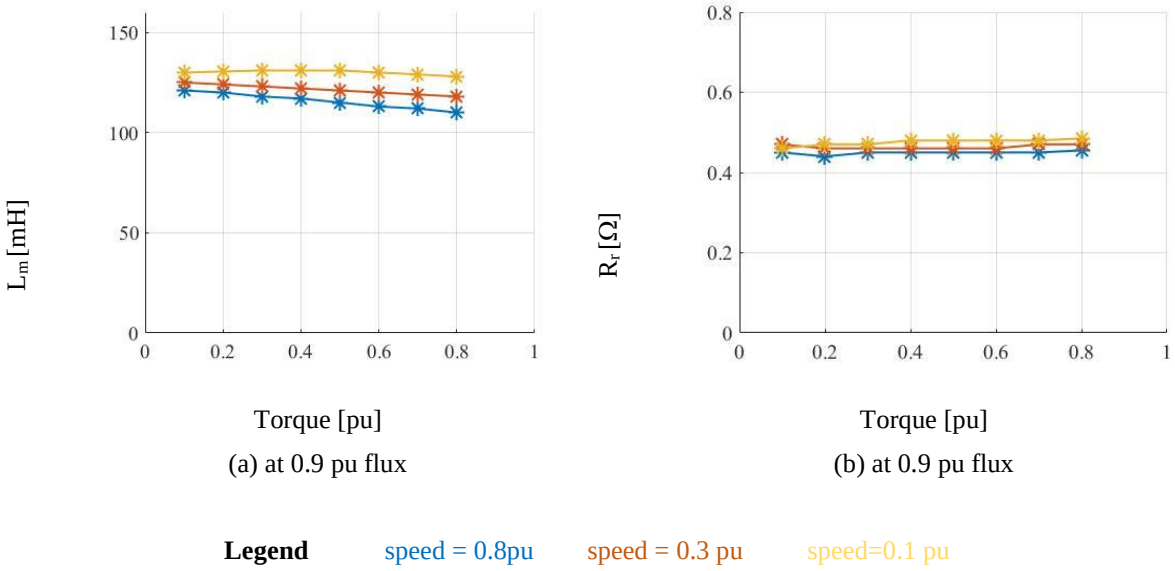

Fig. 4.5-3 MRAS-based real-time parameter estimation using DB-DTFC at different speeds

Fig. 4.5-4 presents MRAS results when integrating the flux observer based MRAS into an IFOC drive. The consistent parameter estimates reveal that the MRAS-based approach can be used in both drives. The magnetizing inductance saturates at the higher torque range, while the rotor resistance does not vary too much. At the low torque range, the rotor resistance estimates become less reliable, since the correlated q-axis current should be close to zero and the useful information in the coherence power is limited. No additional injection signal is required which inherently avoids torque ripple as potential secondary effects.

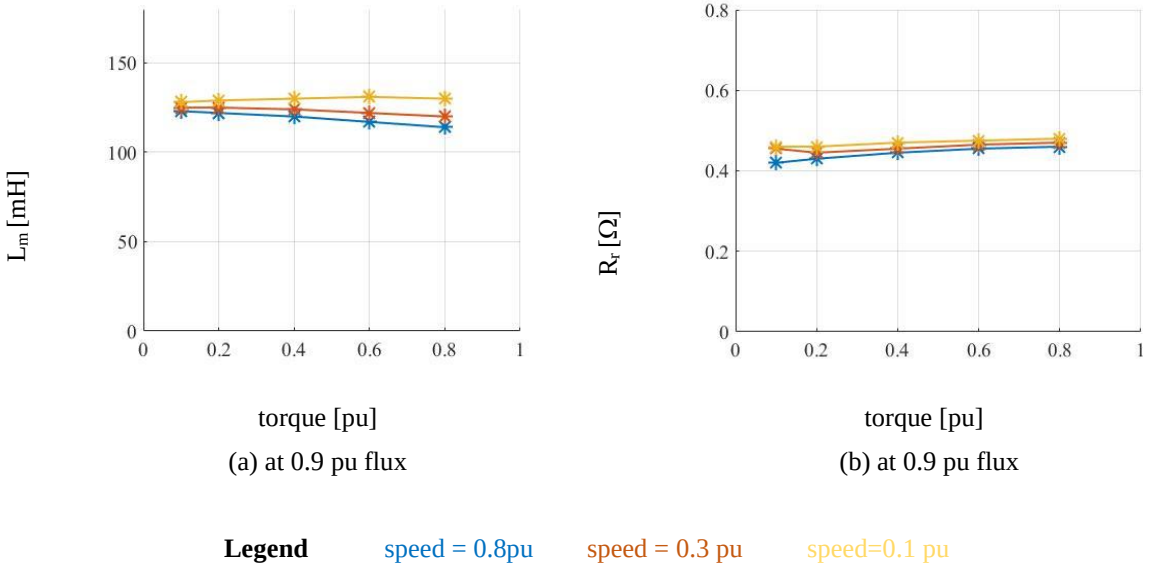

Fig. 4.5-4 MRAS-based real-time parameter estimation using IFOC at different speeds

From both Fig. 4.5-3 and Fig. 4.5-4, it notes that the estimated parameters have small differences/estimation errors at different speeds. The estimation errors occur especially at low speed, which are caused by the inverter dead-time and non-linearity. Since this is flux observer based MRAS parameter estimation and flux observer voltage model is accurate at high speeds, the estimation accuracy is higher at high speeds than it is at low speeds. Voltage-second error from inverter nonlinearity can be decoupled by adding high resolution voltage sensors. Overall, the flux observer based MRAS parameter estimation is more reliable at medium and high speeds and less reliable at speed close to zero.

4.6 Gains Tuning of MRAS Parameter Estimation

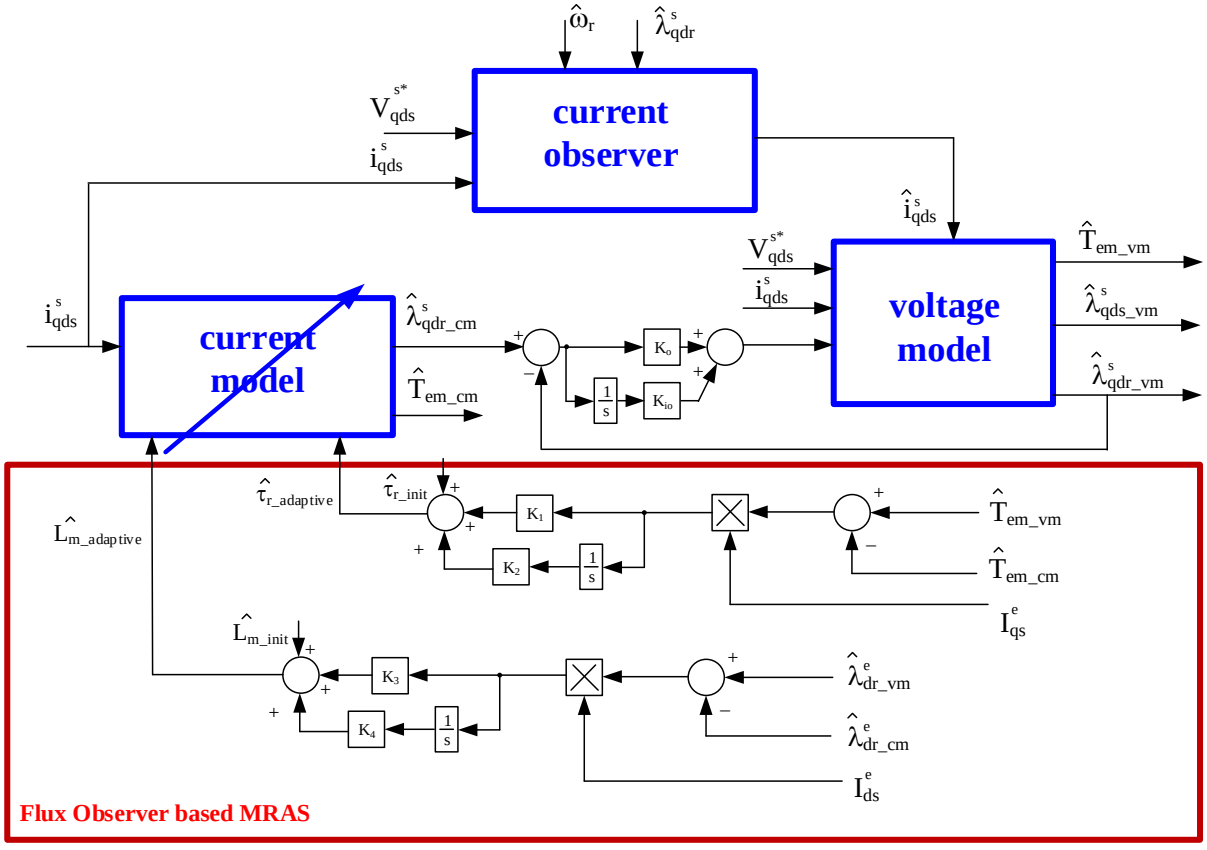

Fig. 4.6-1 Gains tuning of flux observer based MRAS scheme

From the Fig. 4.6-1, there are four gains in the flux observer based MRAS scheme. K_1 and K_2 are the MRAS gains for the rotor time constant estimates. K_3 and K_4 are the MRAS gains for the magnetizing inductance estimates. With different MRAS gains, the system has different estimation dynamics and different converging time. With certain MRAS gains and initial conditions shown in Fig. 4.6-2, the converging time is about 4.5 s.

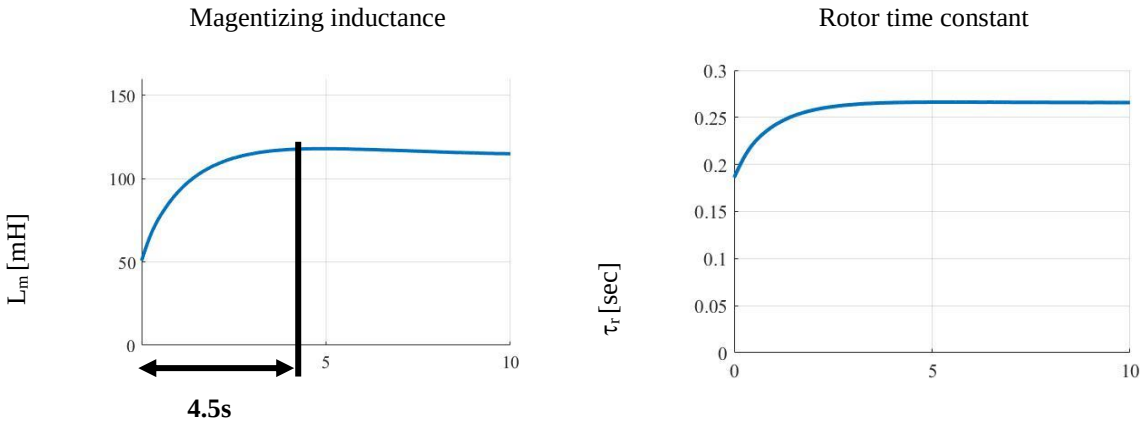

(b) L_m estimation

(d) τ_r estimation

$\hat{L}_m = 50\% L_m$

$\hat{\tau}_r = 70\%\tau_r$

Fig. 4.6-2 Experimental results parameter convergence at 0.7 pu speed, 0.6 pu torque, 0.9 pu flux.

A methodology is needed for achieving the optimized converging time when implementing the MRAS parameter estimation approach. There are two parts of the flux observer based MRAS: magnetizing inductance part and the rotor time constant part. Since it is a non-linear system, it is easier to calculate the optimized gains for each part respectively.

4.6.1 MRAS Gains Tuning for Magnetizing Inductance

To avoid a large step change for the machine parameter, the parameter change in each sample should be less than 10%. In this case, the relationship between the output of magnetizing inductance part, $\hat{L}_{m\_adaptive}$, and gain K_3, shown in Fig. 4.6-1 can be derived from equation (4.6-1):

$$\hat{L}_{m\_adaptive} = K_3 * (\lambda_{dr\_vm} - \lambda_{dr\_cm}) * I_{ds} < 10\% L_m = 0.012 \quad (4.6\text{-}1)$$

Thus, the gain K_3 can be obtained from the equation (4.6-2):

$$K_3 \leq 10\% \, L_m / (\lambda_{dr\_vm} - \lambda_{dr\_cm}) / I_{ds} \approx 0.005 \qquad (4.6\text{-}2)$$

From the equation (4.6-2), the maximum value of K_3 is 0.005. K_4 is the gains of the integration path. In Fig. 4.6-3, the simulation results show different converging time and different MRAS dynamics with fixed K_3 value different K_4 values. In case (a), the K_4 equals to zero. The estimated flux from the current model in green line has an offset with the estimated flux from the voltage model in the red line. Thus, the gain K_4 cannot be zero. In case (b), the K_4 equals to K_3. The estimated flux from the current model in green line takes an excessively long time to converge to the estimated flux from the voltage model in the red line. In case (c), the K_4 is 10 times than K_3. The estimated flux from the current model in green line only takes less than 2 seconds to converge to the estimated flux from the voltage model in the red line. Base on three different case results, if the gain K_4 is 10 times than K_3, the MRAS system would have the fastest dynamics and the optimized converting time for the magnetizing inductance estimation.

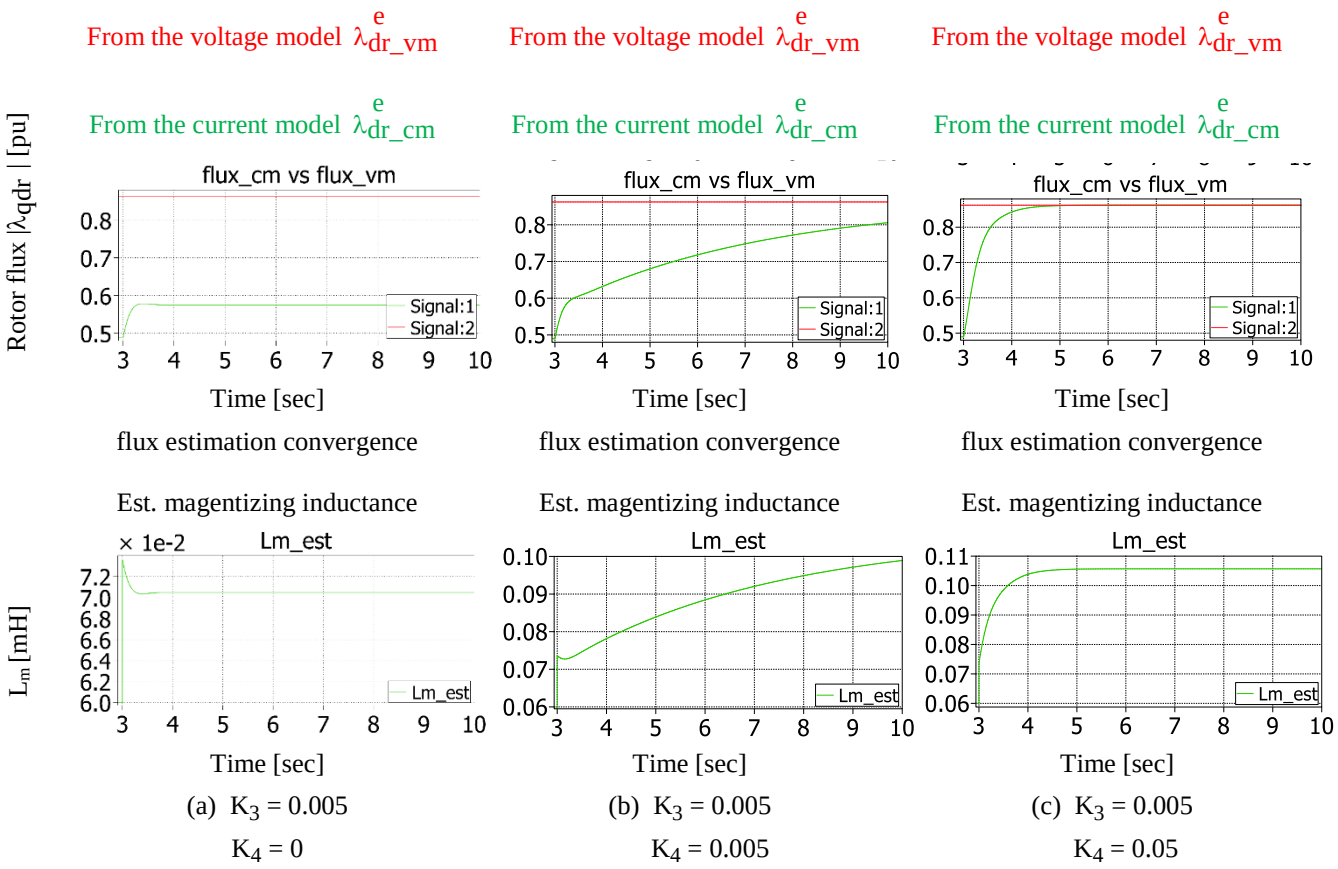

(a) $K_3 = 0.005$ $K_4 = 0$ (b) $K_3 = 0.005$ $K_4 = 0.005$ (c) $K_3 = 0.005$ $K_4 = 0.05$

Fig. 4.6-3 Simulation results MRAS dynamics with different K_4 values

However, the gain K_4 cannot increase further. Fig. 4.6-4 shows the MRAS converging dynamics when the gain K_4 is 0.5, which is 100 times than K_3. Even though the estimated flux of current model converges to the estimated flux from the voltage model in the end, the MRAS system would have some damping and oscillation, which would lead to the whole system unstable.

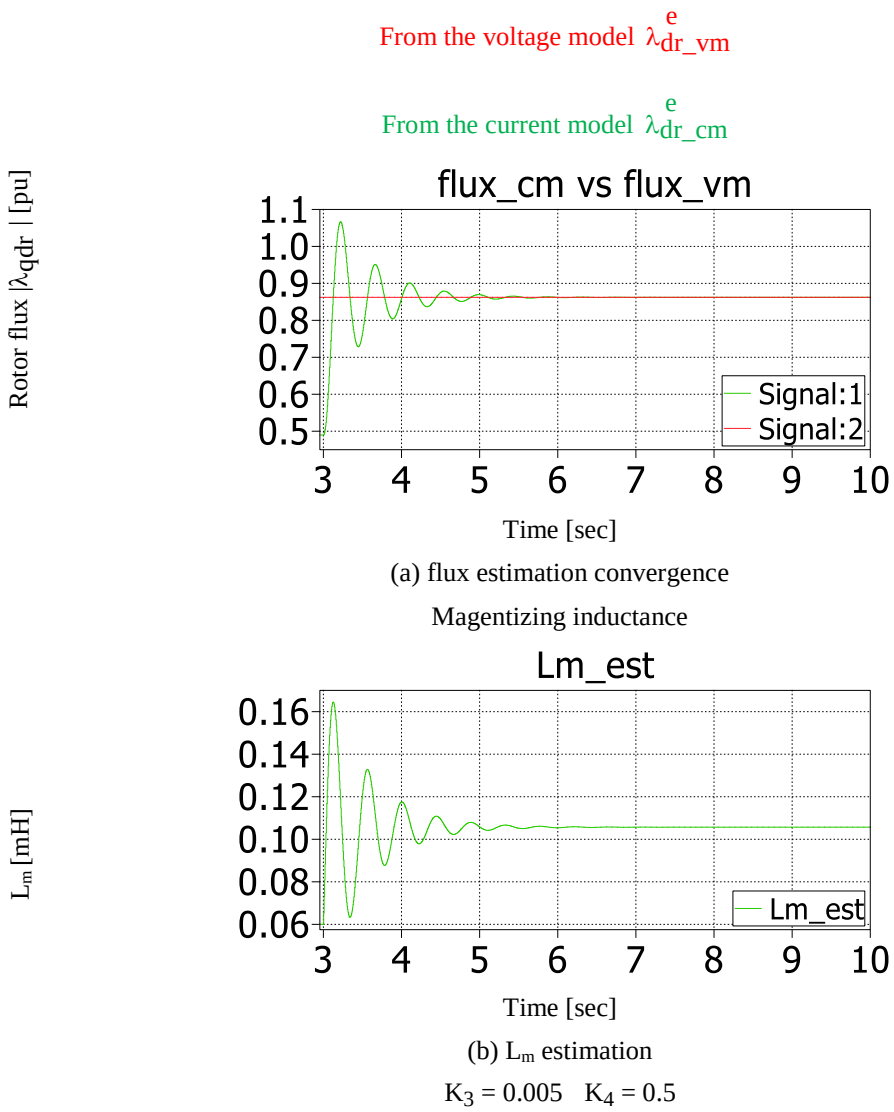

Fig. 4.6-4 Simulation results MRAS dynamics with 0.5 for K_4 value

4.6.2 MRAS Gains Tuning for Rotor Resistance

A similar method can be used for gains K_1 and K_2 tuning.

The relationship between the output of rotor time constant part, $\hat{\tau}_{m\_adaptive}$, and gain K_1, shown in Fig. 4.6-1 can be derived as equation (4.6-3):

$$\hat{\tau}_{r\_adaptive} = K_1 * (T_{em\_vm} - T_{em\_cm}) * I_{qs} < 10\% \ \tau_r = 0.03 \qquad (4.6\text{-}3)$$

Thus, the gain K_1 can be obtained from the equation (4.6-4):

$$K_1 < 10\%\ \tau_r / (T_{em\_vm} - T_{em\_cm}) * I_{qs} \approx 0.0005 \qquad (4.6\text{-}4)$$

From the equation (4.6-4), the maximum value of K_1 is 0.0005. K_2 is the gains of the integration path. In Fig. 4.6-5, the simulation results show different converging time and different MRAS dynamics with fixed K_1 value different K_2 values. Different from the magnetizing inductance gains value, if the gain K_2 is 4 times than K_2, the MRAS system would have the fastest dynamics and the optimized converting time for the rotor time constant estimation.

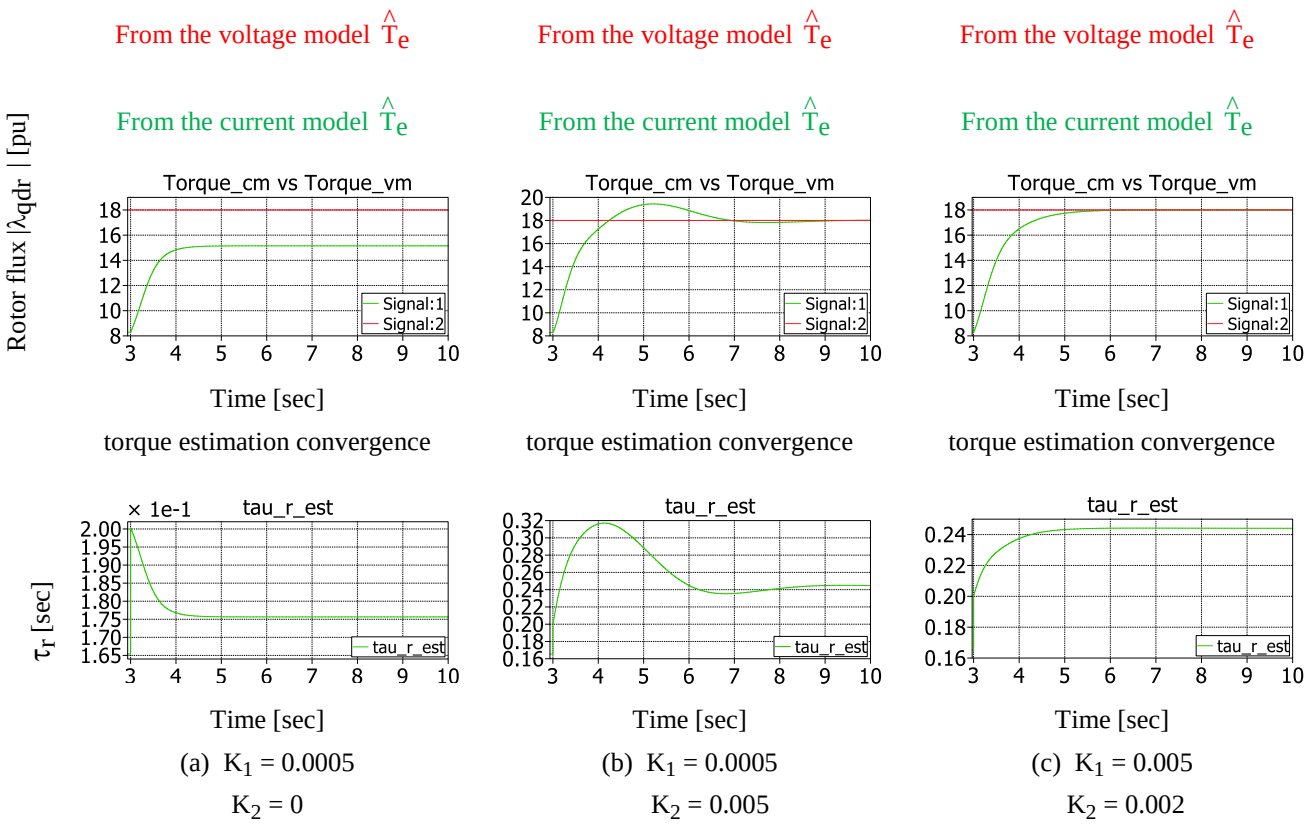

Fig. 4.6-5 Simulation results MRAS dynamics with different K_2 values for τ_r estimation

4.7 Improvements with Parameter Estimation

Chapter 4 and chapter 5 present the real-time parameter estimation by using flux injection method and MRAS method on the existing sensor feedback DB-DTFC respectively. Both methods can be applied for parameter estimation with high accuracy over a wide speed and torque range. The experimental results of the MRAS based method are generally consistent with the estimates of the flux injection based method.

To test the motor T-N curve characteristic (Constant speed control / Constant torque control), the torque command increases slowly. By using the machine parameters on the nameplate (un-tuned parameters), the evaluation of the motor T-N curve characteristic at 0 pu, 0.1 pu, 0.2 pu, 0.5 pu and 1.0 pu are shown in Fig. 4.7-1. The torque command range is from -150% to 150% of the rated torque (-45 Nm ~ +45 Nm). From the Fig. 4.7-1 (a) and (b), they show the DB-DTFC can almost achieve both -150% and +150% of the rated torque with both un-tuned and tuned machine parameters. The tuned machine parameters are obtained from the MRAS method or injection based method since the estimates of the two methods are generally consistent. From another perspective, it also shows the DB-DTFC drive torque producing capability is very stable even with un-tuned machine parameters over the whole speed range.

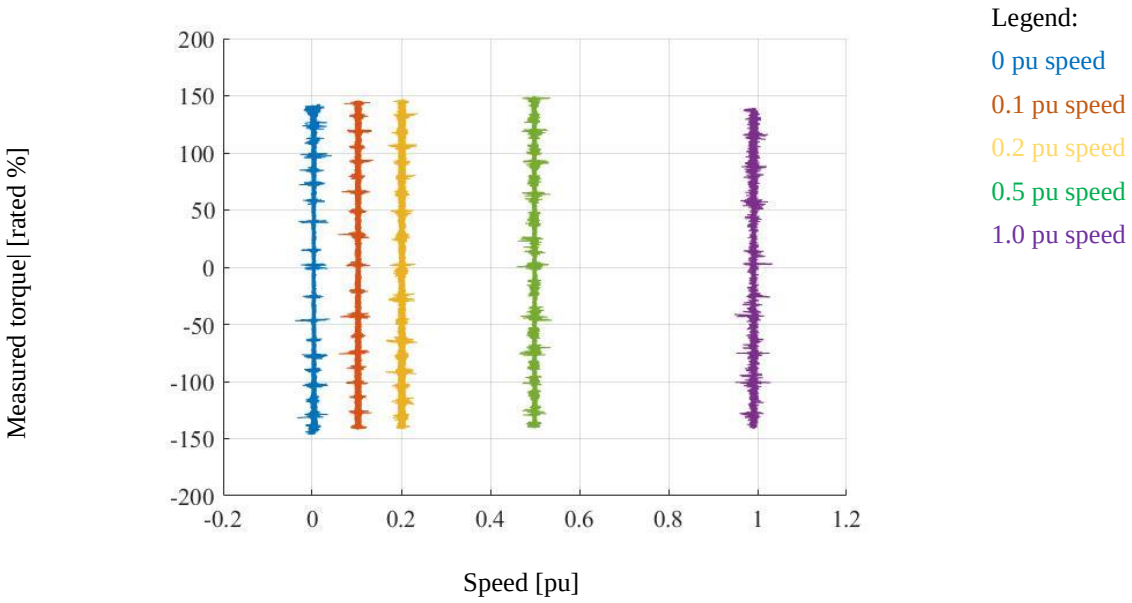

Fig. 4.7-1 (a) T-N curve in DB-DTFC with un-tuned machine parameter

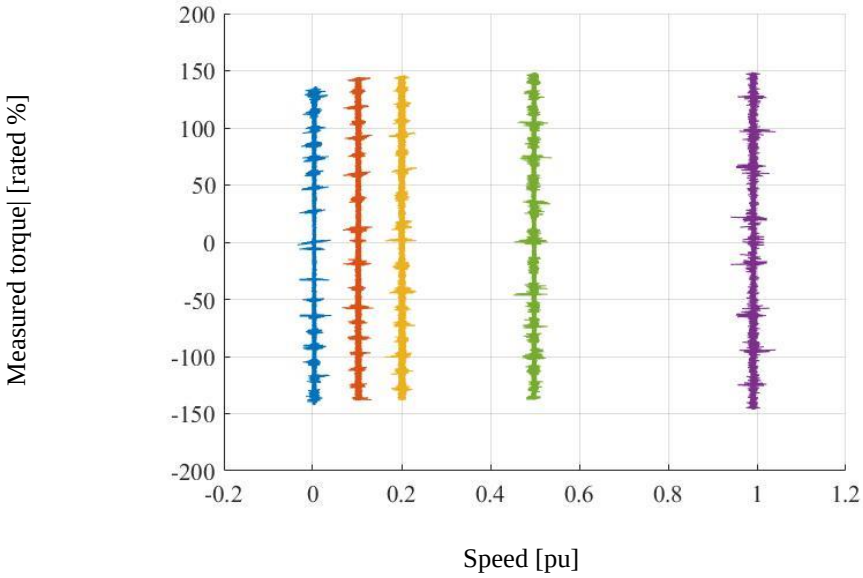

Fig. 4.7-1 (b) T-N curve in DB-DTFC with tuned machine parameter

The Fig. 4.7-2 shows the experimental evaluation of improvements by parameter estimation method with existing encoder feedback DB-DTFC at low speeds. The blue lines are measured torque from the torque sensor. The orange lines are the torque command, which ramps up from zero to 45 Nm (0 pu to 1.5 pu). By using the machine parameters on the nameplate (un-tuned parameters), the baseline evaluation of the motor T-N curve characteristic at 0.1 pu speed and 0.2 pu speed can be obtained, which are shown in blue line the Fig. 4.7-2 (a) and (c) respectively. It is obvious that there is a large torque error in green circles, especially at high load torque, with un-tuned machine parameters.

Tuned parameters can be obtained by injection based parameter estimation over wide speed range or MRAS method parameter estimation at medium and high speeds. It is because the flux observer-based MRAS has higher estimation accuracy at medium and high speed operation for parameter identification in DB-DTFC drives.

The Fig. 4.7-2 (b) and (d) show the improvements by using the two real-time parameter estimation methods at 0.1 pu speed and 0.2 pu speed respectively. It is clear steady state torque error is significantly reduced with the tuned machine parameters from 0 to 1.5 pu load torque at low speeds operation.

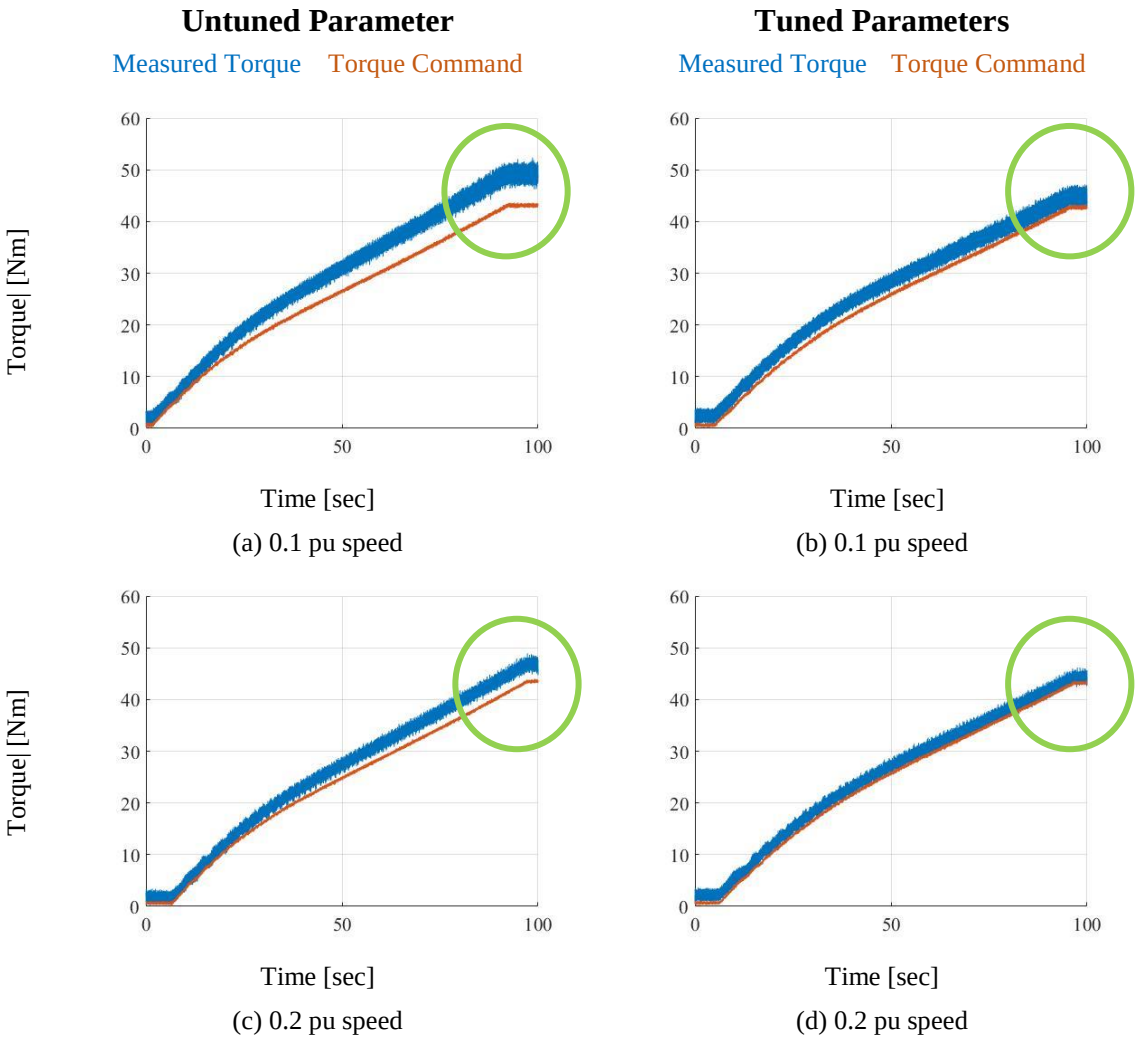

Fig. 4.7-2 Evaluation of improvements by parameter estimation method at low speeds in DB-DTFC

The Fig. 4.7-3 shows the motor T-N curve characteristic with un-tuned and tuned machine parameters at medium and high speed (0.5 pu and 1.0 pu speed). In all Fig. 4.7-3 (a), (b), (c) and (d), the measured torque (blue lines) are overlaid with the torque command (orange lines) over 0 pu and 1.5 pu load torque condition. It means that whether using un-tuned or tuned machine parameters, the DB-DTFC drive has very precise torque control at

medium and high speeds since the flux observer voltage model is accurate at this range. These also demonstrate the DB-DTFC drives are parameter insensitive at medium and high speeds.

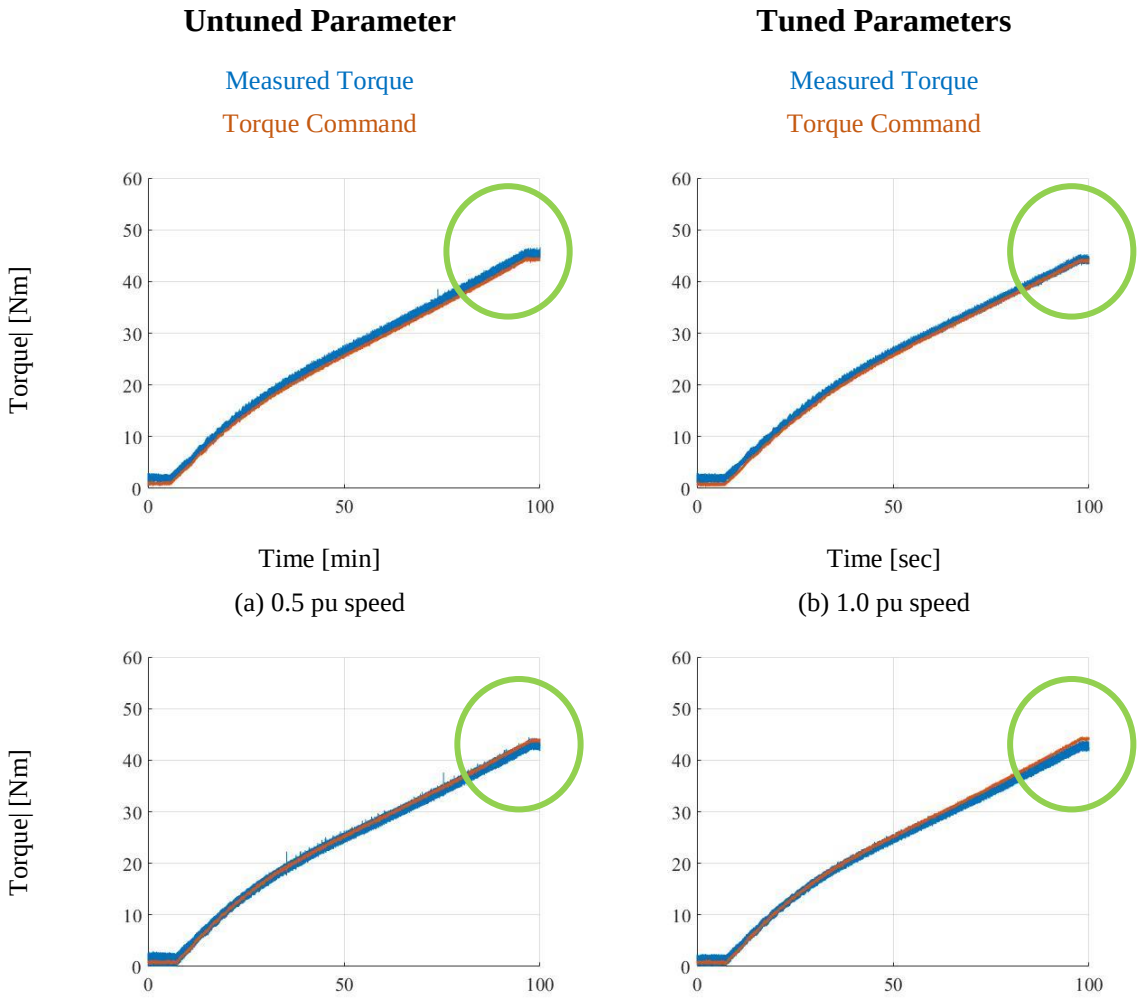

(a) 0.5 pu speed (b) 1.0 pu speed

(c) 0.5 pu speed (d) 1.0 pu speed

Fig. 4.7-3 Experimental evaluation of improvements by parameter estimation method at high speeds in DB-DTFC

4.8 Summary

This chapter explores the injection based real-time parameter estimation method. Key conclusions are summarized as follows:

- Torque ripple for d-axis pulsating voltage injection is significant especially at high speed, due to back-EMF coupling.
- Pulsating flux injection along the torque line in DB-DTFC produces no additional torque ripple, but it induces current harmonics that can be used for parameter estimation.
- High frequency signal injection is suitable for L_{ls} estimation and low frequency signal injection is suitable for R_s and R_r estimation.
- Saturation effects on magnetizing inductance and leakage inductance are significant.
- Magnetizing inductance and leakage inductance will not change at different speeds.
- Parameters are frequency dependent due to skin effects.
- Skin effect can affect estimation accuracy, which should be considered in flux injection-based parameter estimation.
- A more accurate rotor resistance can be estimated by a curve fitting method.
- By using a Gopinath style flux observer, which is embedded in DB-DTFC drives, for MRAS-based parameter estimation, both magnetizing inductance and rotor time constant can be estimated

- The flux observer-based MRAS-based method uses the voltage model as the "reference" (parameter insensitive), and the current model as the "model".
- By forcing the current model to track the voltage model, the estimated parameters, τ_r and L_m, converge to accurate values.
- The MRAS-based parameter estimates become less reliable at low speeds due to inverter dead-time and non-linearity
- The rotor resistance and the magnetizing inductance do not vary significantly at different operating speeds.
- To avoid causing system unstable, the parameter change in each sample should be less than 10%.
- In MRAS-based parameter estimation approach, the convergence time is determined by the MRAS controller gains.
- Large MRAS gains would lead to decreased system damping and instability, but small MRAS gains would excessively increase convergence time.

Chapter 5

Real-time Parameter Estimation for DB-DTFC in Self-Sensing Mode

In chapter 4, the real-time parameter estimation through the flux injection-based approach and the MRAS-based approach have been explored. The estimates through the two different approaches are consistent with each other. The flux injection method for the DB-DTFC drives shows accurate estimation accuracy without any secondary effects, such as induced torque ripple. The MRAS-based method utilizes the DB-DTFC flux observer property to make the current model outputs to converge to voltage model outputs. The two parameters, magnetizing inductance, and rotor resistance, can be estimated at the same time. No additional observer is needed. However, both two methods are developed and evaluated with the encoder for the velocity feedback. The flux injection-based method needs the position information to do the reference frame rotation for extracting the harmonic components. The MRAS-based method also needs the position information in the flux observe current model.

The main objective of this chapter is to explore the two real-time parameter estimation implementation methodologies for DB-DTFC drives in back-EMF based self-sensing mode. Firstly, the improvements of flux injection-based method by using extended back-EMF

self-sensing technique is introduced. Different from the performance with encoder feedback, the flux injection based method induces erroneous speed ripple in back-EMF self-sensing mode. Then, two different approaches are developed and applied to the injection-based method in the self-sensing mode with zero induced speed ripple. In addition, the performance of the MRAS-based method is experimentally evaluated and its limitations are identified.

5.1 Improvements of Flux Injection Method

The first step of signal processing in injection based parameter estimation method is to rotate to the synchronous reference frame by ω_e. The ω_e can be calculated by (5.1-1) in the traditional method.

$$\omega_e = \omega_r - \omega_{sl} \tag{5.1-1}$$

where,

$$\omega_{sl} = \frac{4}{3P} \frac{\hat{T}_{em}}{\hat{\lambda}_{dqr}^{2}} R_r \tag{5.1-2}$$

The slip is calculated by the estimated torque and estimated rotor flux, which is sensitive to machine parameters. Any rotation angle error will lead to the errors in both positive and negative sequence components. The Fig. 5.1-1 shows the positive current components $i_{ds\_cp}^{p}$ with the equation calculation method for the reference frame rotation. By using this method, there is much noise on the desired harmonics due to the inaccurate reference frame rotation. The final estimation accuracy of the flux injection method relies on the

quality of both positive and negative sequence components. Thus, any rotation angle error will cause the parameter estimation accuracy degradation.

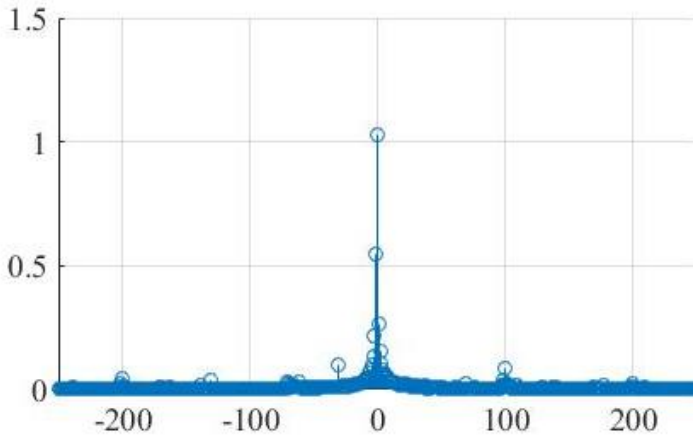

Fig. 5.1-1 Positive current components with traditional reference frame rotation method

To achieve a better signal processing performance, the ω_e should be obtained through a more accurate method rather than the traditional machine equation calculation method. Fig. 5.1-2 shows the flux injection-based parameter estimation with electrical speed estimation for reference frame rotation. Without the slip angle rotation part and feedforward path (T_{em}^{*} path) in Fig. 3.3-1, the proposed observer-based back-EMF self-sensing block becomes to the electrical speed estimation block, which can estimate the electrical speed and position.

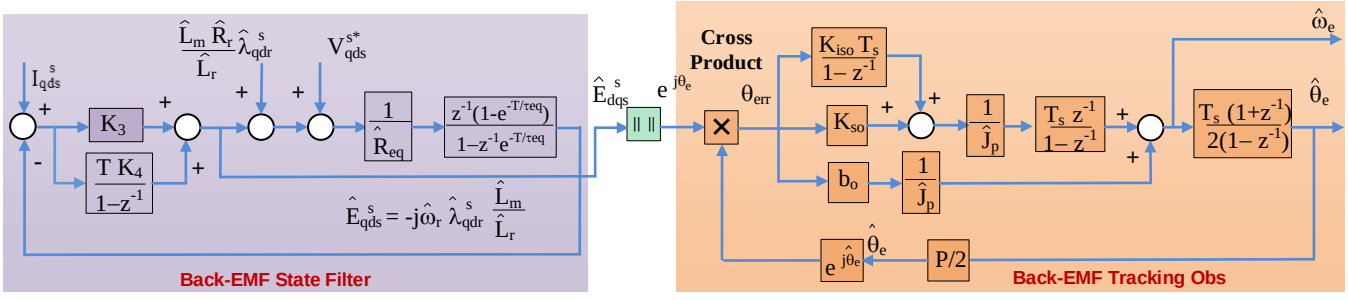

Fig. 5.1-2 Back-EMF state filter cascading a tracking observer for electrical position estimation

Instead of using the equation (5.1-1) and (5.1-2), the electrical position estimation (EPE) block can be used for reference frame rotation. The system block diagram becomes to the Fig. 5.1-3. This approach will improve the reference frame rotation accuracy.

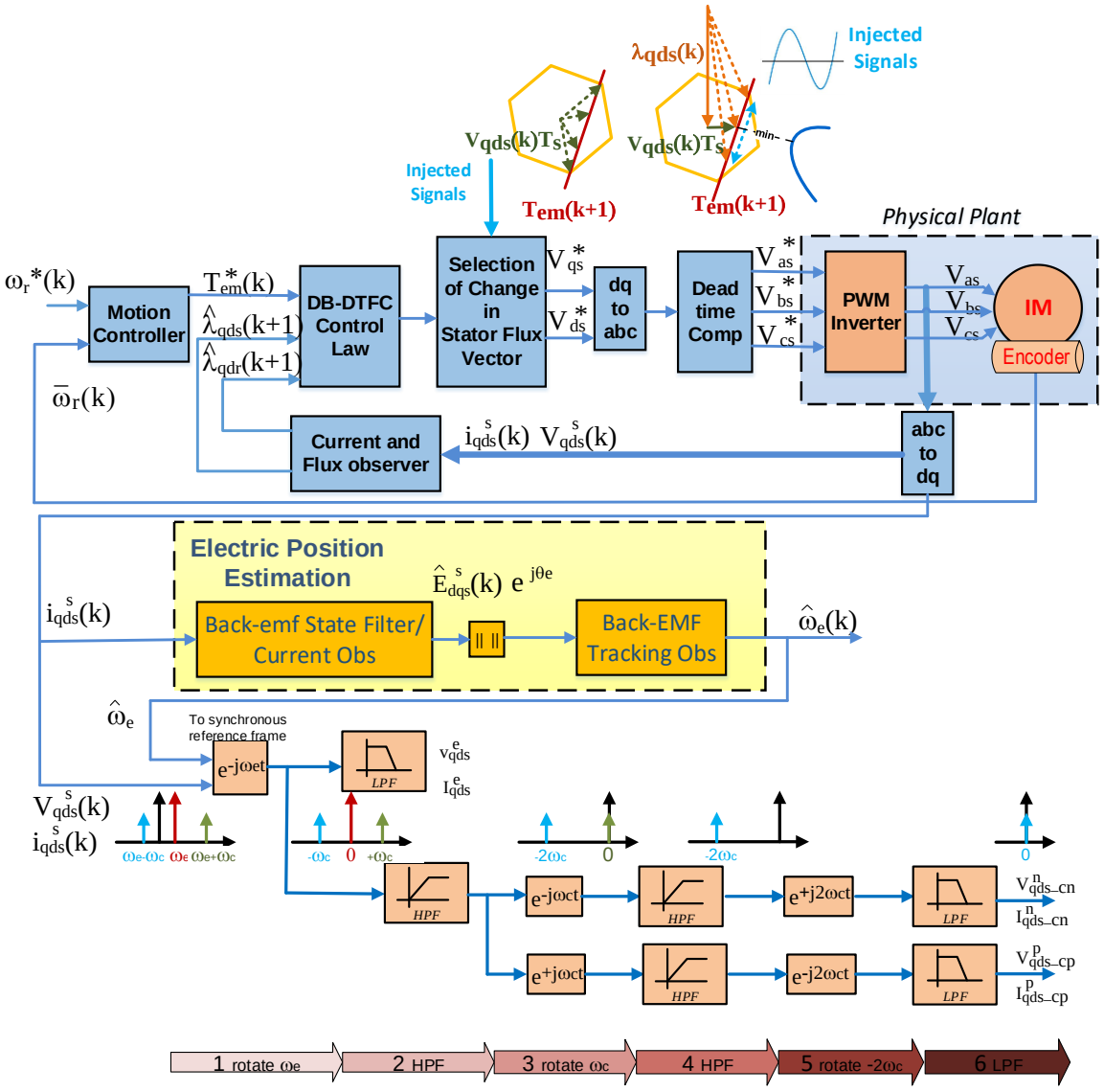

Fig. 5.1-3 Flux injection-based parameter estimation with electrical speed estimation for reference frame rotation

Fig. 5.1-4 shows the reference frame rotation results compared with the traditional machine equation calculation method and the proposed method by using an electrical position estimation block. It can be seen that after the signal processing procedure step one (rotating an angle θ_e), the signal i_{qds}^{e} has much less noise in the Fig. 5.1-3 EPE block in yellow.

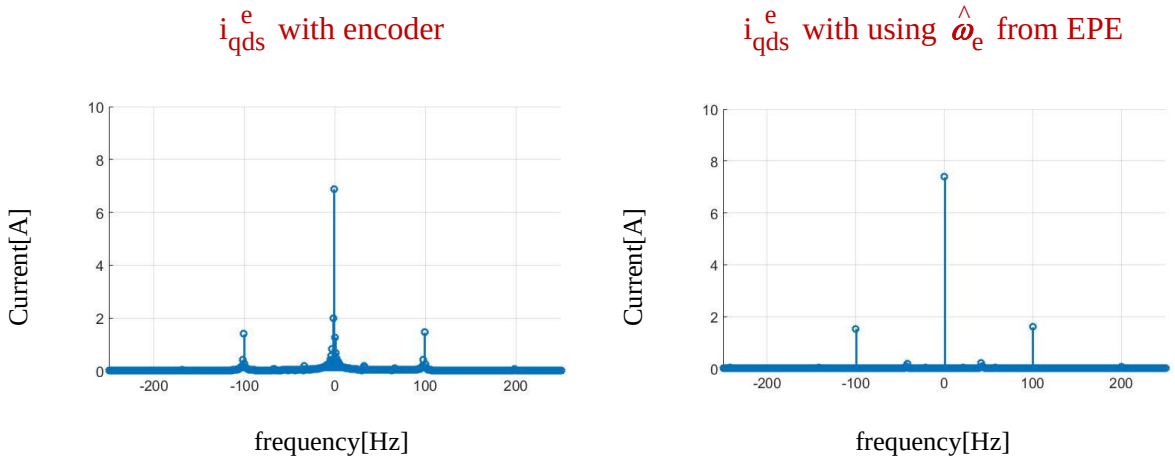

Fig. 5.1-4 Reference frame rotation comparison with and without electrical position estimation

5.2 Flux Injection-Based Parameter Estimation in DB-DTFC Self-Sending Mode

5.2.1 Speed Ripple in Self-Sensing Mode

The flux injection based parameter estimation method with encoder velocity feedback has been present in previous sections. Fig. 5.2-1 (a) shows the block diagram of the flux injection-based parameter estimation in DB-DTFC back-EMF self-sensing.

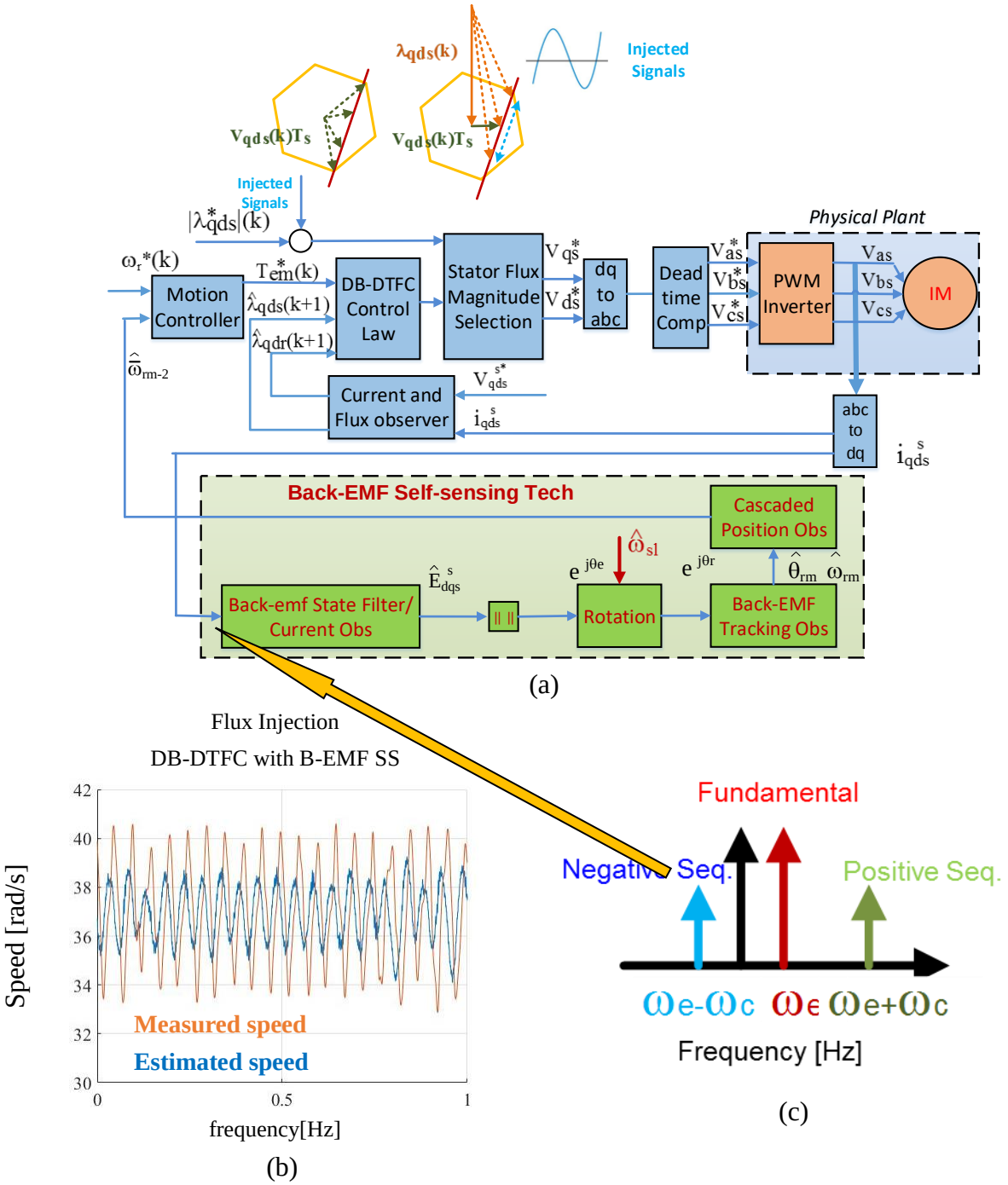

Fig. 5.2-1 Flux injection-based parameter estimation with electrical speed estimation for reference frame rotation

The flux injection-based parameter estimation is based on positive and negative harmonics generated by the injected flux signal. Thus, all the electrical states, such as back-EMF signals, will contain the harmonics at the injected frequency, which is shown in Fig. 5.2-1 (c). The proposed back-EMF state filter will estimate the back-EMF in both fundamental frequency and the injected carrier frequency. However, these harmonics will be treated as a speed variation for the back-EMF self-sensing block. The injected flux linkage induces an erroneous speed ripple, which causes a real speed ripple shown in Fig. 5.2-1 (b).

The harmonics which are induced by the injected flux signal should be eliminated or decoupled for avoiding causing any real speed ripple. In this thesis, two methods, the high pass filter method and the injected signal decoupling method, are proposed. The benefits and the limitation of each method are analyzed and identified.

5.2.2 High Pass Filter Method

No matter what technique is used, the purpose is to remove the harmonics at the injected carrier frequency on the estimated back-EMF to emulate the situation without any injected signal. Since the injected carrier frequency ω_c is known in advance, the simple way is to add a filter to remove the harmonics and to remain the fundamental components. Fig. 5.2-2 shows the high pass filter method to eliminate the speed ripple caused by the injected signal. There are three stages for this method.

First, the input current signals should be rotated by ($\omega_e + \omega_c$) to transfer the injected component as a dc value. After the fast Fourier transform, the fundamental component should be at $-\omega_c$ and the injected component should be at zero in the frequency domain.

Then, using the high pass filter to remove dc value (green line) and to maintain the fundamental component (red line) at frequency $-\omega_c$.

Finally, rotate the fundamental component back to the real excitation reference frame by $-(\omega_e + \omega_c)$. After this, without any positive and negative components, only the fundamental component should be left at frequency $+\omega_e$.

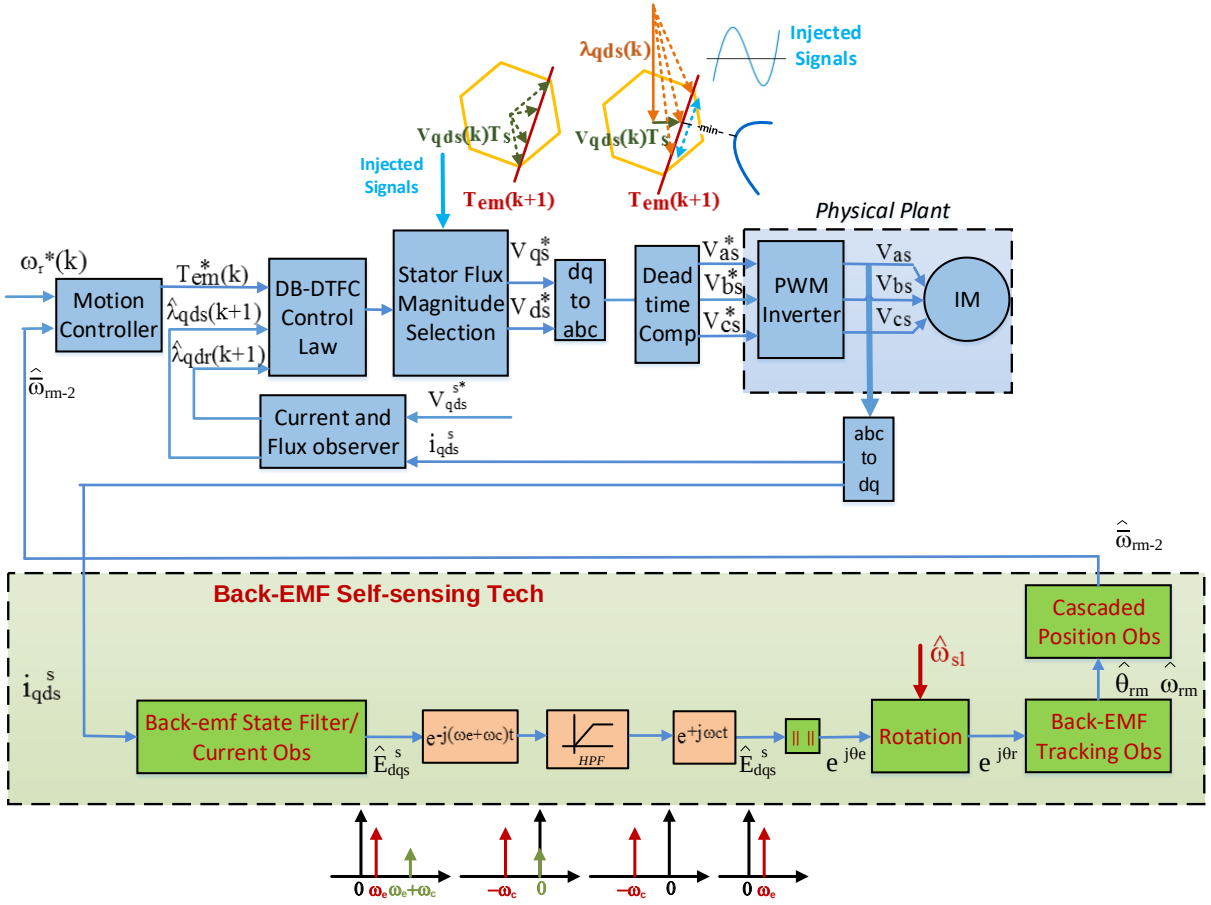

Fig. 5.2-2 High pass filter method to eliminate the speed ripple

The high pass filter method can be easily implemented and can filter the ripple at the injected frequency. However, the whole system dynamic stiffness will be limited by the high pass filter bandwidth. Since the carrier frequency is 20 Hz for resistance estimation on this machine, the high pass filter bandwidth should be smaller than 20 Hz. In general, half of the injected frequency is selected for the high pass filter bandwidth. Thus, the system dynamic stiffness is limited by 10 Hz in this case.

5.2.3 Decoupling Method

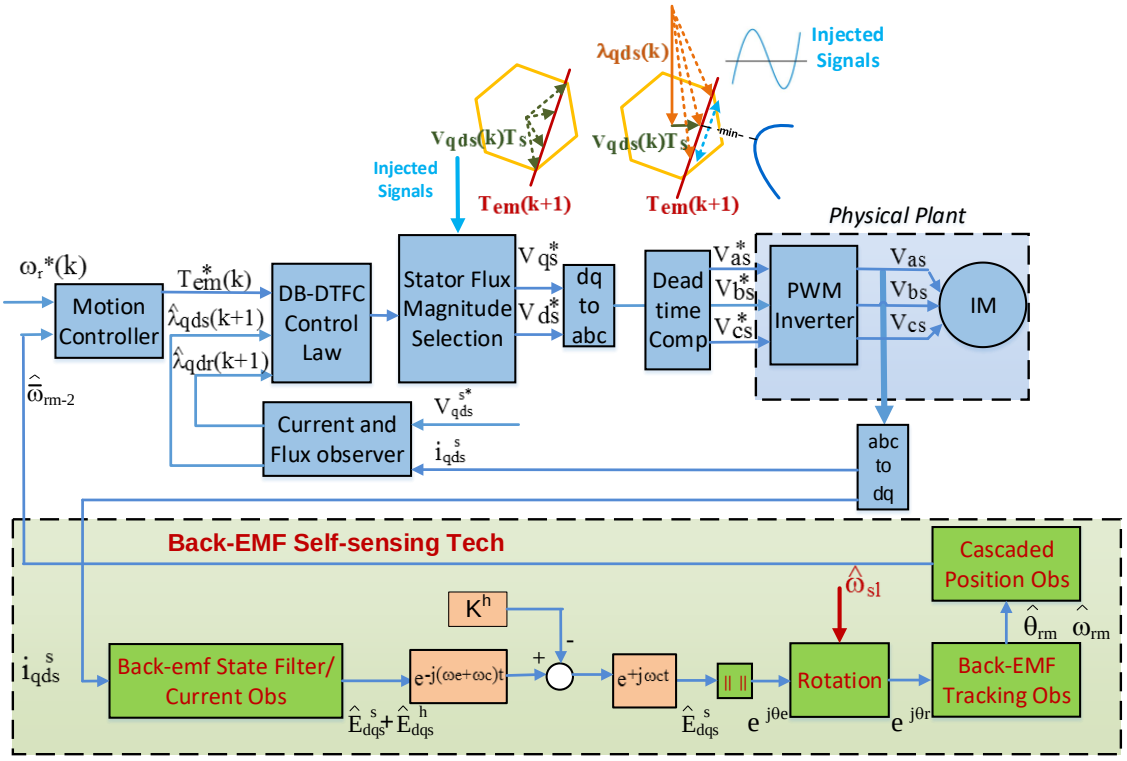

Fig. 5.2-3 Injection signal decoupling method to eliminate the speed ripple

Instead of using any filter on the final estimated back-EMF, the positive and negative components can be decoupled to eliminate the erroneous speed ripple. Since the magnitude

and the frequency of the injected flux signal are known in advance, the magnitude of the induced harmonics can be calculated. If the induced harmonics is subtracted from the estimated back-EMF, the pure fundamental component will be obtained. The induced harmonics are at $\pm(\omega_e + \omega_c)$ in the frequency domain. Fig. 5.2-3 shows the injection signal decoupling method to reduce the speed ripple caused by the injected signal.

The procedures of the injected signal decoupling method are shown in Fig. 5.2-4 (a). The details are described as following:

First, the input current signals should be rotated by $(\omega_e + \omega_c)$ to transfer the injected component as a dc value. This step is the same as the high pass filter method presented above.

Second, since the injected components frequency and magnitude have been known in advance, the injected signal K^h can be subtracted from the estimated back-EMF. In the ideal case, both positive and negative components should be eliminated from the measured current.

Finally, rotate the fundamental component back to the real excitation reference frame by $-(\omega_e + \omega_c)$. After this, only the fundamental component should be left at $+\omega_e$ in the frequency domain.

Different from the synchronous machine, in induction machines, it is difficult to obtain the exact ω_e. In the real case, after the step one, the injected components will be located at a very low frequency in Fig. 5.2-4 (b) rather than at zero frequency as a pure dc in Fig. 5.2-4

(c). With this situation, the very low frequency component in the green line of the Fig. 5.2-4 (b) can be calculated as the variable “offsets” in every short period and then the “offsets” will be subtracted from the estimated back-EMF. In this thesis, one second is set to the period length, which means the “offsets” is calculated and updated in every second.

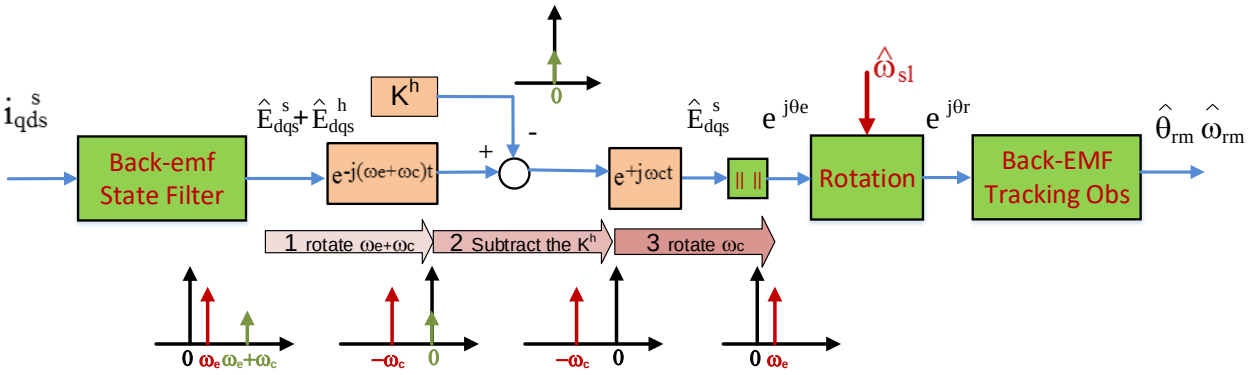

(a)

(b) Real case (c) Ideal case

Fig. 5.2-4 Injection signal decoupling method to reduce the erroneous speed ripple

The performance of the proposed injection signal decoupling method at different speeds is shown in Fig. 5.2-5. Before the enabling the decoupling method, the speed ripple on both measured speed and estimated speed are obvious. By the decoupling method, the speed ripple are significantly reduced, which are shown in the right side of the bold black line in each plot. The low speed limit is 0.2 pu, since the signal-to-noise ratio degrades significantly at the speed lower than 0.2 pu. The system is unstable even with the proposed decoupling method

in this area. The voltage degradation at low speeds is also the reason why the speed ripple increases as the speed ripple decreases with injecting flux signal. More accurate dead-time compensation method or voltage error decoupling method will be helpful to obtain the accurate voltage information, especially at low speeds. This technique will make the system more stiff and stable at lower speeds.

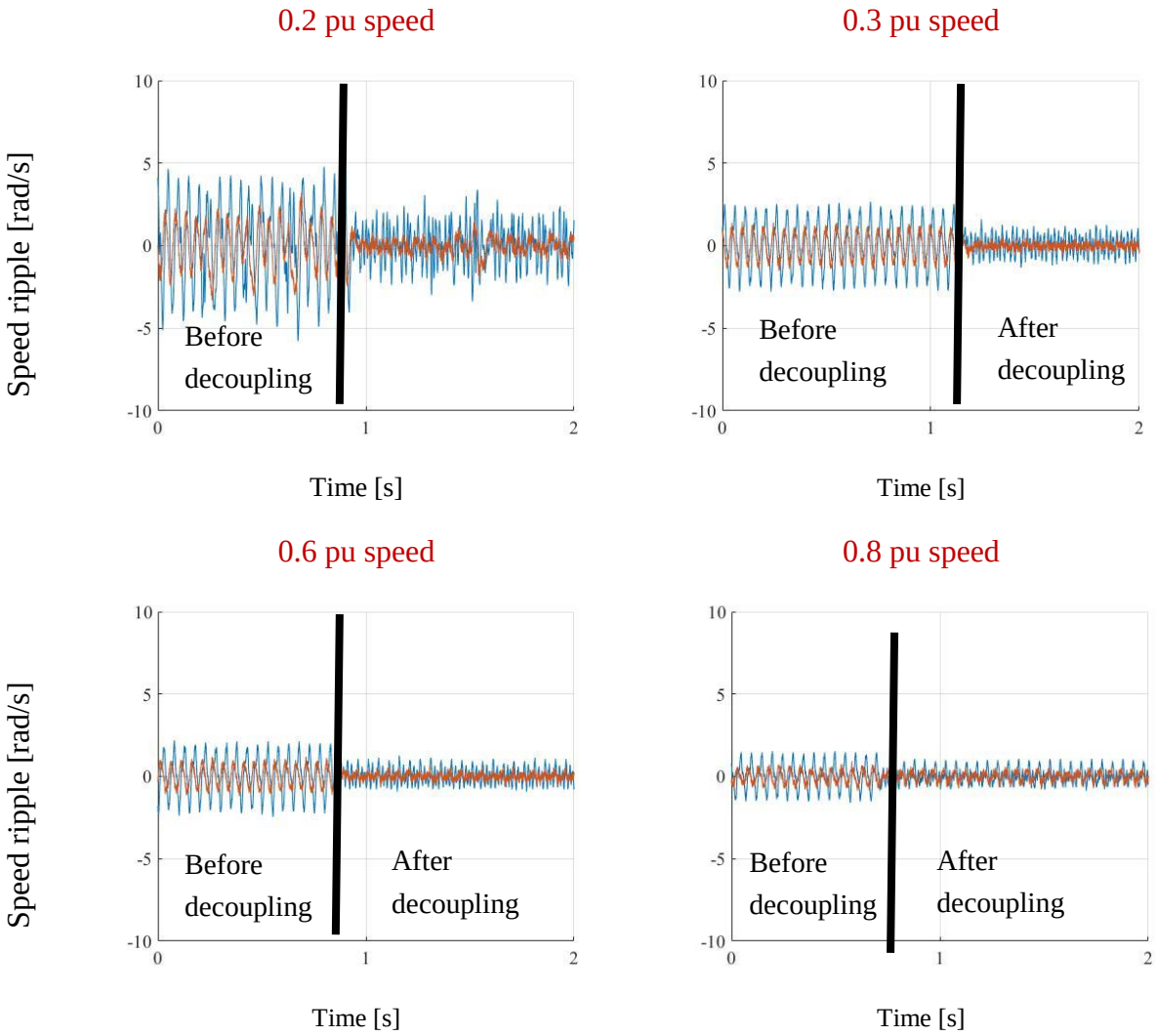

DB-DTFC self-sensing No load. Injected flux signal: 20 Hz 0.1 pu

Legend: **Measured speed** **Estimated speed**

Motion controller f_s = 1 kHz EVs: 10 Hz 1 Hz 0.2 Hz

Back-EMF state filter f_s = 10 kHz EVs: 100 Hz 20 Hz

Back-EMF based motion observer f_s = 1 kHz EVs: 10 Hz 1 Hz 0.2 Hz

Fig. 5.2-5 Injection signal decoupling method performance

An essential benefit of this decoupling method is that it should not affect the system dynamic stiffness. It also does not induce any speed ripple. The system dynamic stiffness is shown in Fig. 5.2-6 with the proposed injection signal decoupling method at 0.2 pu, 0.4 pu and 0.3 pu speed respectively.

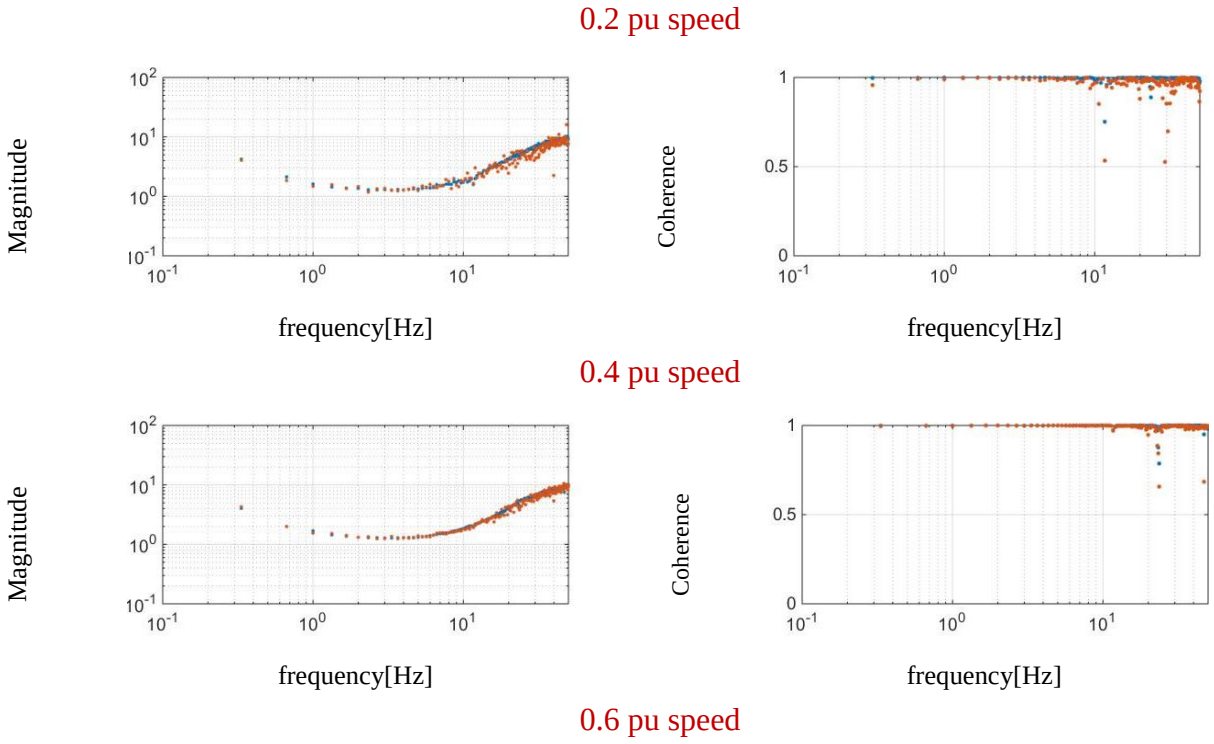

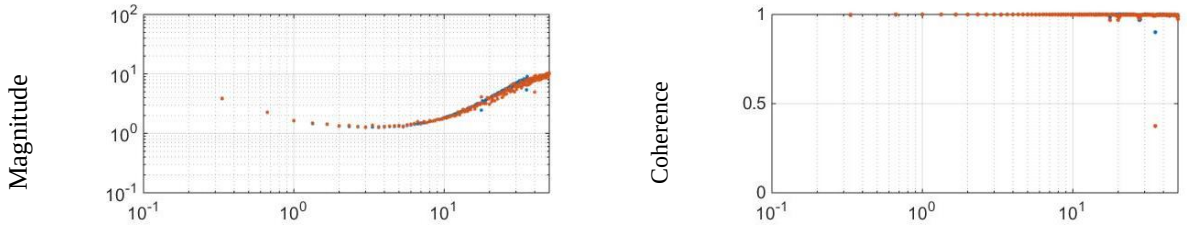

DB-DTFC self-sensing No load., Injected flux signal: 20 Hz 0.1 pu
Motion controller f_S = 1 kHz EVs: 10 Hz 1 Hz 0.2 Hz
Back-EMF state filter f_S = 10 kHz EVs: 100 Hz 20 Hz

Fig. 5.2-6 Experimental results of parameter estimation using the signal injection based approach in DB-DTFC. Injection signals at 0.1 pu flux, 20 Hz

5.3 MRAS-Based Parameter Estimation in DB-DTFC Self-Sending Mode

The MRAS-based parameter estimation method with encoder velocity feedback has been present in previous sections. Fig. 5.3-1 shows the block diagram of the MRAS-based parameter estimation in DB-DTFC back-EMF self-sensing.

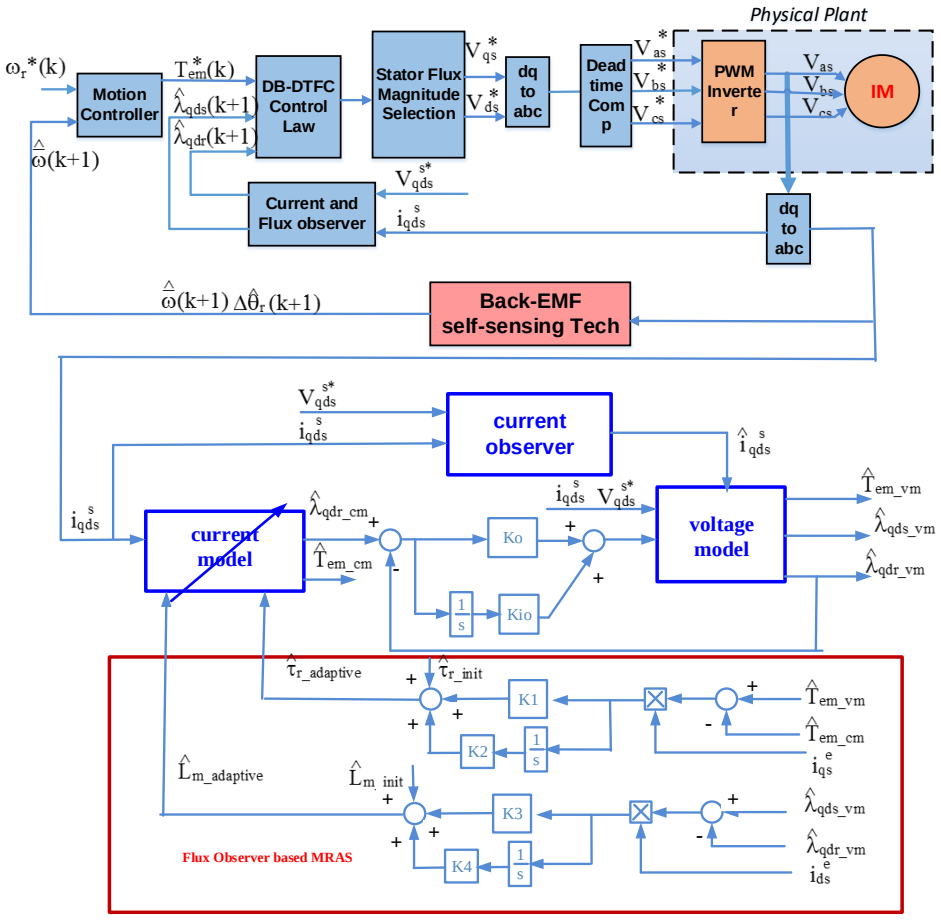

Fig. 5.3-1 MRAS-based parameter estimation in DEB-DTFC self-sensing mode

5.3.1 Magnetizing Inductance Estimation

With the MRAS approach, the magnetizing inductance estimation results at different operating points are shown in Fig. 5.3-2. The test results are similar to the rest results of the MRAS based parameter estimation with encoder feedback. The plot also clearly presents the MRAS estimated saturation effects on the magnetizing inductance with increasing torque.

When the speed is higher than 0.2 pu, the L_m estimates in orange line (0.2 pu speed), yellow line (0.6 pu speed) and purple line (1.0 pu line) are almost overlain together. The estimated L_m is not speed-dependent, however, at extra low speed around the 0.06 pu speed in the blue line, estimation error increases due to volt-sec error.

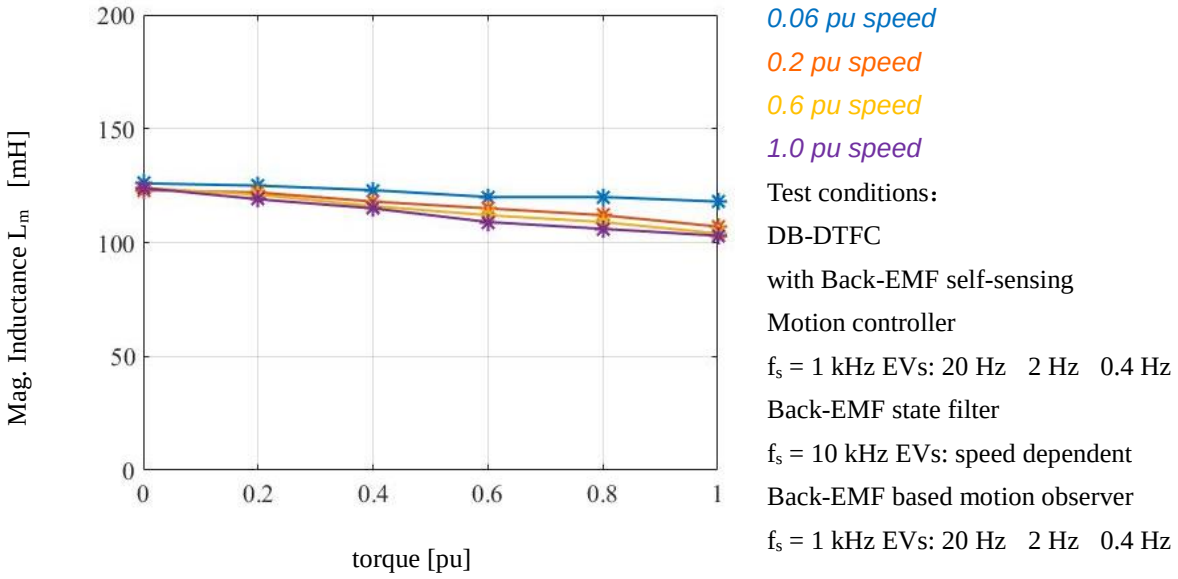

Fig. 5.3-2 Magnetizing inductance estimation comparison at different speeds and different load conditions

5.3.2 Rotor Resistance Estimation

With the MRAS approach, the rotor resistance can also be estimated. The experimental results of the rotor resistance estimation at different operating points are shown in Fig. 5.3-3. The test results are similar to the rest results of the MRAS-based parameter estimation with encoder feedback.

Based on the operating temperature, the results can be divided into two groups. One group tests are operated at 33 °C in the blue line, other groups are operated at the temperature around 38 °C in the orange line, yellow line and purple line respectively. The plot also clearly presents the rotor resistance estimates increases as the temperature increased since the blue line results obtained in lower temperature are lower than all other line results, which are obtained in higher temperature.

Based on the operating speeds, the test results can be categorized into two groups as well. One is a low speed test group (0.06 pu speed and 0.2 pu speed), the other is the medium and high speeds test group (0.6 pu speed and 1.0 pu speed). The test results show R_r estimates highly consistent with each other at 0.6 pu speed and 1.0 pu speed in the yellow line and purple line, but estimation error increases as the speed decreases to 0.2 pu speed. It is due to a volt-sec error at low speeds caused by the inverter nonlinearity.

One drawback of MRAS-based approach for the rotor resistance estimation is that it does not work properly at zero load torque. Since the rotor resistance is estimated through the torque estimates from the current model are adaptively converged to the torque estimates from the voltage model. If the load torque is zero, the torque from the test is very small, which is closed to zero. In this case, the torque estimates from the current model and voltage model in MRAS system are almost zero, which it is hard for the system to estimate the accurate value. This is

the reason why there are relatively large estimation errors with zero load torque at different speeds in the Fig. 5.3-3.

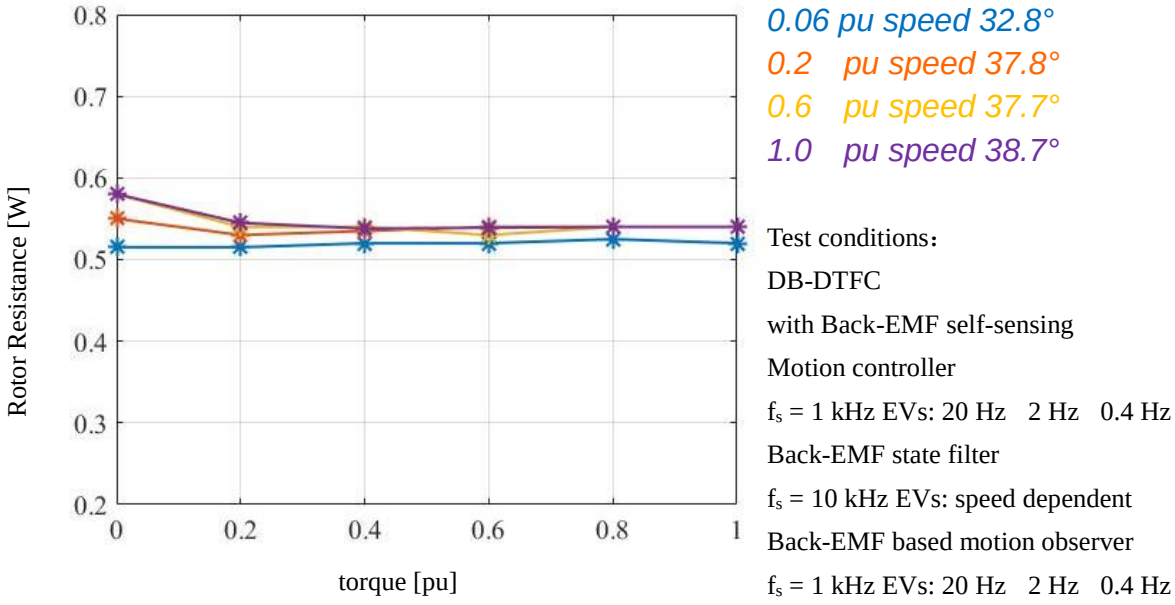

Fig. 5.3-3 Rotor resistance estimation comparison at different speeds and different load conditions

5.4 Summary

This chapter explores the Model Reference Adaptive System based real-time parameter estimation method. Key conclusions are summarized as follows:

- The estimated slip frequency is used for reference frame rotation in the traditional method, which is sensitive to machine parameters.
- Using the estimated electrical speed from the electrical position estimation block is more accurate for reference frame rotation.

- The injection flux linkage induces an erroneous speed ripple which causes a real speed ripple in self-sensing mode.
- In the high pass filter approach, the system dynamic stiffness will be limited by the high pass filter bandwidth.
- Without inducing any speed ripple, an injection signal decoupling method can reduce the speed ripple significantly by subtracting the positive and negative components of the measured current.
- The injection signal decoupling method will not affect the system dynamic stiffness.
- To decrease the bandwidth while maintaining the flux estimation accuracy requires more accurate voltage information, especially at low speeds.
- For magnetizing inductance estimation, the MRAS-based parameter estimation works well in self-sensing mode at different speeds and load conditions.
- The test results of MRAS-based parameter estimation in self-sensing mode are similar to the rest results with the encoder feedback.
- At no load condition, it is difficult to estimate τ_r, since the outputs $|\hat{T}_{em}|$ from both current and voltage model outputs are near zero
- The accurate voltage information is required to improve the MRAS-based parameter estimation, especially at low speeds.

Chapter 6

Comparative Evaluation and Simplifications of the Two Methods

In chapter 4 and 5, the real-time parameter estimation through the flux injection-based approach and the MRAS-based approach with either encoder feedback or back-EMF tracking feedback have been explored. In the self-sensing mode, the injection flux linkage would induce an erroneous speed ripple which would cause a real speed ripple. A signal decoupling method can reduce the speed ripple significantly. However, because of signal-to-noise ratio decreases sharply at low speeds, the lowest operation speed for the injection-based parameter estimation with the signal decoupling approach is 0.2 pu speed. For the MRAS-based parameter estimation method, it can work well in self-sensing at different speeds, even at 0.1 pu speed.

The main objective of this chapter is to investigate the differences in performance between the two parameter estimation methods in both self-sensing and encoder feedback mode for DB-DTFC drives. Based on the comparative evaluation of the two parameter estimation methods, the opportunities to improve either system by recognizing synergies between the two parameter estimation methods are identified. In addition, the absolute and

relative computational load and processing power requirement for each method are evaluated.

6.1 Comparison of the Two Methods

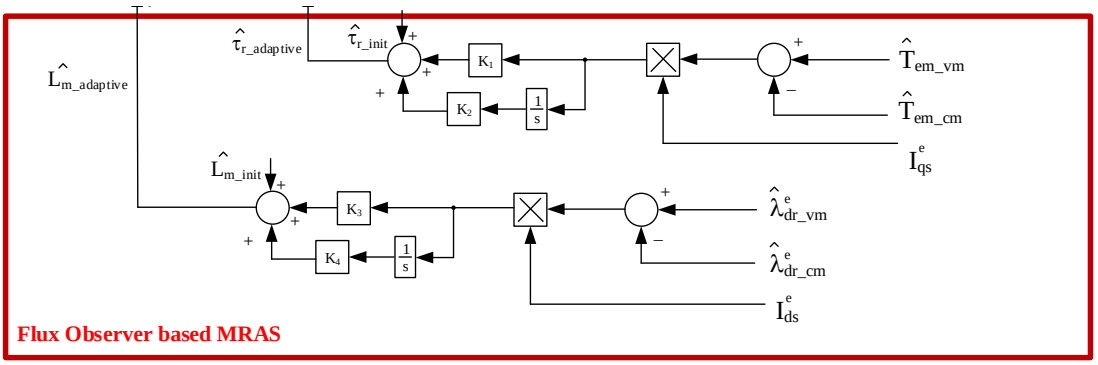

(a)

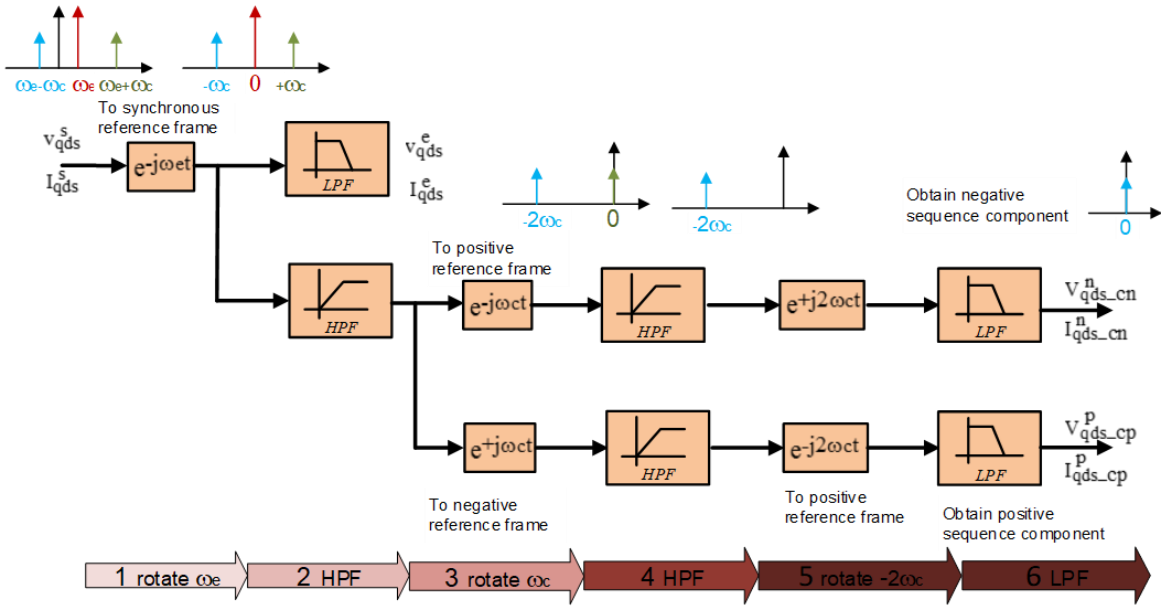

(b)

Fig. 6.1-1 (a) MRAS-based parameter estimation method;
(b) Flux injection-based parameter estimation method

The MRAS-based parameter estimation method forces errors from the current model and voltage model to zero to estimation parameters. The proposed flux observer-based MRAS system utilizes the torque path and flux path to estimate τ_r and L_m respectively, as shown in Fig. 6.1-1 (a). However, at no load condition, the MRAS-based method cannot estimate τ_r, since the estimated torque error ($\hat{T}_{em\_current\_model}$ - $\hat{T}_{em\_voltage\_model}$) is near zero, which leads the MRAS system not converging. To avoid a large step change of machine parameters, the MRAS system need take several seconds to make the estimated parameters converge to the accurate values. It means the MRAS-based method, which cannot detect highly dynamic changes, works with steady state operating conditions.

Compared to with the MRAS-based method, the flux injection-based method utilizes harmonics induced by the injected flux signal to extract parameter information, shown in Fig. 6.1-1 (b). Thus, the flux injection method has better dynamic performance and can estimate parameters over the entire loading conditions.

Compared to the encoder feedback performance, in the self-sensing mode, the MRAS-based method and flux injection-based method have several different properties:

- MRAS-based parameter estimation would not work at very low speeds (<0.05 pu speed), due to the limitation of the self-sensing performance.

- Even with the signal decoupling approach, the flux injection-based parameter estimation cannot work at the speed lower than 0.2 pu speed, since the signal-to-noise ratio degrades significantly at speeds lower than 0.2 pu.
- The flux injection-based parameter estimation needs the signal decoupling approach, which needs extra computational load, to reduce the erroneous speed ripple.

Based on the discussion above, the properties of the two parameter estimation methods with either encoder feedback or back-EMF tracking feedback can be summarized as follows, shown in Table 6.1-1 and Table 6.1-2.

Table 6.1-1 The summary of the two parameter estimation methods with encoder feedback

	MRAS method	Flux Injection method
Estimated parameters	L_m and R_r	R_s, R_r, L_{ls} and L_{lr}
Estimation time	Several seconds	Less than one second
Calculation time	26 μs	24 μs
Dynamics condition	Steady state	Steady state and dynamic
Load condition	> 0.1 pu	Entire load conditions
Speed condition	Not for extra low speeds	Entire speed conditions

Table 6.1-2 The summary of the two parameter estimation methods with back-EMF tracking feedback

	MRAS method	Flux Injection method
Erroneous speed ripple	No	Yes
Decoupling needed	No	Yes

Load condition	> 0.1 pu	Entire load conditions
Speed condition	> 0.05 pu	> 0.2 pu

Computation time for each method is implemented and evaluated on the AIX controller with FPGA/DSP system at 100 MHz main frequency. It also includes 1 MB SRAM, 4 MB FLASH and 64 MB SDRAM.

6.2 Simplification of the Two Methods

Section 6.1 mainly compares the two parameters estimation methods. Some properties, such as estimated parameters, load conditions and speed conditions, are inherent to each method, which cannot be changed. Based on the theory of each method, the simplification work should be done to reduce the DSP calculation load.

6.2.1 MRAS-Based Method Simplification in DB-DTFC Drives

The MRAS-based parameter estimation method with back-EMF tracking for self-sensing has been presented in previous sections. Fig. 5.3-1 shows that the MRAS-based parameter estimation is built based on a Gopinath style flux observer, which is independent from the flux observer in DB-DTFC drives. Since the flux observer has been already embedded in DB-DTFC drives, there is no need for an additional flux observer for MRAS-based parameter estimation method. Thus, the simplification approach for the MRAS-based method can be followed as Fig. 6.2-1.

Since the flux observer is a part of DB-DTFC drives, this simplification approach is only available for DB-DTFC drives. However, for IFOC drives, the flux observer needs to be implemented for the MRAS-based method.

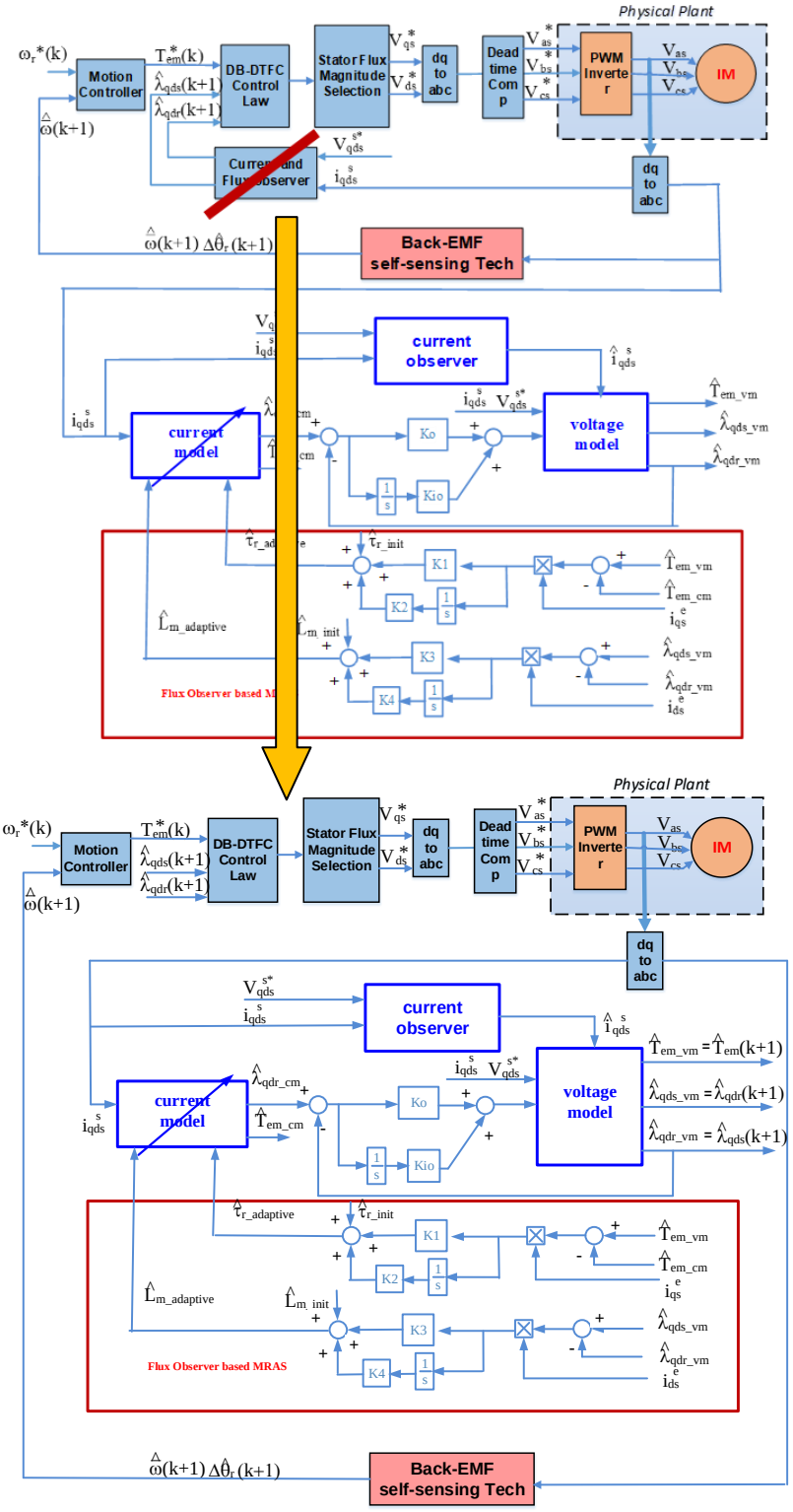

Fig. 6.2-1 The simplification approach of MRAS-based parameter estimation in DEB-DTFC self-sensing mode

6.2.2 Flux Injection-Based Method Simplification in DB-DTFC Drives

The signal processing procedures take large amount of time in the flux injection-based parameter estimation method, shown in Fig. 4.3-1. If the total number of signal processing steps was reduced, the DSP processing time would be decreased. The simplification approach can be implemented as shown in Fig. 6.2-2.

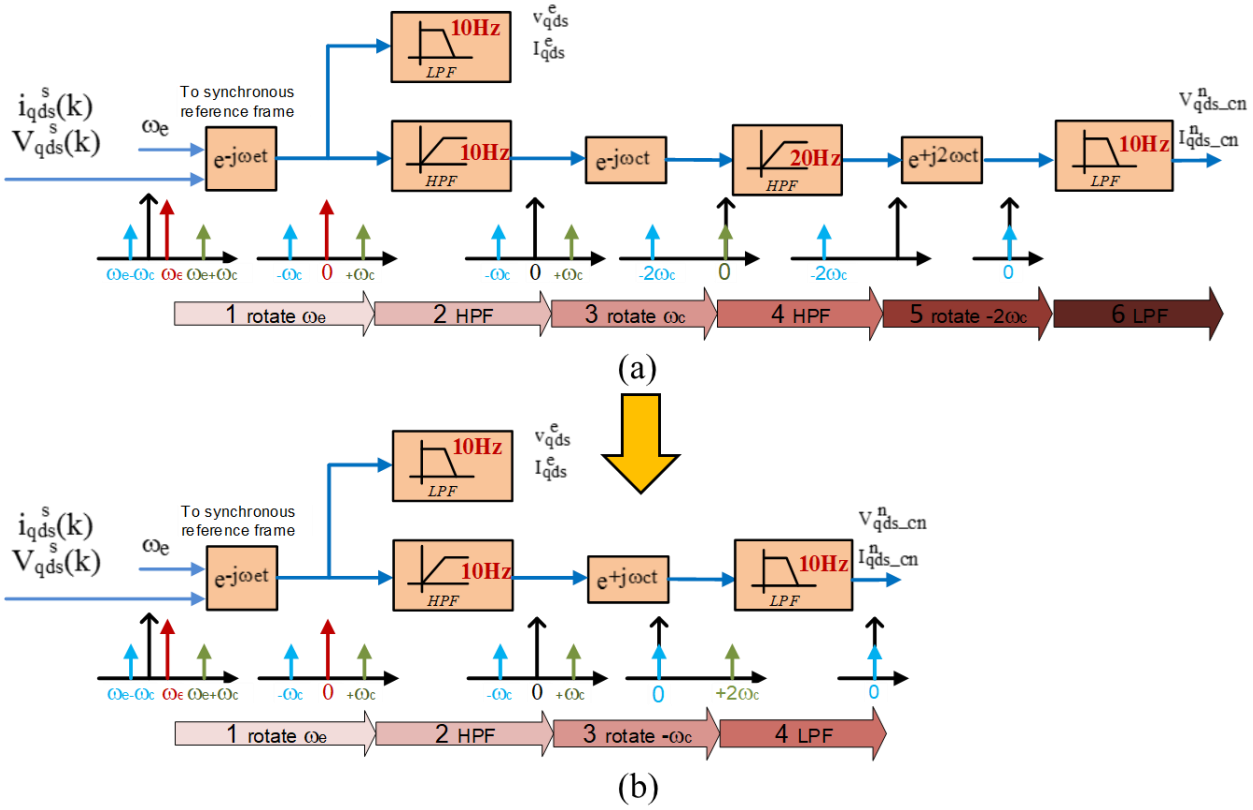

Fig. 6.2-2 The simplification approach of flux injection-based parameter estimation

By directly using a low pass filter in step four directly, the processing steps can be reduced from six to four. In this case, steps 4 and 5 from the original method are eliminated as shown in Fig. 6.2-2 (b).

6.2.3 Experimental Results of Computational Time Reduction

The simplification approaches of the MRAS-based method and flux injection-based method have been discussed in section 6.2.1 and 6.2.2 respectively. Fig. 6.2-3 shows the computational time reduction performance for each parameter estimation method. After the MRAS-based method simplification, the computational time is reduced by 43% from 26 μs (the blue bar) to 15 μs (the yellow bar). After the flux injection-based method simplification, the computational time is reduced by 25% from 24 μs to 18 μs.

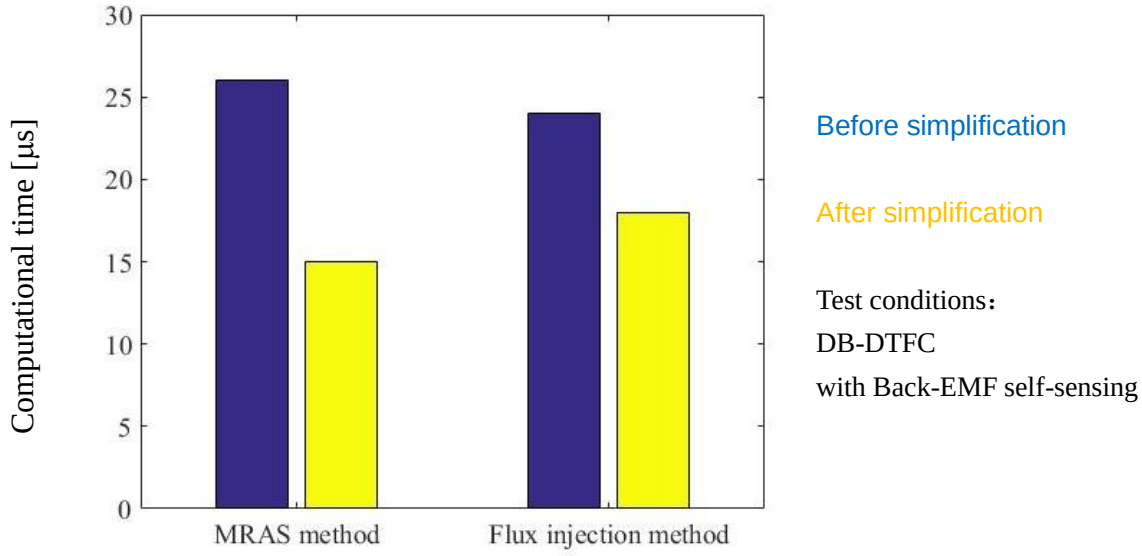

Fig. 6.2-3 Computational time comparison before and after simplification in DB-DTFC drives

6.3 Summary

This chapter compares the differences between the MRAS-based parameter estimation and the flux injection-based parameter estimation method. In addition, the simplification approaches for each method are proposed to reduce the DSP computational load. Key conclusions are summarized as follows:

- The MRAS-based method can only estimate magnetizing inductance with no or light load conditions. The flux injection-based method can work over the entire load range.
- The MRAS-based method is only suitable for steady state conditions. The flux injection-based method works in both steady state and dynamic conditions.
- The computational time of both two methods can be reduced in a DSP system.
- Based on the properties of each method, the simplification approaches are proposed respectively for DB-DTFC drives.
- After the simplification approaches, the computational time of the MRAS-based method is reduced by 43% and the computational time of the flux injection-based method is reduced by 25%.

Chapter 7

Real-Time Parameter Estimation System

The real-time parameter estimation through the flux injection-based approach and the MRAS-based approach with either encoder feedback or back-EMF tracking feedback have been discussed from many perspectives in previous chapters. Each method has its own advantages and disadvantages. No single real-time parameter estimation method can estimate the full set of machine parameters over the whole speed range and the whole load range, especially in back-EMF tracking self-sensing mode.

The main objective of this chapter is to utilize the advantages of each parameter estimation method to develop a real-time parameter estimation system. The proposed system, which contains two methods: an MRAS-based method and a flux injection-based method. The system selects different methods at different operating regions. In addition, the system executes each method in a certain sequence. By over-tuning and de-tuning machine parameters based on the nameplate values and the accurate values, the performance of the operating region-based real-time parameter estimation system is evaluated and discussed in this chapter.

7.1 Parameter Estimation System for IM DB-DTFC Self-Sensing Drives

The properties of the MRAS-based and the flux injection-based parameter estimation methods in back-EMF self-sensing mode have been discussed in section 6.1. The MRAS-based parameter estimation method can estimate magnetizing inductance and rotor resistance. The flux injection-based method can estimate rotor resistance, stator resistance and leakage inductance. Ideally, if both methods were used simultaneously, the full set of machine parameters would be estimated. To estimate the full set of machine parameters, the real-time parameter estimation system, which contains both the MRAS-based and flux injection-based method, can be built.

Fig. 7.1-1 shows the parameter estimation system for induction machine DB-DTFC self-sensing drives, using dual parameter estimation methods. The system utilizes the flux observer embedded in DB-DTFC drives for the MRAS method and contains the simplified flux injection-based method. Since it is a back-EMF self-sensing drive, the back-EMF self-sensing technology in the bottom green block of the Fig. 7.1-1 contains the erroneous speed ripple decoupling part.

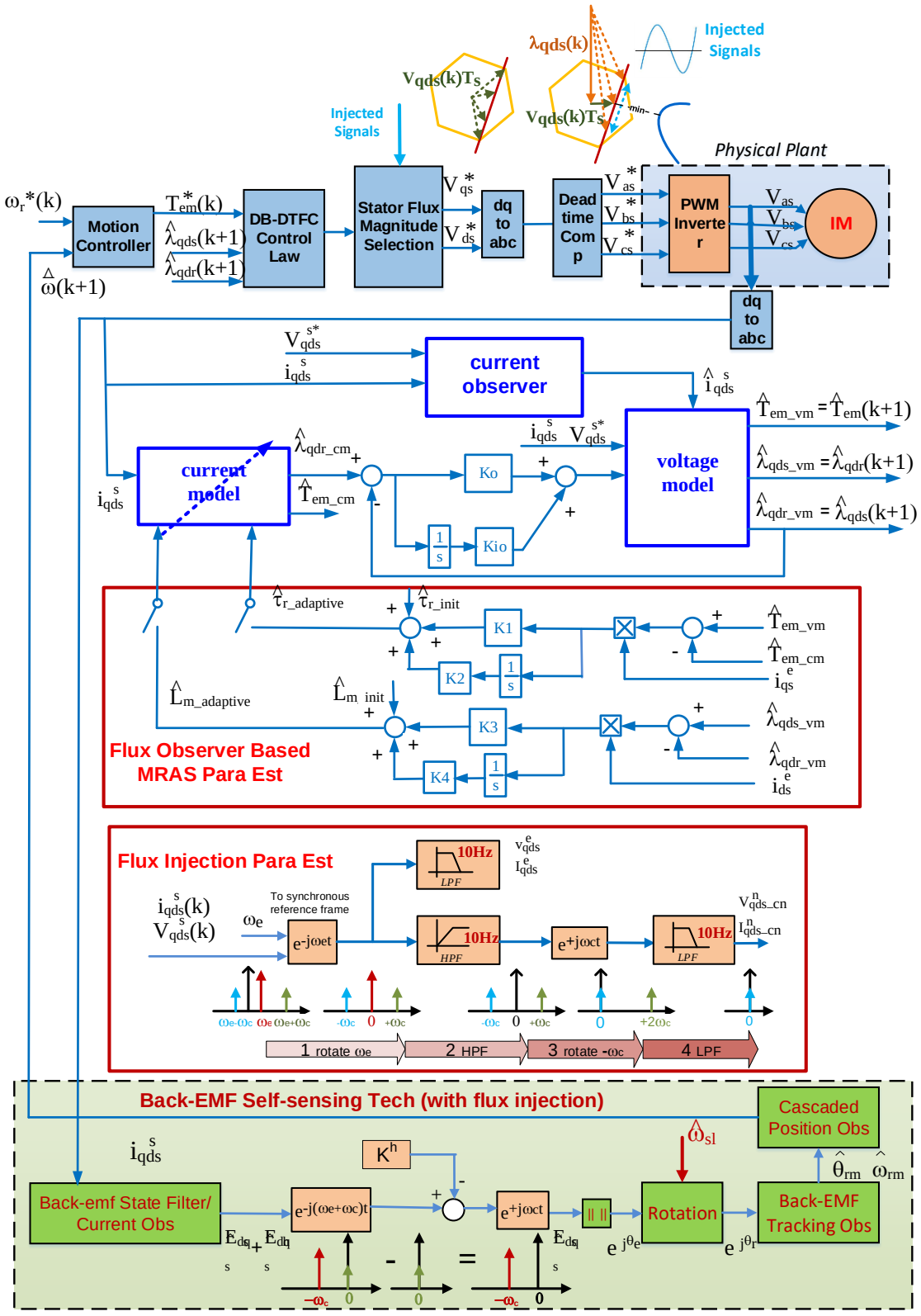

Fig. 7.1-1 Parameter Estimation System for IM DB-DTFC Self-Sensing Drives

7.2 Operating Region-Based Real-Time Parameter Estimation System in Back-EMF Self-Sensing Mode

In back-EMF self-sensing mode, the MRAS-based method cannot work at a speed lower than 0.05 pu, which is limited by self-sensing performance; the flux injection-based method cannot work at the speed lower than 0.2 pu speed, which is limited by the flux injection decoupling performance with self-sensing speed control.

Based on the properties of each method, an operating region-based real-time parameter estimation system in the self-sensing mode can be developed, shown in Fig. 7.2-1.

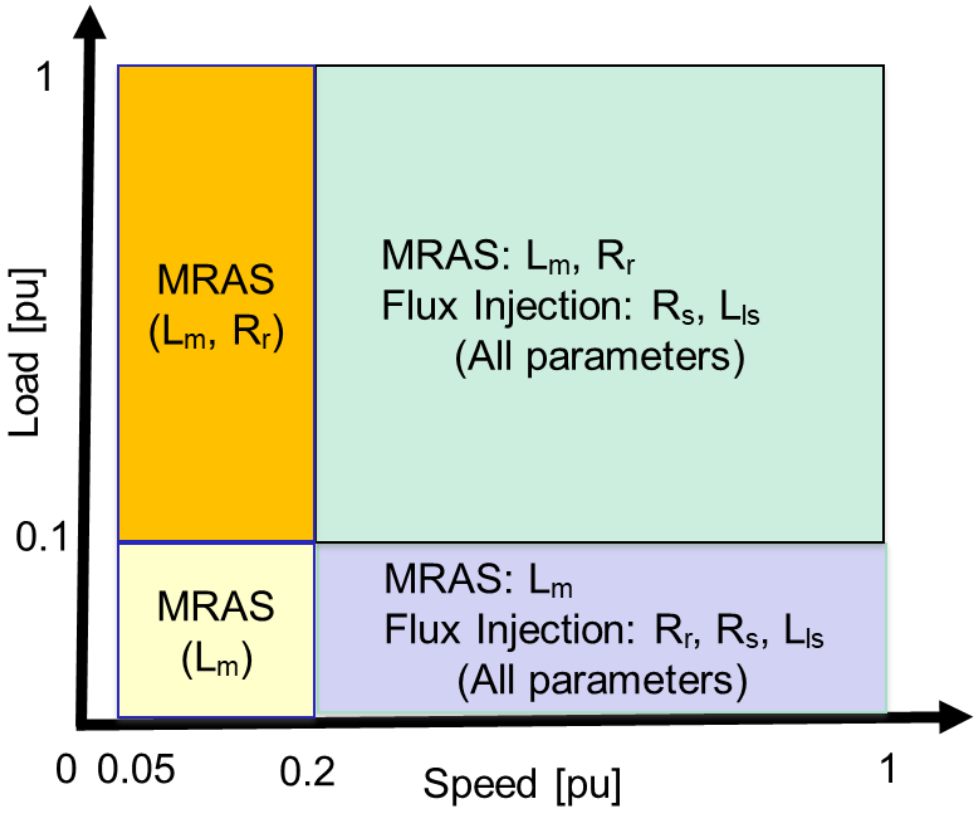

Fig. 7.2-1 Operating region-based real-time parameter estimation system

In Fig. 7.2-1, the lowest operating speed for the real-time parameter system is 0.05 pu. Within the speed range 0.05 pu to 0.2 pu, only the MRAS-based parameter estimation method is enabled, while higher than 0.2 pu speed the flux injection method provides reliable estimates in the self-sensing mode. The MRAS-based method cannot estimate the rotor resistance with light/no load, within the 0.05 pu to 0.2 pu speed and 0 to 0.1 pu load region, the parameter estimation system can only estimate the magnetizing inductance, shown in the yellow block in Fig. 7.2-1. Within the same speed range, as the load increases, the system can estimate both magnetizing inductance and rotor resistance, shown in the orange block. If the operating speed is larger than 0.2 pu, both the MRAS-based method and flux injection-based method are enabled and so the full set of machine parameters can be estimated when the speed over 0.2 pu, there are also two regions divided by load condition, shown in the purple and green blocks. In the purple region, only the magnetizing inductance is estimated by the MRAS-based method and all other parameters are estimated by flux injection-based method. Otherwise, in the green block region, both the magnetizing inductance and rotor resistance are estimated by the MRAS-based method.

The real-time parameter estimation system is executed in controllers using the processing sequence, shown in Fig. 7.2-2.

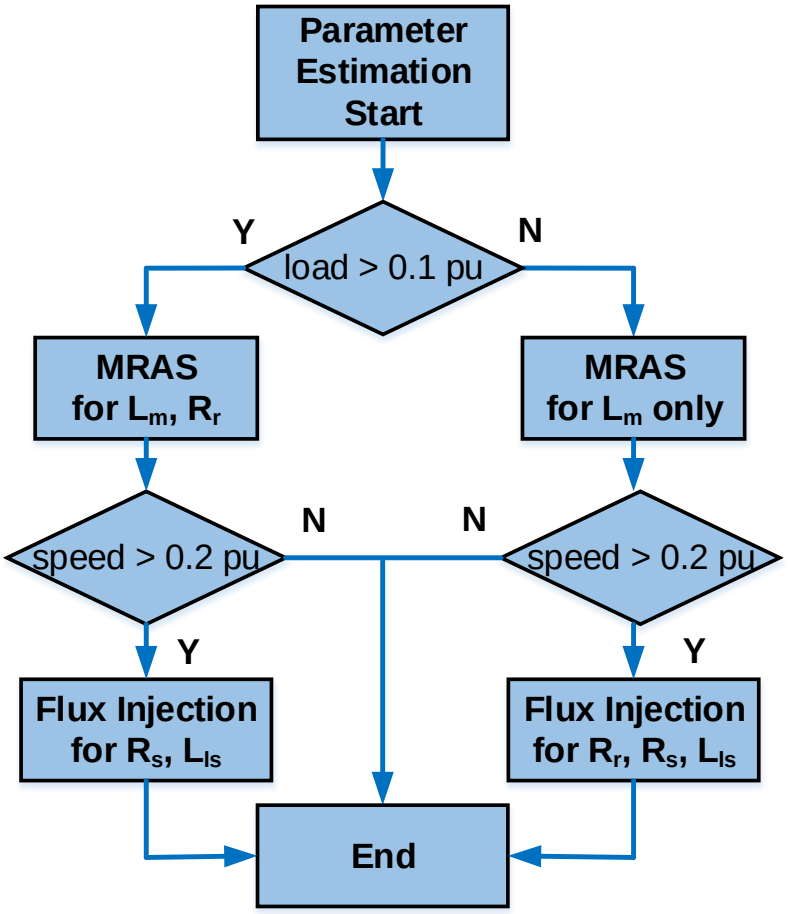

Fig. 7.2-2 Real-time parameter estimation system processing sequence

From the Fig. 7.2-2, it shows the system will determine whether to estimate the Rr by the load condition. If the load is larger than 0.1 pu, the MRAS-based parameter estimation method will estimate both magnetizing inductance and rotor resistance. Otherwise, the MRAS-based method will estimate only magnetizing inductance. Then, the system will determine the speed condition. If the speed is larger than 0.2 pu, the flux injection-based parameter estimation method will be enabled to estimate the rest of the machine's parameters. Otherwise, the parameter estimation system will be disabled.

7.3 Experimental Results in Self-Sensing Mode

The real-time parameter estimation system and the DSP execute sequence have been discussed in section 7.2. This section mainly describes the performance of the proposed real-time parameter estimation system. First, the system estimation performance is shown with the nameplate parameters at different test conditions using back-EMF tracking for self-sensing. Then, the system estimation performance is evaluated with the initial errors based on the tuned values.

7.3.1 The Estimation Performance with Nameplate Values

In this section, the machine is operating at different speed and different load conditions with the nameplate parameter values in the self-sensing mode. Then, the parameter estimation system is enabled to estimate the machine parameters at each test condition. The parameters of the selected induction machine are nameplate values, shown in Table 2.1-1.

The experimental results of the proposed real-time parameter estimation system performance at different speed and load conditions with the initial machine nameplate values in the self-sensing mode are shown in Fig. 7.3-1. The blue lines are the estimates at 0.1 pu speed, the orange lines show the estimates at 0.5 pu speed and the yellow lines shows the estimated at 1.0 pu speed.

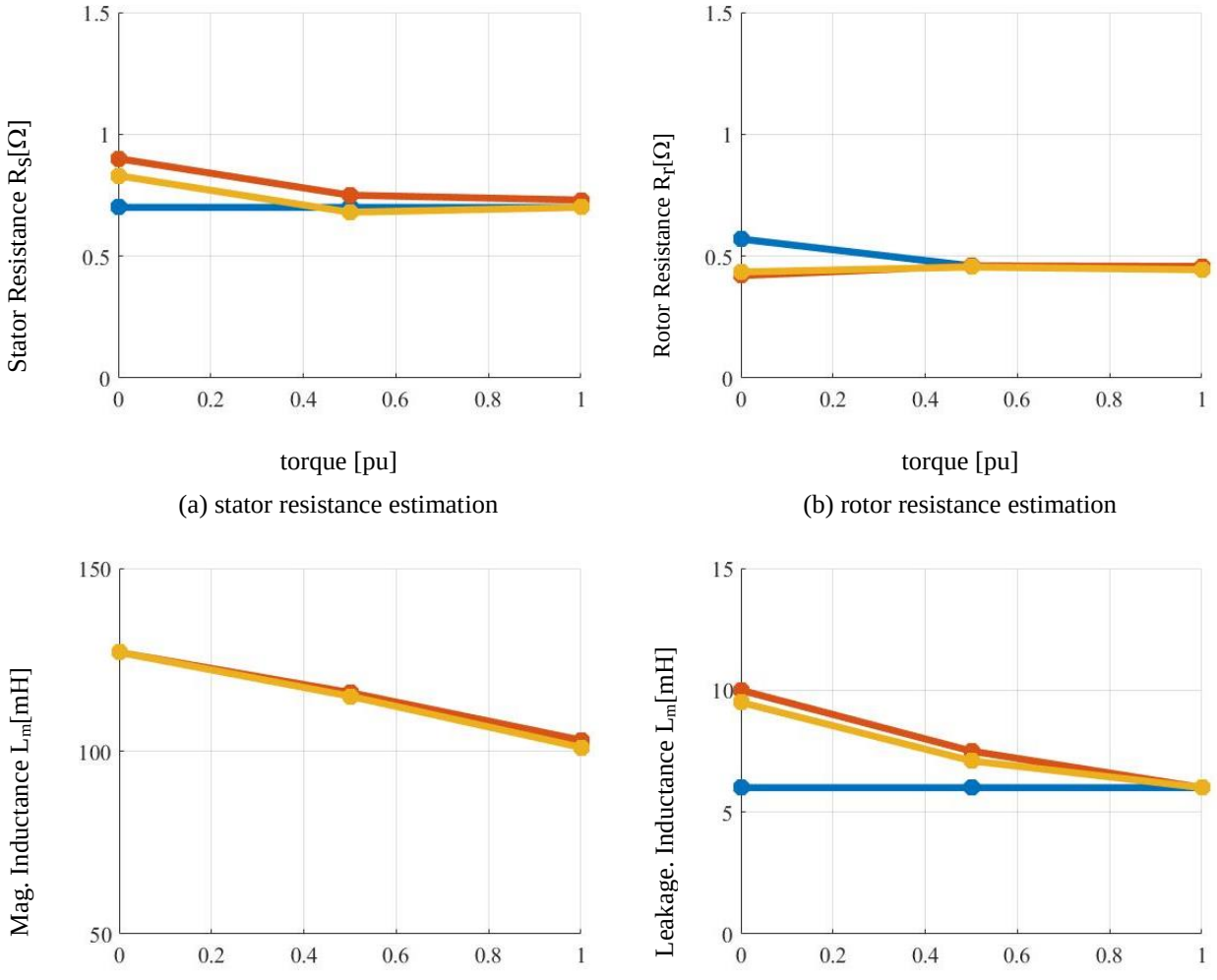

DB-DTFC with B-EMF self-sensing

Motion controller f_s = 1 kHz EVs: 20 Hz 2 Hz 0.4 Hz

Back-EMF state filter f_s = 10 kHz EVs: 200 Hz 40 Hz

Back-EMF based motion observer f_s = 1 kHz EVs: 20 Hz 2 Hz 0.4 Hz

Fig. 7.3-1 Real-time parameter estimation system performance at different speed and load conditions with the initial machine nameplate values in the self-sensing mode

In Fig. 7.3-1-(c), magnetizing inductance estimates are reduced at different load levels due to saturation. However, the estimated magnetizing inductance is not affected by variable

speeds as the three lines in Fig. 7.3-1-(c) are overlaid together. The blue line at zero load in Fig. 7.3-1-(a), (b) and (d) shows more errors than it is in Fig. 7.3-1-(c), since at 0.1 pu speed and no load condition, the stator resistance, rotor resistance and leakage inductance cannot be estimated. Thus, the estimated values of stator resistance, rotor resistance, and leakage inductance at 0.1 pu speed no-load condition are the same as the nameplate values. Since the flux injection method is not enable at 0.1 pu speed, the stator flux and the leakage inductance are kept the same as the nameplate values at different load conditions. This is the reason why the blue line in Fig. 7.3-1-(a) and (d) is kept flat.

The orange line and yellow line in Fig. 7.3-1-(d) shows that the saturation effect on leakage inductance is significant due to the different load levels. However, leakage inductance is not affected by variable speeds.

The experimental results in Fig. 7.3-1-(a) and (b) shows the estimated stator resistance and rotor resistance do not vary much, and are not affected by different load conditions.

7.3.2 The Estimation Performance with Initial Error Based on Tuned Values

In real cases, the machine parameters change as the machine operating conditions change. This section discusses the proposed system estimation performance with over tuned and detuned parameters. The objective of this test is to verify whether the proposed real-time parameter estimation system can provide reliable estimates with a different set of initial parameter errors. The testing conditions are divided into five groups, which are shown in

Table 7.3-1. Each group contains nine tests, covering 0.1 pu to 1.0 pu speed range and 0.0 pu to 1.0 pu load range.

Table 7.3-1 The initial values of parameter estimation system performance verification

Group No.	1	2	3	4	5
	Well-tuned	Resistance over-tuned	Resistance detuned	Inductance over-tuned	Inductance de-tuned
R_s	100%	120%	80%	100%	100%
R_r	100%	120%	80%	100%	100%
L_m	100%	100%	100%	120%	80%
L_{ls}	100%	100%	100%	120%	80%
L_{lr}	100%	100%	100%	120%	80%

Fig. 7.3-2 and Fig. 7.3-3 shows the experimental results of the proposed real-time parameter estimation system performance with initial parameter errors at different speed and load conditions in self-sensing mode. At 0.1 pu speed, the stator resistance and leakage inductance estimation are not available. At 0.1 pu speed and zero load condition, the rotor resistance cannot be estimated as well. With over-tuned and detuned initial machine parameters, the parameter estimation system estimates, shown in orange lines and yellow lines in Fig. 7.3-2 and Fig. 7.3-3, are consistent with the well-tuned parameter values, shown in blue lines at different speed and load conditions.

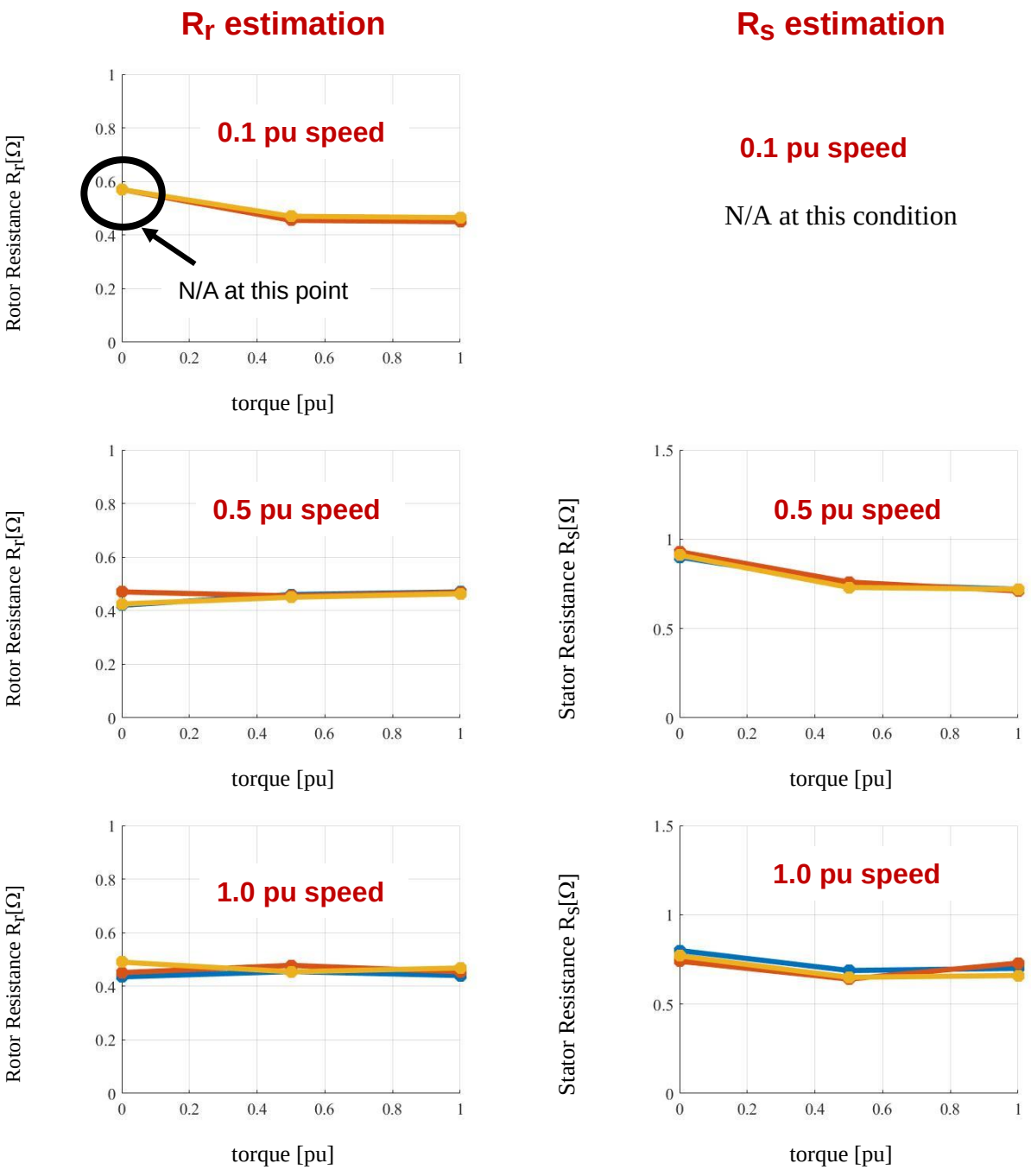

DB-DTFC with B-EMF self-sensing

Motion controller f_s = 1 kHz EVs: 20 Hz 2 Hz 0.4 Hz

Back-EMF based motion observer f_s = 1 kHz EVs: 20 Hz 2 Hz 0.4 Hz

Fig. 7.3-2 Real-time parameter estimation system performance for rotor resistance and stator resistance estimation with initial errors in the self-sensing mode

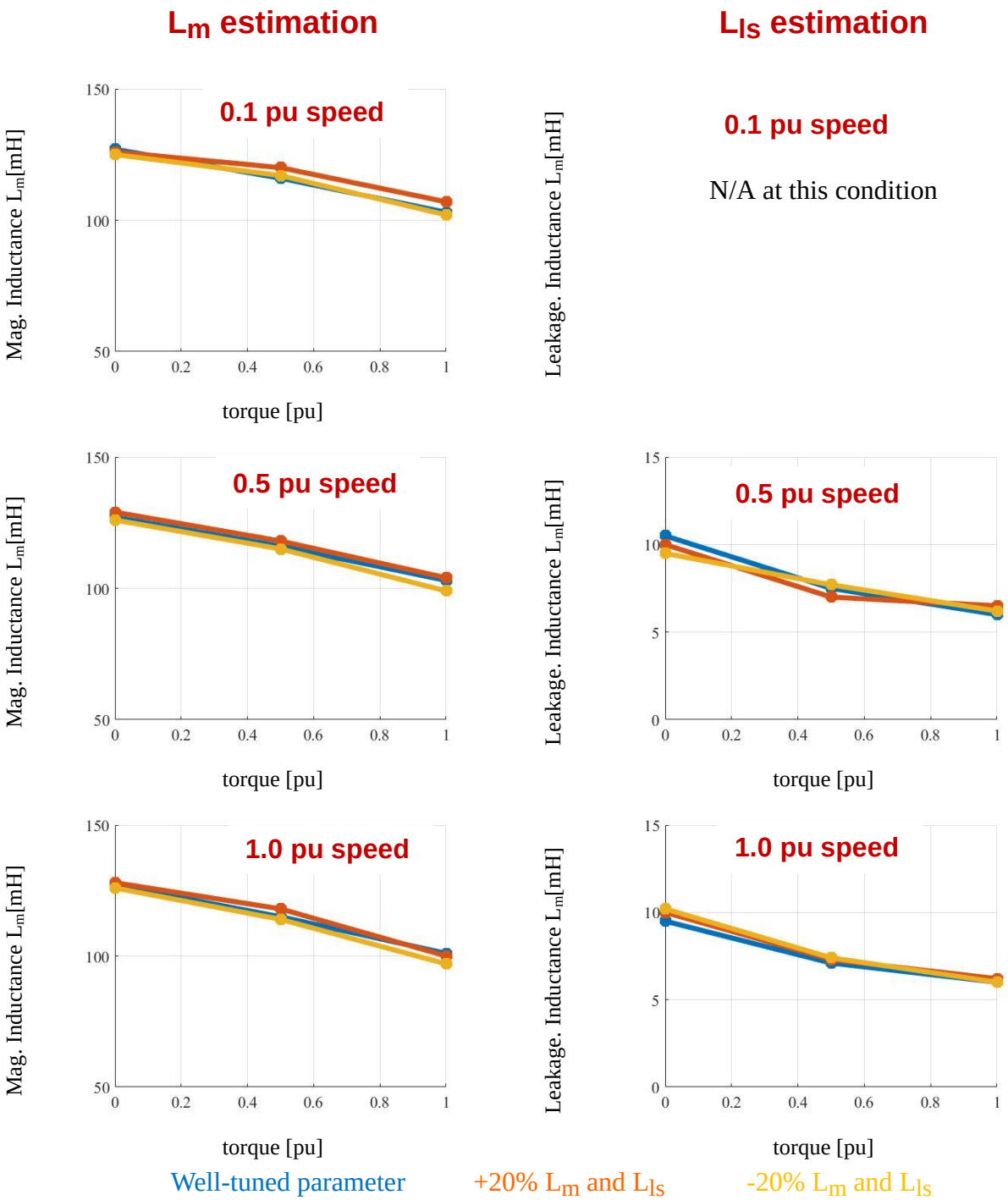

DB-DTFC with B-EMF self-sensing

Motion controller f_s = 1 kHz EVs: 20 Hz 2 Hz 0.4 Hz

Back-EMF based motion observer f_s = 1 kHz EVs: 20 Hz 2 Hz 0.4 Hz

Fig. 7.3-3 Real-time parameter estimation system performance for magnetizing inductance and leakage inductance estimation with initial errors in the self-sensing mode

The rotor resistance and stator resistance in Fig. 7.3-2 are independent on torque and speed conditions. The magnetizing inductance and leakage inductance in Fig. 7.3-3 decreases as the load increases, due to machine saturation.

7.4 Speed Ripple and Torque Ripple in Self-Sensing Mode

This section describes the speed ripple and torque ripple with the two real-time parameter estimation methods in self-sensing mode.

7.4.1 The Speed Ripple in Self-Sensing Mode

Fig. 7.4-1 shows the experimental results of speed ripple of the two methods at different loads with correct machine parameters. Fig. 7.4-1-(a) shows the speed ripple of the flux injection method and Fig. 7.4-1-(b) shows the speed ripple of the MRAS method. The flux injection method only works at medium and high speed. The speed ripple of the flux injection method is a little higher than it is using the MRAS method. The speed ripple of MRAS at 0.1 pu speed is higher than it is at medium and high speed due to the signal-to-noise ratio increasing at low speeds.

At the same speeds, the speed ripple of flux injection method shown in Fig. 7.4-1-(b)is relatively higher than it is using the MRAS method shown in Fig. 7.4-1-(b).

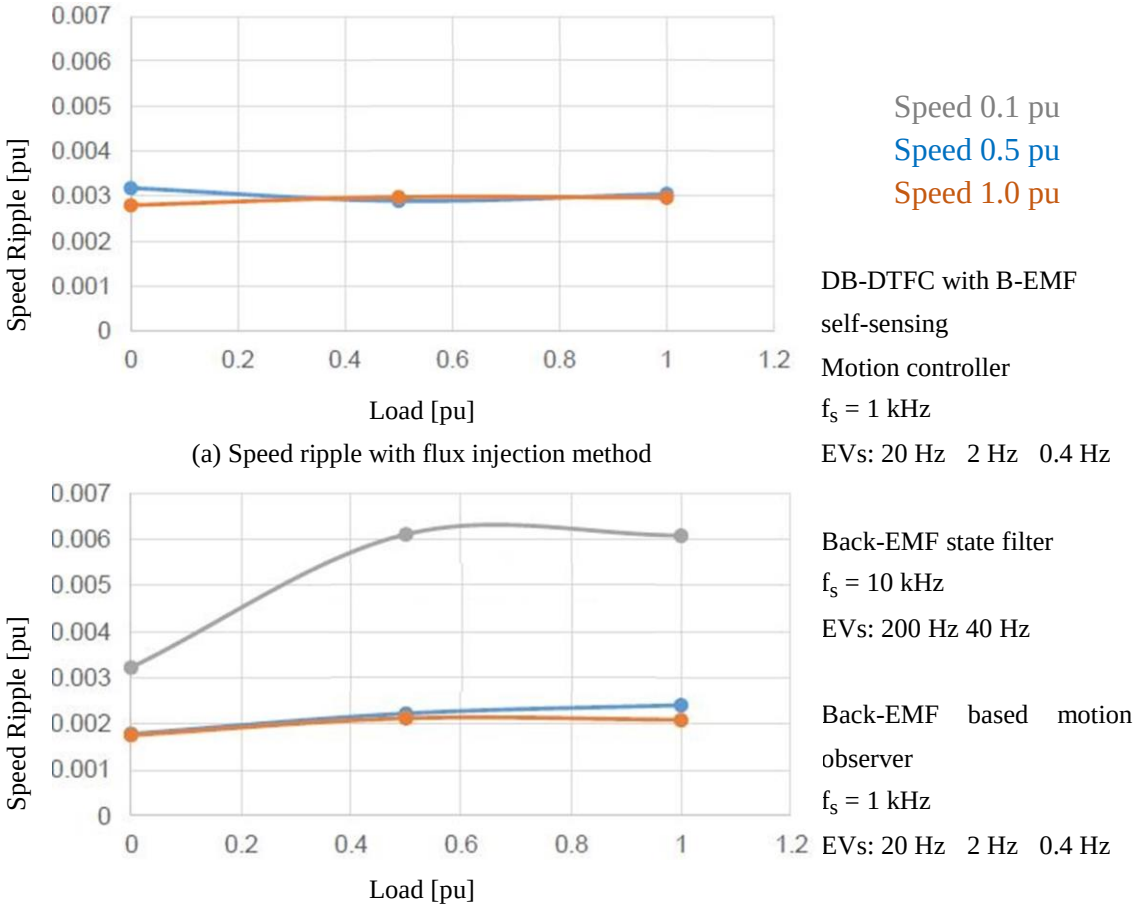

(a) Speed ripple with flux injection method

(b) Speed ripple with MRAS method

Fig. 7.4-1 Experimental results of speed ripple of the two methods at different loads with correct machine parameters

7.4.2 The Torque Ripple in Self-Sensing Mode

Fig. 7.4-2 shows the experimental results of torque ripple of the two methods at different loads with correct machine parameters. Fig. 7.4-2-(a) and (b) also shows the torque ripple at different loads of both flux injection method and MRAS method are higher than they are at medium and low speed due to the load side. DB-DTFC has been demonstrated to achieve the torque command at every instant within the inverter hexagon, so the DB-DTFC algorithm would not induce any torque ripple.

Since the load machine is controlled by traditional IFOC algorithm, which does not have speed dependent cross-coupling decoupling, the machine model's cross-coupling at high speeds is stronger than it is at low speeds. Thus, the torque ripple at high speeds from the current regulator in the load side is higher than the torque ripple at low speeds.

If the IFOC drive in the load side is with cross-coupling decoupling, the torque ripple at full speeds in the orange line of Fig. 7.4-2-(a) will be reduced to the blue line or even lower.

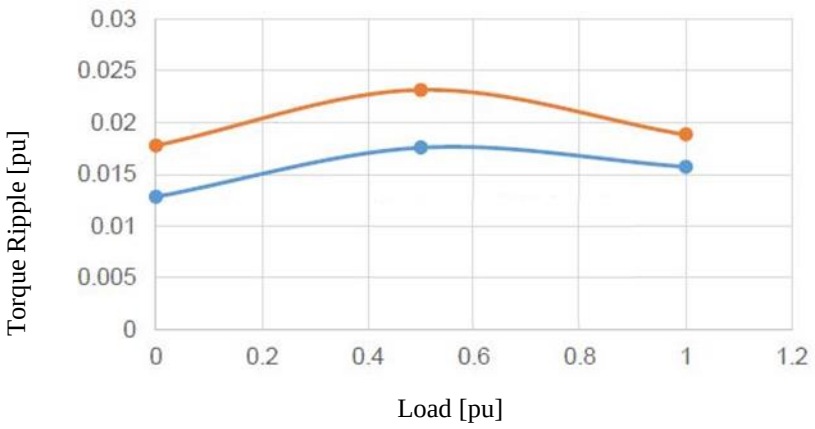

(a) Torque ripple with flux injection method

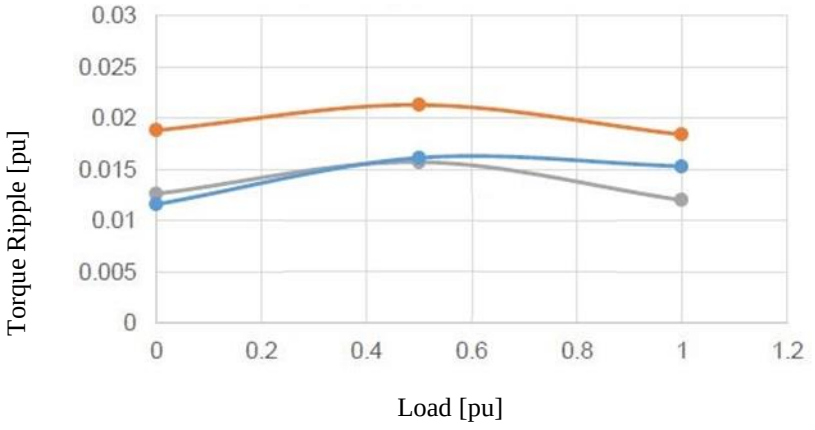

(b) Torque ripple with flux injection method

Speed 0.1 pu
Speed 0.5 pu
Speed 1.0 pu

DB-DTFC with
B-EMF self-sensing
Motion controller
f_s = 1 kHz
EVs: 20 Hz 2 Hz
0.4 Hz

Back-EMF state
filter
f_s = 10 kHz
EVs: 200 Hz 40 Hz

Back-EMF based
motion observer
f_s = 1 kHz
EVs: 20 Hz 2 Hz
0.4 Hz

Fig. 7.4-2 Experimental results of torque ripple of both the MRAS method and flux injection method at different speeds

Fig. 7.4-3 shows the experimental results of the torque ripple of the flux injection method at different loads with incorrect machine parameters. Fig. 7.4-2-(a) and (b) also shows the torque ripple at different loads with incorrect inductance and resistant respectively. The torque ripple at high speed in the orange line and yellow line are higher than the torque ripple at lower speeds in the blue line and gray line. The torque ripple at high speeds is caused by the IFOC algorithm cross-coupling in the load side.

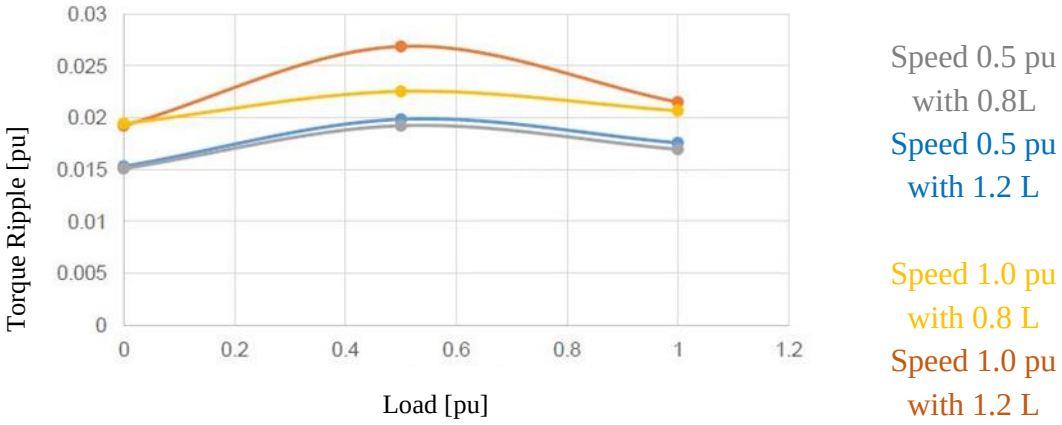

(a) Torque ripple of flux injection method with incorrect inductance

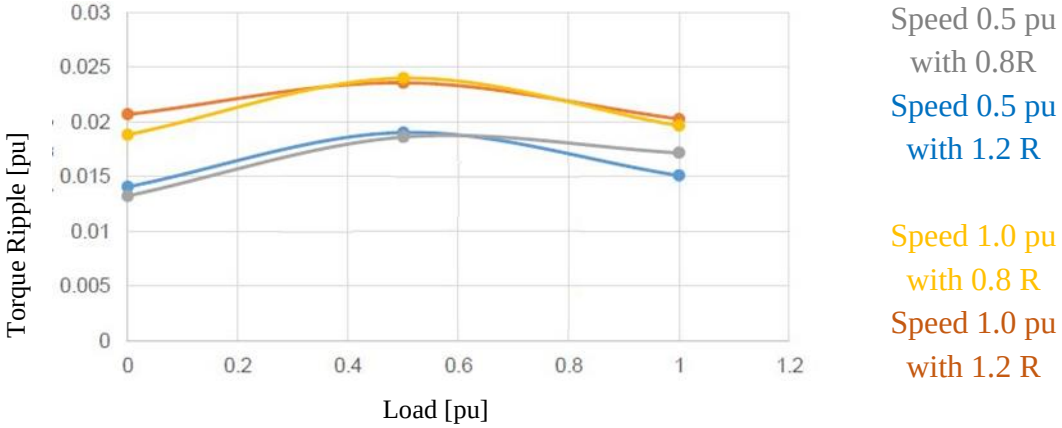

(b) Torque ripple of flux injection method with incorrect resistance

Fig. 7.4-3 Experimental results of torque ripple of both the flux injection method at different speeds with incorrect machine inductance and resistance (R_r and R_s)

7.5 Summary

This chapter explores a real-time parameter estimation system that utilizes advantages of the MRAS-based method and flux injection-based method in the self-sensing mode. The key conclusions are summarized as follows:

- The real-time parameter estimation system contains two methods to estimate the full set of machine parameters over a wide operating range.
- The real-time parameter estimation system cannot estimate all the parameter at low speed conditions, due to the limitation of the self-sensing.
- The real-time parameter estimation system is based on the operating region.
- The real-time parameter estimation system is executed in controllers using an operating point dependent algorithm.
- In the self-sensing mode, the real-time parameter estimation system provides reliable estimates, with various machine initial parameter values.
- The speed ripple of the flux injection method is a little higher than it is using the MRAS method.
- The speed ripple of MRAS at 0.1 pu speed is higher than it is at medium and high speed due to the signal-to-noise ratio increasing at low speeds.

Chapter 8

DB-DTFC Drive Dynamics

As discussed in chapter one, the system with flux observer and the DB-DTFC algorithm has very fast torque dynamics. It is necessary to examine the real torque command tracking bandwidth of DB-DTFC control system. However, there is no torque meter that can measure the torque dynamics at 500 Hz or higher. Thus, in the torque command tracking test, the estimated torque from the flux observer is normally used for comparison which will be presented in section 8.1. There is another way to demonstrate the DB-DTFC by using the measured state rather than the estimated state. The speed varying is the result of the torque change, so speed command tracking is a more straightforward and directly measurable method to evaluate the DB-DTFC dynamic response. The high frequency speed command tracking is a challenge since the signal coherence degrades at high frequency. Section 8.2 presents the methodology to evaluate the speed command tracking at high frequency (up to 500 Hz). In addition, it is essential to explore the physical limitations of high bandwidth speed command tracking testing.

The encoder feedback provides an accurate position and speed feedback, however, in the self-sensing mode, the errors on the estimated position would affect the system speed response and torque response, especially at high frequency. Thus, another topic in this

chapter is to investigate and demonstrate the high frequency speed command tracking of DB-DTFC back-EMF self-sensing drives with the real-time parameter estimation system. The effects of the parameter variations on the high dynamics are also discussed and analyzed in this chapter.

8.1 Torque Command Tracking Comparison

Torque dynamics is one of the most important characteristics of the drive system. Compared to IFOC or other control methods, the primary advantage of DB-DTFC is the fast torque dynamics. The test is conducted by injecting a chirp signal on a torque command in a motion controller, as shown in Fig. 8.1-1.

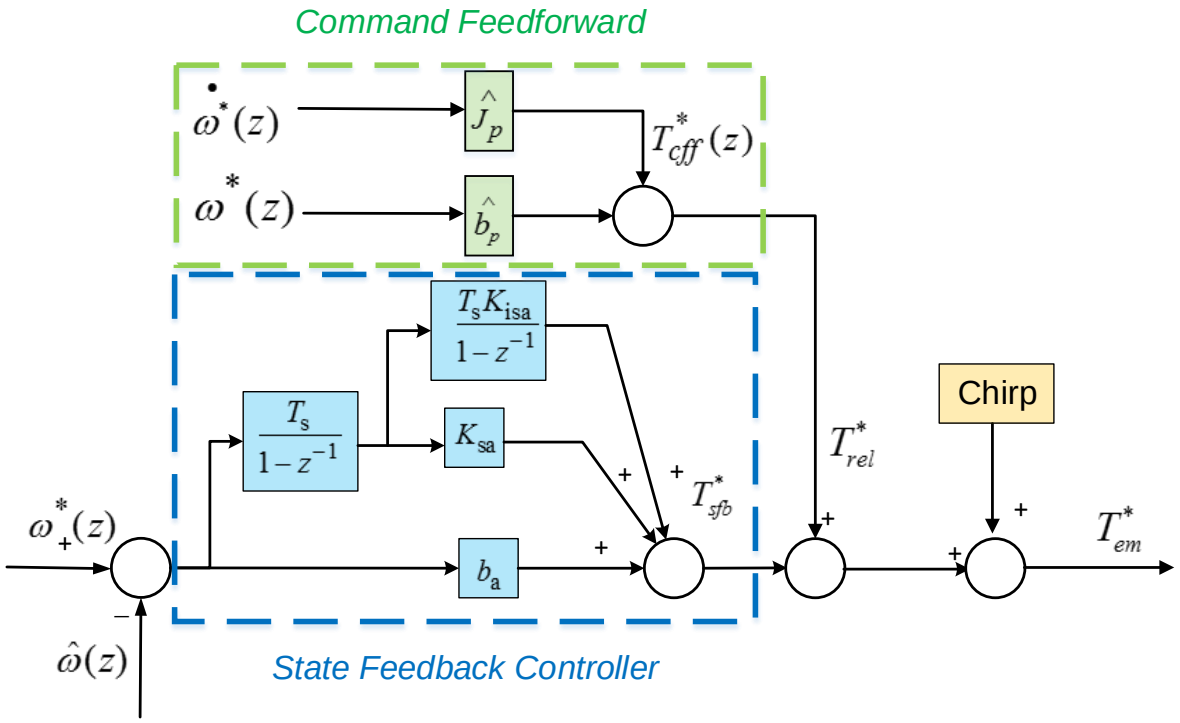

Fig. 8.1-1 Digital state feedback motion controller with velocity, position, and integral position loops

$\hat{T}_{em}$ and T^*_{em} values are collected when the test machine is operating in IFOC and DB-DTFC. By analyzing frequency response, the torque command tracking comparison is shown in Fig. 8.1-2.

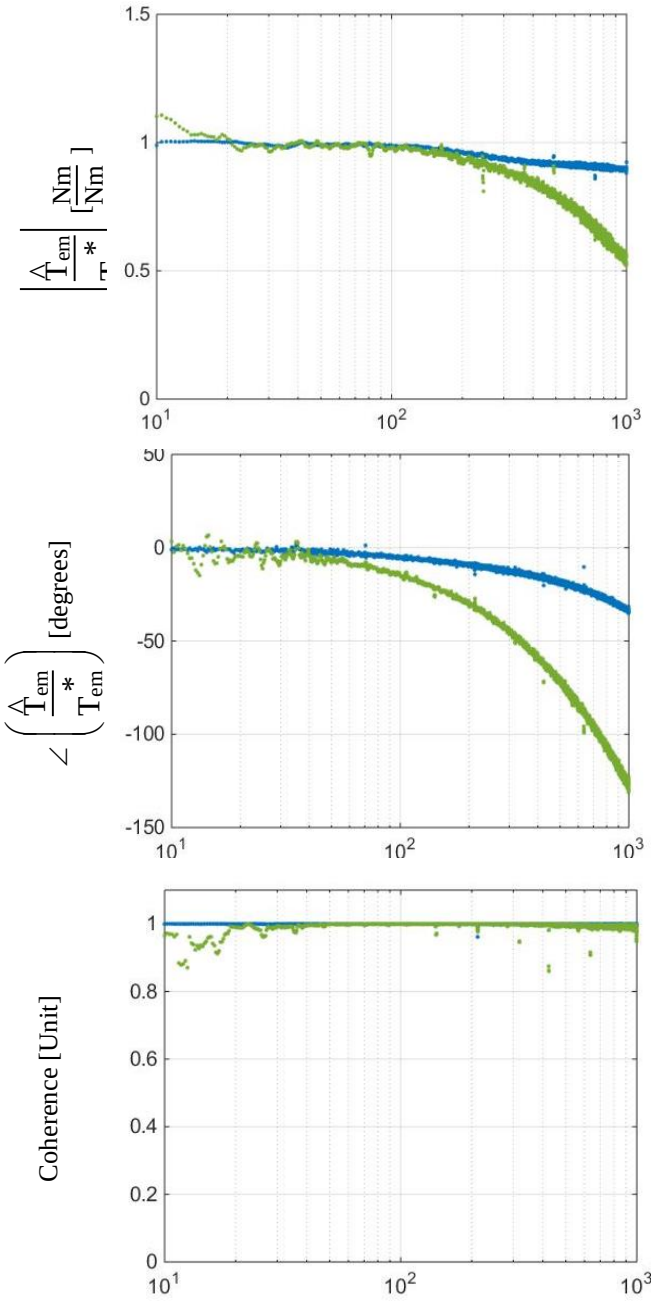

Fig. 8.1-2 Torque response FRF between IFOC and DB-DTFC

In the same test condition, it is clear that the DB-DTFC torque command tracking bandwidth, shown in blue line, can achieve 1kHz, which is much higher than the IFOC

torque command tracking (about 500Hz), depicted in the green line. A re-plot of the phase comparison in the linear scale in Fig. 8.1-3 shows it is obvious that the DB-DTFC has a slightly linear phase lag. At 1kHz, the estimated torque under DB-DTFC control only has 35° degree phase lag; this is shown in blue line. However, it has nearly 130° degree phase lag under IFOC control; this is shown in orange line.

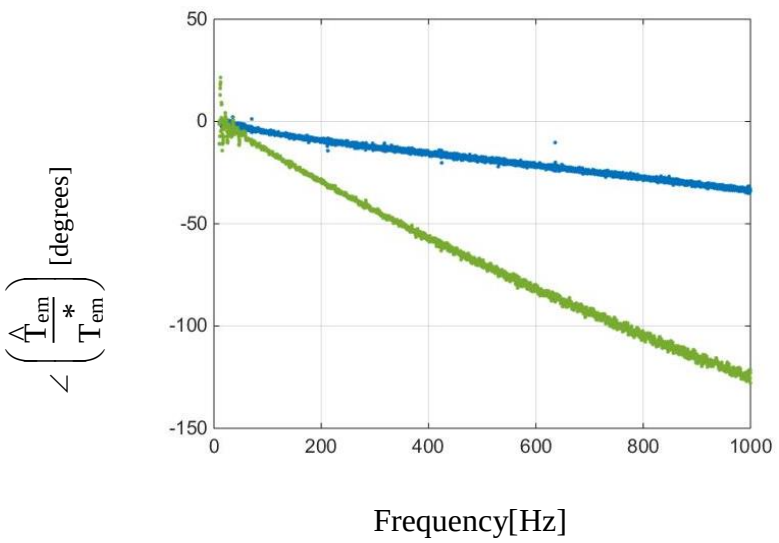

Legend:
DB-DTFC Torque cmd tracking
IFOC Torque cmd tracking
Test conditions：
Speed command: 0.4pu
Motion observer
EVs: 50Hz 5Hz 1Hz
Motion controller
EVs: 50Hz 5Hz 1Hz
FOC with current regulator
EVs: 500Hz 50Hz
Inject a chirp on the speed cmd:
Range: 1-250Hz
Amplitude: 0.75 rad/s
Average: 3

Fig. 8.1-3 Phase lag of torque response FRF between IFOC and DB-DTFC in linear scale

8.2 High Frequency Speed Command Tracking

Speed dynamics is another important characteristic of the drive system. The speed response is the result of the torque response. Since the torque dynamics of DB-DTFC are much faster than that of IFOC, the speed response of DB-DTFC should be faster than that of IFOC as well. The traditional test is conducted by tracking a chirp speed command in a motion controller shown in Fig. 8.2-1.

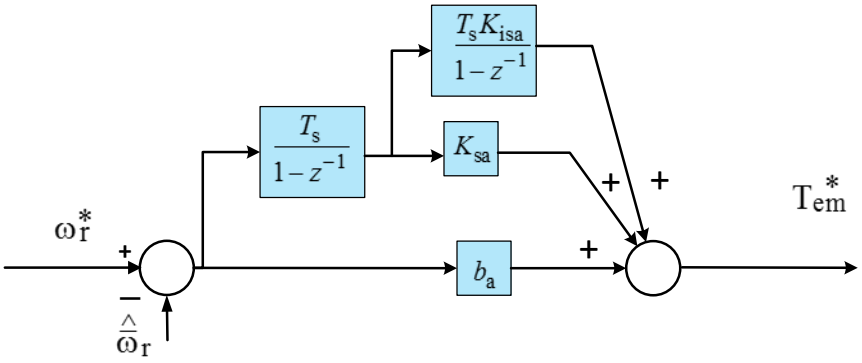

Fig. 8.2-1 Traditional motion controller for speed command tracking evaluation

Values for $\bar{\omega}$ and $\bar{\omega}^*$ are collected when the test machine is operating in DB-DTFC. By conducting frequency response analysis, the speed command tracking comparison is shown in Fig. 8.2-2. The coherence at high frequency degrades significantly. Moreover, the motion controller bandwidth limits the high frequency speed command tracking measurement.

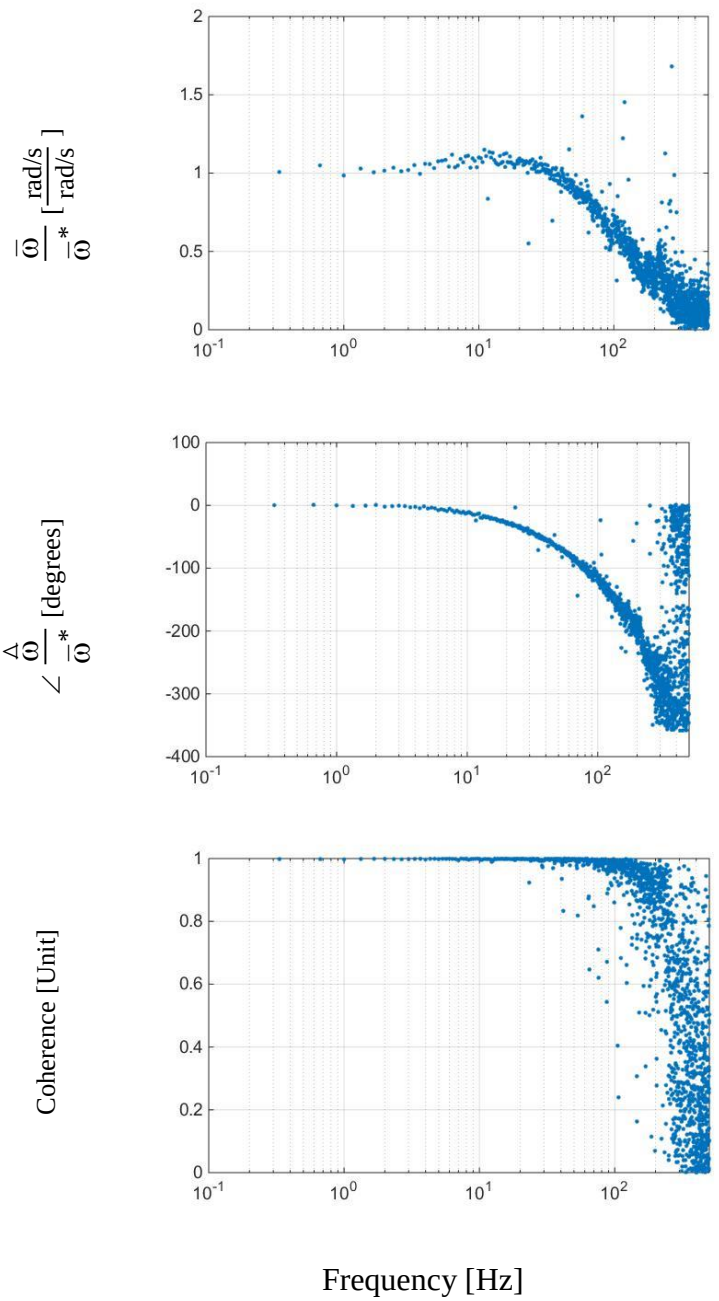

Legend:
DB-DTFC speed cmd tracking

Test conditions：
Speed command: 0.4pu
Motion observer:
f_s = 1 kHz
EVs: 50Hz 5Hz 1Hz
Motion controller:
f_s = 1 kHz
EVs: 50Hz 5Hz 1Hz
FOC with current regulator:
f_s = 10 kHz
EVs: 500Hz 50Hz
The speed cmd:
Range: 1-200Hz
Average: 4
Amplitude: 0.6 rad/s (right)
Offset: 0.4 pu

Fig. 8.2-2 Speed response FRF between IFOC and DB-DTFC

Instead of only using the traditional motion controller, the Fig. 8.2-3 shows the proposed method for high frequency speed command tracking measurement. The single sine wave rather than the chirp signal should be used for improving the coherence at high frequency.

Computed torque command feedforward, T^*_{cff}, is actually a reference for the torque loop. Since the project focuses on the high frequency and the single sine wave is small, the b_p path in the torque command feedforward can be ignored for convenience.

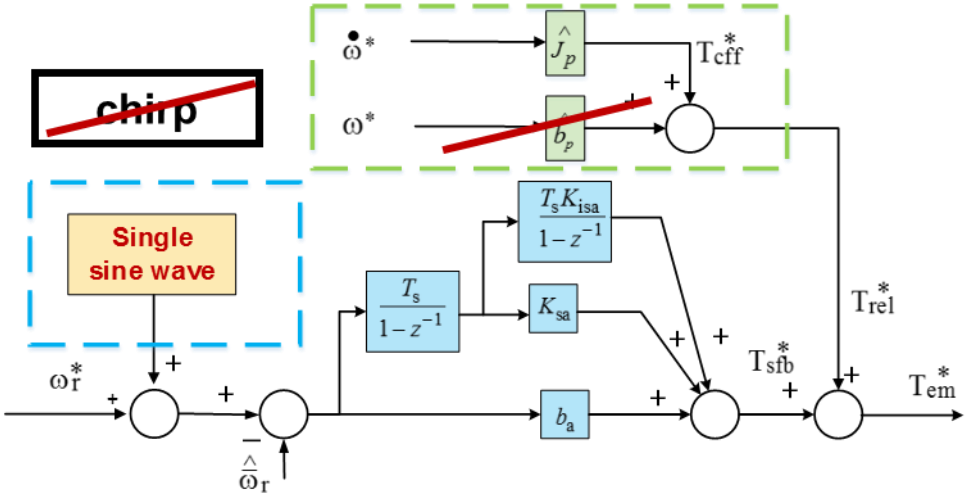

Fig. 8.2-3 Proposed the block diagram of speed command tracking evaluation

The whole block diagram for the high frequency speed command tracking comparison between IFOC and DB-DTFC can be obtained in Fig. 8.2-4. The IFOC current regulator and DB-DTFC torque modulator are sampled in 10 kHz. The motion controller is sampled in 1 kHz. Thus, theoretically the maximum measurable torque command tracking frequency is 5 kHz ($f_{s\_torque}/2$) and the maximum measurable speed command tracking frequency is 500 Hz ($f_{s\_motion}/2$). The anti-aliasing filter is added for removing the anti-aliasing noise and improving the test accuracy.

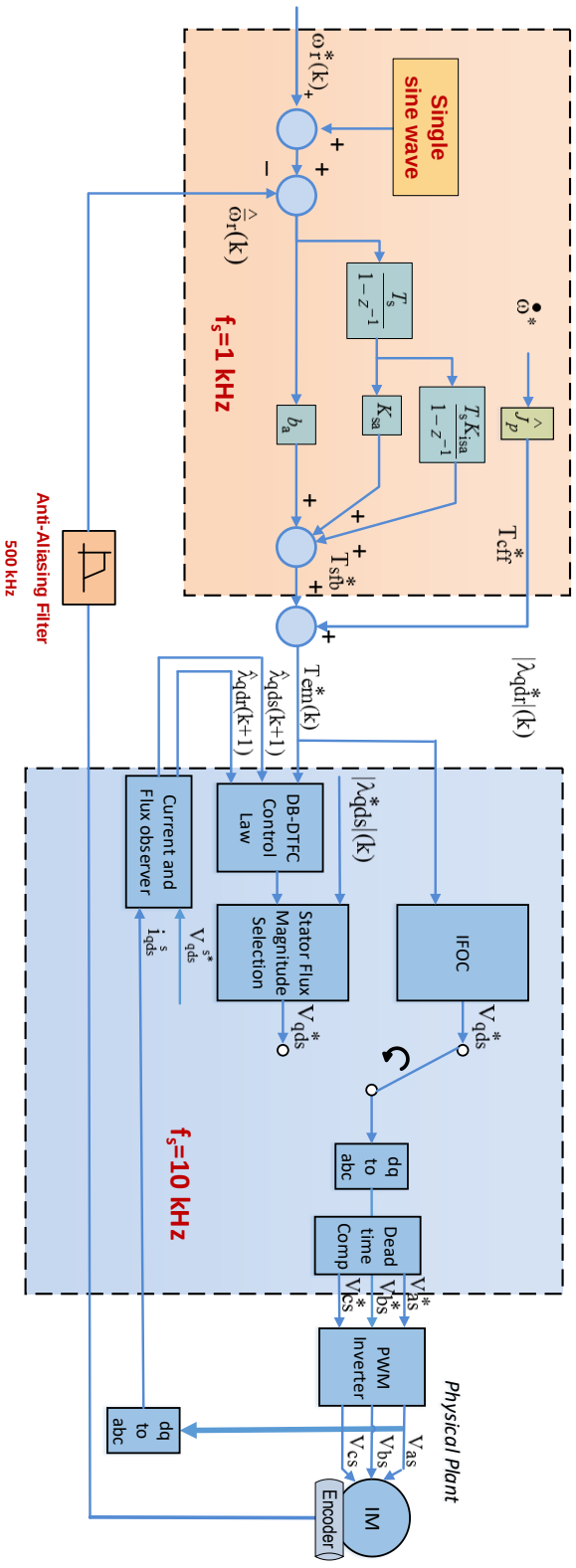

Fig. 8.2-4 Proposed the system block diagram of speed command tracking comparison between IFCO and DB-DTFC

The Fig. 8.2-5 shows speed response FRF comparison between DB-DTFC and IFOC with different current regulator bandwidth. The measured average speed $\bar{\omega}$ from the encoder is used for comparison. T_{cff} cannot be larger than 1 pu, otherwise, the system would reach the voltage limits. To avoid the voltage limits, the single sine wave amplitude is reduced from 0.4 rad/sec to 0.3 rad/s when the sine wave frequency is higher than 300 Hz. The magnitude of DB-DTFC speed command tracking FRF still maintains at one even at 450 Hz, shown in blue dots, which means the DB-DTFC speed loop can achieve 450 Hz with the 1 kHz motion controller sampling frequency. The light red dots, red dots, and dark red dots are operated with 200 Hz, 300 Hz and 400 Hz IFOC current regulator bandwidth respectively. From the plots, the IFOC speed command tracking bandwidth is limited by the current regulator bandwidth. The higher current regulator bandwidth, the higher speed command tracking bandwidth will be. It is obvious that DB-DTFC has much higher speed command tracking bandwidth a smaller phase lag than IFOC.

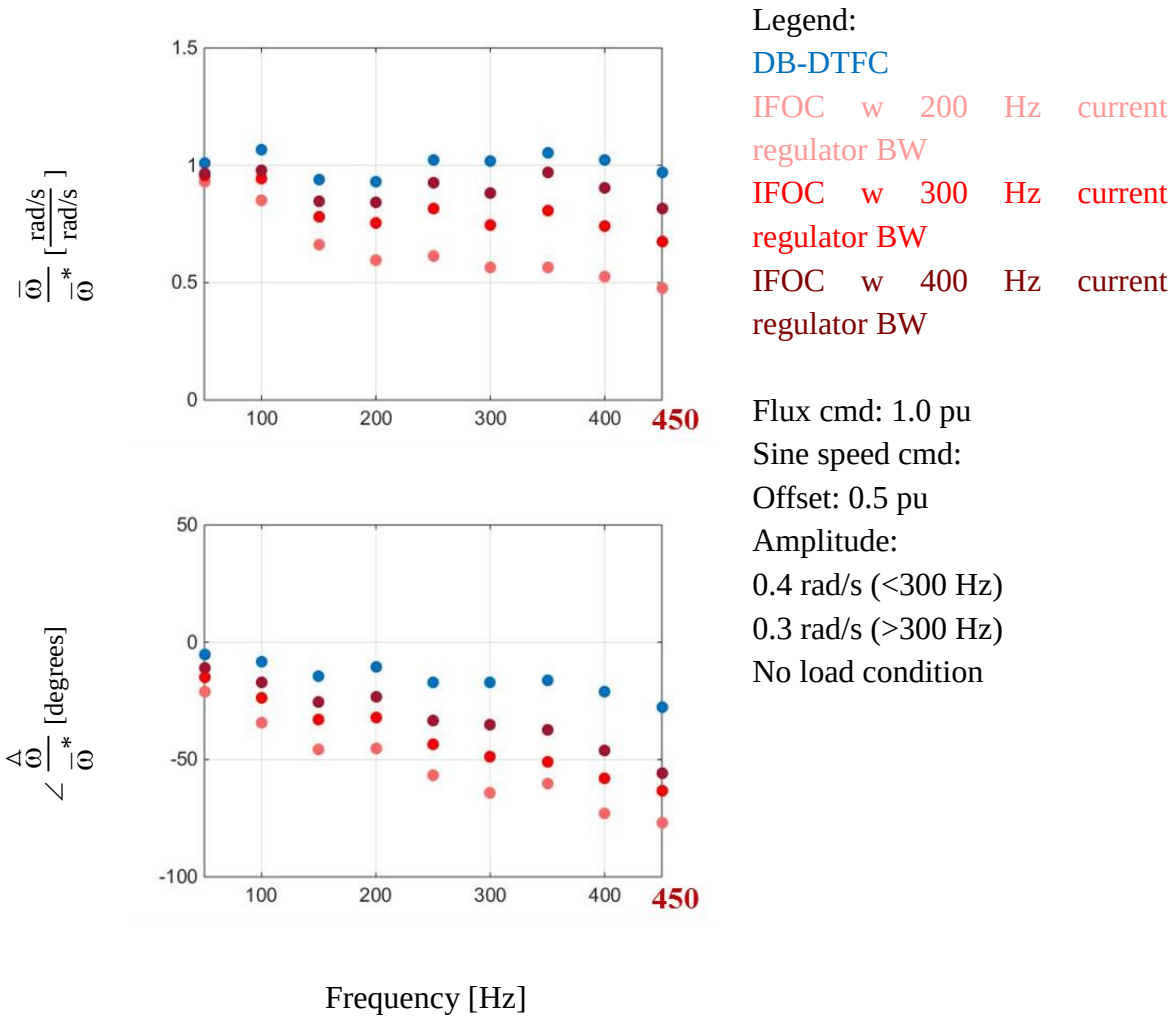

Fig. 8.2-5 Speed response FRF comparison between DB-DTFC and IFOC with different current regulator bandwidth

The Fig. 8.2-6 shows speed response FRF comparison between DB-DTFC and IFOC with de-tuned, well-tuned and over-tuned magnetizing inductance. The IFOC current regulator bandwidth is set to 400 Hz. The light color dots are operated with 0.8 pu L_m and the dark color dots are operated with 1.2 pu L_m. From the Fig. 8.2-6, the light blue dots, blue dots and dark blue dots at each frequency almost overlay together, which demonstrates the DB-DTFC drive speed command tracking bandwidth is insensitive to machine parameter L_m. However, the

light red dots, red dots and dark red dots at each frequency totally separate from each other. It is because the IFOC drive torque production is sensitive to L_m.

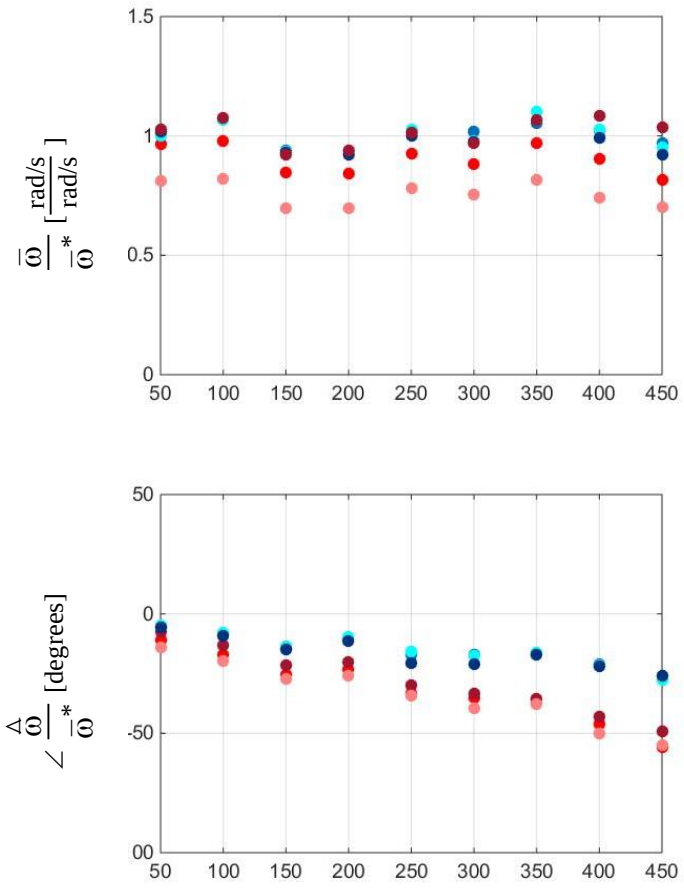

Legend:
DB-DTFC w 0.8 pu L_m
DB-DTFC w 1.0 pu L_m
DB-DTFC w 1.2 pu L_m

IFOC w 0.8 pu L_m
IFOC w 1.0 pu L_m
IFOC w 1.2 pu L_m

IFOC 400 Hz current regulator BW
Flux cmd: 1.0 pu

Sine speed cmd:
Offset: 0.5 pu
Amplitude:
0.4 rad/s (<300 Hz)
0.3 rad/s (>300 Hz)
No load condition

Fig. 8.2-6 Speed response FRF comparison between DB-DTFC and IFOC with de-tuned, well-tuned and over-tuned magnetizing inductance

8.3 Speed Command Tracking in Self-Sensing Mode with the Real-Time Parameter Estimation System

In the self-sensing mode, the encoder position feedback is no longer available. The parameter sensitivity about the torque production and the speed estimation have been discussed in section 3.3. However, the discussion and the experimental results are based on the steady state condition. The objective of this section is to investigate the DB-DTFC back-EMF self-sensing drive speed dynamics difference with and without the real-time parameter estimation system.

Frist, the speed command tracking bandwidth with the nameplate parameter values is evaluated and compared on both DB-DTFC drives and IFOC drives in the self-sensing mode.

Second, based on the over-tuned and detuned nameplate parameters, the speed command tracking bandwidth is evaluated to investigate the parameter sensitivity on system dynamics, especially at high frequency.

Last, the speed command tracking bandwidth improvement with the real-time parameter estimation is evaluated at 0.1 pu, 0.5 pu, and 1.0 pu speed.

8.3.1 The Speed Command Tracking Bandwidth with Nameplate Values in Self-Sensing Mode

The block diagram for speed command tracking comparison between IFOC and DB-DTFC in the back-EMF self-sensing mode can be obtained in Fig. 8.3-1. Since the IFOC

drive needs position information for the coordinate transformation, large error or ripple on the estimated speed would lead to IFOC self-sensing drive unstable. Larger IFOC current regulator bandwidth will lead to larger noise on the voltage commands, thus, the IFOC self-sensing drives will be less stable. In YASKAWA A1000 drives, the current regulator bandwidth is set to 150 Hz in the self-sensing mode. The motion state filter bandwidth is set to 400 Hz.

The amplitude of the sine wave is 0.5 rad/s. The frequency of the sine wave is varying from 50 Hz to 450 Hz. When the machine is operating at a certain speed in DB-DTFC drive or IFOC drive in the self-sensing mode, the single sine wave is added on the top of the constant speed command. The real speed is measured by an encoder for the frequency response analysis.

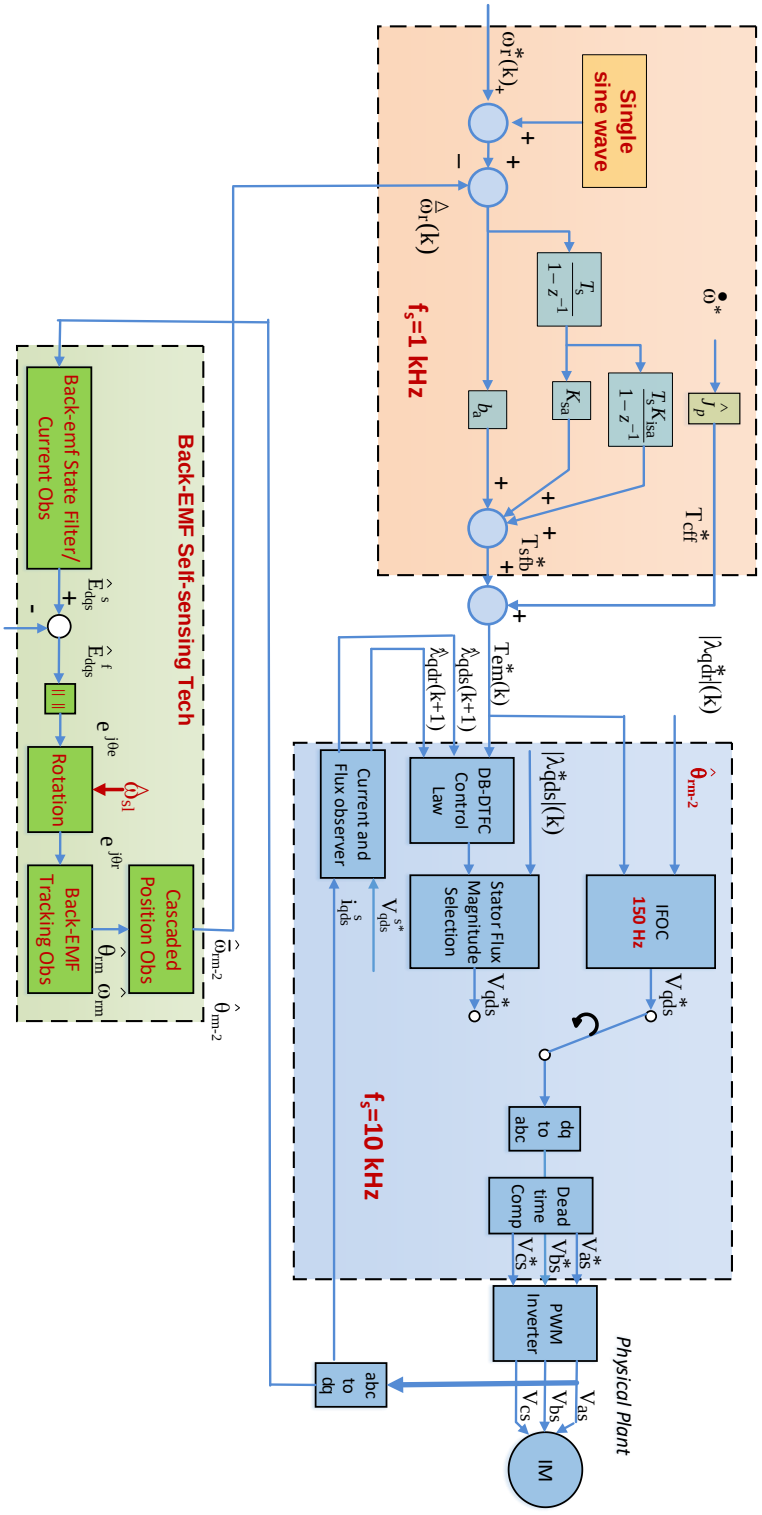

Fig. 8.3-1 Speed command tracking comparison between IFCO and DB-DTFC in back-EMF self-sensing mode

Fig. 8.3-2 shows the speed command tracking bandwidth comparison between DB-DTFC and IFOC with nameplate values in self-sensing mode.

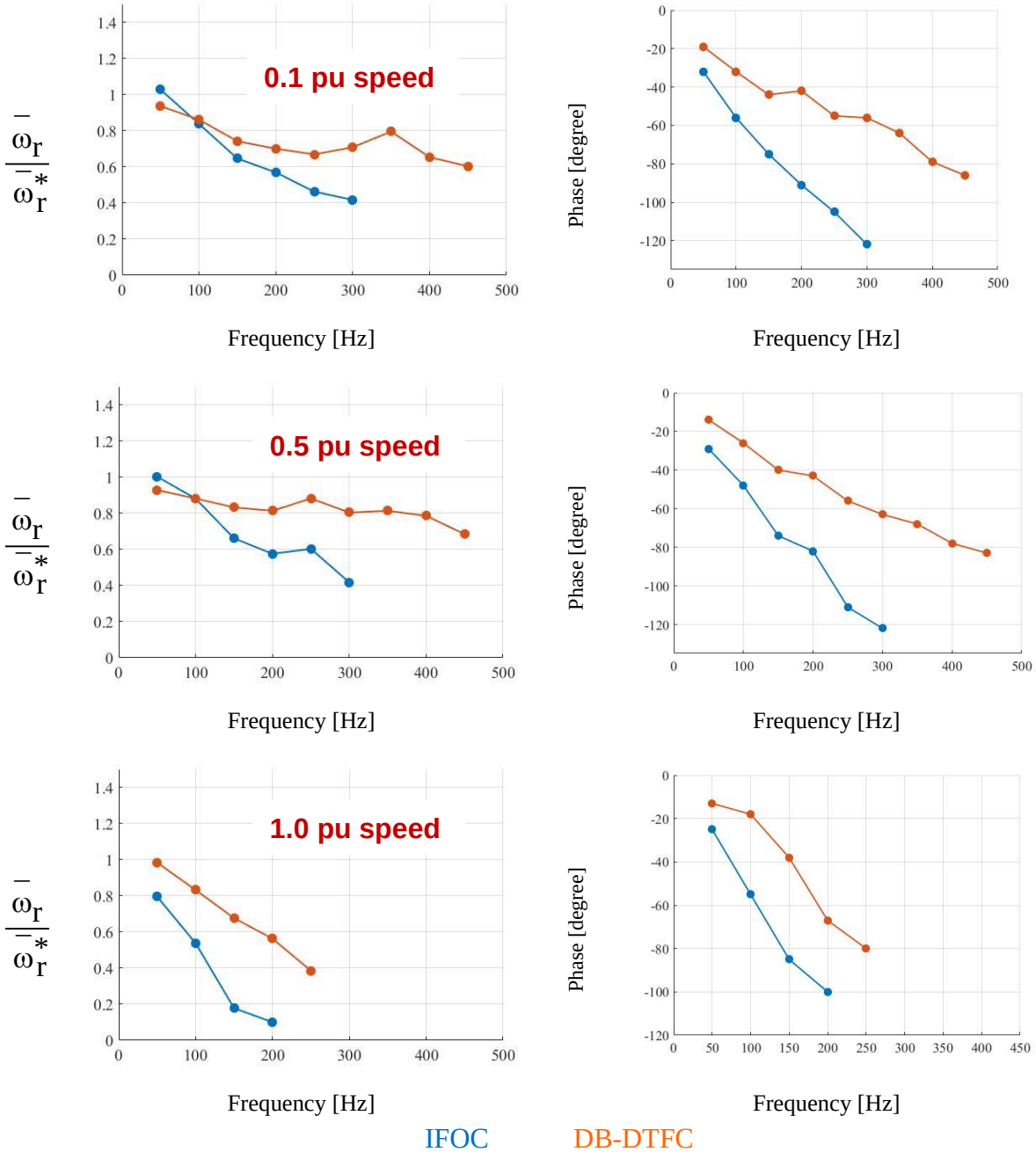

Fig. 8.3-2 The speed command tracking bandwidth comparison between DB-DTFC and IFOC with nameplate values in self-sensing mode

The speed command tracking bandwidth of DB-DTFC drive in the orange line is much higher than it is in IFOC drive in the blue line in Fig. 8.3-2.

At 0.1 pu speed, the speed command tracking bandwidth of DB-DTFC drive is 200 Hz, which is smaller than it is at 0.5 pu speed (435 Hz). It is because that DB-DTFC is sensitive at low speeds due to the flux observer current model dominates the flux estimates. With that been said, the nameplate values are not accurate, since the speed command tracking bandwidth at 0.5 pu speed is higher than it is at 0.1 pu speed.

At 1.0 pu speed, the speed command tracking performance of both DB-DTFC and IFOC performance is degraded, since the voltage limits the measurable speed command tracking bandwidth. To measure higher speed command tracking for DB-DTFC drive, a higher resolution encoder is needed. In this case, a measurable single sine wave with a smaller amplitude can be used, which will require less voltage-second to achieve.

8.3.2 The Speed Command Tracking Bandwidth with Over-tuned and Detuned Nameplate Values in Self-Sensing Mode

Fig. 8.3-3, Fig. 8.3-4 and Fig. 8.3-5 show the speed command tracking bandwidth comparison between with over-tuned, detuned nameplate parameters at 0.1 pu, 0.5 pu and 1.0 pu speed in the self-sensing mode respectively.

The three plots show the synergy, DB-DTFC back-EMF self-sensing drive, is sensitive to machine parameters. The solid yellow line is the performance of DB-DTFC drive with +20% of nameplate values. The solid purple line is the performance of DB-DTFC drive with -20% of nameplate values. The dash orange line is the performance of DB-DTFC drive with the nameplate parameters. The dash blue line is the performance of IFOC drive with nameplate parameters.

0.1 pu speed No load test

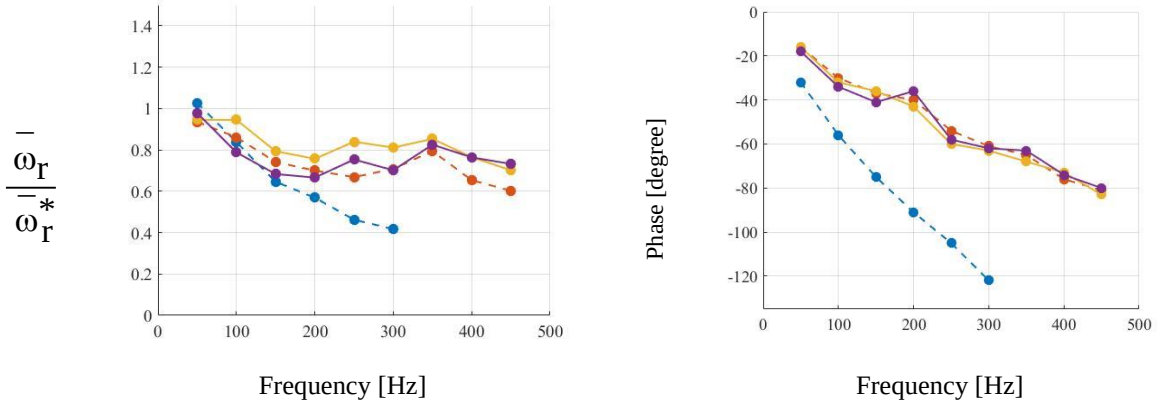

(a) Initial mistuned R_r and R_s

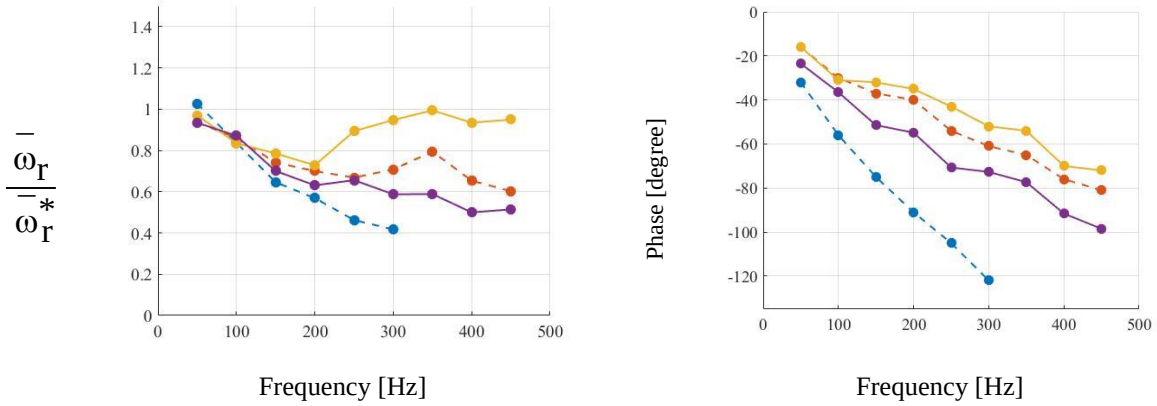

(b) Initial mistuned L_m

--- IFOC with nameplate para. --- DB-DTFC with nameplate para.

—DB-DTFC with 120% nameplate values —DB-DTFC with 80% nameplate values

Fig. 8.3-3 The speed command tracking bandwidth comparison between DB-DTFC and IFOC with initial nameplate parameter errors in self-sensing mode at 0.1 pu speed

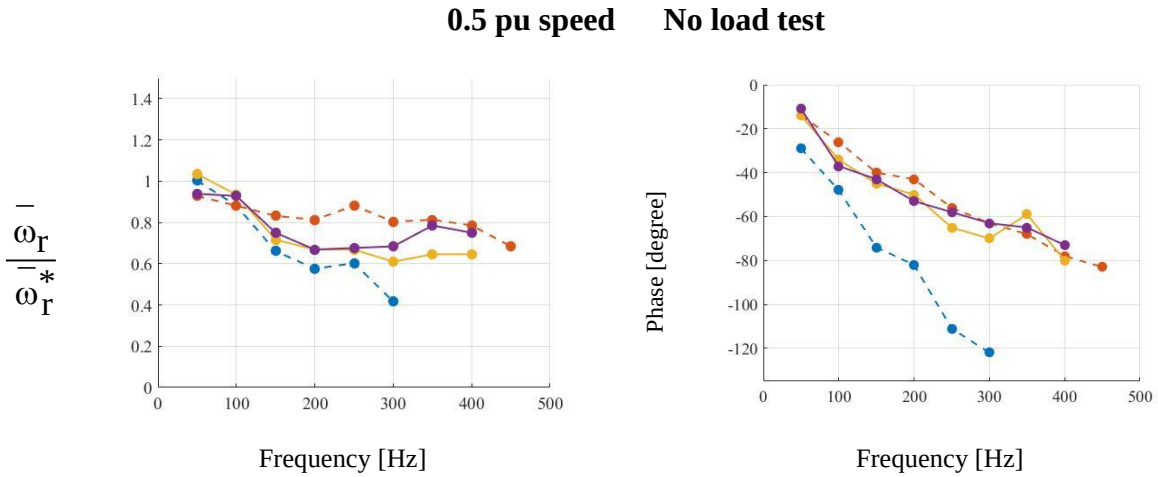

(a) Initial mistuned R_r and R_s

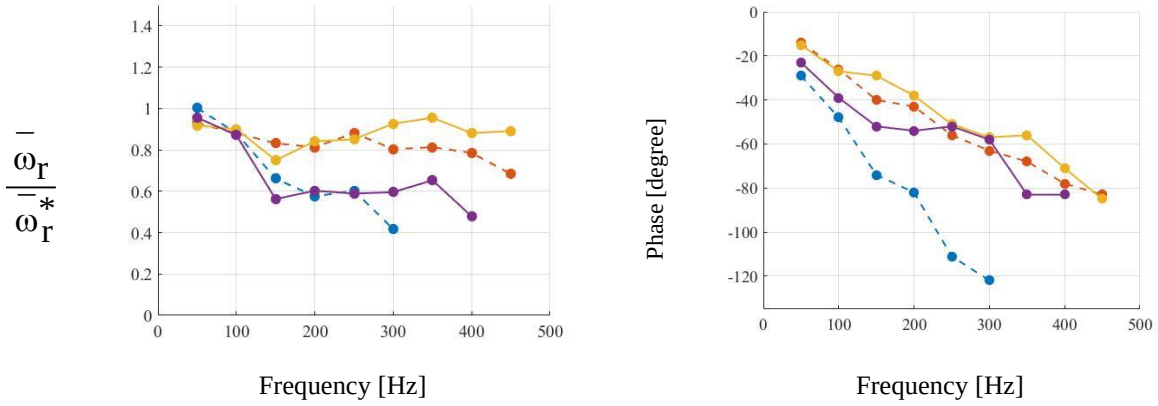

(b) Initial mistuned L_m

--- IFOC with nameplate para. --- DB-DTFC with nameplate para.

—DB-DTFC with 120% nameplate values —DB-DTFC with 80% nameplate values

Fig. 8.3-4 The speed command tracking bandwidth comparison between DB-DTFC and IFOC with nameplate values in self-sensing mode at 0.5 pu speed

Fig. 8.3-3 and Fig. 8.3-4 shows the machine parameter effects the DB-DTFC back-EMF self-sensing drive speed command tracking bandwidth at low and medium speeds. The

difference of the orange line, the yellow line and the purple line in Fig. 8.3-3-(b) and Fig. 8.3-4-(b) is larger than they are in Fig. 8.3-3-(a) and Fig. 8.3-4-(a), which means the system is more sensitive to magnetizing inductance than to resistance.

1.0 pu speed No load test

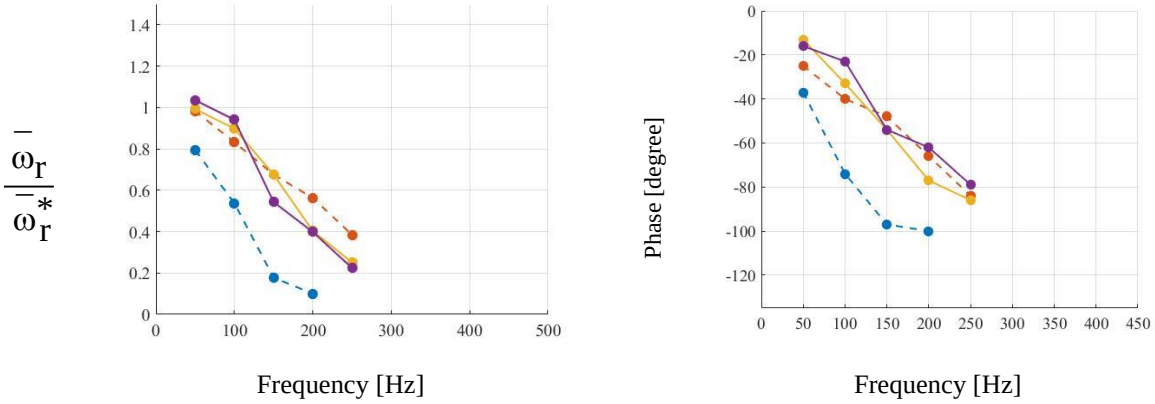

(a) Initial mistuned R_r and R_s

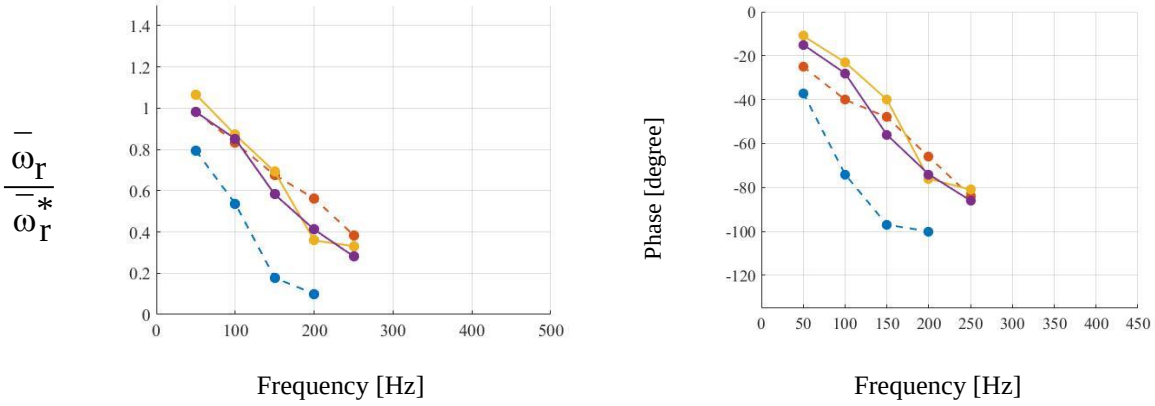

(b) Initial mistuned L_m

--- IFOC with nameplate para. --- DB-DTFC with nameplate para.

—DB-DTFC with 120% nameplate values —DB-DTFC with 80% nameplate values

Fig. 8.3-5 The speed command tracking bandwidth comparison between DB-DTFC and IFOC with nameplate values in self-sensing mode at 1.0 pu speed

At 1.0 pu speed, the speed command tracking performance of DB-DTFC with different parameters are similar to each other, shown in Fig. 8.3-5. The voltage limits the measurable speed command tracking bandwidth at high speed.

8.3.3 The Speed Command Tracking Bandwidth with Parameter Estimation System in Self-Sensing Mode

Fig. 8.3-3 and Fig. 8.3-4 shows the DB-DTFC self-sensing drive is sensitive to machine parameter. Thus, an accurate machine is needed for a high performance DB-DTFC self-sensing drive with high speed command tracking bandwidth.

Fig. 8.3-6 illustrates the speed command tracking bandwidth comparison with and without parameter estimation system in self-sensing mode at different speeds. The yellow line shows the speed command tracking bandwidth with the proposed parameter estimation system. The orange line shows the speed command tracking bandwidth with nameplate parameters. Compared to the performance with the nameplate parameters in orange lines, the yellow lines are closer to zero dB in magnitude plots and have less phase lag in phase plots at different speeds. It is because the proposed parameter estimation system can provide accurate machine parameters and extend the DB-DTFC self-sensing speed command tracking bandwidth.

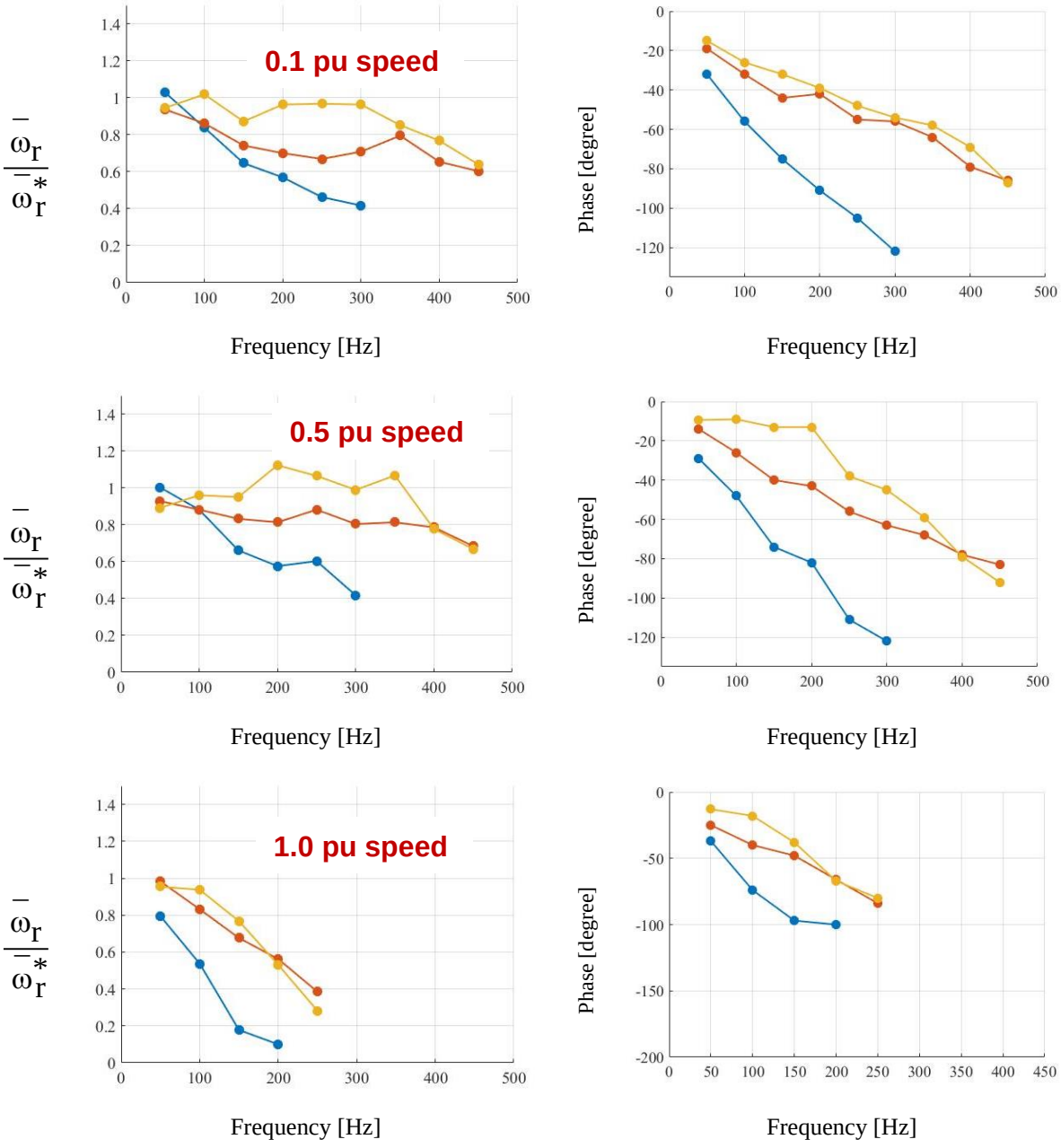

Fig. 8.3-6 The speed command tracking bandwidth comparison with and without parameter estimation system in self-sensing mode at different speeds

8.4 Summary

This chapter explores the torque command tracking and speed command tracking with IFOC and DB-DTFC. Key conclusions are summarized as follows:

- DBDTFC has higher torque command tracking bandwidth and smaller phase lag than IFOC.
- In the torque command tracking phase plot, DB-DTFC has a phase lag that is linear with frequency, and which yields much lower phase lag than IFOC.
- The IFOC current regulator bandwidth is the main limitation for the torque command tracking and speed command tracking.
- Computed torque command feedforward is actually a reference for the torque loop.
- Single since wave should be used for improving the coherence at high frequency and Anti-aliasing filter should be added to improve the accuracy.
- With encoder feedback, DB-DTFC drive has higher speed command tracking bandwidth and smaller phase lag than IFOC. DB-DTFC almost achieves the maximum measurable speed command tracking frequency (500 Hz) with 1 kHz motion controller sampling frequency.
- Machine parameter effects the DB-DTFC back-EMF self-sensing drive speed command tracking bandwidth.

- the DB-DTFC back-EMF self-sensing drive is more sensitive to magnetizing inductance than to resistance.
- In the self-sensing mode with nameplate parameters, the speed command tracking bandwidth of DB-DTFC drive is much higher than it is in IFOC drive.
- In the self-sensing mode, the proposed parameter estimation system can provide accurate machine parameters and extend the DB-DTFC self-sensing speed command tracking bandwidth.

Chapter 9

Conclusions, Contributions and Recommended Future Work

9.1 Conclusions

The following list summarizes the key conclusions of this research project.

9.1.1 Back-EMF Based Self-sensing and System Robustness

- DB-DTFC with back-EMF self-sensing has higher dynamic stiffness, especially at low speeds than the IFOC and back-EMF self-sensing.
- DB-DTFC utilizes speed feedback for the voltage-second command calculation, so the actual position estimation error does not lead to system instability in the motion control loop for DB_DTFC drives.
- Estimated slip frequency, which is sensitive to machine parameters, is needed by the back-EMF tracking observer to estimate rotor speed.
- With encoder feedback, IFOC is sensitive to L_m and R_r over the entire speed range, however, DB-DTFC is sensitive to L_m and R_r only at low speeds.
- At medium and high speed conditions, DB-DTFC has significantly less parameter sensitivity than IFOC.

- At low speeds, both IFOC and DB-DTFC drives are sensitive to L_m and R_r due to their use of the current model for flux estimation.
- In self-sensing mode, the flux observer bandwidth is reduced to allow that the flux observer voltage model dominates at low speeds self-sensing.
- The lower limits of flux observer bandwidth are established by the flux estimation errors resulting from the volt-second errors from the inverter.
- The proposed back-EMF based self-sensing structure induces additional parameter sensitivity to the whole system.
- As the motor speed decreases, the effects of $R_s i_{qds}^s$ to the flux observer voltage model estimation accuracy increases.
- Traditionally, as the motor speed decreases, the bandwidth of the tracking observer is decreased to keep the system stable, which leads to lower system dynamic stiffness.
- The back-EMF state filter bandwidth is a degree-of-freedom for self-sensing system.
- At low speeds, the back-EMF state filter bandwidth can be reduced without causing unacceptable phase distortion for back-EMF self-sensing.
- As speed decreases, the back-EMF state filter bandwidth can be decreased, without sacrificing the closed loop motion control system dynamic stiffness.
- A speed dependent back-EMF state filter bandwidth methodology can improve the self-sensing performance at low speeds.

9.1.2 Real-time Parameter Estimation for Encoder-Based DB-DTFC

- Since the flux observer current model is sensitive to parameters, estimation is necessary to provide more accurate machine parameters to pursue precise torque control for DB-DTFC drives, especially at low speeds.
- Torque ripple for d-axis pulsating voltage injection is significant especially at high speed, due to back-EMF cross-coupling.
- Pulsating flux injection along the DB-DTFC torque line produces no additional torque ripple, even though its current harmonics can be used for parameter estimation.
- Skin effect can affect estimation accuracy, which should be considered in flux injection-based parameter estimation.
- High frequency signal injection is suitable for L_{ls} estimation and low frequency signal injection is suitable for R_s and R_r estimation.
- High frequency signal injection in the synchronous frame makes the leakage inductance reactance dominate the impedance, which can be used for L_{ls} estimation.
- The synchronous frame injected signal frequency should be high enough to be separated from the “zero” fundamental frequency.
- A relatively low injected signal frequency is recommended for R_r and R_s estimation since the leakage inductance reactance is close to R_s within this range.
- Saturation effects on magnetizing inductance and leakage inductance are significant.

- Magnetizing inductance and leakage inductance will not change at different speeds.
- Rotor resistance estimates from injection-based curve fitting methods are consistent with those from MRAS-based parameter estimation.
- By using a Gopinath style flux observer for MRAS-based parameter estimation, both magnetizing inductance and rotor time constant can be estimated.
- In MRAS-based parameter estimation approach, the convergence time is determined by the MRAS controller gains.
- Too large MRAS gains would lead to system damping and instability, and too small MRAS gains would excessively increase convergence time.

9.1.3 Real-time Parameter Estimation with Self-Sensing DB-DTFC

- The estimated slip frequency is used for reference frame rotation in the traditional method, which is sensitive to machine parameters.
- Using the estimated electrical position from the electrical position estimation block is more accurate for the reference frame rotation.
- The injection flux linkage induces an erroneous speed ripple which causes a real speed ripple in self-sensing mode.
- In terms of the high pass filter approach, the system dynamic stiffness will be limited by the high pass filter bandwidth.

- The injection signal decoupling method can reduce the speed ripple significantly by decoupling the positive and negative components/harmonics of the measured current.
- The injection signal decoupling method will not affect the system dynamic stiffness except at the injected frequency.
- In induction machines, it is difficult to obtain the exact ω_e, thus, after signal rotation an angle $(\theta_e + \theta_c)$, the injected signal components would not be a pure dc value/offset.
- In practice, after rotating an angle $(\theta_e + \theta_c)$, the harmonic components values can be calculated in real-time and are subtracted from the estimated back-EMF signals.
- The speed limit for the injection signal decoupling method is around the frequency where the signal-to-noise ratio degrades significantly.
- The speed limit for the injection-based method can be pushed lower by the signal-to-noise ratio improvement with voltage-second sensing technology.
- MRAS-based parameter estimation method can estimate machine parameters in self-sensing mode at different speeds and different load conditions.
- The test results of MRAS-based parameter estimation in self-sensing mode are similar to the test results with encoder feedback.
- L_m and R_r are not speed dependent, but estimation error increases as the speed decreases due to volt-second errors.

- To decrease the bandwidth while maintaining the flux estimation accuracy requires more accurate voltage information, especially at low speeds.
- Accurate terminal voltage information is required to improve the MRAS-based parameter estimation, especially at low speeds.

9.1.4 Real-time Parameter Estimation System

- The real-time parameter estimation system utilizes the advantages of the two parameter estimation methods and can estimate the full set of machine parameters over a wide operating range.
- The real-time parameter estimation system cannot estimate all the parameter at low speed conditions, due to the limitation of the self-sensing.
- The real-time parameter estimation system selects certain methods based on system operating region.
- The real-time parameter estimation system is executed in DSP controllers with a certain processing sequence.
- In self-sensing mode, the real-time parameter estimation system can provide reliable estimates, with various machine initial parameter errors.

9.1.5 Comparative Evaluation and Simplifications of the Two Methods

- The MRAS-based method can only estimate magnetizing inductance with no or light load conditions. The flux injection-based method can work over the entire load range.

- The MRAS-based method is only suitable for steady state conditions. The flux injection-based method works in both steady state and dynamic conditions.
- The computational load of both two methods can be reduced in a DSP system.
- Based on the properties of each method, the simplification approaches are proposed respectively for DB-DTFC drives.
- After the simplification approaches, the computational time of MRAS-based method is reduced by 43% and the computational time of flux injection-based method is reduced by 25%.

9.1.6 DB-DTFC Drives Dynamics

- The torque command tracking and the speed command tracking are two metrics to show the system dynamic torque production response.
- DBDTFC has higher torque command tracking bandwidth and smaller phase lag than IFOC.
- In the torque command tracking phase plot, DB-DTFC has a phase lag that is linear with frequency, and which yields much lower phase lag than IFOC.
- The IFOC current regulator bandwidth is the main limitation for the torque command tracking and speed command tracking.
- Computed torque command feedforward is actually a reference for the torque loop.

- Single sine wave should be used for improving the coherence at high frequency and Anti-aliasing filter should be added to improve the accuracy.
- With encoder feedback, DB-DTFC drive has higher speed command tracking bandwidth and smaller phase lag than IFOC. DB-DTFC almost achieves the maximum measurable speed command tracking frequency (500 Hz) with 1 kHz motion controller sampling frequency.
- Machine parameter affects the DB-DTFC back-EMF self-sensing drive speed command tracking bandwidth.
- The DB-DTFC back-EMF self-sensing drive is more sensitive to magnetizing inductance than to resistance.
- In the self-sensing mode with nameplate parameters, the speed command tracking bandwidth of DB-DTFC drive is much higher than it is in IFOC drive, especially at medium and high speeds.
- In the self-sensing mode, the proposed parameter estimation system can provide accurate machine parameters and extend the DB-DTFC self-sensing speed command tracking bandwidth.

9.2 Contributions

The following list summarizes the key contributions of this research.

9.2.1 Real-time Parameter Estimation System with Self-Sensing DB-DTFC

- Developed an operating region-based parameter estimation system that integrates both MRAS-based and flux injection-based methods and extracts a full set of machine parameters over a wide operating range in self-sensing mode.
- Developed an approach for an appropriate converging sequence of the proposed real-time parameter estimation system with incorrect initial parameters.
- Developed two approaches to reduce the erroneous and the real speed ripple, caused by the injected signal, for injection-based parameter estimation in self-sensing mode.
- Developed a decoupling method for injection-based parameter estimation in DB-DTFC self-sensing drives, without affecting torque and speed dynamics.
- Developed an electrical position estimation block to improve the signal quality of positive and negative sequence components for flux injection-based methods.
- Developed the executive sequence for the real-time parameter estimation system based on speed and load conditions.
- Developed a synergy of the DB-DTFC self-sensing drive with MRAS-based parameter estimation method for L_m and R_r estimation.

- Developed a synergy of the DB-DTFC self-sensing drive with flux injection based parameter estimation method for L_{ls}, R_s and R_r estimation.

9.2.2 Real-time Parameter Estimation for Encoder-Based DB-DTFC

- Developed a general solution for flux injection-based parameter estimation in induction machine DB-DTFC drive with encoder feedback.
- Developed a simplification approach for MRAS-based parameter estimation method by utilizing the flux observer already embedded in DB-DTFC drives.
- Developed a simplification approach in the signal processing procedures for flux injection-based parameter estimation method in DB-DTFC drives.
- Developed a methodology of appropriate injection frequency selection for estimating different parameters in flux injection-based method.
- Developed a methodology for improving the estimation accuracy of the injection-based method by considering rotor bar skin effect.
- Developed an approach to investigate the torque ripple between the pulsating flux injection in DB-DTFC drives and d-axis injection for traditional IFOC drives at different speeds.
- Develop the methodology for MRAS gains tuning for optimized convergence time without affecting system stability in parameter estimation.

- Developed an approach to compare the advantages of synergies of the DB-DTFC drives with the two parameter estimation methods with encoder feedback.

9.2.3 High Frequency Speed Command Tracking in Self-sensing Mode

- Developed a methodology for high frequency speed command tracking bandwidth evaluation for comparing IFOC and DB-DTFC in the self-sensing mode.
- Developed an approach to evaluate the improvements with real-time parameter estimation system for both DB-DTFC and IFOC drives over a wide speed and torque range in self-sensing mode.
- Developed a method to investigate the parameter sensitivities on the maximum speed command tracking bandwidth between DB-DTFC and IFOC drives.
- Developed two metrics for high torque dynamics evaluation through torque command tracking and speed command tracking.

9.2.4 Robustness of Back-EMF Based Self-sensing

- Developed a back-EMF based self-sensing structure for IM machines via observer in IM DB-DTFC, which includes back-EMF state filter, back-EMF tracking observer and cascaded motion observer.

- Developed the speed dependent back-EMF state filter bandwidth method to improve back-EMF self-sensing performance at low operating speeds.
- Developed a methodology to identify the parameter sensitivities of the synergies between DB-DTFC and IFOC with the back-EMF based self-sensing, especially at low and extra low speeds.
- Investigated the robustness, stability and estimation accuracy of the proposed back-EMF based self-sensing technology.

9.3 Recommended Future Work

In addition to the content already presented in this thesis, some recommended future work is described as follows:

9.3.1 State Filter System Design

- To develop a real-time dynamic loss modeling for system loss minimization including the induction machine losses as well as the inverter losses using DB-DTFC.
- To develop a state filter based on the induction machine model to generate feasible flux command trajectories based on different load profiles.
- To investigate the physical model-based torque command state filter and speed command state filter for avoiding infeasible torque and speed commands.

9.3.2 Voltage Sensor for DB-DTFC Drives

- To install voltage sensors with different bandwidth for providing the motor terminal voltage, which is more accurate than the voltage command for machine control.
- To improve the performance of both parameter estimation methods by using the measured voltage, especially at low speeds.
- To propose a methodology for the appropriate voltage sensor selection to ensure accuracy voltage delivery and economic cost.
- To quantitatively evaluate the improvements in torque and flux control accuracy as well as self-sensing performance with different bandwidth voltage sensors.

9.3.3 General Solution for Observer Based Self-Sensing

- To identify the differences between back-EMF tracking, flux tracking and voltage tracking for the motion control self-sensing.
- To develop a methodology for optimized signal selection of the inputs to the tracking observer.
- To investigate the benefits and the limits of different physics-based discrete time models for processing the selected signal.
- To develop a general solution of observer-based self-sensing, especially focus on the low speed performance.

9.3.4 Induction Machine System Loss Minimization

- To develop a real-time dynamic loss modeling for system loss minimization including the induction machine losses as well as the inverter losses using DB-DTFC.
- To investigate the loss spatial distribution within the induction machine as well as the loss partitioning within the inverter.
- To investigate the scaling effect of loss manipulation for high power machines

Bibliography

[1] R.D. Lorenz, "The emerging role of dead-beat, direct torque and flux control in the future of induction machine drives," in *Proc. 2008 11th International Conference on Optimization of Electrical and Electronic Equipment. OPTIM*, 2008, pp. XIX–XXVII.

[2] N.T. West, "Effective real time implementation of dead-beat direct torque and flux control for AC induction machines by effective real time implementation," Master's Thesis, University of Wisconsin, Madison, WI, 2006.

[3] T. Obermann, "Deadbeat-direct torque and flux control motor drive over a wide speed, torque and flux operating space using a single control law," Master's Thesis, University of Wisconsin, Madison, 2010.

[4] D.W. Novotny, T.A. Lipo, T.M. Jahns, *Introduction to Electric Machines and Drives*. Wisconsin Electric Machine and Power Electronic Consortium, 2009.

[5] D.W. Novotny and T.A. Lipo, *Vector Control and Dynamics of AC Drives*. New York: Oxford University Press Inc, 1996.

[6] P.L. Jansen, "The ingegration of state estimation, control, and design for induction machines," Ph.D. dissertation, University of Wisconsin, Madison, WI, 1994.

[7] Y. Wang, "Investigation of loss manipulation in drives via Integration of multi-level inverters with deadbeat-direct torque and flux control," Master's Thesis, University of Wisconsin, Madison, WI, 2013.

[8] P.L. Jansen and R.D. Lorenz, "A physically insightful approach to the design and accuracy assessment of flux observers for field oriented induction machine drives," *IEEE Trans. Ind. Appl.*, vol. 30, no. 1, pp. 101–110, 1994.

[9] G.C. Verghese and S.R. Sanders, "Observers for flux estimation in induction machines," *IEEE Trans. Ind. Electron.*, vol. 35, no. 1, pp. 85–94, 1988.

[10] H. Rehman, a Derdiyok, M.K. Guven, and L. X. L. Xu, "A new current model flux observer for wide speed range sensorless control of an induction machine," *IEEE Transactions on Power Electronics*, vol. 17. pp. 1041–1048, 2002.

[11] K.D. Hurst, T.G. Habetler, G. Griva, F. Profumo, and P.L. Jansen, "A self-tuning closed-loop flux observer for sensorless torque control of standard induction machines," *IEEE Trans. Power Electron.*, vol. 12, no. 5, p. 807–815, Sep., 1997.

[12] N.T. West and R.D. Lorenz, “Digital implementation of stator and rotor flux-linkage observers and a stator-current observer for deadbeat direct torque control of induction machines,” *IEEE Trans. Ind. Appl.*, vol. 45, no. 2, p. 729–736, Mar./Apr., 2009.

[13] C. Lascu, I. Boldea, and F. Blaabjerg, “A modified direct torque control for induction motor sensorless drive,” *IEEE Trans. Ind. Appl.*, vol. 36, no. 1, pp. 122–130, 2000.

[14] F. Briz, M.W. Degner, and R.D. Lorenz, “Analysis and design of current regulators using complex vectors,” *IEEE Trans. Ind. Appl.*, vol. 36, no. 3, pp. 817–825, 2000.

[15] H. Kim, M.W. Degner, J. M. Guerrero, F. Briz, and R.D. Lorenz, “Discrete-time current regulator design for AC machine drives,” *IEEE Trans. Ind. Appl.*, vol. 46, no. 4, pp. 1425–1435, 2010.

[16] S. N. Vukosavic and E. Levi, “A Method for Transient Torque Response Improvement in Optimum Efficiency Induction Motor Drives,” *IEEE Trans. Energy Convers.*, vol. 18, no. 4, pp. 484–493, 2003.

[17] A. M. Khambadkone and J. Holtz, “Fast current control for low harmonic distortion at low switching frequency,” *IEEE Trans. Ind. Electron.*, vol. 45, no. 5, pp. 745–751, 1998.

[18] S. Sangwogwanich, S. Okuma, Y. Uchikawa, K. Iwata, and M. Ishida, “Time-Optimal Single-Step Velocity Response Control Scheme for Field-Oriented Induction Machines Considering Saturation Level,” *IEEE Trans. Power Electron.*, vol. 6, no. 1, pp. 108–117, 1991.

[19] R.D. Lorenz, “ME 547, Physics-based Modeling for Computer Control Handout 07.”

[20] A.R. Bergen and J. R. Ragazzini, “Sampled-data processing techniques for feedback control systems,” *AIEE Trans.*, vol. 73, no. 600, pp. 236–247, 1954.

[21] B.H. Kenny, “Deadbeat-direct torque and flux control of induction machine using self-sensing at low and zero speed,” Ph.D. dissertation, University of Wisconsin, Madison, WI, 2001.

[22] C.M. Bouxsein, “Injection-based self-sensing with deadbeat-direct torque and flux control for surface-mounted PM synchronous machines,” Master’s Thesis, University of Wisconsin, Madison, WI, 2015.

[23] B. F. Bradley, “Loss minimizing fluxtrajectories for repetitive known cyclical loading in deadbeat-direct torque and flux control induction machine drives,” Master’s Thesis, University of Wisconsin, Madison, WI, 2012.

[24] Z.D. Hurst, “Evaluation of Dynamic Trajectories for Deadbeat- Direct Torque and Flux Control (DB-DTFC) during Voltage Limited Operation by,” 2011.

[25] Y. Shi, “Investigation of loss minimizing stator flux trajectories for dynamic load trajectories on induction machine under deadbeat-direct torque and flux control,” Master’s Thesis, University of Wisconsin, Madison, WI, 2014.

[26] J.S. Lee, R.D. Lorenz, and M. Anibal Valenzuela, “Time optimal and loss minimizing deadbeat-direct torque and flux control for interior permanent magnet synchronous machines,” *2012 IEEE Energy Convers. Congr. Expo.*, pp. 2568–2575, 2012.

[27] T.R. Obermann, Z.D. Hurst, and R.D. Lorenz, “Deadbeat-direct torque & flux control motor drive over a wide speed, torque and flux operating space using a single control law,” in *2010 IEEE Energy Conversion Congress and Exposition, ECCE 2010 - Proceedings*, 2010, pp. 215–222.

[28] B.E. Heinbokel, “Robustness analysis and evaluation of deadbeat-direct torque and flux control for induction machines,” Master’s Thesis, University of Wisconsin, Madison, WI, 2008.

[29] W. Xu, “Dynamic loss modeling for loss minimizing control of IPMSM using DB-DTFC not operating in voltage or current limits,” Ph.D. dissertation, University of Wisconsin, Madison, WI, 2013.

[30] S. Kim and S. Sul, “Sensorless control of AC motor — Where are we now?,” in *Proc. 2011 Int. Conf. Electrical Machines and Systems. ICEMS*, 2011, pp. 1–6.

[31] J. Holtz, “Sensorless control of induction machines with or without signal injection?,” *IEEE Trans. Ind. Electron.*, vol. 53, no. 1, p. 7–30, Feb., 2006.

[32] R.D. Lorenz, “Practical issues and research opportunities when implementing zero speed sensorless control,” *Electrical Machines and Systems, 2001. ICEMS 2001. Proceedings of the Fifth International Conference on*, vol. 1. pp. 1–10 vol.1, 2001.

[33] H.M. Flieh, “Self-sensing deadbeat-direct torque and flux control for surface mount permanent magnet synchronous machine,” Master’s Thesis, University of Wisconsin, Madison, WI, 2014.

[34] T.F. Graf, “Implementation and evaluation of non-injection based flux tracking self-sensing for SPMSMs from zero to high speeds using a voltage sensor,” Master’s Thesis, University of Wisconsin, Madison, WI, 2014.

[35] M.J. Corley, “Position and velocity estimation of PMSM using terminal measurements,” Master’s Thesis, University of Wisconsin, Madison, WI, 1993.

[36] C.-Y. Yu, “Variable flux, DC bus voltage control, and self-sensing for flux intensifying IPMSM,” Ph.D. dissertation, University of Wisconsin, Madison, WI, 2014.

[37] J. Holtz, “Sensorless position control of induction motors-an emerging technology,” *IEEE Trans. Ind. Electron.*, vol. 45, no. 6, pp. 840–851, 1998.

[38] F. Genduso, R. Miceli, C. Rando, and G.R. Galluzzo, “Back-EMF Sensorless Control Algorithm for High Dynamics Performances PMSM,” *IEEE Trans. Ind. Appl.*, vol. 57, no. 6, p. 1–9, Jun., 2009.

[39] P. Kshirsagar *et al.*, “Implementation and sensorless vector-control design and tuning strategy for SMPM machines in fan-type applications,” *IEEE Trans. Ind. Appl.*, vol. 48, no. 6, p. 2402–2413, Nov./Dec., 2012.

[40] Y. Li, Z.Q. Zhu, D. Howe, and C.M. Bingham, “Improved rotor position estimation in extended back-EMF based sensorless PM brushless AC drives with magnetic saliency,” in *Proc. 2007 IEEE Int. Electr. Mach. Drives Conf. IEMDC*, 2007, vol. 1, pp. 214–219.

[41] P.M. Johnson, K. Bai, and X. Ding, “Back-EMF-Based Sensorless Control Using the Hijacker Algorithm for Full Speed Range of the Motor Drive in Electrified Automobile Systems,” *IEEE Trans. Transp. Electrif.*, vol. 1, no. 2, p. 126–137, Aug., 2015.

[42] A. Darba, F. De Belie, and J. Melkebeek, “Sensorless commutation and speed control of Brushless DC-machine drives based on the back-EMF symmetric threshold-tracking,” in *Proc. 2013 IEEE International Electric Machines and Drives Conference, IEMDC*, 2013, pp. 492–497.

[43] R.W. Hejny, “Degradation of dynamic stiffness at low speeds when using back-emf tracking for closed loop speed control,” Master’s Thesis, University of Wisconsin, Madison, WI, 2008.

[44] J. Holtz and Q. Juntao, “Sensorless vector control of induction motors at very low speed using a nonlinear inverter model and parameter identification,” *Ind. Appl. IEEE Trans.*, vol. 38, no. 4, pp. 1087–1095, 2002.

[45] S. Morimoto, K. Kawamoto, M. Sanada, and Y. Takeda, “Sensorless control strategy for salient-pole PMSM based on extended EMF in rotating reference frame,” *IEEE Trans. Ind. Appl.*, vol. 38, no. 4, p. 1054–1061, Jul./Aug., 2002.

[46] H. Kim, M.C. Harke, and R.D. Lorenz, “Sensorless control of interior permanent-magnet machine drives with zero-phase lag position estimation,” *IEEE Trans. Ind. Appl.*, vol. 39, no. 6, p. 1726–1733, Nov./Dec., 2003.

[47] C. Schauder, “Adaptive speed identification for vector control of induction motors without rotational transducers,” *Ind. Appl. IEEE Trans.*, vol. 28, no. 5, p. 1054–1061, Sep./Oct., 1992.

[48] T. Saitoh, T. Okuyama, and T. Matsui, “An automated secondary resistance identification scheme in vector controlled induction motor drives,” in *IEEE Industry Applications Society Annual Meeting*, 1989, pp. 594–600 vol.1.

[49] Y. H. Kim and Y.S. Kook, “High performance IPMSM drives without rotational position sensors using reduced-order EKF,” *IEEE Trans. Energy Convers.*, vol. 14, no. 4, pp. 868–873, 1999.

[50] S.K. Sul, “Control of Power Electronics - past, present, future of high frequency signal injection techniques,” *Invit. Present. WEMPEC 35th Annu. Rev.*, no. May, 2016.

[51] H. Kubota, K. Matsuse, and T. Nakano, “DSP- based speed adaptive flux observer of induction motor,” *IEEE Trans. Ind. Appl.*, vol. 29, no. 2, p. 344–348, Mar./Apr., 1993.

[52] G. Yang and T.-H. Chin, “Adaptive-speed identification scheme for a vector-controlled speed sensorless inverter-induction motor drive,” *IEEE Trans. Ind. Appl.*, vol. 29, no. 4, pp. 820–825, 1993.

[53] H. Kubota, I. Sato, Y. Tamura, K. Matsuse, H. Ohta, and Y. Hori, “Regenerating-Mode Low-Speed Operation of Sensorless Induction Motor Drive,” *IEEE Trans. Ind. Appl.*, vol. 38, no. 4, pp. 1081–1086, 2002.

[54] H. Kubota and K. Matsuse, “Speed sensorless field-oriented control of induction motor with\nrotor resistance adaptation,” *IEEE Trans. Ind. Appl.*, vol. 30, no. 5, pp. 1219–1224, 1994.

[55] A. Qiu and H. Kojori, “Sensorless control of permanent magnet synchronous motor using extended Kalman filter,” *Can. Conf. Electr. Comput. Eng. 2004 (IEEE Cat. No.04CH37513)*, pp. 1557–1562, 2004.

[56] M. Barut, S. Bogosyan, and M. Gokasan, “Speed-sensorless Eestimation for induction motors using extended kalman filters,” *IEEE Trans. Ind. Electron.*, vol. 54, no. 1, pp. 272–280, 2007.

[57] Y. Zhang, Z. Zhao, T. Lu, L. Yuan, W. Xu, and J. Zhu, “A comparative study of luenberger observer , sliding mode observer and extended kalman filter for sensorless vector control of induction motor drives,” in *Energy Conversion Congress and Exposition*, 2009, pp. 2466–2473.

[58] Y.-R. Kim, S.-K. Sul, M.-H. Park, I. Motor, and U. Extended, "Speed sensorless vector control of induction motor using extended Kalman filter," *Ind. Appl. IEEE Trans.*, vol. 30, no. 5, pp. 1225–1233, 1994.

[59] P.L. Jansen and R.D. Lorenz, "Transducerless position and velocity estimation in induction and salient AC machines," *IEEE Trans. Ind. Appl.*, vol. 31, no. 2, p. 240–247, Mar./Apr., 1995.

[60] H. K. Khalil, E.G. Strangas, and S. Jurkovic, "Speed observer and reduced nonlinear model for sensorless control of induction motors," *IEEE Trans. Control Syst. Technol.*, vol. 17, no. 2, p. 327–339, Mar., 2009.

[61] M. Montanari, S. M. Peresada, C. Rossi, and A. Tilli, "Speed Sensorless Control of Induction Motors Based on a Reduced-Order Adaptive Observer," *IEEE Trans. Control Syst. Technol.*, vol. 15, no. 6, p. 1049–1064, Nov., 2007.

[62] L. A. Jones and J.H. Lang, "A state observer for the permanent-magnet synchronous motor," *IEEE Trans. Ind. Electron.*, vol. 36, no. 3, pp. 374–382, 1989.

[63] H. Kim, "Online parameter estiamtion, current regulation, and self-sesning for IPM synchroous machine drives," Ph.D. dissertation, University of Wisconsin, Madison, WI, 2004.

[64] R.D. Lorenz, "Observers and state filters in drives and power electronics," in *Proc. 2002 International Conference on Optimization of Electrical and Electronics Equipment OPTIM*, 2002, vol. 2, no. 2, pp. 4–12.

[65] B. Chen, W. Yao, F. Chen, and Z. Lu, "Parameter sensitivity in sensorless induction motor drives with the adaptive full-order observer," *IEEE Trans. Ind. Electron.*, vol. 62, no. 7, pp. 4307–4318, 2015.

[66] M.S. Zaky and M.K. Metwaly, "Sensorless Torque/Speed Control of Induction Motor Drives at Zero and Low Frequencies with Stator and Rotor Resistance Estimations," *IEEE J. Emerg. Sel. Top. Power Electron.*, vol. 4, no. 4, pp. 1416–1429, 2016.

[67] R. Kumar and S. Das, "Eigenvalue-based relative parameter sensitivity analysis for optimised performance of sensorless induction motor drives," *IET Electr. Power Appl.*, vol. 10, no. 8, pp. 723–734, 2016.

[68] S. Bolognani, L. Peretti, and M. Zigliotto, "Parameter sensitivity analysis of an improved open-loop speed estimate for induction motor drives," *IEEE Trans. Power Electron.*, vol. 23, no. 4, pp. 2127–2135, 2008.

[69] H.A. Toliyat, E. Levi, and M. Raina, “A review of RFO induction motor parameter Eestimation techniques,” *IEEE Power Engineering Review*, vol. 22, no. 7. p. 52, 2002.

[70] R. Krishnan and A.S. Bharadwaj, “A review of parameter sensitivity and adaptation in indirect vector controlled induction motor drive systems,” *IEFE Trans. POWFR FLECTRONICS*, vol. 6, no. 1, 1991.

[71] W.H. Kwon, C.H. Lee, K.S. Youn, and G.H. Cho, “Measurement of rotor time constant taking into account magnetizing flux in the induction motor,” *IEEE Ind. Appl. Soc. Annu. Meet.*, no. 2, pp. 88–92 vol.1, 1994.

[72] P. Vas, “Sensorless Vector and Direct Torque Control,” *Power*, vol. 1., p. 768, 1998.

[73] A.M. Khambadkone and J. Holtz, “Vector-Controlled Induction Motor Drive with a Self-Commissioning Scheme,” *IEEE Trans. Ind. Electron.*, vol. 38, no. 5, pp. 322–327, 1991.

[74] D.W. Novotny and T.A. Lipo, “An Automated Rotor Time Constant Measurement System for Indirect Field-Oriented Drives,” *IEEE Trans. Ind. Appl.*, vol. 24, no. 1, pp. 151–159, 1988.

[75] M. Ruff, A. Bunte, and H. Grotstollen, “A new self-commissioning scheme for an asynchronous motor drive system,” in *IEEE Industry Applications Society Annual Meeting*, 1994, pp. 616–623 vol.1.

[76] M. Sumner and G. M. Asher, “Autocommissioning for voltage-referenced voltage-fed vector-controlled induction motor drives,” *Electr. Power Appl. IEE Proc. B*, vol. 140, no. 3, pp. 187–200, 1993.

[77] M. Sumner and G.M. Asher, “Self-commissioning for voltage-referenced voltage fed vector controlled induction motor drives,” *PESC `92 Rec. 23rd Annu. IEEE Power Electron. Spec. Conf.*, no. 1, pp. 0–5, 1992.

[78] C. Paleologu, J. Benesty, and S. Ciochiňa, “A robust variable forgetting factor recursive least-squares algorithm for system identification,” *IEEE Signal Process. Lett.*, vol. 15, pp. 597–600, 2008.

[79] C. H. Fang, S. K. Lin, and S. J. Wang, “On-line parameter estimator of an induction motor at standstill,” *Control Eng. Pract.*, vol. 13, no. 5, pp. 535–540, 2005.

[80] R.P. Vieira, R.Z. Azzolin, and H.A. Grundling, “Parameter identification of a single-phase induction motor using RLS algorithm,” in *2009 Brazilian Power Electronics Conference, COBEP2009*, 2009, pp. 517–523.

[81] Y. He, Y. Feng, and Y. Wang, “Estimating the electrical parameters of induction motors at standstill using RLS method,” in *2nd International Symposium on Power Electronics for Distributed Generation Systems, PEDG 2010*, 2010, pp. 358–363.

[82] Y. He, Y. Wang, Y. Feng, and Z. Wang, “Estimating the electrical parameters of induction motors at standstill using RLS method,” *IEEE Trans. Power Electron.*, vol. 27, no. 2, pp. 905–915, 2012.

[83] J.A. Riveros *et al.*, “Parameter identification of multiphase induction machines with distributed windingspart 2: Time-domain techniques,” *IEEE Trans. Energy Convers.*, vol. 27, no. 4, pp. 1067–1077, 2012.

[84] M. Vélez-Reyes, W.L. Fung, and J.E. Ramos-Torres, “Developing robust algorithms for speed and parameter estimation in induction machines,” *Proc. IEEE Conf. Decis. Control*, vol. 3, pp. 2223–2228, 2001.

[85] P. J. R. de Oliveira, P. F. Seixas, L. A. Aguirre, and Z. M. A. Peixoto, “Parameter estimation of a induction machine using a continuous time model,” *Iecon ’98 - Proc. 24th Annu. Conf. Ieee Ind. Electron. Soc. Vols 1-4*, pp. 292–296, 1998.

[86] T. Matsuo and T.A. Lipo, “A Rotor Parameter Identification Scheme for Vector-Controlled Induction Motor Drives,” *IEEE Trans. Ind. Appl.*, vol. IA-21, no. 4, p. 624–632, May, 1985.

[87] H.A. Toliyat and A.A.G. Hosseiny, “Parameter estimation algorithm using spectral analysis for vector controlled induction motor drives,” *IEEE Int. Symp. Ind. Electron.*, pp. 90–95, 1993.

[88] H. Sugimoto and S. Tamai, “Secondary resistance identification of an induction-motor applied model reference adaptive system and its characteristics,” *IEEE Trans. Ind. Appl.*, vol. IA-23, no. 2, pp. 296–303, 1987.

[89] Y. S. Kwon, J. H. Lee, S. H. Moon, B. ki Kwon, C. H. Choi, and J. K. Seok, “Standstill parameter identification of vector-controlled induction motors using the frequency characteristics of rotor bars,” *IEEE Trans. Ind. Appl.*, vol. 45, no. 5, pp. 1610–1618, 2009.

[90] M. Carraro and M. Zigliotto, “Automatic Parameter identification of inverter-fed induction motors at standstill,” *IEEE Trans. Ind. Electron.*, vol. 61, no. 9, pp. 4605–4613, 2014.

[91] L. Peretti and M. Zigliotto, “Automatic procedure for induction motor parameter estimation at standstill,” *IET Electr. Power Appl.*, vol. 6, no. 4, p. 214, 2012.

[92] D. E. Borgard, G. Olsson, and R. D. Lorenz, “Accuracy issues for parameter estimation of field oriented induction machine drives,” *IEEE Trans. Ind. Appl.*, vol. 31, no. 4, pp. 795–801, 1995.

[93] H. Chai and P. P. Acarnley, “Induction motor parameter estimation algorithm using spectral analysis,” *IEE Proc. Electr. Power Appl.*, vol. 139, no. 3, pp. 165–174, 1992.

[94] K. Tungpimolrut, F.-Z. Peng, and T. Fukao, “A robust rotor time constant estimation method for vector control\nof induction motor under any operating conditions,” *Proc. IECON’94 - 20th Annu. Conf. IEEE Ind. Electron.*, vol. 1, 1994.

[95] L. He, S. Cheng, Y. Du, R.G. Harley, and T.G. Habetler, “Stator temperature estimation of direct-torque-controlled induction machines via active flux or torque injection,” *IEEE Trans. Power Electron.*, vol. 30, no. 2, pp. 888–899, 2015.

[96] L. He, R.G. Harley, and T.G. Habetler, “A DC-flux-injection Approach for Thermal Monitoring of Induction Machines with Direct Torque Control,” pp. 2115–2122, 2013.

[97] R.D. Lorenz and D. B. Lawson, “A simplified approach to continuous on-line tuning of field-oriented induction machine drives,” *IEEE Trans. Ind. Appl.*, vol. 26, no. 3, pp. 420–424, 1990.

[98] K.T. Hung and R.D. Lorenz, “A rotor flux error-based, adaptive tuning approach for feedforward field oriented induction machine drives,” *Conf. Rec. 1990 IEEE Ind. Appl. Soc. Annu. Meet.*, pp. 589–594, 1990.

[99] L. Zhen and L. Xu, “Sensorless field orientation control of induction machines based on a mutual MRAS scheme,” *IEEE Trans. Ind. Electron.*, vol. 45, no. 5, pp. 824–831, 1998.

[100] K. Wiedmann and A. Mertens, “Self-sensing control of PM synchronous machines including online system identification based on a novel MRAS approach,” in *3rd IEEE International Symposium on Sensorless Control for Electrical Drives, SLED 2012*, 2012.

[101] L.J. Garces, “Parameter adaption for the speed-controlled Sstatic AC drive with a squirrel-cage induction motor,” *IEEE Trans. Ind. Appl.*, vol. IA-16, no. 2, pp. 173–178, 1980.

[102] M. Koyama, M. Yano, I. Kamiyama, and S. Yano, “Microprocessor-based vector control system for induction motor drives with rotor time constant identification function,” *Ind. Appl. IEEE Trans.*, vol. IA-22, no. 3, pp. 453–459, 1986.

[103] T.M. Rowan, R.J. Kerkman, and D. Leggate, “A simple on-line adaption for indirect field orientation of an induction machine,” *IEEE Trans. Ind. Appl.*, vol. 27, no. 4, pp. 720–727, 1991.

[104] R. Krishnan and F.C. Doran, “A method of sensing line voltages for parameter adaptation of inverter-fed induction motor servo drives,” *IEEE Trans. Ind. Appl.*, vol. IA-23, no. 4, pp. 617–622, 1987.

[105] G. Griva, M. Cipolla Ficarra, and F. Profumo, “Design of a Speed Regulator for Induction Motor Drives Based on Model Reference Robust Control,” *Ind. Electron. ISIE ’97., Proc. IEEE Int. Symp.*, pp. 485–488, 1997.

[106] Y. Wang, N. Niimura, and R.D. Lorenz, “Real-Time Parameter Identification and Integration on Deadbeat-Direct Torque and Flux Control (DB-DTFC) Without Inducing Additional Torque Ripple,” *IEEE Trans. Ind. Appl.*, vol. 52, no. 4, p. 3104–3114, Jul./ Aug., 2016.